Univerzita Karlova v Praze
Matematicko-fyzikální fakulta

Dizertační práce

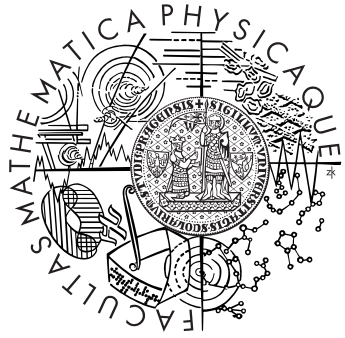

Michal Macek

Statistické aspekty kolektivní dynamiky atomových jader

Studijní program:	Fyzika, Jaderná fyzika
Vedoucí dizertační práce:	Doc. RNDr. Pavel Cejnar, Dr.
	Ústav částicové a jaderné fyziky

Charles University in Prague
Faculty of Mathemetics and Physics

PhD Thesis

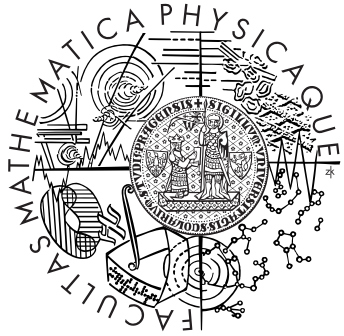

Michal Macek

Statistical aspects of collective dynamics in atomic nuclei

Study Programme: Physics, Nuclear Physics
Thesis Supervisor: Doc. RNDr. Pavel Cejnar, Dr.
Institute of Particle and Nuclear Physics

Contents

Figure 1: Empedocles (cca. 495-435 BC) in his philosophical poem *On the Nature* infers that the attractive and repulsive forces of Love and Strife cause our world, Cosmos, to oscillate between the state of ultimate order and beauty, called Sphairos (the sphere), and a totally disordered state, for which he adopted the mythological name Chaos.

Název práce:	*Statistické aspekty kolektivní dynamiky atomových jader*
Autor:	*Mgr. Michal Macek*
Katedra (ústav):	*Ústav částicové a jaderné fyziky*
Vedoucí diplomové práce:	*Doc. RNDr. Pavel Cejnar, Dr.* *Ústav částicové a jaderné fyziky*
E-mail vedoucího:	cejnar@ipnp.troja.mff.cuni.cz

Abstrakt: *Tato doktorská práce poskytuje souhrn vybraných článků zabývajících se teoretickým a numerickým studiem nízkoenergetické kolektivní dynamiky atomových jader. Články byly publikovány nebo nedávno odeslány k recenzi do mezinárodních fyzikálních časopisů a autor této práce se na nich podílel jako hlavní autor nebo spoluautor. Jevy pozorované v kolektivní dynamice jader byly zkoumány s pomocí dvou často požívaných modelů a to modelu interagujících bosonů (IBM) a v menší míře geometrického kolektivního modelu (GCM). "Statistické aspekty" v názvu práce se vztahují hlavně k prolínajícím se regulárním a chaotickým typům chování, které pozorujeme jednak mezi atributy kvantových vlastních stavů, jednak v chování klasických limit modelů. Hlavní pozornost byla věnována souvislostem mezi mírami regularity/chaosu a přítomností přesných a přibližných dynamických symetrií. Důležitým předmětem studia byly rovněž souvislosti mezi vlastnostmi klasických a kvantových řešení modelů a to jednak v integrabilním režimu, jednak ve smíšeném režimu obsahujícím současně prvky regularity i chaosu.*

Title:	*Statistical Aspects of Collective Dynamics in Atomic Nuclei*
Author:	*Mgr. Michal Macek*
Department:	*Institute of Particle and Nuclear Physics*
Supervisor:	*Doc. RNDr. Pavel Cejnar, Dr.* *Institute of Particle and Nuclear Physics*
Supervisor's e-mail:	cejnar@ipnp.troja.mff.cuni.cz

Abstract: *The current PhD thesis presents a collection of selected articles related to the theoretical and numerical study of low-energy collective dynamics of atomic nuclei. The articles were published or recently submitted to international physics journals and were authored or co-authored by the author of the thesis. The effects in collective dynamics have been studied within the framework of two common models—the interacting boson model (IBM) and to a lesser extent the geometric collective model (GCM). The "statistical aspects" in the title relate predominantly to the interplay of ordered and chaotic behavior observed in properties of quantum eigenstates as well as in the classical limits of the models. The main attention was devoted to correlations between the measures of regularity/chaos and the presence of exact and approximate dynamical symmetries. An important subject of the studies were also the relationships between the properties of the classical and quantum solutions of the models both in the integrable regime as well as in the mixed regime containing elements of regularity and chaos simultaneously.*

Preface

An apparent disorder and the contrasting emergence of various types of order observed in nature have attracted the attention and imagination of people perhaps since prehistoric ages and inspired different branches of art as well as the scientific thought. It is not very clear whether this fascination will ever fade away.

In our work, we have taken a look into the realm of quantum many body systems, studying in particular the atomic nuclei, which enabled us to observe and in some cases understand a rich variety of dynamical phenomena on the verge of order and disorder. We were interested predominantly in the interconnection between different forms of symmetry (and the ways of breaking it) and the interplay of regular and chaotic features in the dynamics. Apart from studying the quantum dynamics, we inspected also the classical dynamics derived from it, and looked for the correspondence between classical and quantum signatures of the phenomena.

As an analytical specimen, we have adopted the interacting boson model (IBM) of nuclear collective motion [Iach87], which had been widely used to describe the dynamics of low-energy nuclear quadrupole vibrations and rotations[1] since its formulation by Arima and Iachello in 1975 [Arim75]. The IBM is expressed entirely in the language of the group theory, which greatly facilitates the study of symmetries. Further, since it is in general non-integrable, attaining the complete integrability (hence fully regular behavior) only in some particular domains[2] of the control parameter values, it shows both the regular and chaotic dynamics [Alha90, Whel93].

The current PhD thesis summarizes the scientific results of the author obtained during the last five years in the field of order and chaos and their relation to dynamical symmetries studied in the collective nuclear dynamics. Since the main results have been already described in detail in several articles published in international refereed journals [**J1**]–[**J8***] or within conference proceedings [**P1***]–[**P8**], the current thesis is built-up substantially of the reprints of selected articles included in Appendix A. As the articles are in each case a common achievement of several collaborators, we endow each reprint with a brief review of the contents containing also a specification of the author's direct contribution. The reviews are inserted in front of each reprinted article. The reprints are preceded by Chapter 1, which provides a brief general introduction[3] into the topics of classical and quantum chaos and into the algebraic models and (generalized) dynamical symmetries,

[1] We have used here the original form of IBM, which neither includes the excitations of higher multipolarity, nor distinguishes the neutron and proton degrees of freedom, nor incorporates the fermionic degrees of freedom. Numerous extensions of the model however exist up to date, as discussed in Sec. 1.2.

[2] These correspond to various (mutually incompatible) dynamical symmetries of the model.

[3] Specific introductions are always found in the concrete articles in Appendix A.

the Chapter 2, which provides a structured synopsis of the results obtained and the Chapter 3 which contains the full list of author's publications.

Before starting the actual exposition of the topics, the author enjoys the chance to express his deep thanks to many people without whom this work, with which the author experienced plentiful moments of joy and inspiration, would not come to light. First of all it comes to Pavel Cejnar, who has been an enthusiastic, patient and inspiring advisor and indeed a great friend, to Pavel Stránský who has pioneered many things, which the author has rooted his thesis upon, and who has been a perfect companion both at school as well as on numerous common trips abroad, to Jan Dobeš for his interest and many insightful ideas which have substantially pushed forward especially the most recent common works. No less the author's thanks belong to his parents, brother and sisters for their universal support and inspiration, and to many friends with whom he had the joy to live through the last years.

The author declares that he has completed the PhD thesis himself and used only the mentioned literature. He agrees with using this PhD thesis freely.

in Prague, April 18th, 2010 Michal Macek

Chapter 1

Introduction

1.1 Chaos and Sphairos in Classical and Quantum Mechanics

This chapter will be devoted to general signatures of order and disorder observed in classical and quantum mechanics, for which we have adopted the names "sphairos" and "chaos" in the title. Both these words originate in the ancient greek culture[1] and while the usage of sphairos remained limited to denote the geometrical sphere (for ancient Greeks the most perfect geometrical body), the word chaos infiltrated the general vocabulary of numerous languages and attained various meanings.

During the twentieth century, a mathematically defined concept of deterministic chaos was introduced to describe a broad collection of phenomena encountered in classical non-linear systems[2] studied in subjects ranging from physics to social sciences. Later the term "quantum chaos" found its application also in quantum mechanics, although quantum mechanics is a strictly linear theory. The term became popular in connection with effects observed in quantum systems, whose classical counterparts are chaotic[3]. We shall discuss this in more detail below.

In all our further considerations, we shall limit our attention to the physics of Hamiltonian (i.e. energy-conserving) systems with a finite number of d degrees of freedom. We shall overview briefly some relevant phenomenology of classical and quantum chaos (and sphairos) in combination with some methods that we have used to obtain results underlying this thesis (see the Chapter 2 and the Appendix A). A more detailed and general introduction into classical chaos can be found in the monographs [Lich83, Nico95], while the Refs. [Gutz90, Stoc99, Reic92, LesH91] similarly introduce into the topics of quantum chaos.

[1] According to the greek mythology (see for example Hesiod, *Theogonia*), the structure of the world results from the more or less voluntary actions of the gods of Olympus, each of which is connected with a part of the physical universe, Cosmos. The Olympian gods were born in a sequence which begins with Chaos, a vague divine primordial entity or condition. The early greek philosophers, like Empedocles in Fig. 1, pursued for an alternative explanation of the order and disorder in the world on the basis of some inherent principles of nature, in contrast to the voluntary action.

[2] The systems governed by non-linear equations of motion.

[3] Some people prefer instead the name "quantum chaology" to describe the science concerned with quantum systems with chaotic classical counterparts, see Refs. [Berr87, LesH91].

Chaos in classical mechanics

In the Hamiltonian formulation of classical mechanics, the state of a system is described by a set of canonical coordinates q_i and their conjugate momenta p_i, $i = 1, ..., d$, which span the $2d$-dimensional phase space of the system. The time evolution of the system is governed by the Hamilton equations of motion

$$\frac{dq_i}{dt} = \frac{dH}{dp_i}\,, \qquad \frac{dp_i}{dt} = -\frac{dH}{dq_i}\,, \tag{1.1}$$

obtained as derivatives of the Hamiltonian $H(q_i, p_i) = E$, which represents the energy E of the system as a function of the canonical coordinates and momenta. The equations (1.1) are a set of $2d$ differential equations of the first order in time t for the quantities $q_i(t)$, $p_i(t)$ and therefore their solutions (trajectories) are unique. This means in particular that the phase space trajectories cannot cross (unlike trajectories in the configuration space spanned solely by q_i) [Gutz90]. If the energy is constant, the trajectories are restricted to a $(2d-1)$-dimensional energy manifold.

The term deterministic chaos relates here to the peculiar behavior of some systems for which the equations (1.1) are non-linear and in which an arbitrarily small initial deviation[4] $\delta\vec{q}(t_0), \delta\vec{p}(t_0)$ may grow exponentially in time t. Since in practice, we cannot determine the initial state of the system (hence also the actual trajectory) with infinite precision, the exponential divergence[5] of neighboring trajectories makes the long-time prediction of the motion impossible. This makes the motion seem "chaotic" although the motion equations are themselves fully deterministic [Gutz90, Lich83, Nico95].

In contrast to the dynamical picture of chaos described above, we can obtain a different (structural) picture, if we consider all the phase-space points lying on the energy manifold as possible initial conditions giving rise to a simultaneous flow of trajectories[6], similarly to a hydrodynamic flow of fluids. This flow may separate different parts of the energy manifold into distinct submanifolds of dimension $\tilde{d} \leq (2d-1)$, so that each of these submanifolds is filled with a different class of trajectories. The topology of these manifolds is markedly different, depending on whether the chaotic dynamics is present or not. Two extreme cases are represented by the integrable and the ergodic systems.

The integrable systems are completely free of chaotic behavior and their dynamics is relatively simply ordered. A classical Hamiltonian system in d dimensions is said to be integrable (see e.g. [Gutz90]) if:

1. there exist d independent integrals of motion $I_i(\vec{q}, \vec{p})$, $i = 1, .., d$, for which $dI_i/dt = \{I_i, H\} = 0$.

2. I_i are constants in involution, this means precisely that $\{I_i, I_j\} = 0$, $\forall i, j$.

[4] In the following, $\vec{q}$ and $\vec{p}$ denote the d-dimensional vectors of canonical coordinates and their conjugate momenta, respectively.

[5] Usually characterized by Lyapounov exponents, see e.g. [Lich83, Gutz90].

[6] According to the Liouville theorem, this flow in incompressible, i.e. the volume corresponding to an arbitrary collection of neighboring points is invariant as these points travel across the phase space in time, see e.g. [Lich83].

The conserved quantities I_i constrain all trajectories onto d-dimensional submanifolds immersed inside the $2d$-dimensional phase space. Additionally, the involution leads to a very special topology of the manifolds: they are equivalent to d-dimensional tori[7]. Notice that the Hamiltonian systems in $d = 1$ are trivially integrable, since the only necessary integral of motion is provided by the Hamiltonian itself.

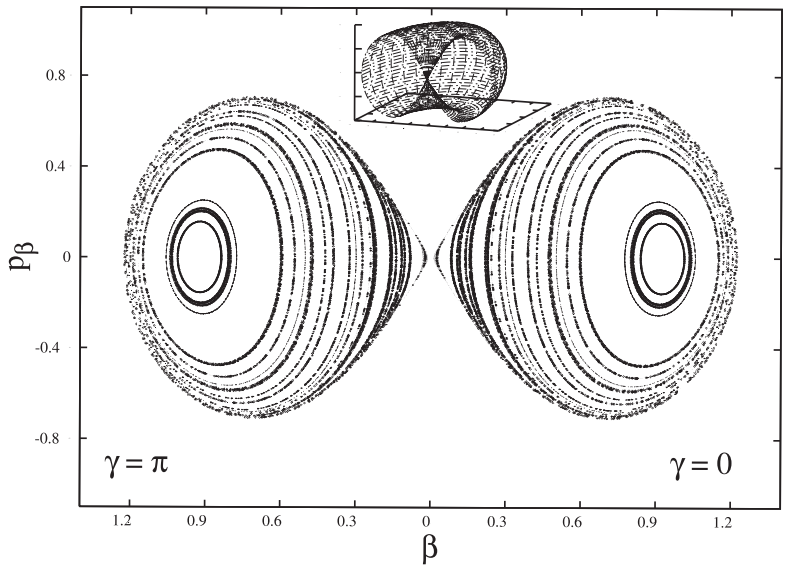

Figure 1.1: An illustration of a degenerate torus being pinched at the central vacancy (inset). The main panel displays a Poincaré section clearly revealing integrable classical dynamics in IBM generated by the Hamiltonian (1.13) with $(\eta, \chi) = (0.6, 0)$. Trajectories passing the plane of the section generate points lying on (topological) circles, which correspond to the sections through the invariant tori. (Adapted from Ref. [**J3**])

In integrable systems, it is possible to introduce a special set of canonical coordinates—the so called action-angle variables θ_i, J_i—in which the dynamics is explicitly linear: the actions J_i are constants of motion with $dJ_i/dt = 0$, while the angles θ_i are cyclic and change linearly with time so that $d\theta_i/dt = \omega_i = \text{const.}, \forall i$. The values of the actions J_i or alternatively of the frequencies ω_i can be used to distinguish the individual invariant tori. In some integrable systems it is possible however, that specific topological obstructions prevent any unique set of action-angles θ_i, J_i to be defined globally within the whole phase space, as it was identified in [Duis80]. The simplest of these obstructions is called monodromy [Duis80, Cush80, Sado99, Sado06] and is related to some degenerate, pinched tori (which are typically related to unstable equilibrium points of the potential energy) present in the phase space of the system, see Refs. [**J2***, **J3**] in Appendix A. An example of a pinched torus is shown in Fig. 1.1.

If the integrals of motion are absent (apart from the energy), the trajectories may explore a subset of the energy manifold with dimension higher than d. In the extreme case of the ergodic systems, the initial conditions taken in almost all points of the energy manifold evolve into trajectories, which in the $t \to \infty$ limit

[7]Content of the Arno'ld-Liouville theorem, see e.g. [Lich83].

approach arbitrarily close to any point of the energy manifold. The only exceptions to this behavior are the periodic trajectories (orbits), which are isolated in a "sea" of ergodic trajectories [Gutz90].

If the integrability is broken by a weak perturbation[8], the KAM theorem[9] clarifies that the tori do not disintegrate immediately. On the contrary, most tori survive being only slightly deformed for small values of the perturbation strength. As the perturbation strength increases, the decay starts in the vicinity of resonant tori which contain periodic trajectories (since the frequencies ω_i are in rational proportions). What happens is that the originally continuous family of periodic orbits forming the surface of the resonant torus disintegrates, leaving only a finite set of isolated periodic trajectories[10].

An extremely useful tool to visualize all the types of motion described above in systems with $d = 2$ are the Poincaré sections. We can obtain them by cutting the phase space by a plane and then registering the successive passages of individual trajectories through this plane. The two independent directions within the plane (often representing a canonical coordinate q and a momentum p conjugate to it, cf. Fig. 1.1) correspond to the remaining degrees of freedom, which are not constrained by the two equations determining the plane position and the energy manifold. In case of an integrable system, we observe either chains of isolated points (corresponding to periodic trajectories) or lines with circular topology (corresponding to quasiperiodic trajectories), which reveal the invariant tori being cut by the plane. In ergodic systems, we observe mostly random sequences of points which fill the accessible domain (constrained by the fixed energy) of a dimension higher than one, together with finite sequences of points corresponding to isolated periodic trajectories. In mixed regular/chaotic systems, the Poincaré sections consist of a combination of ergodic surfaces, which are separated by lines corresponding to the surviving KAM tori and some finite sets of points generated by the periodic trajectories.

Chaos in quantum mechanics

The notion of integrability can be transmitted into quantum mechanics naturally via the canonical quantization, where the functions defined within the phase space spanned by q_i, p_i are replaced by corresponding linear operators, such that their commutation relations parallel the behavior of classical Poisson brackets. A quantum system in d dimensions is then said to be integrable if there exists a set of d independent operators $\hat{I}_i, i = 0, ..., d$, which mutually commute $[\hat{I}_i, \hat{I}_j] = 0$ and involve also the Hamiltonian $\hat{H}$, so that $d\hat{I}_i/dt = -\frac{i}{\hbar}[\hat{I}_i, \hat{H}] = 0$. The eigenstates of the Hamiltonian are then simultaneous eigenstates of the operators $\hat{I}_i$ and are hence endowed by a set of d quantum numbers.

However, finding direct analogies for the regular and chaotic classical behavior as described in previous paragraphs is in the quantum mechanical world difficult[11], fundamentally due to the linearity of the Schrödinger equation of motion.

[8] This situation is in the literature known as soft chaos.

[9] The final form and proof is due to A. N. Kolmogorov [Kolm54], V. I. Arno'ld [Arno63] and J. Moser [Mose62], whose names are hidden in the abbreviation.

[10] The Poincaré-Birkhoff theorem specifies, that the remaining periodic trajectories form an alternating sequence of stable and unstable periodic orbits [Birk35].

[11] For example in systems with time dependent Hamiltonians (not considered in this work) the effect

In particular, the evolution operator $\exp\{-\frac{i}{\hbar}\hat{H}t\}$ acting on an arbitrary pair of states $|\phi_1\rangle$, $|\phi_2\rangle$ conserves their overlap $\langle\phi_1|\phi_2\rangle$, so that the perhaps most intuitive expectation about chaotic behavior—a kind of fast divergence of different states, similar to the divergence of chaotic classical trajectories—is not realized[12]. There are nevertheless significant differences between quantum systems whose classical counterparts show regular behavior and those whose classical counterparts are chaotic. Below, we will review briefly various aspects of this as revealed during the last about thirty years of intensive studies, which gave some justification to the term "quantum chaos".

An important and nowadays standard tool of distinguishing the signatures of chaos in quantum systems is rooted in statistical measures of correlations between eigenenergies. In 1984, Bohigas et al. [Bohi84] came with a conjecture stating that the spectra of quantum chaotic systems should display the same properties as ensembles of random matrices[13]. The appropriate ensemble depends on the symmetry of the particular system under time reversal—Gaussian orthogonal (GOE) matrices correspond to time-reversal-invariant systems, while the Gaussian unitary (GUE) matrices correspond to the non-invariant systems[14]. The random matrix ensembles show characteristic "level repulsion" (exactly or nearly degenerate levels are rare), in particular the nearest neighbor spacing (NNS) distribution is of the Wigner form

$$P(s) \approx s^{\alpha} e^{-\frac{\pi}{4}s^2}\,, \tag{1.2}$$

where s is the level spacing and $\alpha = 1, 2$ for GOE and GUE, respectively. This behavior is observed (and hence the Bohigas conjecture supported) in a wide variety of systems with chaotic classical counterparts (see e.g. [Stra09a] and references therein). In contrast, the systems with regular classical counterparts were proven to display NNS with Poisson distribution (see [Berr77])

$$P(s) \approx e^{-s}\,, \tag{1.3}$$

which in contrast displays no level repulsion[15]. The spectra of mixed regular/chaotic systems are frequently described by a one-parametric interpolation suggested by Brody [Brod81] having the form

$$P(s) \approx s^{\omega} e^{-\mathcal{N}_{\omega} s^{\omega+1}}\,, \tag{1.4}$$

with $\mathcal{N}_{\omega} = \Gamma(\frac{\omega+2)}{\omega+1})^{\omega+1}$. Setting the parameter $\omega = 0$, we obtain the Poisson distribution, while with $\omega = 1$ we reach the Wigner distribution corresponding to GOE[16]. Let us note that before actually performing the statistical analysis

of quantum suppression of chaos has been described [Berr87, Hogg82, Eise94].

[12] Detailed comparison of the time evolution of classical and quantum mechanical probability distributions can be found in Refs. [Ball98, Ball02].

[13] For an introduction to the random matrix theory see the book [Meht04].

[14] Another standard, but slightly less well known class are the systems with Kramers degeneracy, whose spectra are described by Gaussian symplectic matrices (GSE), see e.g. [Haak91].

[15] Levels differing in their quantum numbers are not mixed by the Hamiltonian and are hence allowed to cross. The complete set of quantum numbers—which is not guaranteed to exist in non-integrable systems—is provided by the commuting operators $\hat{I}_i$.

[16] Although frequently used in practice, the Brody distribution presents a mathematical interpolation lacking a physical background. An alternative distribution was derived by Berry and Robnik [Berr84] and expresses the mixed spectrum as a superposition of Poisson and Wigner types of spectra, where the first part comes from the quantization of the remnant KAM tori, while the latter corresponds to the chaotic dynamics.

in particular systems, it is important to separate the spectra corresponding to different obviously conserved quantities like the angular momentum and parity j^π. Failing to do so would lead to level degeneracies being observed even in completely chaotic systems and would bias the NNS distribution more towards the Poisson distribution.

The statistical properties of semiclassical quantum spectra, in particular the fluctuations in the level density $\rho(E)$, were shown to depend essentially on the properties of the classical periodic trajectories [Gutz90, Stoc99]. The contributions of the periodic orbits can be expressed in the form of so-called trace formulas, whose concrete forms depend on the regular/chaotic type of the classical dynamics. The first one of these was derived by Gutzwiller [Gutz71] and holds for chaotic systems with isolated periodic orbits. Later, Berry and Tabor [Berr76] formulated an expression valid in integrable systems, where the non-isolated orbits continuously cover the surfaces of the invariant tori. The periodic orbit theory can be conveniently applied in systems with hard wall potentials (classical/quantum billiards) [Stoc99], where all periodic orbits can be determined simply from the geometry of the cavity bounded by the "walls" of the potential. It becomes more difficult in systems with a "soft" potential, where the periodic orbits have to be usually discovered by detailed numerical exploration of the phase space. Nevertheless, the strongest level density fluctuations can be captured well considering only the shortest periodic orbits, as was shown in Refs. [**J2***, **J5***] in case of the interacting boson model of the nucleus, see Chapter 2 and Appendix A.

The spectral statistics are able to distinguish the regularity/chaoticity of the dynamics in a certain, sufficiently broad energy interval[17]. The information about the regular/chaotic character of individual levels[18] is however not accessible in these approaches. A useful alternative for this purpose is provided by the "lattice method" proposed by Peres in 1984 [Pere84a]. The method is not rigorously quantitative, but—rather in analogy to the Poincaré section method in classical mechanics [Gutz90]—it enables a qualitative distinction between regular and chaotic motion. Regular/chaotic dynamics is inferred from the regular/chaotic form of particular spectral lattices [Pere84a, Reic92, Ree99, Shri90].

The Peres lattices are formed by the expectation values $O_i = \langle\psi_i|\hat{O}|\psi_i\rangle$ of an arbitrary operator $\hat{O}$ plotted against the energies $E_i = \langle\psi_i|\hat{H}|\psi_i\rangle$ of the Hamiltonian eigenstates $|\psi_i\rangle$, $i = 1, 2, 3, ...$[19]. Due to arguments based on semiclassical quantization, the lattices of points (E_i, O_i), $i = 1, 2, 3, ...$ show regular patterns in integrable systems, cf. Fig. 1.2. In chaotic systems on the other hand, the Peres spectral lattices are formed by visually disordered collections of points. In partially regular systems, which are neither completely integrable nor fully chaotic, the lattices show a combination of ordered and disordered patterns. We extend the Peres method slightly and investigate also the variances of the operators $\mathrm{var}[\hat{O}] = \langle\psi_i|\hat{O}^2|\psi_i\rangle - \langle\psi_i|\hat{O}|\psi_i\rangle^2$, which bring additional information on the

[17] Such that the number of levels contained in the interval allows for a statistical analysis.

[18] According to Percival conjecture [Perc73], the spectrum of a mixed regular/chaotic system should contain statistically independent sets of levels corresponding to regular and chaotic dynamics, respectively.

[19] Note that in integrable systems, the Peres lattices coincide with the "joint spectra" of different commuting operators used to study the quantum monodromy, see [**J2***, **J3**] and references therein.

dynamical symmetry content of $|\psi_i\rangle$, see Fig. 1.2.

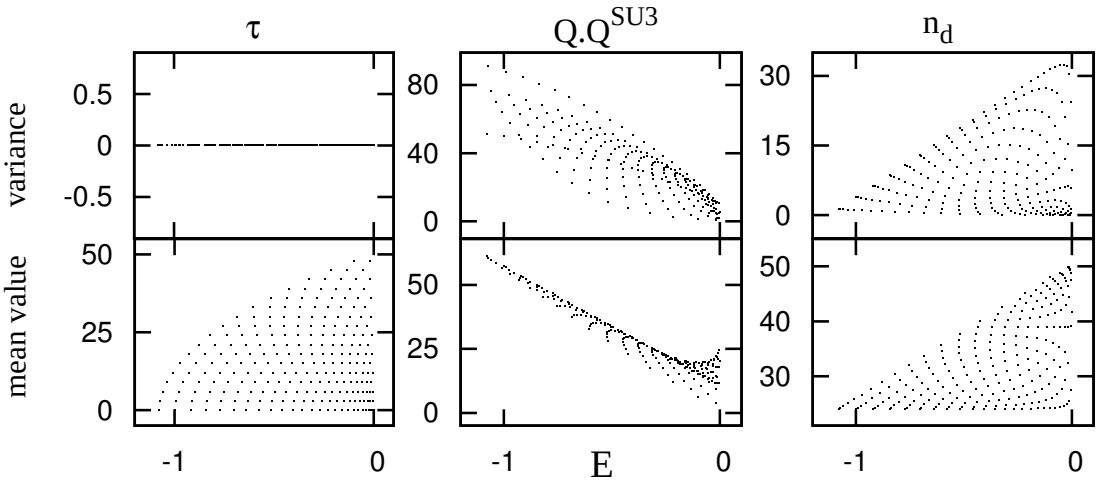

Figure 1.2: The Peres lattices corresponding to various incompatible quantities (as indicated above each column) calculated in the integrable O(6) limit of IBM with the Hamiltonian (1.13) at $(\eta, \chi) = (0, 0)$ and $N = 50$ bosons. The Peres lattices of the mean values are accompanied by the corresponding variance lattices in the upper row. The regularity of all lattices is obvious, in agreement with the Peres' proposal. The zero values of the variance of the O(5) quantum number τ (seniority) throughout the spectrum indicate the underlying O(5) symmetry.

Apart from distinguishing regular and chaotic dynamics[20], the method provides an excellent heuristic for identification of various dynamical symmetries as well as their generalizations like the partial dynamical symmetry and the quasi dynamical symmetry (explained in more detail in Sec. 1.2) as was demonstrated in Refs. [**J6***, **J7***, **J8***]. Especially the variance lattices are very convenient for disclosing partial dynamical symmetries, since a zero variance of a quantity indicates, that there is an exact quantum number associated to it for a particular state $|\psi_i\rangle$.

[20] Peres lattices have been used extensively for distinguishing ordered and chaotic structures in collective dynamics of nuclei in Refs. [Stra09b, **P7**, **P5***].

1.2 Dynamical Symmetry and its Generalizations in Algebraic Models of Many Body Systems

Algebraic Models

The first notable applications of symmetry in physics came about in attempts to describe the geometric arrangements of atoms in molecules and crystals and were limited to discrete symmetries. In fact they paralleled closely the notion of symmetries in arts, where it traditionally denotes "good proportion or order"[21]. A significant development and generalization was facilitated by applications of the theory of Lie groups and algebras (for a brief introduction with applications to physics, see e.g.[Iach09]). The elements of a Lie group depend on a set of continuous parameters and are generated by the elements of the corresponding Lie group.

In the so-called algebraic models, the Hamiltonian H is constructed explicitly as a function of generators[22] of a certain Lie group G_0, i.e.

$$H = f(g_1, \ldots, g_{\mathrm{rank}(G_0)}) \,. \tag{1.5}$$

Advantage of these models in applications rests in the finite dimension of the Hilbert space, which in principle allows for an exact solution by numerical diagonalisation without the necessity of truncations. Moreover, in several important special cases, explicit analytical solutions can be obtained through the group-theoretical tools. Many of these models proved to be extremely useful especially in understanding the structure of complex many body systems, like atomic nuclei, atomic clusters and molecules [Gosh59, Iach87, Iach95], as well as in the particle physics [Baru64, Doth65].

In nuclear physics, probably the most well known examples include the Elliot SU(3) shell model [Elli58], the Lipkin Meshkov Glick SU(2) model [Lipk65], various versions of the Interacting Boson Model [Arim75, Iach87] and recently the Algebraic Collective Model [Rowe04g, Rowe05g]. In the molecular physics, different versions of the Vibron model are used [Iach95, Fran05].

The range of applications of algebraic models is very broad, certainly not limited only to their primary determination, being the description of experimentally observed properties of many body systems. Here they provide an invaluable tool for systematics of the often very complex energy spectra and other observables. Apart from that, their computational efficiency also provides a benchmark for testing the accuracy of various mean-field and other many body techniques [Ring05, Nege82]. They also turn out to be very suitable for studying some rather general physical phenomena like the quantum phase transitions (see e.g. [Cejn10] for a review) and our main topic—the interplay of order and chaos, where they directly allow to investigate the connection to exact and approximate symmetries.

[21] This is approximately the meaning of the Greek word $\sigma\upsilon\mu\mu\varepsilon\tau\rho\iota\alpha$ composed of $\sigma\upsilon\nu$ (with, together) and $\mu\varepsilon\tau\rho\sigma\nu$ (measure, proportion).

[22] The set of generators of a Lie group form a Lie algebra, see e.g. [Iach09].

Invariant and Dynamical Symmetries

Let us turn our attention now to a few concepts of exact symmetry followed by some of their generalizations in a little detail. We speak about an *invariant symmetry* (IS) of the Hamiltonian H with respect to a group G_0 in case that H commutes with all the generators g_j of the group, with $j = 1, \ldots, \mathrm{rank}(G_0)$. This leads to a spectral degeneracy of the states $|\psi_j\rangle$, which produced by an application of the different generators on the same initial state $|\psi_j\rangle = g_j|\psi\rangle$.

In contrast to the IS situation, if H does not commute with all the generators but only with the Casimir operators[23] of G_0 together with the Casimir operators related to a chain of its subgroups

$$G_0 \supset G_1 \supset G_2 \supset \ldots \supset G_k\,, \tag{1.6}$$

we speak about a *dynamical symmetry*[24] (DS) of the Hamiltonian H with respect to G_0 (and its subgroups, which are however usually omitted for the sake of brevity of notation[25]). Notice that often, more than one reduction chain of the type (1.6) starting from of G_0 may exist, such that different chains contain incompatible (i.e. mutually non-commuting) subgroups $G_i, G_i', \ldots$ at any position $i \in \{1, \ldots, k\}$ within the chain. An example will be given below in the discussion of the Interacting Boson Model.

Since the generators of G_0 do not commute with H, the energy of the states $|\psi_j\rangle = g_j|\psi\rangle$ now differs and the IS with respect to G_0 is broken. Nevertheless, the eigenstates of H are still endowed by the quantum numbers corresponding to the Casimir operators $C(G_i)$ of the whole chain and form irreducible representations (irreps) of the group chain (1.6). Clearly, a systematic application of the generators on any eigenstate of H enables to generate the spectrum of H, therefore the algebra of the generators g_j is often called the *spectrum generating algebra*.

An algebraic system with a DS with respect to G_0 is easily obtained if the Hamiltonian H is constructed solely from the Casimir operators related to the chain (1.6), so that

$$H_{\mathrm{DS}} = \tilde{f}[C(G_0), C(G_1), \ldots, C(G_k)]\,. \tag{1.7}$$

The smallest group G_i, $i \in [1, k]$ in the decomposition (1.6), whose Casimir operator is present in the Hamiltonian (1.7) represents the largest IS group of the Hamiltonian (1.7), while the groups larger than G_i correspond only to DS.

It is important to note that the presence of a dynamical symmetry implies complete integrability[26] of a Hamiltonian, since the Casimir operators $C(G_0)$,..., $C(G_k)$ corresponding to the DS group chain provide a complete set of quantities commuting mutually as well as with the Hamiltonian, hence there is a complete set of constants in involution and a complete set of quantum numbers labeling the eigenstates.

[23] A Casimir operator commutes with all elements of a given Lie algebra.

[24] Although the first notion of dynamical symmetries dates perhaps back to 1920's and the paper by Pauli [Paul26], a clearer recognition of their general significance came only much later [Gosh59, Baru64, Doth65].

[25] Clearly, if H commutes with $C(G_0)$, it commutes also with $C(G_1)$, etc..., so the subgroups correspond to DS automatically.

[26] The inverse implication is not true in general, cf. [Zhan88, Alha90].

Partial and Quasi Dynamical Symmetries

While trying to apply the algebraic methods and models to realistic systems, it is often found that the assumed symmetry is only approximate and is fulfilled by only some of the states but not by others. A corresponding Hamiltonian describing the above situation is not invariant under the group G_0, nor does it commute with the Casimir invariants of G_0, so that various irreps are in general mixed in its eigenstates. This empirically rather common behavior was formalized and named the *partial dynamical symmetry* (PDS) in [Alha92], where a general algorithm to construct Hamiltonians with PDS was given[27].

Later the concept of PDS (corresponding to say, G_0) was enriched distinguishing three different forms, see [Levi07], linked to the situations when:

I. Some but not all of the eigenstates possess a complete set of quantum numbers corresponding to G_0.

II. All of the eigenstates are endowed by quantum numbers corresponding to some, but not all subgroups in the DS chain starting with G_0.

III. The hybrid situation, when some of the eigenstates possess some of the quantum numbers of the DS chain starting with G_0.

An interesting observation was made in [Levi96], where the authors studied the effect of PDS on the increase of regularity of both the classical and quantum the dynamics of a particular PDS model. Intuitively, one would expect some "near-to-linear" dependence between an arbitrary measure of regularity and the fraction of symmetric states in a PDS system. It was revealed however, that the suppression of chaos in the classical limit due to PDS may be extremely strong even in case that the relative fraction of symmetric states in the quantum version goes to zero in the semiclassical limit. A satisfying explanation thereof is still missing.

Another way of breaking DS which seems to be realized frequently in various models is the so-called *quasi dynamical symmetry* (QDS), a concept introduced by D. Rowe et. al. [Carv86, Rowe88, Roch88]. Many systems, if observed with a given level of accuracy, seem to carry the fingerprint of dynamical symmetries (DS) in the spectrum of energy as well as other observables despite the fact that their Hamiltonian H contains a perturbations expected at first sight to break the symmetry badly. A well-known example is the SU(3)-QDS of the shell model, see e.g. [Roch88]. Here for example, the exact Elliot SU(3) is broken by the spin-orbit and major shell mixing interactions, which leads to a complete fragmentation of the eigenstates into the individual SU(3) irreps. Nevertheless, the mixing amplitudes preserve a very high degree of coherence, so that observable quantities (transition strengths) retain the basic properties of the unbroken SU(3). Quasi dynamical symmetries corresponding to various dynamical symmetry groups were apart from the shell model studied for example also in the interacting boson model [Rowe04, Rose05] or the geometric collective model [Turn05].

[27] A case of an approximate PDS was noticed in the problem of the hydrogen atom in a magnetic field. A dynamical symmetry that exists for weak fields, is broken at strong fields except for the quasi-Landau levels, see [Alha92] and references therein. Later, significant attention was dedicated to identification of PDS in collective nuclear spectra, see e.g. [Levi96p, Isac99, Levi02].

The presence of QDS is closely connected with the concept of *embedded representations* of a particular symmetry group G_0 [Rowe88, Roch88]. Loosely speaking, embedded representations appear, if the eigenstates of H do not belong to any precise representation of G_0 but are in a way *coherent* linear combinations of numerous different G_0-representations. To understand this, imagine a dynamical symmetry group chain $G_1 \subset G_0$, such that G_1 is conserved by H, while G_0 is not. Further take a basis $|g_0, g_1\rangle$ with good G_0- and G_1-labels. The eigenstates form embedded representations $|QDS; \bar{g}_0, g_1\rangle$, if there exist such sets of g_1-labeled states, that the mixing coefficients $\alpha_{g_0}^{(\bar{g}_0,g_1)}$ in the expansion $|QDS; \bar{g}_0, g_1\rangle = \sum_{g_0} \alpha_{g_0}^{(\bar{g}_0,g_1)} |DS; g_0, g_1\rangle$ do not depend on g_1 within the individual sets $\bar{g}_0$. The independence of g_1 may often be considered just approximate [Rowe04, Rose05, **J6***].

Interacting Boson Model

The Interacting Boson Model (IBM) of nuclear collective dynamics [Iach87] exemplifies all the concepts described above. The original version of IBM (called often IBM-1) traces back to 1975 when Arima and Iachello [Arim75] reformulated some older bosonic models of nuclei entirely within the framework of group theory. They considered two types of bosons—the first one with total angular momentum $l = 0$, called the s boson and the second one with $l = 2$, called the d boson[28]. Later, the model gained various refinements, among others the distinction of the protonic and neutronic degrees of freedom (IBM-2), the introduction of bosons with higher multipolarities (IBM-3, etc.) and the incorporation of fermionic degrees of freedom (IBFM - the Interacting Boson Fermion Model)[29], see [Iach87, Iach91]. The IBM represents in a way an intermediate step between the microscopic shell model with strong pairing residual interactions[30] and the completely phenomenological collective model of Bohr and Mottelson [Bohr52, Bohr53], which describes collective quadrupole excitations of the nucleus.

In the following, we will concentrate on IBM-1, whose Hilbert space is formed by all possible sequences of the creation operators $s^\dagger$ (s boson), $d_\mu^\dagger$ (five components of the d boson with $\mu = -2, -1, 0, 1, 2$) acting on the boson vacuum $|0\rangle$. Together with the corresponding annihilation operators, these operators can be arranged into 36 bilinear combinations $b_\alpha^\dagger b_\beta$ (introducing here $\alpha\,, \beta = 0, 1, \ldots, 5$ and $b_0^\dagger \equiv s^\dagger$, $b_1^\dagger \equiv d_{-2}^\dagger, \ldots, b_5^\dagger \equiv d_2^\dagger$), which close the U(6) algebra. IBM restricts the possible operators acting on the system only to the combinations of sums and products of the U(6) generators $b_\alpha^\dagger b_\beta$. It is clear that such operators preserve the decomposition of the Hilbert space into subspaces corresponding to different total numbers of bosons $N = 0, 1, 2, 3, \ldots$. In fact, the conservation of the total boson number N represents a substantial difference of IBM in comparison with the collective model. In applications to particular even-even nuclei[31], N is chosen to be equal to the number of valence nucleons or holes divided by 2.

[28] The monopole and quadrupole degrees of freedom are known to be the most important collective degrees of freedom in nuclei. The choice of the s and d bosons reflects both this fact, as well as the character of the interactions between valence nucleons, which prefer coupling to pairs with total angular momentum 0 and 2.

[29] IBFM allows also for a supersymmetric approaches and the research based on it has lead to the first experimental observation of (broken) supersymmetry in nature [Iach91].

[30] Which lead to Cooper-pair-like behavior of the nucleonic pairs.

[31] Description of odd-even or odd-odd is possible only in terms of the IBFM extension.

In IBM-1, there are three fundamental dynamical symmetry chains [Iach87]:

$$\begin{aligned} &\nearrow \quad \mathbf{U(5)} \quad \rightarrow \mathrm{O}(5) \searrow && (1.8)\\ \mathrm{U}(6) \rightarrow \quad &\mathbf{O(6)} \quad \rightarrow \mathrm{O}(5) \rightarrow \mathrm{O}(3)\,, && (1.9)\\ &\searrow \quad \mathbf{SU(3)} \quad \nearrow && (1.10) \end{aligned}$$

which begin with U(6) and end with the rotational group in three dimensions O(3) required to be the invariant symmetry group of any nuclear Hamiltonian. The particular selections of the bilinear U(6) generators $b^\dagger_\alpha b_\beta$ forming each of the chains can be found in [Iach87]. We note that for the chains (1.9) and (1.10), there are two different possibilities, which differ by the relative phases chosen between $s^\dagger$ and $d^\dagger_\mu$. These are conventionally denoted as O(6), $\overline{\mathrm{O}(6)}$ and SU(3), $\overline{\mathrm{SU}(3)}$. Hence there are five different dynamical symmetries of IBM-1 in total.

The IBM-1 Hamiltonian is usually considered to include one- and two-body terms having the following general form

$$\hat{H} = E_0 + \sum_{\alpha\beta} \epsilon_{\alpha\beta} b^\dagger_\alpha b_\beta + \frac{1}{2} \sum_{\alpha\beta\gamma\delta} v_{\alpha\beta\gamma\delta} b^\dagger_\alpha b^\dagger_\beta b_\gamma b_\delta \,. \tag{1.11}$$

It is further required to be (i) Hermitian, (ii) invariant with respect to the O(3) rotations, and (iii) invariant with respect to the inversion of time, which is expressed by complex conjugation of the coefficients $\epsilon_{\alpha\beta}$, $v_{\alpha\beta\gamma\delta}$ and the transformation $s^\dagger \rightarrow s^\dagger$, $d^\dagger_\mu \rightarrow (-)^\mu d^\dagger_{-\mu}$ (note that since both s and d bosons are of positive parity, they are automatically invariant with respect to space inversion). These constraints reduce the number of independent control parameters to only seven.

The electromagnetic transition operators of different mutipolarities l are in the IBM-1 represented by linear combinations of the elements of the U(6) algebra $\hat{T}^{(l)} = \sum_{\alpha,\beta} K_{\alpha\beta} \left[b^\dagger_\alpha \times b_\beta\right]^{(l)}$, with $\alpha\,, \beta = 0, 1, \ldots, 5$, coupled to a total angular momentum $l = 0, 1, 2, 3, 4$. Let us note that since the parity of all IBM-1 states is even, the only relevant transitions involve E(0), M(1), E(2), M(3) and E(4).

The Hamiltonian (1.11) may be equivalently transformed to a linear combination of Casimir operators corresponding to the chains (1.8)–(1.10) in order to display the individual dynamical symmetry limits explicitly, giving

$$\begin{aligned} \hat{H} = k_0 \quad &+ \quad k_1 C_1[U(5)] + k_2 C_2[U(5)] + k_3 C_2[O(6)] \\ &+ \quad k_4 C_2[SU(3)] + k_5 C_2[O(5)] + k_6 C_2[O(3)]\,. \end{aligned} \tag{1.12}$$

The explicit forms of the Casimir operators (in various conventions) can be found e.g. in the books [Iach87, Fran05].

The three fundamental dynamical symmetries (1.8)–(1.10) can be simultaneously incorporated even in Hamiltonians with essentially two control parameters [Warn82, Lipa85, Whel93]. In the publications reprinted in Appendix A we adopt the particular form, which depends essentially on $\eta \in [0, 1]$ and $\chi \in [-\sqrt{7}/2, 0]$:

$$\hat{H}(\eta, \chi) = \frac{\eta}{N} \hat{n}_d - \frac{1-\eta}{N^2} \hat{Q}(\chi) \cdot \hat{Q}(\chi)\,, \tag{1.13}$$

and which contains the d-boson number operator[32] $\hat{n}_d = d^\dagger \cdot \tilde{d}$ and the quadrupole operator $\hat{Q}_m(\chi) = d^\dagger_m s + s^\dagger \tilde{d}_m + \chi[d^\dagger \tilde{d}]^{(2)}_m$. Scaling by the total number of bosons N ensures that the bounds of energy spectrum do not change for asymptotic values of N and is useful especially while constructing the classical limit[33]. We neglect here the overall scaling coefficient of the Hamiltonian (i.e. we express energy in units of this coefficient). Eigenstates of (1.13) are for general (η, χ) labeled by the U(6)-label N and the O(3)-label l corresponding to the angular momentum operator $\hat{L}_m = \sqrt{10}[d^\dagger \tilde{d}]^{(1)}_m$.

The U(5), SU(3) and O(6) limits are reached setting (η, χ) to $(1, \chi)$, $(0, -\sqrt{7}/2)$ and $(0, 0)$, respectively and correspond to the vertices of the so-called Casten triangle, which is commonly drawn to represent the parametric space of (1.13), see e.g. [**J5***]. The $\overline{\mathrm{SU(3)}}$ can also be obtained with $(\eta, \chi) = (0, +\sqrt{7}/2)$ and in fact the whole $\chi > 0$ domain is just a mirror image of the $\chi < 0$ one, see Ref. [Joli01]. Notice that the whole transition between U(5) and O(6) [characterized by $\chi = 0$] is endowed with the O(5) symmetry, which is a common subgroup of the latter two, see Eq. (1.8).

The regular and chaotic properties of low lying states in even-even nuclei were using IBM studied for the first time in Refs. [Alha90, Alha91a] on the case of the SU(3)–O(6) transition. Later they were extended to include also the U(5) limit and the whole interior of the Casten triangle [Alha91b, Whel93] with a parametrization equivalent to the one in Eq. (1.13). The Hamiltonian (1.13) is integrable (hence fully regular) in the dynamical symmetry limits[34] and additionally along the $\chi = 0$ edge where the integrability is guaranteed by the O(5) symmetry. Inside the Casten triangle, the dynamics is chaotic or mixed regular/chaotic, depending on the values of (η, χ) as well as the energy E [Alha90, Alha91a, Alha91b]. Let us note, that the rather peculiar energy-dependence of the measures of chaos (cf. Figs. 1.3, 1.4) make IBM[35] substantially different from the paradigmatic systems of regularity/chaos studies—the classical and quantum billiards [Gutz90, Stoc99].

Having specified the position of the dynamical symmetries of the Hamiltonian (1.13) connected to integrable dynamics, let us now turn our attention to the possible partial and quasi dynamical symmetries within the Casten triangle in connection to the regularity/chaoticity of the dynamics therein[36].

[32] Notice that we utilize here the convention $\tilde{d}_\mu \equiv (-)^\mu d_{-\mu}$ and the scalar product notation related to the standard tensor coupling via $\hat{A}^{(l)} \cdot \hat{B}^{(l)} \equiv (-)^l \sqrt{2l+1}[\hat{A}^{(l)} \hat{B}^{(l)}]^{(0)}_0$, which is very common in the IBM literature.

[33] For details about the classical limit of IBM, see [Hatc82] or also [**J2***, **J5***, **D1***] and references therein.

[34] More precisely, it is "overintegrable" due to additional "missing labels" of the reductions O(5) $\supset$ O(3) and SU(3) $\supset$ O(3), see [Whel93].

[35] And similarly also the related geometric collective model, whose chaotic properties were investigated thoroughly in Refs. [Stra06, Stra09a, Stra09b].

[36] We remind that although the Hamiltonian (1.13) contains all the fundamental DS of IBM-1, it still covers only a part of the complete parametric space of the model. Here we shall concentrate on the question of possible appearance of PDS and QDS in the Casten triangle solely, omitting other domains [There exist IBM Hamiltonians tailored to display special PDS, see e.g. [Levi07] which are distinct from (1.13)].

The integrable $\chi = 0$ edge connecting the U(5) and O(6) vertices, is particularly richly endowed with these phenomena:

1. We observe a PDS of type II (all states with some quantum numbers) corresponding to U(5) and O(6), due the underlying O(5) symmetry, conserving the labels corresponding to the O(5)$\supset$ O(3) reduction.

2. The low lying states display a transition between QDS corresponding to U(5) and O(6), see [Rowe04][37], which are separated by the second order quantum phase transition point at $\eta = 0.8$, see [Joli02].

Similarly to the second point, the low lying states along the $\chi = -\sqrt{7}/2$ edge connecting U(5) and SU(3) show a transition between QDS of the corresponding types [Rose05][38]. The transition occurs at the first order phase transitional point at $\eta \approx 0.8$, see [Joli02]. Unlike in the first point, no PDS is present along this edge.

An interesting question arises with the possible presence of PDS and QDS inside the Casten triangle—especially in connection with the highly[39] regular arc (AW arc) disclosed by Alhassid and Whelan [Alha91a] between the SU(3) and U(5) vertices. The first expectations about an underlying PDS were not confirmed, but the increased regularity seems to be connected to an increased occurrence frequency of states showing a SU(3) QDS. The SU(3) QDS is typical for the low-lying states throughout the whole axially deformed part of the Casten triangle, see [**J6***] in Appendix A, and can be identified by rotational bands showing coherent mixing of SU(3) irreps in their decomposition[40]. At the AW arc however, rotational bands with coherent SU(3) decompositions appear additionally also at intermediate and high energies and their appearance coincides considerably with the areas of high regularity, see [**J7***, **J8***] in Appendix A.

[37] There are indications, that the QDS affect essentially the whole spectrum along the U(5)–O(6) edge [**J2***, **J3**], excluding only a narrow region at $E \approx 0$, which corresponds to an excited state quantum phase transition. The indication of U(5) QDS for $E > 0$ and O(6) for $E < 0$ is evident in the joint spectra of seniority and energy, see [**J2***, **J3**] in Appendix A. But while an analytical explanation for the O(6) QDS is given by the shifted harmonic approximation, for the U(5) QDS in the interval $\eta \in [0, 0.8]$ it is still missing (note the for $\eta \in [0.8, 1]$, U(5) QDS is explainable by the valid RPA, see [Rowe04]).

[38] Unlike in the integrable case U(5)–O(6), the high energy spectrum is chaotic and obviously free of any QDS.

[39] but not completely

[40] This is a typical behavior of embedded representations of SU(3), cf. [Rose05].

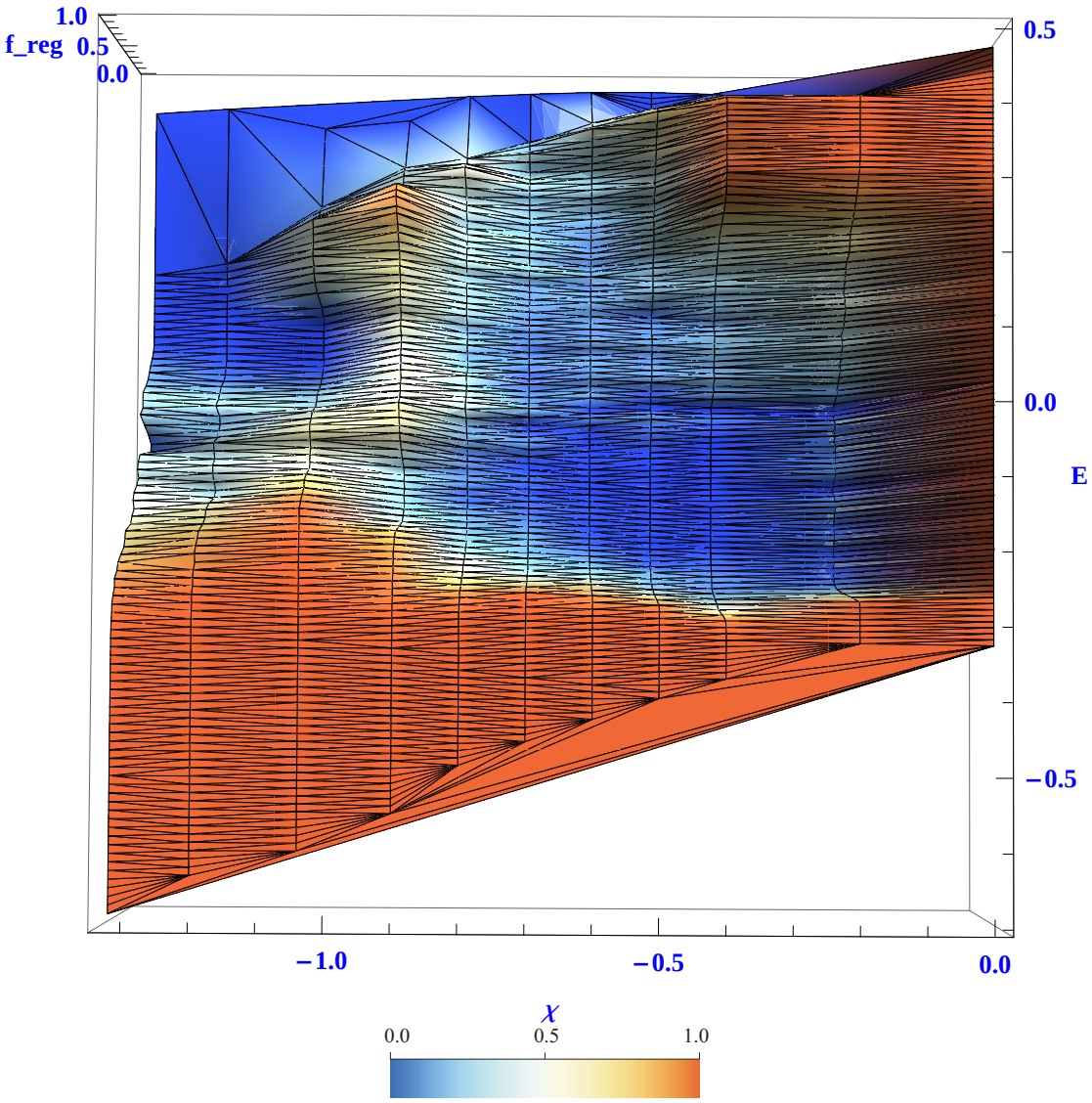

Figure 1.3: Classical regular fraction f_{reg} of the phase space volume $\Omega(E)$ calculated in the plane $\chi \times E$ using the classical limit of the Hamiltonian (1.13) with $\eta = 0.5$. The values of f_{reg} are color coded so that the most chaotic parts ($f_{\mathrm{reg}} \to 0$) are blue, while the most regular parts ($f_{\mathrm{reg}} \to 1$) are red. The colored area covers the whole interval of accessible energies between the global minima and maxima of the potential E_{min} and E_{max}. We note only that our calculations suffer numerical instability at high energies, cf. [**J8***], so that the upper part with the obviously coarser mesh corresponds to these inaccessible areas. The semiregular Alhassid-Whelan arc is clearly visible around $\chi = -0.9$. It seems to be a joint effect of two distinct regular regions, one based at high energies, while the other at low energies. These two regions merge at energy $E \approx 0$. The picture complements the behavior of f_{reg} shown in Refs. [**J5***, **P5***, **J7***, **J8***] to be found in Appendix A.

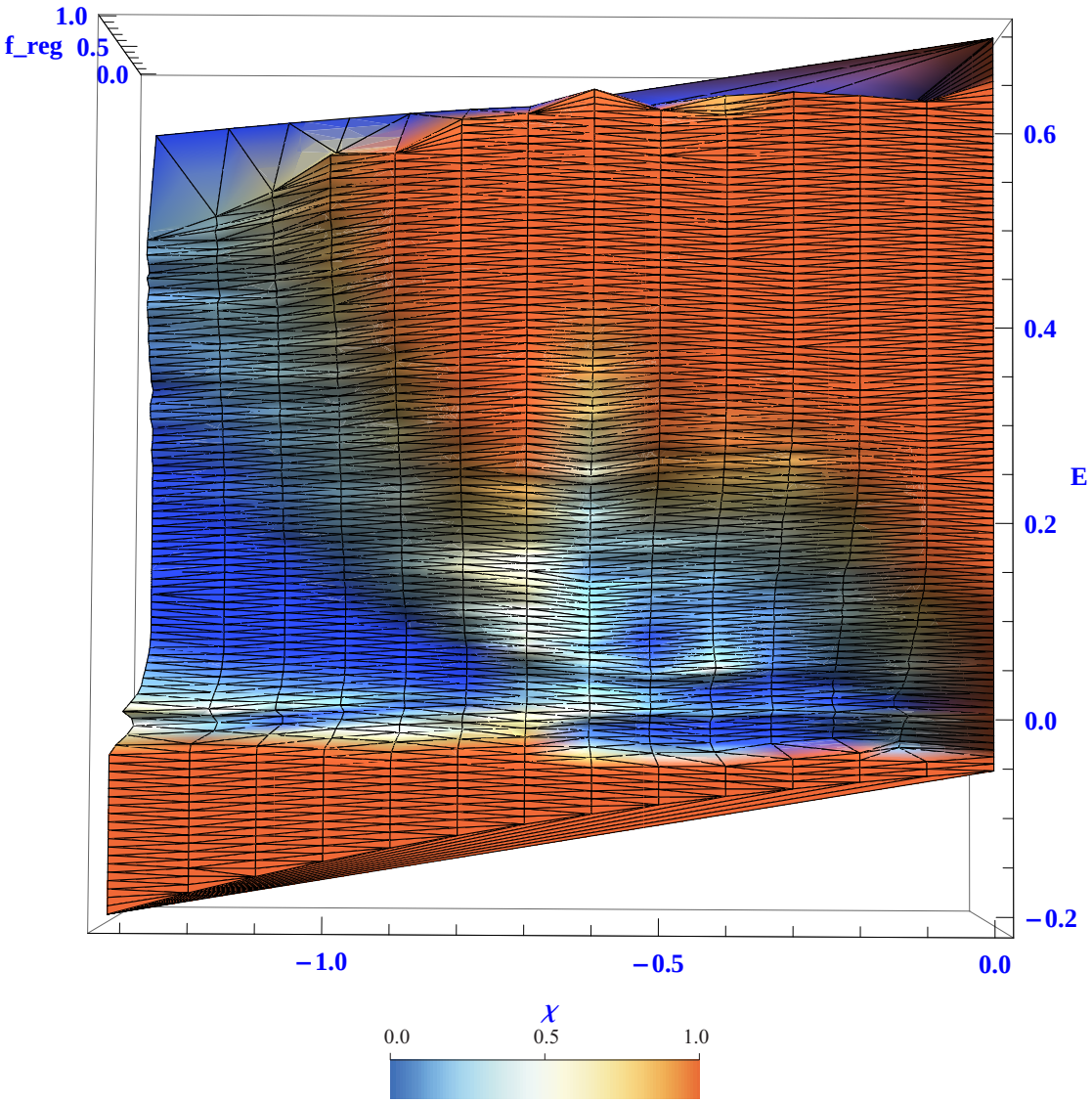

Figure 1.4: Classical regular fraction $f_{\rm reg}$ as in Fig. 1.3, but for $\eta = 0.7$. The semiregular Alhassid-Whelan arc has now migrated to $\chi \approx -0.7$.

Chapter 2

Synopsis of the Results Obtained

This chapter provides a structured overview of the results published in the articles attached in Appendix A. The aim is to highlight the most important points and illustrate the connections between the results obtained in different publications.

2.1 Integrable Dynamics in the Interacting Boson Model

While studying the integrable domains in IBM, we have concentrated on the quantum and classical dynamics along the O(6)–U(5) edge of the Casten triangle, where the underlying O(5) symmetry guarantees integrability all along the edge, which is parametrized by η, while the other parameter is fixed to $\chi = 0$. The relevant publications are [**J1**, **J2***, **J3**], to be found in the Appendices A.1 and A.2. The double-article [**J1**, **J2***] was created already during the master study of the author, but we nevertheless include it here since it provides an essential background for the article [**J3**] as well as for [**J5***]. An article that directly builds upon the results of these three articles, but is not a part of this thesis is [**J4**].

The main points of the articles include:

- In [**J1**], the evolution of the quantum spectrum along the O(6)–U(5) edge of the Casten triangle is investigated. A surprising bunching of $l = 0$ levels is observed at the energy $E = 0$. The bunching is disentangled separating the sets of states with distinct seniority quantum number v [it is the O(5) label], which shows that the spectra are compressed as the levels approach $E = 0$ and that the compression is strongest for $v = 0$ and getting weaker for higher seniorities. The compression is explained using the Pechukas-Yukawa equations.

- In [**J2***], an alternative explanation of the spectral compression is given using the semiclassical periodic orbit theory of spectral fluctuations. Classical orbits of zero seniority are found to have a diverging period $T \to \infty$ at $E = 0$, which is the energy of a local maximum of the classical potential energy surface and hence corresponds to an unstable equilibrium point. The diverging period causes the contributions of these trajectories to the semiclassical Berry-Tabor formula (which specifies the effects of periodic orbits on the semiclassical level density fluctuations) to diverge.

- The classical trajectories are found to have significantly different structures at high and low energies, with an abrupt change taking place at $E = 0$.
- The energy $E = 0$ is identified as the energy of classical as well as quantum monodromy in [**J2***].
- In [**J3**] the energy of the monodromy $E = 0$ is found to demarcate the collapse of the shifted harmonic approximation (SHA) [Rowe04], which analytically transforms the O(6) solutions at $\eta = 0$ to solutions with $\eta > 0$ and hence underlies the O(6) quasi dynamical symmetry related to $E < 0$ eigenstates for $\eta \in [0, 0.8]$. The collapse of SHA is used to identify the line of excited state quantum phase transition at the monodromy energy $E = 0$ which affects all (and only) the seniority $v = 0$ states.
- The connection between the monodromy and the excited state quantum phase transition is generalized to any systems with Mexican hat type of potential.

2.2 Non-integrable Dynamics in the Interacting Boson Model

The studies of the non-integrable dynamics in the interior of the Casten triangle were originally motivated mainly by the attempts to explain the increased regularity found by Alhassid and Whelan [Alha91b] along an arc-like path (AW arc) connecting the SU(3) and U(5) vertices of the triangle. Partial dynamical symmetries (PDS) were suspected to be the hidden cause. In the first paper of the series [**J5***] we have used essentially the same methods as in the studies of the integrable dynamics described in Sec. 2.1. Incidentally, we have discovered a bunching pattern in the evolution of the quantum spectra being very similar to the one found along the O(6)–U(5) transition. Now the level bunching is located slightly above $E = 0$, unlike in the O(6)–U(5) case. The corresponding level density fluctuation has again been linked to the properties of classical orbits via a semiclassical trace formula. At low energies, a degeneracy line of β and γ vibrations was identified to lie very close to the line of AW arc in the axially deformed region of the Casten triangle (near to the spherical region, the two lines separate significantly).

The application of the Peres lattice method to investigate the quantum spectra visually using a $2d$ lattice, see especially [**P5***], greatly facilitated the identification of PDS connected to the standard dynamical symmetries. In fact, the presence of PDS in the interior of the Casten triangle was disproved, since no states showing zero variance corresponding to the Casimir operators of DS present in the Casten triangle were found [**J6***]. Later, the Peres lattices were found to indicate perfectly the angular momentum multiplets corresponding to the SU(3) quasi dynamical symmetry (QDS). Indeed, SU(3) QDS was found to be a frequent inhabitant of the Casten triangle, see [**J6***, **J7***, **J8***].

The investigations performed here were inspired and motivated mainly by Refs. [Alha91b, Cejn98, Levi96, Rowe04, Rose05].

The main points of the articles include:

- In [**J5***], the evolution of the quantum spectrum along the AW arc and in its near vicinity is inspected. A significant bunching of $l = 0$ levels, similar to the one found along the O(6)–U(5) transition is observed slightly above $E = 0$. The bunching fades away both with increasing the angular momentum and moving away from the AW arc. The numbers of crossing $l = 0$ levels show here [in contrast to the integrable O(6)–U(5) case] a pattern typical for the SU(3) limit.

- Three major families of regular classical orbits are identified to appear at the AW arc in the vicinity of $E \approx 0$. Two of these families show equal time periods of their central periodic orbits at an energy which corresponds to the degeneracies of the $l = 0$ levels within the bunching pattern. Energy dependence of the periods and actions of the three major families of orbits explain the quantum level density fluctuation, through their contribution to the semiclassical trace formula.

- The AW arc is found to lie close to a degeneracy line of single β and γ vibrations, which originates in the equal stiffness of the potential around its global minima in this region. The degeneracy line is calculated analytically in a mean field approximation using the intrinsic coherent state formalism.

- In [**P5***], the Peres lattice method is used to draw the spectra of IBM throughout the Casten triangle. The regularity of the Peres lattices is shown to correspond very well with the regularity of the classical phase space f_{reg}, so the Peres method provides an obviously good heuristic to reveal quantum regularity/chaos. The applicability of virtually arbitrary quantities as bases for the Peres method is demonstrated—the regular and chaotic features disclosed by Peres lattices corresponding to various operators are shown to be equivalent, in particular the lattices corresponding to any operators are completely regular in case of an integrable system (cf. also Fig. 1.2 in Chapter 1 of this thesis).

- In [**J6***], the Peres lattices are used to reveal mutually similar structures among the low-lying regular states of different angular momenta l in the axially deformed part of the Casten triangle. These states, whose appearance is found to be bounded from above roughly by the saddle point energy E_{sad} of the potential energy surface, are shown to belong to quasi SU(3) multiplets by investigating their decompositions in the SU(3) basis, their excitation energy ratios following the rotor $l(l+1)$ dependence and their interband as well as intraband $B(E2)$ transition rates following the Alaga rules [Alag55]. Structure of these rotational bands is explained analytically by a mean field approximation using intrinsic coherent states. Hence the validity of SU(3) QDS was identified and explained in a much larger region of the Casten triangle than observed previously [Rose05].

- In [**J7***, **J8***], rotational bands similar to those described in the previous point are surprisingly found and then studied in detail also at intermediate and high energies. Occurrence of these high-energy rotational bands is

highest in the vicinity of the AW arc, and their occurrence frequency in general shows significant correlation with variations of the measures of regularity/chaos of purely vibrational $l = 0$ modes. The correlation indicates that the regularity of intrinsic vibrational modes has a strong effect on adiabatic separation of vibrations and rotations. In contrast, the chaotic vibrational states seem to be mixed easily if the rotation comes into play.

- The degeneracy of low-energy β and γ vibrations was in Ref. [**J6***] shown to be responsible for a novel type of non-analytic behavior of several observable quantities, predominantly of the inter- and intra-band $B(E2)$ transition rates and the excitation energy ratios. The degeneracy thus leads to a critical behavior, which is not exactly a ground state quantum phase transition (QPT), since the properties of the ground state band remain intact, but which affects already the lowest vibrational excitations and so is actually very near to a QPT.

Bibliography

[Alag55] G. Alaga, K. Adler, A. Bohr, B. R. Mottelson, *Dan. Mat. Fys. Medd.* **29**, no.9 (1955).

[Alha90] Y. Alhassid, A. Novoselsky, N. Whelan, *Phys. Rev. Lett.* **65**, 24, 2971 (1990).

[Alha91a] Y. Alhassid, N. Whelan, *Phys. Rev. C* **43**, 6, 2637 (1991).

[Alha91b] Y. Alhassid, N. Whelan, *Phys. Rev. Lett.* **67**, 816 (1991).

[Alha92] Y. Alhassid, A. Leviatan, *J. Phys. A Math. Gen.* **25**, L1265-Ll271 (1992).

[Arim75] A. Arima, F. Iachello, *Phys. Rev. Lett.* **35**, 1069 (1975).

[Arno63] V. I. Arno'ld, *Rus. Math. Sur.* **18**, 5, 9 (1963); *Rus. Math. Sur.* **18**, 6, 9 (1963).

[Baru64] A. O. Barut, *Phys. Rev.* **135**, 3B, B839 (1964).

[Ball98] L. E. Ballentine, S. M. McRae, *Phys. Rev. A* **58**, 3, 1799 (1998).

[Ball02] L. E. Ballentine, *Phys. Rev. A* **65**, 6, 062110, (2002).

[Berr76] M. V. Berry, M. Tabor, *Proc. R. Soc. Lond. A***349**, 101 (1976).

[Berr77] M. V. Berry, M. Tabor, *Proc. R. Soc. A* **356**, 375, (1977).

[Berr84] M. V. Berry, M. Robnik, *J. Phys. A* **17**, 2413 (1984).

[Berr87] M. Berry, *Proc. R. Soc.* **A 413**, p. 183 (1987); *Physica Scripta* 40, 335 (1989).

[Birk35] G. D. Birkhoff, *Mem. Pont. Acad. Sci. Novi Lyncaei* **1**, 85 (1935).

[Bohi84] O. Bohigas, M. J. Giannoni, C. Schmidt, *Phys. Rev. Lett.* **52**, 1 (1984).

[Bohr52] A. Bohr, *K. Dan. Vidensk. Selsk., Mat.-Fys. Medd.* **26**, 14 (1952).

[Bohr53] A. Bohr, B. R. Mottelson, *K. Dan. Vidensk. Selsk., Mat.-Fys. Medd.* **27**, 16 (1953).

[Brod81] T. A. Brody, J. Flores, J. B. French, P. A. Mello, A. Pandey, S. S. M. Wong, *Rev. Mod. Phys.* **53**, 385 (1981).

[Capr08] M. Caprio, P. Cejnar, F. Iachello, *Ann. Phys. (N.Y.)* **323**, 1106 (2008).

[Carv86] J. Carvalho, R. Le Blanc, M. Vassanji, D. J. Rowe and J. McGrory, *Nucl. Phys.* **A 452**, 240 (1986).

[Casta90] O. Castanõs, A. Frank, R. Lopez-Peña, *J. Phys. A: Math. Gen.* **23**, 5141 (1990).

[Cejn98] P. Cejnar, J. Jolie, *Phys. Lett. B* 420, 241 (1998); *Phys. Rev. E* **58** 387 (1998).

[Cejn10] P. Cejnar, J. Jolie, R. F. Casten, *Rev. Mod. Phys.*, in press.

[Cush80] R. H. Cushman, J. J. Duistermaat, *Bull. Am. Math. Soc.* 19, 475–479 (1988).

[Diep80] A. E. L. Dieperink, O. Scholten, F. Iachello, Phys. Rev. Lett. **44**, 1747 (1980); A. E. L. Dieperink, O. Scholten, *Nucl. Phys.* **A346** 125 (1980).

[Doth65] Y. Dothan, M. Gell-Mann, Y. Ne'eman, *Phys. Lett.* **17**, 2, 148 (1965).

[Duis80] J. J. Duistermaat, *Commun. Pure Appl. Math.* **33**, 687 (1980).

[Eise94] E. Eisenberg, N. Shnerb, *Phys. Rev. E* **49**, R941 (1994).

[Elli58] J. P. Elliott, *Proc. R. Soc. A* **245**, 128, 562 (1958).

[Fran05] A. Frank, P. Van Isacker, *Symmetry Methods in Molecules and Nuclei* (S y G Editores, Mexico, D.F., 2005).

[Fran09] A. Frank, J. Jolie, P. Van Isacker, *Symmetries in Atomic Nuclei: from Isospin to Supersymmetry*, (Springer Science+Business Media, New York, 2009).

[Gosh59] S. Goshen, H. J. Lipkin, *Ann. Phys.* **6** 301, (1959).

[Gutz71] M. C. Gutzwiller, *J. Math. Phys* **12,** 34 (1971).

[Gutz90] M. C. Gutzwiller, *Chaos in Classical and Quantum Mechanics* (Springer, New York, 1990).

[Haak91] F. Haake, *Quantum Signatures of Chaos* (Springer, Berlin, 1991).

[Hatc82] R. L. Hatch, S. Levit, *Phys. Rev. C* **25**, 614 (1982).

[Hogg82] T. Hogg, B. A. Huberman, *Phys. Rev. Lett.* **48**, 711 (1982).

[Iach87] F. Iachello, A. Arima, *The Interacting Boson Model* (Cambridge University Press, Cambridge, UK, 1987).

[Iach91] F. Iachello, P. Van Isacker, *The Interacting Boson Fermion Model* (Cambridge University Press, Cambridge, UK, 1987).

[Iach95] F. Iachello, R. D. Levine, *Algebraic Theory of Molecules* (Oxford University Press, Oxford, UK, 1995).

[Iach09] F. Iachello, *Lie Algebras and Applications*, (Springer Berlin Heidelberg, 2009).

[Isac99] P. Van Isacker, *Phys. Rev. Lett.* **83**, 21, 4269 (1999).

[Joli01] J. Jolie, R. F. Casten, P. von Brentano, V. Werner, *Phys. Rev. Lett.* **87**, 162501 (2001).

[Joli02] J. Jolie, P. Cejnar, R. F. Casten, S. Heinze, A. Linnemann, V. Werner, *Phys. Rev. Lett.* **89**, 182502 (2002).

[Kell58] J. B. Keller, *Ann. Phys. (NY)*, 4, 180–188 (1958).

[Kolm54] A. N. Kolmogorov, *Dokl. Akad. Nauk SSSR* 98, 527 (1954).

[Kram26] H. A. Kramers, *Z. Phys.* **39**, 828–840 (1926).

[LesH91] *Chaos and Quantum Physics: Proceedings of the Les Houches Summer School, Course LII, 1-31 August, 1989*, ed. M.-J. Gianonni, A. Voros, J. Zinn-Justin, (North-Holland, Amsterdam, 1991).

[Levi96] A. Leviatan, N. Whelan, *Phys. Rev. Lett.* **77**, 26, 5202 (1996).

[Levi96p] A. Leviatan, *Phys. Rev. Lett.* **77**, 5, 818 (1996).

[Levi02] A. Leviatan, P. Van Isacker, *Phys. Rev. Lett.* **89**, 22, 222501 (2002).

[Levi07] A. Leviatan, *Phys. Rev. Lett.* **98**, 242502 (2007).

[Lich83] A. J. Lichtenberg, M. A. Liebermann, *Regular and Stochastic Motion,*(Springer-Verlag, New York, 1983).

[Lipa85] P. O. Lipas, P. Toivonen, D. D. Warner, *Phys. Lett.* **B155**, 295 (1985).

[Lipk65] H. J. Lipkin, N. Meshkov, A. J. Glick, *Nucl. Phys.* **62**, 188 (1965).

[Meht04] M. L. Mehta, *Random Matrices*, (Elsevier, 2004).

[Mose62] J. Moser, *Nachrichten der Akademie der Wissenschaften in Göttingen: II. Mathematisch-Physikalische Klasse* **1**, 1 (1962).

[Nege82] J. W. Negele, *Rev. Mod. Phys.* **54**, 4, 913 (1982).

[Nico95] G. Nicolis, *Introduction to Nonlinear Science,* (Cambridge University Press, Cambridge, UK, 1995).

[Paul26] W. Pauli, *Z. Phys.* **36**, 336 (1926).

[Perc73] I. C. Percival, J. Phys. B **6**, L229 (1973).

[Pere84a] A. Peres, *Phys. Rev. Lett.* **53**, 1711 (1984).

[Pere84b] A. Peres, *Phys. Rev. A* **30**, 1610 (1984).

[Ree99] S. Ree, L. E. Reichl, *Phys. Rev. E* **60**, 1607 (1999).

[Reic92] L. E. Reichl, *The Transition to Chaos in Conservative Classical Systems: Quantum Manifestations* (Springer-Verlag, New York, 1992).

[Ring05] P. Ring, P. Schuck, *The Nuclear Many-Body Problem*, (Springer, 2005).

[Roch88] P. Rochford and D. J. Rowe, *Phys. Lett.* **B 210**, 5 (1988).

[Rowe88] D. J. Rowe, P. Rochford and J. Repka, *J. Math. Phys.* **29**, 572 (1988).

[Rowe04] D. J. Rowe, *Nucl. Phys.* **A745**, 47 (2004).

[Rowe04g] D. J. Rowe, *Nucl. Phys.* **A 735**, 372 (2004).

[Rowe04P] D. J. Rowe, in *Computational and Group-Theoretical Methods in Nuclear Physics*, ed. by J. Escher, O. Castaños, J. G. Hirsch, S. Pittel and G. Stoitcheva (World Scientific, Singapore, 2004), p.165.

[Rose05] G. Rosensteel, D. J. Rowe, *Nucl. Phys.* **A759**, 92 (2005).

[Rowe05g] D. J. Rowe, P. S. Turner *Nucl. Phys.* **A 753**, 94–105 (2005).

[Sado99] D. A. Sadovskií, B. I. Zhilinskií, *Phys. Lett. A* **256**, 235–244 (1999).

[Sado06] D. A. Sadovskií, B. I. Zhilinskií, Molecular Physics **104**, 2595 (2006).

[Shri90] N. Shrivastava, C. Kaufmann, G. Muller, *J. Appl. Phys.* **67**, 5627 (1990).

[Skok01] Ch. Skokos, *J. Phys. A: Math. Gen.* **34** 10029 (2001).

[Stoc99] H.-J. Stöckmann, *Quantum Chaos. An Introduction* (Cambridge Universty Press, Cambridge, UK, 1999).

[Stra06] P. Stránský, M. Kurian, P. Cejnar, *Phys. Rev. C* **74**, 014306 (2006).

[Stra09a] P. Stránský, P. Hruška, P. Cejnar, *Phys. Rev. E* **79**, 046202 (2009).

[Stra09b] P. Stránský, P. Hruška, P. Cejnar, *Phys. Rev. E* **79**, 066201 (2009).

[Stra09P] P. Stránský, *PhD thesis*, Charles University in Prague, Faculty of Mathematics and Physics (2009). [164 pages]

[Turn05] D. Turner, D.J. Rowe, *Nucl. Phys.* **A756**, 333 (2005).

[Waal03] H. Waalkens, A. Junge, H.R. Dullin, *J. Phys. A* **36**, L307–L314 (2003).

[Waal04] H. Waalkens, H. R. Dullin, P. H. Richter, *Physica* D 196 265–310 (2004).

[Warn82] D. D. Warner, R. F. Casten, *Phys. Rev. Lett.* **48**, 1385 (1982).

[Went26] G. Wentzel, *Z. Phys.* **38**, 518–529 (1926).

[Whel93] N. Whelan, Y. Alhassid, *Nucl. Phys.* **A556**, 42 (1993).

[Zhan88] W. Zhang, C. C. Martens, D. H. Feng and J. Yuan, *Phys. Rev. Lett.*, **61**, 2167 (1988) .

Chapter 3

List of Author's Publications

This chapter lists all the scientific articles that contain contributions by the author of this PhD thesis and which were either published during the years 2005-2010 or have currently been submitted for publication.

The list is separated into three parts, which include respectively:

1. articles in international refereed journals [**J1**]–[**J8***],
2. articles published within conference proceedings [**P1***]–[**P8**],
3. internal publications of the Charles University in Prague [**D1***].

Each of the parts (1–3) is ordered chronologically starting from the oldest works, which often provide background for the newer ones. The order hence somewhat represents the logical line of thoughts. The articles with a substantial contribution of the author are marked by asterisk*. The oldest articles [**J1**, **J2***] and [**P1***, **P2**] contain results obtained already as a part of the master thesis of the author [**D1***].

Bibliography

[J1] **Evolution of spectral properties along the O(6)-U(5) transition in the interacting boson model. I. Level dynamics**,
S. Heinze, P. Cejnar, J. Jolie, M. Macek,
Phys. Rev. C **73**, 014306 (2006). [10 pages]

[J2*] **Evolution of spectral properties along the O(6)-U(5) transition in the interacting boson model. II. Classical Trajectories**
M. Macek, P. Cejnar, J. Jolie, S. Heinze,
Phys. Rev. C **73**, 014307 (2006). [11 pages]

[J3] **Monodromy and excited-state quantum phase transitions in integrable systems: collective vibrations of nuclei**,
P. Cejnar, M. Macek, S. Heinze, J. Jolie, J. Dobeš,
J. Phys. A: Math. Gen. **39**, L515 (2006). [7 pages, Letter to the Editor]

[J4] **Coulomb analogy for non-hermitian degeneracies near quantum phase transitions**,
P. Cejnar, S. Heinze, M. Macek,
Phys. Rev. Lett. **99** (2007) 100601. [4 pages, Letter]

[J5*] **Classical and quantum properties of the semiregular arc inside the Casten triangle**,
M. Macek, P. Stránský, P. Cejnar, S. Heinze, J. Jolie, J. Dobeš,
Phys. Rev. C **75**, 064318 (2007). [13 pages]

[J6*] **Transition from gamma-rigid to gamma-soft dynamics in the interacting boson model: Quasicriticality and quasidynamical symmetry**,
M. Macek, J. Dobeš, P. Cejnar,
Phys. Rev. C **80**, 014319 (2009). [15 pages]

[J7*] **Regularity-induced separation of intrinsic and collective dynamics**,
M. Macek, J. Dobeš, P. Stránský, P. Cejnar,
submitted to *Phys. Rev. Lett.* [4 pages, Letter]

[J8*] **Occurrence of high-lying rotational bands in the interacting boson model**,
M. Macek, J. Dobeš, P. Cejnar,
submitted to *Phys. Rev.* **C**. [12 pages]

[**P1***] **Classical chaos in the interacting boson model**,
M. Macek, P. Cejnar,
in Proc. of *Capture Gamma-Ray Spectroscopy and Related Topics 12*, ed. A. Woehr, A. Aprahamian, AIP Conference Proceedings 819, p.570 (2005). [2 pages]

[**P2**] **Regular and chaotic nuclear vibrations**,
P. Cejnar, M. Macek, P. Stránský, M. Kurian,
in Proc. of *Capture Gamma-Ray Spectroscopy and Related Topics 12*, ed. A. Woehr, A. Aprahamian, AIP Conference Proceedings 819, p.487 (2005). [6 pages]

[**P3***] **Order and chaos in the interacting boson model**,
M. Macek, P. Stránský, P. Cejnar,
Phys. Atom. Nucl. **70**, 1592 (2007). [5 pages]

[**P4**] **Order and chaos in the geometric collective model**,
P. Stránský, P. Cejnar, M. Macek,
Phys. Atom. Nucl. **70**, 1572 (2007). [5 pages]

[**P5***] **Peres lattices in nuclear structure**,
M. Macek, P. Stránský, P. Cejnar,
Int. J. Mod. Phys. E, **18**, 1058 (2009). [4 pages]; see also arXiv: 0810.2949 [nucl-th].

[**P6**] **Quantum phase transitions and nuclear structure**,
P. Cejnar, P. Stránský, M. Macek,
Int. J. Mod. Phys. E, **18**, 965 (2009). [10 pages]

[**P7**] **Peres lattices in nuclear structure and beyond**,
P. Stránský, M. Macek, P. Cejnar, J. Dobeš,
in Proc. of *13th International Symposium on Capture Gamma-Ray Spectroscopy*, Cologne, 2008, AIP Conderence Proceedings Series **1090**, 174 (Springer-Verlag, New York, 2009). [5 pages]

[**P8**] **Chaotic dynamics in collective models of nuclei**,
P. Stránský, M. Macek, P. Cejnar, A. Frank, R. Fossion, E. Landa,
submitted to *IOP Journal of Physics: Conference Series*. [6 pages]

[**D1***] **Classical Chaos in Collective Nuclear Models**,
M. Macek,
diploma thesis, Charles University in Prague, Faculty of Mathematics and Physics (2005). [124 pages]

Appendix A

Reprint of Selected Publications

A.1 Evolution of spectral properties along the O(6)-U(5) transition in the interacting boson model. I. Level dynamics [J1]; Evolution of spectral properties along the O(6)-U(5) transition in the interacting boson model. II. Classical Trajectories [J2*]

[*Phys. Rev. C* **73,** 014306 and 014307 (2006)]

This article, consisting of two parts, deals with various aspects of the fully integrable dynamics along the O(6)–U(5) edge of the symmetry triangle of the interacting boson model (IBM). The author's contribution to these studies has been obtained as part of his master thesis and is not directly related to this PhD thesis. We reprint the full text for the readers' convenience, since it provides an introduction and reference to the following publications, especially Refs. [**J3**, **J5***].

The Part I, Level Dynamics, shows that both, the evolution of individual levels, as well as of the bulk of the spectrum of IBM can be interpreted using the Pechukas-Yukawa equations, which provide an intuitive analogy between the behavior of quantum levels and a gas of particles in one dimension interacting via Coulomb force. A bunching (a level density oscillation) of angular momentum $l = 0$ levels is observed in the numerically obtained spectrum throughout the O(6)–U(5) transition to occur at energy $E \approx 0$, where also the effect of quantum monodromy is identified. These observations have lead to the identification of an excited-state quantum phase transition (ESQPT) later in Ref. [**J3**]. Also the eigenstate dynamics along the O(6)–U(5) transition is discussed and some characteristic behavior of the eigenstates related to the later-identified ESQPT is shown.

The Part II, Classical Trajectories, deals with the classical limit of IBM and studies detailed properties of the classical orbits along the O(6)–U(5) transition. The semiclassical periodic orbit theory for integrable systems (Berry-Tabor formula) is used to interpret the level density fluctuations observed in Part I. A significant change of the character of classical trajectories is observed as the energy of the local maximum at $E = 0$ is passed, see Fig. 4. The classical monodromy

is identified at this energy value.

Author of this thesis contributed substantially to the Part II, where he performed all the numerical calculations of the classical trajectories with their subsequent analysis. He noticed that (i) the occurrence-rate of the simplest periodic orbits shows a sharply-peaked behavior at certain energy values $E_{\rm bif}$, specifically linked to their β- and γ-vibrational frequency ratio, see Fig. 5, (ii) the orbits undergo bifurcations at the energy $E_{\rm bif}$, as plotted in Fig. 6 and that (iii) at the energy $E = 0$, some trajectories with diverging time period $T \to \infty$ occur. All these effects were identified as possible sources of the strong level density fluctuations in the semiclassical spectra. The occurrence of the 4/1-type orbits with diverging period T has lead to the identification of the classical monodromy, see also Ref. [**J3**].

Evolution of spectral properties along the O(6)-U(5) transition in the interacting boson model. I. Level dynamics

Stefan Heinze,[1] Pavel Cejnar,[2] Jan Jolie,[1] and Michal Macek[2]
[1]*Institute of Nuclear Physics, University of Cologne, Zülpicherstrasse 77, D-50937 Cologne, Germany*
[2]*Faculty of Mathematics and Physics, Charles University, V Holešovičkách 2, CZ-18000 Prague, Czech Republic*
(Received 5 April 2005; published 23 January 2006)

We investigate the evolution of quantal spectra and the corresponding wave functions along the [O(6)-U(5)] ⊃ O(5) transition of the interacting boson model. The model is integrable in this regime, and its ground state passes through a second-order structural phase transition. We show that the whole spectrum as a function of the Hamiltonian control parameter as well as structures of all excited states exhibit rather organized and correlated behaviors, which provide deeper insight into the nature of this transitional path.

DOI: 10.1103/PhysRevC.73.014306 PACS number(s): 21.60.Fw, 21.10.Re, 05.45.Mt

I. INTRODUCTION

Properties of the interacting boson model (IBM) [1] in transitional regimes between various dynamical symmetries have been extensively studied mainly in connection with zero-temperature quantum phase transitions [2,3]. In any of such transitions, the structures of the ground state and a few low-lying states change abruptly (for the system size tending to infinity) at a certain critical point located between the two dynamical-symmetry limits, see, e.g., Refs. [4–9]. This behavior finds experimental evidence (in a finite-N approximation) in observed variations of nuclear shapes in some isotopic or isotonic chains of nuclei.

The IBM phase transitions are of the first order, except for the isolated point of a second-order transition, which is located at the intersection of borders between spherical and deformed, and between prolate and oblate shapes in the parameter space [4–6]. To pass this point, one commonly starts from the O(6) dynamical symmetry and proceeds to U(5) via the line of unbroken O(5) dynamical symmetry. The deformed-to-spherical second-order phase transition on this path manifests itself as a nonanalytic but continuous change of the ground-state deformation, in contrast to the discontinuous changes observed along the other (even infinitely close) transitional paths. This type of phase structure of the parameter space agrees with the classical Landau theory of thermodynamic phase transitions, which is applicable at zero temperature if the role of thermodynamic variables is taken by the model control parameters [7,8], and with catastrophe theory [2,5].

The above-mentioned [O(6)-U(5)] ⊃ O(5) transitional path also differs from the others in that it does not destroy the integrability of the Hamiltonian. Due to the underlying O(5) dynamical symmetry [10], the integrals of motion along the whole transition form a complete set of commuting operators, and the Hamiltonian eigenproblem can be solved analytically [11,12]. This was used for an explicit calculation of some second-order phase-transitional observables [13]. Recent studies of the O(6)-U(5) transitional path were also based on the concepts of the $E(5)$ critical-point dynamical symmetry [14,15] and the quasidynamical symmetry [16].

The ultimate mechanism that is on the deepest level responsible for the occurrence of ground-state phase transitions of various orders in quantum many-body systems remains unclear. For example, the distinction between the IBM first- and second-order phase transitions was shown [9] to be connected with different densities of unavoided energy crossings (branch points) in the complex-extended parameter space, which in the $N \to \infty$ limit accumulate infinitely close to critical points on the real axes (in analogy with similar behaviors of complex zeros of partition functions in thermodynamic phase-transitional systems). However, many questions—among them the role of integrability in the process of dynamical-symmetry breaking—still remain unanswered.

The present work contributes to the mapping of this relatively new territory of physics by studying in detail various spectral observables associated with the integrable phase-transitional path in the IBM. In particular, we investigate the evolution of energies and wave functions of individual Hamiltonian eigenstates with zero angular momentum along the whole [O(6)-U(5)] ⊃ O(5) line. It is shown that this transitional class of IBM exhibits rather peculiar features.

We will combine two totally different, but mutually related general approaches: (i) the theory of level dynamics, initiated by Pechukas and Yukawa [17], also known as the dynamical Coulomb-gas analogy, and (ii) the semiclassical theory of quantal spectra represented by the Gutzwiller and Berry-Tabor trace formulas [18]. Results obtained by applying both these approaches will be presented in two parts: approach (i) is discussed in the present article (Part I), which gives numerical results on level dynamics; approach (ii) will be used in the following article (Part II) [19].

The Pechukas-Yukawa theory describes the dynamics of individual levels and the interaction matrix elements via a set of coupled differential equations, where the varying Hamiltonian control parameter plays the role of time. It enables one to understand the evolution of spectral observables with the control parameter (including eventual phase transitions) in a more intuitive way, using the parallel with a classical ensemble of charged particles moving in one dimension.

The trace formulas, on the other hand, describe a snapshot of the energy spectrum at each fixed value of the control parameter (time) by expressing the quantum density of states (as a function of energy) through properties of periodic orbits in the classical limit of the system. Since both methods (i) and (ii) translate the original problem to the classical language, they often provide deeper understanding of specific behaviors

observed on the quantum level. Also in our case, the most significant features of the IBM in the [O(6)-U(5)] $\supset$ O(5) transitional regime will be elucidated by both kinds of classical concepts involved in the above approaches.

The plan for this part of the paper is the following: In Sec. II, we will briefly describe the quantum Hamiltonian under study, its integrals of motion and phase-transitional features. Section III presents numerical results on the level dynamics and their interpretation in the framework of the Pechukas-Yukawa theory. The accompanying changes in the structure of wave functions are then discussed in Sec. IV. Finally, Sec. V contains partial conclusions of this part of the study.

II. QUANTUM HAMILTONIAN

The interacting boson model [1] describes shapes and collective motions of atomic nuclei in terms of an ensemble of N interacting s and d bosons with angular momenta 0 and 2, respectively. To analyze the evolution of properties of this model along the O(6)-U(5) transitional path, we adopt the Hamiltonian

$$\hat{H}(\eta) = a\left[-\frac{1-\eta}{N^2}(\hat{Q}\cdot\hat{Q}) + \frac{\eta}{N}\,\hat{n}_d\right], \tag{1}$$

where the dimensionless control parameter $\eta \in [0, 1]$ changes the proportion of both competing terms and drives the system between the O(6) ($\eta = 0$) and U(5) ($\eta = 1$) dynamical symmetries. The operator $\hat{n}_d = (d^\dagger \cdot \tilde{d}) = N - \hat{n}_s$ represents the d-boson number, while $\hat{Q} \equiv \hat{Q}^{(2)}_0 = [s^\dagger\tilde{d} + d^\dagger\tilde{s}]^{(2)}$ stands for the O(6)-U(5) quadrupole operator. The energy scale is set by an arbitrary factor a, which in the following will be fixed at the value $a = 1$ MeV.

Hamiltonian (1) is a special case of a more general Hamiltonian of the same form, but with the quadrupole operator given by $\hat{Q}^{(2)}_\chi = \hat{Q}^{(2)}_0 + \chi[d^\dagger\tilde{d}]^{(2)}$, where $\chi \in [-\frac{\sqrt{7}}{2}, +\frac{\sqrt{7}}{2}]$ is an additional control parameter. Equation (1), where $\chi = 0$, can be decomposed [20] into a linear combination of Casimir invariants corresponding to the O(6), O(5), O(3), and U(5) algebras, with no admixture of SU(3), SU(3), and O(6) invariants; i.e., it describes the [O(6)-U(5)] $\supset$ O(5) transitional line in the extended Casten triangle [6].

The above Hamiltonian can also be rewritten as

$$\hat{H}(\eta) = (1-\eta)\hat{H}(0) + \eta\hat{H}(1) = \hat{H}_0 + \eta\hat{V}, \tag{2}$$

which is the form well known from various studies of quantum phase transitions. Assuming $a = 1$, we obtain

$$\hat{H}_0 = -\frac{1}{N^2}(\hat{Q}\cdot\hat{Q}), \tag{3}$$

$$\hat{V} = \frac{1}{N}\,\hat{n}_d + \frac{1}{N^2}(\hat{Q}\cdot\hat{Q}). \tag{4}$$

The evolution of Hamiltonian (2) with η can be treated in a perturbative way since $\hat{H}(\eta+\delta\eta) = \hat{H}(\eta) + \delta\eta\,\hat{V}$. Note that the powers of N in denominators of Eqs. (1), (3), and (4) guarantee convenient scaling of the Hamiltonian with variable boson number $N \gg 1$.

It can be easily shown that for Hamiltonian (2), the ground-state average $\langle V\rangle_\eta \equiv \langle\psi_1(\eta)|\hat{V}|\psi_1(\eta)\rangle = \frac{dE_1(\eta)}{d\eta}$ [where $E_1(\eta)$ and $|\psi_1(\eta)\rangle$ are the ground-state energy and wave function, respectively] is a nonincreasing function of η. Therefore, if $\hat{V}$ is nonnegative—as in our specific case, see Eq. (4)—then an instantaneous satisfaction of $\langle V\rangle_{\eta_c} = 0$ at some critical point η_c implies that the average gets fixed for all $\eta \geqslant \eta_c$, freezing both the energy and wave function of the ground state. At this point, the system may exhibit (for $N \to \infty$) a ground-state phase transition of order $\kappa \geqslant 2$. If the second derivative of energy changes discontinuously from a value $\frac{d^2E_1(\eta)}{d\eta^2} = \frac{d\langle V\rangle_\eta}{d\eta} < 0$ at $\eta = \eta_{c-}$ to zero at $\eta = \eta_{c+}$, the transition is of the second order. Higher-order transitions [2,3] would require additional constraints, namely, $\frac{d^k\langle V\rangle_\eta}{d\eta^k}|_{\eta_c-} = 0$ for $k < \kappa$.

It is not difficult to see that for the specific Hamiltonian in Eq. (1) the ground-state average of $\hat{V}$ indeed interpolates between a positive value at $\eta = 0$ and zero at $\eta = 1$. However, the phase-transitional scenario is generically allowed only in the limit of infinite Hilbert-space dimensions, thus $N \to \infty$, when the ground-state energy as a function of η may acquire nonanalytic character. The asymptotic critical point is located at $\eta_c = \frac{4}{5} = 0.8$. At this point, the deformed ground-state configuration, given by a mixed-boson condensate $|\psi_1\rangle \propto (s^\dagger + \beta_{gs}d^\dagger_0)^N|0\rangle$, changes into the pure s-boson condensate, $|\psi_1\rangle \propto (s^\dagger)^N|0\rangle$, characterizing the spherical U(5) phase. In the left vicinity of the critical point, the ground-state "deformation parameter" β_{gs} drops to zero as $\beta_{gs} \propto \sqrt{\eta_c - \eta}$ [7], and the corresponding value of $\langle V\rangle_\eta$ behaves according to $N \to \infty$ asymptotic formula $\langle V\rangle_\eta \propto (\eta_c - \eta)$ [9]. Thus both β_{gs} and $\langle V\rangle_\eta$ can be considered as order parameters describing a second-order quantum phase transition, $\kappa = 2$, with critical exponents $\frac{1}{2}$ and 1, respectively.

The limits $\hat{H}(0)$ and $\hat{H}(1)$ of Eq. (1) possess the O(6) and U(5) dynamical symmetries, respectively. Since the dynamical-symmetry Hamiltonians are constructed using solely observables "in involution" (the Casimir invariants of the respective algebraic chain), they are always integrable [21]. Moreover, because the O(5) dynamical symmetry underlying both O(6) and U(5) limits is not broken in the transitional regime, the integrability of Hamiltonian (1) is preserved for all values of η [20,22]. Indeed, one can find five mutually commuting integrals of motion, the same number as the dimension of the classical configuration space (given by two geometric parameters and three Euler angles [23]). Four of these integrals can be associated with the following quantum numbers: energy $E_i(\eta)$ given by the Hamiltonian $\hat{H}(\eta)$, squared angular momentum $l(l+1)$ represented by $\hat{L}^2$ (where $\hat{L} = \sqrt{10}[d^\dagger\tilde{d}]^{(1)}$), its projection m determined from $\hat{L}_z$, and the seniority v defined through the $v(v+3)$ eigenvalue of the O(5) Casimir invariant [1]

$$\hat{C}_2[\mathrm{O}(5)] = \tfrac{1}{5}(\hat{L}\cdot\hat{L}) + 2(\hat{T}_3\cdot\hat{T}_3), \tag{5}$$

where $\hat{T}_3 = [d^\dagger\tilde{d}]^{(3)}$. The fifth integral of motion, connected with the so-called missing label $\hat{n}_\Delta$ of the O(5) $\supset$ O(3) reduction, is not given explicitly, but its existence is guaranteed by the fact that there must be five independent commuting operators in the complete set, so the Hamiltonian (which is made of four of them) commutes with the fifth one [21]. Note that in this paper we will only consider the set of states with zero angular momentum, $l = 0$.

III. EIGENVALUE DYNAMICS

A. Pechukas-Yukawa equations

Drawing the dependence of all individual level energies $E_i(\eta)$ for Hamiltonian (2) on the control parameter, one obtains a picture containing n continuous curves that resemble trajectories $x_i(t)$ of an ensemble of particles in one dimension. Indeed, as shown by Pechukas and Yukawa [17], the quantum-mechanical perturbation theory applied to Eq. (2) allows for a *dynamical interpretation* such that the motion of levels is described in terms of a set of Hamilton-type first-order differential equations. These can be associated with a gas of particles interacting via two-dimensional Coulomb force:

$$\frac{d^2E_i}{d\eta^2} = 2\sum_{j(\neq i)} \frac{|V_{ij}|^2}{E_i - E_j} \tag{6}$$

(analogous to $\frac{d^2x_i}{dt^2} = \frac{1}{2\pi\epsilon_0}\sum_{j(\neq i)} \frac{q_iq_j}{x_i - x_j}$). In contrast to the ordinary gas dynamics, however, the "product charge" $|V_{ij}|^2 = |\langle\psi_i(\eta)|\hat{V}|\psi_j(\eta)\rangle|^2 \leftrightarrow q_iq_j \equiv Q_{ij}$ cannot be factorized and varies as the "time" $\eta \leftrightarrow t$ elapses. Thus the product charges (alias interaction matrix elements) are also dynamical variables, subject to specific evolution, and the system's phase space is larger than $2n$. Besides Eq. (6), we have

$$\frac{dV_{ij}}{d\eta} = \sum_{k(\neq i,j)} \frac{E_i + E_j - 2E_k}{(E_i - E_k)(E_j - E_k)} V_{ik}V_{kj} - \frac{V_{ii} - V_{jj}}{E_i - E_j} V_{ij} \tag{7}$$

for $i \neq j$ (assuming an appropriate choice of phases), and

$$\frac{dE_i}{d\eta} = V_{ii}. \tag{8}$$

A transparent derivation of these formulas can be found, e.g., in Ref. [24].

Equations (6)–(8) are equivalent to the well-known Pechukas-Yukawa set of equations, although we use here their original form instead of the usual one [24], which was introduced by Yukawa [17]. The system described by these equations of motion is deterministic and even integrable. If all energies and interaction matrix elements are known at a single point η (for instance, $\eta = 0$), the equations determine E_i and V_{ij} for all other η values.

Let us stress that we have tacitly assumed (as is evident from the energy denominators of the dynamical equations) that the initial spectrum of eigenvalues is nondegenerate. Since the product charge $|V_{ij}|^2$ in Eq. (6) is nonnegative, the levels never touch each other unless their mutual interaction completely vanishes. In absence of symmetry-dictated zeros of the interaction matrix, the coincidence of simultaneous convergences $|V_{ij}|^2 \to 0$ and $E_{i+1} - E_i \to 0$ is extremely unlikely, which gives rise to the well-known no-crossing rule for level energies. The presence of symmetries, however, induces the disappearance of V_{ij} for certain sets of states which, therefore, can cross. In case of Hamiltonian (1), this concerns levels with different values of angular momentum l and levels with different seniority v.

B. Level bunching around $E \approx 0$

Figure 1 shows the dynamics of all levels with $l = 0$ along the $\eta \in [0, 1]$ path between the O(6) and U(5) dynamical symmetries of Hamiltonian (1). The calculation was performed by numerical diagonalization of the Hamiltonian for $N = 40$ bosons. One can observe numerous level crossings,

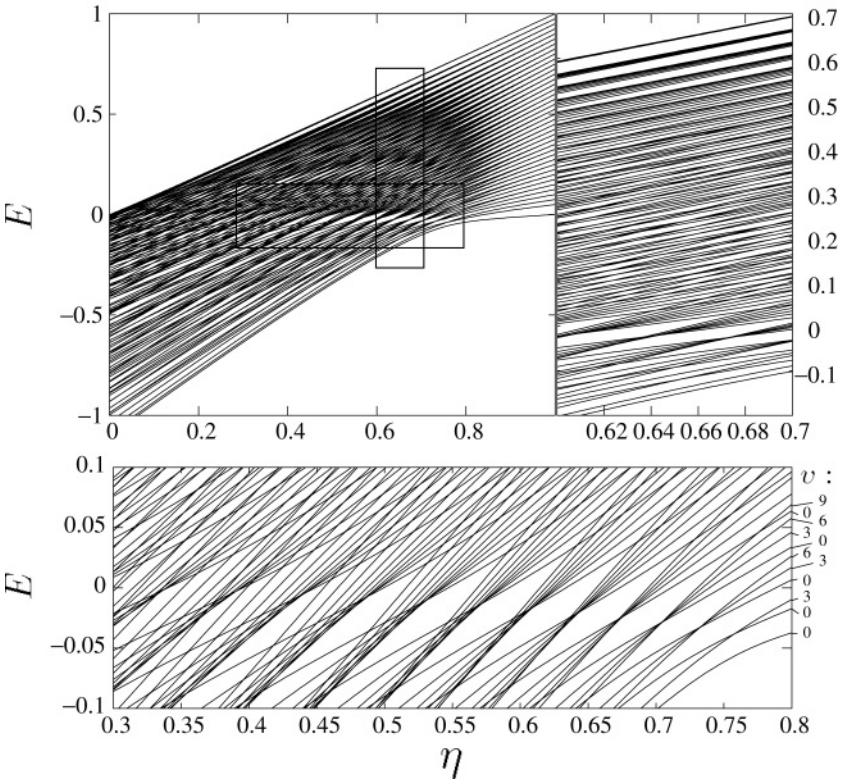

FIG. 1. Spectrum of Hamiltonian (1) with $N = 40$ as a function of η for $l = 0$ levels with all seniorities. Vertical and horizontal rectangles are expanded in the upper right and lower panels, respectively. Seniority is assigned to several levels in the lower panel.

particularly in the region around $E \approx 0$ (the horizontal rectangle, expanded in the lower panel), which is a consequence of the unbroken O(5) dynamical symmetry of the system. Indeed, the seniority quantum numbers, as marked for a few levels on the rightmost side of the lower panel, differ for any pair of levels that cross at some point. We will see below that the crossings disappear after separation of levels with different seniorities into several figures.

The pattern of consecutive compressions and dilutions of the spectrum in the region around $E \approx 0$ is one of the most apparent attributes of Fig. 1 (see the lower panel). A striking feature of this pattern is the regular sequence that characterizes the total number of levels involved in individual bunches: when descending from $\eta = 0.8$ to ≈ 0.4, the sequence goes 1, 2, 3, 4, ... At first, the different seniority states seem to cross exactly at the same point (within the available numerical precision); but with η descending below 0.65, the higher seniorities get increasingly out of focus, and the bunching pattern becomes more and more diffuse. Nevertheless, the structure of alternating clusters and gaps extends over a wide range $\eta \in [0.3, 0.8]$. Secondary "interference" patterns are also visible at other energies (see the vertical rectangle of Fig. 1, extended in the upper right-hand-side panel), but these are much weaker than the main one.

The energy $E \approx 0$, where the bunching pattern appears, is significant because it corresponds to the local maximum at $\beta = 0$ of the classical potential [1,23] corresponding to Hamiltonian (1). The bunching of levels thus develops just at the value of energy where the classically accessible range of the deformation parameters, $\beta \in [\beta_{\min}, \beta_{\max}]$, extends due to $\beta_{\min}$ becoming zero. The connection of the bunching pattern with the IBM classical dynamics will be elaborated in Part II of this contribution [19].

C. Shock-wave scenario

Figure 2 demonstrates that the level bunching pattern can be deconvoluted by separating states with different seniorities. Here we show the level dynamics for $v = 0$ (this set includes the ground state) and $v = 18$, with the boson number $N = 80$. Clearly, the $v = 0$ levels in panel (a) form a smooth flow with a "shock wave" propagating from the top of the spectrum (at $\eta = 0$) to the ground state (at $\eta = 0.8$). The mutual distances $\Delta E_i = E_{i+1} - E_i$ of individual $v = 0$ levels as functions of η are shown in Fig. 3(a), where we can clearly identify points of the closest approach of neighboring states as the wave propagates through the ensemble. Note that because of the energy denominator in Eq. (6), a minimal spacing of levels tends to induce maximal "force" acting on the relevant levels, which is basically the mechanism that keeps the wave moving. This is also why the wave initiates in the upper (densest) part of the spectrum (at $\eta = 0$, the distance of nearest levels linearly decreases with i, while at $\eta = 1$ it is constant, cf. Fig. 3).

On the other hand, the dynamics of the $v = 18$ levels, shown in panels (b) of both figures, exhibits much weaker interactions. The flow in Fig. 2(b) looks almost laminar, and the minimal distances in Fig. 3(b) (still disclosing interactions) are about twice as large as in the $v = 0$ case. It can be checked that the weakening of level interactions proceeds gradually as v increases.

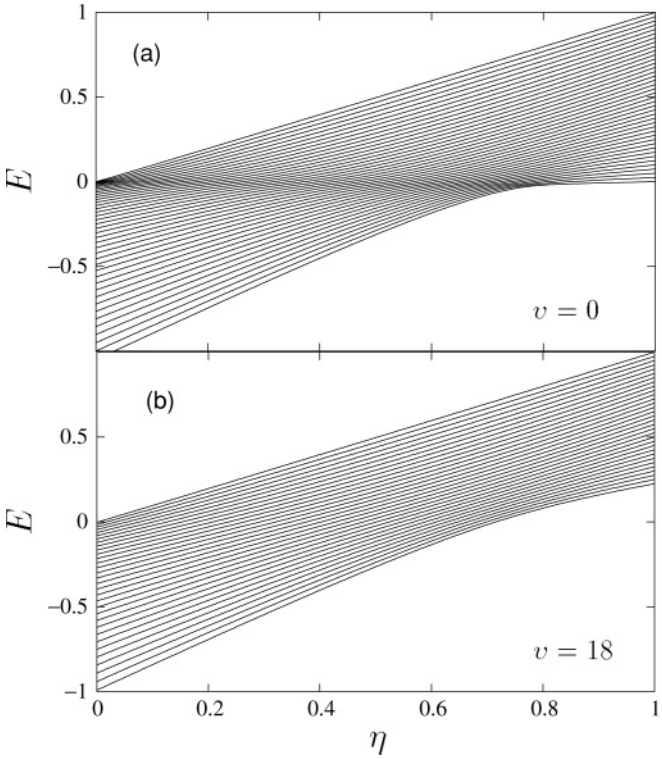

FIG. 2. Spectrum of Hamiltonian (1) with $N = 80$ for $l = 0$ levels with seniority $v = 0$ and $v = 18$.

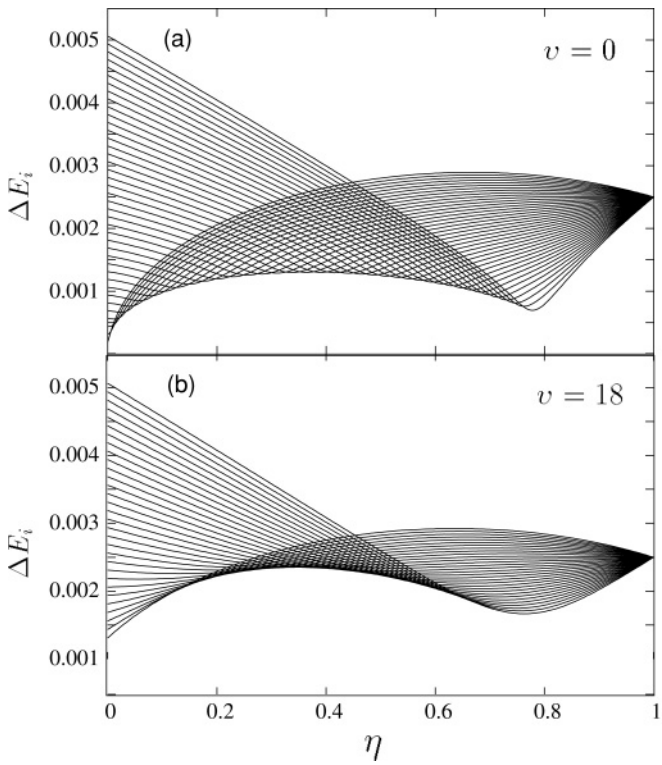

FIG. 3. Distances of neighboring levels from Fig. 2.

The shock-wave interpretation of Fig. 2(a) is particularly appealing if used as tentative reasoning for the ground-state phase transition at $\eta_c = 4/5$. It seems that this transition results from a highly ordered sequence of structural changes that propagates from upper to lower parts of the spectrum and terminates at the ground state just at the critical point. This mechanism, however, needs to be verified by an analysis of wave functions and will be further discussed in Sec. IV.

Closely related to the regular evolution of level energies is the organized pattern of the Hamiltonian branch points in the complex plane of parameter η [25]. It is shown for $N = 20$ in Fig. 4 for (a) $v = 0$ and (b) $v = 6$. Branch points are places in the complex-extended parameter space where two (or more) Hamiltonian complex eigenvalues become degenerate [26]. A branch point located on the real η-axis would imply a real crossing of the corresponding levels, which does not typically happen (for levels with different symmetry quantum numbers). On the other hand, if a given branch point is not on, but sufficiently close to the real axis, one observes an avoided crossing of the relevant levels at the corresponding value of η. Recall that a sequence of such avoided crossings is significant for the "shock wave." A cumulation of branch points in infinitesimal vicinity (for $N \to \infty$) of the critical point η_c was recently shown [9] to constitute the essential triggering mechanism for the IBM quantum phase transitions of both orders.

For each seniority, there are altogether $n(n-1)/2$ complex conjugate pairs of branch points, where n is the dimension of the given seniority subspace. Because of numerical constraints, we can only show results for moderate dimensions that correspond to the lower boson number $N = 20$. As can be seen in Fig. 4, branch points for both seniorities form rather regular patterns. In the $v = 0$ case, we notice a chain of points at $\eta < 0.8$ that approaches close to the real axis. These points clearly correspond to the sequence of avoided crossings shown (for a higher boson number) in Fig. 2(a). With increasing seniority, the pattern gets more and more separated from the real axis [see the example in (b)], which results in a weakening of level interactions, as observed (for different values of N and v) in Fig. 2(b). Note that such an organized behavior of branch points is a characteristic of only the [O(6)-U(5)] $\supset$ O(5) transitional class, where the separation of seniorities is possible (cf. Ref. [9]).

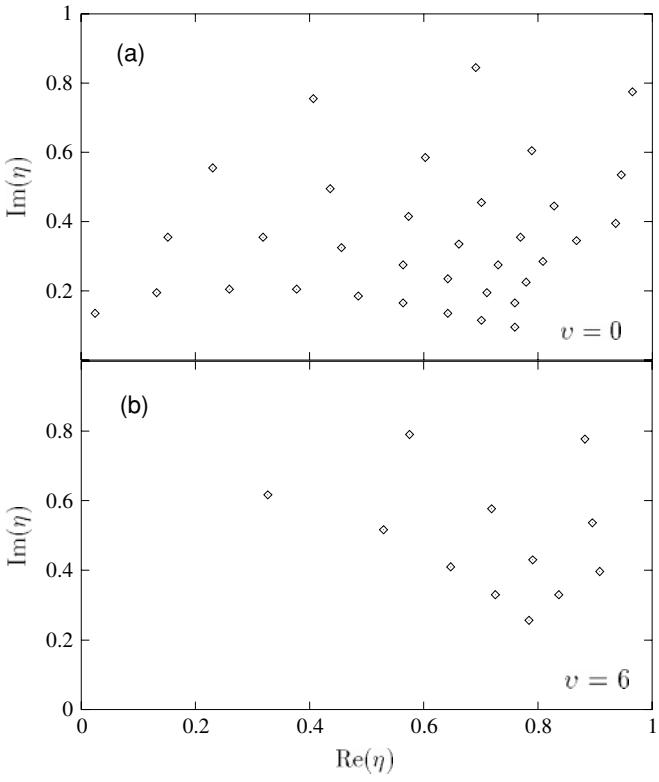

FIG. 4. Branch points of Hamiltonian (1) with $N = 20$ for $l = 0$ states with seniorities $v = 0$ and $v = 6$.

D. Focal point and spectral invariant

A more detailed view of Fig. 2(a) discloses that almost all $v = 0$ levels on the $\eta = 0$ side (except perhaps a few at the top of the spectrum) point to a virtually sharp focus on the $\eta = 1$ side. Indeed, an unperturbed evolution (with no mutual interactions between levels) would lead to a crossing of individual lines at the point $(\eta, E) = (1, \frac{1}{2})$, which we call an (approximate) focal point of the [O(6)-U(5)] $\supset$ O(5) transition.

From Eq. (8), we see that (η_f, E_f) will be a focal point of Hamiltonian (2) if $\langle\psi_i(0)|\hat{H}(\eta_f)|\psi_i(0)\rangle = E_f$; so in our particular case, we have

$$\langle\psi_i(0)|\hat{n}_d|\psi_i(0)\rangle \approx \frac{N}{2}, \tag{9}$$

where $|\psi_i(0)\rangle$ are the Hamiltonian eigenvectors with $v = 0$ at $\eta = 0$. This means that the average number of d bosons in individual O(6) eigenstates with zero seniority stays nearly constant across the whole spectrum. Figure 5(a), where the n_d average is shown explicitly along the whole $\eta \in [0, 1]$ path for all $v = 0$ levels with $N = 80$, supports this rule; see the $\eta = 0$ limit (graphically it is difficult to distinguish, whether the convergence of all curves to the $N/2$ point is exact or not, but numerical values indicate that it is only approximate). With a lower precision, the validity of the above "spectral invariant" can be extended to higher seniorities, but with increasing v there are more and more upper states that do not fit, see Fig. 5(b), which shows $\langle n_d\rangle_i$ for the $v = 18$ levels.

Even in the SU(3)-U(5) and $\overline{\text{SU(3)}}$-U(5) transitions, when $\hat{Q}$ in Hamiltonian (1) is replaced by $\hat{Q}_\chi$ with $\chi = -\sqrt{7}/2$ or $\chi = +\sqrt{7}/2$ and the seniority is not conserved, one finds a similar approximate invariant, namely $\langle\psi_i(0)|\hat{n}_d|\psi_i(0)\rangle \approx 3N/4$, where $|\psi_i(0)\rangle$ represent the SU(3) or $\overline{\text{SU(3)}}$ eigenvectors (the complete $l = 0$ spectrum for these transitions can be found in Ref. [8]).

Note that we first detected these invariants geometrically, from the focal points. The impact of such invariants on the level dynamics can be enormous since focal points represent an essential condition for the initial compression of the Coulomb gas, which results in stronger interactions between levels. This

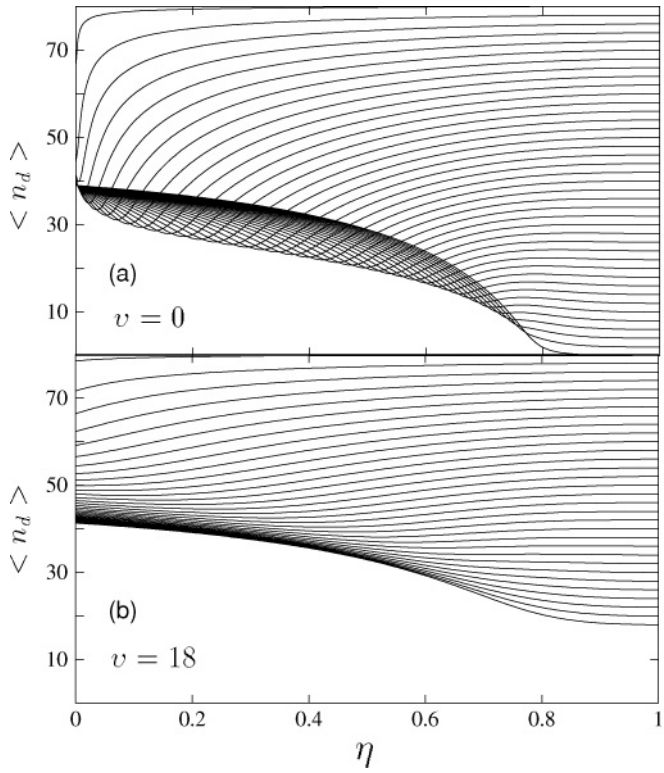

FIG. 5. Average number of d bosons for $v = 0$ and $v = 18$ states with $l = 0$ and $N = 80$.

compression triggers the formation of the "shock wave" in the densest part of the spectrum, see Sec. III C. Therefore, the existence of an initial (exact or approximate) focal point may belong to the main causes that eventually lead to a phase transition at some point.

E. Finite-N phase transitions

Although we are dealing here with the spherical-deformed transition induced by varying parameter η in Hamiltonian (1), one should realize that the [O(6)-U(5)] $\supset$ O(5) transitional path itself coincides with the separatrix between prolate and oblate deformed phases [5,6]. The prolate-oblate first-order phase transition for $N \to \infty$ at any fixed value of $\eta \in [0, \frac{4}{5})$ can be induced by varying parameter χ in the generalized Hamiltonian of the form (1) with $\hat{Q}$ replaced by $\hat{Q}_\chi$.

It was shown [13] that in the O(6) dynamical symmetry, a discontinuous prolate-oblate change of the ground state structure can be observed even for *finite* boson numbers. Indeed, if one explicitly includes the O(5) Casimir invariant (5) into the Hamiltonian with a coefficient such that the $v = 0$ ground-state at $(\eta, \chi) = (0, 0)$ becomes degenerate with the lowest states of other seniorities, a crossing of the ground-state configurations will occur for any value of N when passing the O(6) point in the χ direction.

We are now in a position to extend this mechanism to the whole $\eta \in [0, \frac{4}{5})$ transitional region. The basic trick—the fact that levels with different seniorities can be made degenerate—remains the same. After subtracting the component corresponding to the O(5) Casimir invariant [20] from the general χ-dependent Hamiltonian of the form (1), we arrive at the expression

$$\hat{H}'(\eta, \chi) \propto \frac{\eta - 1}{N^2} \left\{ (\hat{Q}_\chi \cdot \hat{Q}_\chi) - \frac{1}{2}\hat{C}_2[\mathrm{O}(5)] \right\} + \frac{\eta}{N}\hat{n}_d, \quad (10)$$

which exhibits the desired property: for any fixed value of $\eta < \frac{4}{5}$ and any finite boson number N, the ground state as a function of χ changes discontinuously at $\chi_c = 0$.

We therefore extend the region of possible finite-N prolate-oblate phase transitions to the whole prolate-oblate separatrix, using the integrability of [O(6)-U(5)] $\supset$ O(5) IBM Hamiltonians. Note, however, that phase transitions at finite dimensions, induced by unavoided crossings of levels involving the ground state, are not robust enough to survive at finite temperatures. Indeed, if the temperature increases from zero to an infinitesimally small value, nonzero populations of both levels result in a smooth dependence of the free energy on the control parameter, and the phase-transitional behavior is washed out.

F. Bulk properties of the spectrum

It is clear that the strongest influence on a given level comes typically from its neighbors at the places of avoided crossings. Besides these binary interactions (involved in the shock-wave propagation), there exists also a component of the total force acting on each individual level that originates from the bulk of the whole ensemble. In this subsection, we will consider two global measures of this bulk component.

First, we consider the overall compression of all levels, represented by the energy dispersion (squared "spread") of the spectrum, $\Delta_E^2 = \frac{1}{n}\sum_i (E_i - \bar{E})^2$, where $\bar{E} = \frac{1}{n}\sum_i E_i$ is a center-of-mass energy. A straightforward calculation yields the expression

$$\Delta_E^2 = \left[\frac{\mathrm{Tr}\hat{H}_0^2}{n} - \frac{\mathrm{Tr}^2\hat{H}_0}{n^2}\right] + 2\eta\left[\frac{\mathrm{Tr}(\hat{H}_0\hat{V})}{n} - \frac{\mathrm{Tr}\hat{H}_0\mathrm{Tr}\hat{V}}{n^2}\right] + \eta^2\left[\frac{\mathrm{Tr}\hat{V}^2}{n} - \frac{\mathrm{Tr}^2\hat{V}}{n^2}\right], \quad (11)$$

which shows that the spectral dispersion is a quadratic function with a minimum at

$$\eta_0 = -\frac{n\mathrm{Tr}(\hat{H}_0\hat{V}) - \mathrm{Tr}\hat{H}_0\mathrm{Tr}\hat{V}}{n\mathrm{Tr}\hat{V}^2 - \mathrm{Tr}^2\hat{V}}. \quad (12)$$

For $\eta \approx \eta_0$, the strengths of both terms $\hat{H}_0$ and $\eta\hat{V}$ of Hamiltonian (2) are comparable, so the strongest effects of mixing take place in the surrounding region. For $\eta \gg \eta_0$ or $\eta \ll \eta_0$, on the other hand, the spectrum just blows up, the Hamiltonian being dominated by ηV.

For $v = 0$ and $v = 18$ subsets of the spectrum with $N = 80$, the function (11) is shown in Figs. 6(a) and 6(b). We see that the $v = 0$ levels are maximally compressed at $\eta_0 \approx 0.56$, i.e., in the region just before the phase transition. For higher seniorities, the minimum moves toward $\eta_c = 4/5$. Note that a similar conclusion can be made for $\chi \neq 0$, when of course the seniority is not conserved and the contribution of all $l = 0$ levels must be summed up. For $\chi = \pm\sqrt{7}/2$, for

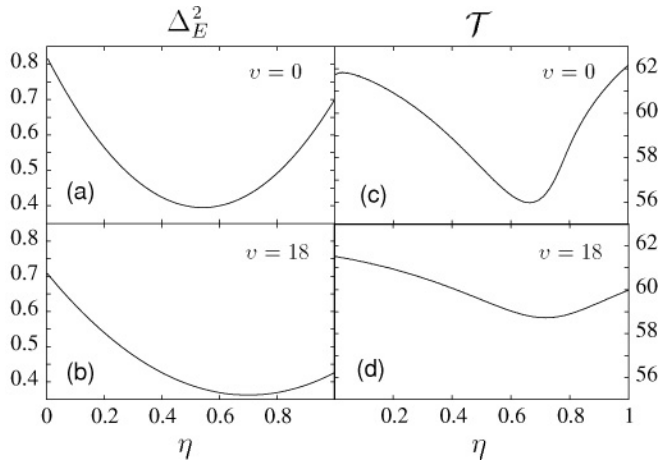

FIG. 6. Dispersion (11) of the spectrum and the kinetic energy from Eq. (13) for $v = 0$ and 18 states, corresponding to $l = 0$ and $N = 80$.

instance, the energy dispersion forms a sharp minimum directly at $\eta_0 \approx 0.8$.

The second quantity we will use here to characterize the bulk component of the force is the total product charge $\mathcal{Q} = \sum_{i>j} Q_{ij} = \sum_{i>j} |V_{ij}|^2$. It is related to the sum

$$\underbrace{\frac{1}{2}\sum_i \left(\frac{dE_i}{d\eta}\right)^2}_{\mathcal{T}} + \underbrace{\frac{1}{2}\sum_{i\neq j} |V_{ij}|^2}_{\mathcal{V}} = \frac{1}{2}\mathrm{Tr}\hat{V}^2 \equiv \mathcal{E}, \qquad (13)$$

which is an integral of motion of the Pechukas-Yukawa model, known as the total energy [24]. Since $\frac{d}{d\eta}\mathcal{E} = 0$, the second term that represents the potential energy $\mathcal{V} = \mathcal{Q}$ is at any value of η just a complement of the first, kinetic term $\mathcal{T}$. For $\eta \gg \eta_0$ and $\eta \ll \eta_0$ [assuming for a while $\eta \in (-\infty, +\infty)$], the eigenbasis of $\hat{H}(\eta)$ virtually coincides with the eigenbasis of $\hat{V}$ so that $\mathrm{Tr}\hat{V}^2 \approx \sum V_{ii}^2 = 2\mathcal{T}$ and $\mathcal{V} \approx 0$. In these regions, the gas just freely expands. On the other hand, around η_0 the kinetic and potential terms in Eq. (13) are comparable, and the interaction may generate nontrivial effects.

The kinetic energy from Eq. (13) for levels with $v = 0$ and $v = 18$, respectively, is shown in Figs. 6(c) and 6(d). In both cases, we observe a minimum of $\mathcal{T}$ very close to the critical point; for $v = 0$, the minimum is located at $\eta \approx 0.67$. This means that $\mathcal{V} = \mathcal{Q}$ is maximal at the same place, implying the strongest overall strength of level interactions. For higher seniorities, the minimum gets shallower and moves toward η_c.

We saw that both the compression of the spectrum and total interaction strength are maximal in the region of control parameters around η_0 which immediately precedes the phase transition at η_c. Conversely, Eq. (12) yields a reasonable rough estimate of the parameter range of a general Hamiltonian (2) where eventual phase transitions may be located.

IV. EIGENSTATE DYNAMICS

Besides dynamics of individual Hamiltonian eigenvalues $E_i(\eta)$, one can also analyze structural changes of the corresponding eigenstates $|\psi_i(\eta)\rangle$. These two aspects of spectral evolution are mutually correlated, since the matrix elements V_{ij}, which carry information on wave functions, belong to dynamical variables involved in Pechukas-Yukawa equations (6)–(8).

In Fig. 5, we already observed the evolution of the average number of d bosons $\langle n_d\rangle_i$ in the $v = 0$ and $v = 18$ eigenstates. This information is now supplemented by Fig. 7, where the η dependence of the whole distribution $P_i(n_d)$ of n_d is shown for selected $N = 80$ Hamiltonian eigenstates, namely the $v = 0$ states with $i = 1$, 10, 20, and 30 (ordered with increasing energy). For l and v fixed, the probability

$$P_i(n_d)|_\eta = \sum_{\tilde{n}_\Delta, m} |\langle n_d, v, \tilde{n}_\Delta, l, m|\psi_i(\eta)\rangle|^2 \qquad (14)$$

for each η is determined as the projection of the state $|\psi_i(\eta)\rangle$ onto the subspace of the U(5) eigenstates with n_d equal to the given number. In the U(5) limit, the distribution is concentrated on a single value $n_d = 2i - 2$ (with zero seniority, the value of n_d must be even), but it quickly spreads over a broad range of n_d as η decreases from 1 to 0.

Figure 7 shows four qualitatively different ways for how this delocalization proceeds. For the ground state, $i = 1$, the value of n_d remains zero as far as $\eta > \eta_c$, and then it suddenly increases (with decreasing η), forming a ridge around the average that goes approximately as $\langle n_d\rangle_1 \propto \sqrt{\eta_c - \eta}$, in agreement with the phase-transitional predictions; cf. Fig. 5(a). For excited states, the gradual spread of wave functions in n_d can be compared to the propagation of waves on a string. The string is initially (at $\eta = 1$; the "time" is now thought to go backward) subject to an instantaneous point perturbation and the resulting waves propagate in both $n_d = 0$ and $n_d = N$ directions asymmetrically. The pattern of wave propagations changes with i: for instance, the speed of the upper wave is lower for higher excited states. When the lower front of the wave reaches the $n_d = 0$ limit, it either gets reflected (this happens for lower excited states, see the $i = 10$ example) or stops there (for higher excited states, see $i = 20$ and 30 cases).

It is interesting that the value of η where the wave reaches the lower endpoint $n_d = 0$ coincides with the range where the shock wave affects the given level, see Figs. 2(a) and 3(a). This can be checked for a larger set of levels in Fig. 5(a). The dependences of individual n_d averages exhibit well-pronounced minima that correspond to the stopping or reflection of the lower wave front at $n_d = 0$ and that reasonably coincide with the moments of passage of the shock wave.

Also shown in the insets of Fig. 7 is the U(5) wave-function entropy,

$$S_i^{\mathrm{U}(5)} = -\sum_{n_d=0}^{N} P_i(n_d) \ln P_i(n_d), \qquad (15)$$

which measures the overall spread of the instantenous eigenvector $|\psi_i(\eta)\rangle$ in the U(5) basis [20]. Assuming a quasiuniform distribution of the ith state over a certain set of the $\hat{n}_d$ eigenstates, one finds that the effective number of components

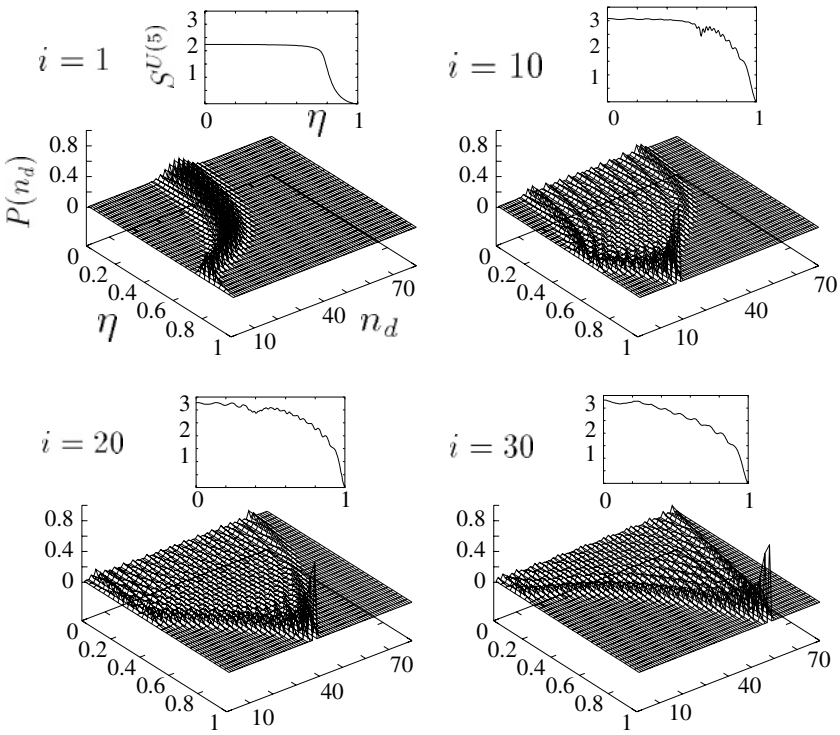

FIG. 7. Distribution of the d-boson number n_d in four $l = v = 0$ eigenstates of Hamiltonian (1) with $N = 80$ as a function of η. Insets show the corresponding U(5) wave-function entropy.

is given by $n_i^{\text{eff}} = \exp S_i^{\text{U(5)}}$. This number is approximately equal to half of the width (at a given value of η) of the n_d distribution corresponding to the respective level (taking into account that odd n_d values are not populated for $v = 0$).

As can be seen in Fig. 7, the widths of the n_d distributions and the corresponding U(5) entropies grow with decreasing η as far as the distribution touches the $n_d = 0$ limit (the level gets into the shock-wave region). After this point, the width and entropy stay approximately constant. If proceeding from the O(6) side, i.e., returning to the forward direction of time, we can say that the process of localization of level i in the U(5) basis *starts* approximately when the shock wave hits the level. This supports and further specifies the shock-wave scenario described in Sec. III C. We must stress, however, that for excited states, the transition to the U(5) structure after passing the shock wave is only gradual. A sudden phase-transitional type of change is reserved for the ground state only.

As indicated by the $i > 1$ examples in Fig. 7, the decrease of the U(5) wave-function entropy exhibits some undulations, connected with quantum interferences of the amplitudes corresponding to populations of individual n_d. It is surprising that vertical coordinates of the main oscillations are about constant for the whole ensemble of states. This is demonstrated in Fig. 8, where we show the U(5) wave-function entropy for all $v = 0$ and $v = 18$ states ($N = 80$). Clearly, if one proceeds from state to state, the undulations are shifted in η, but remain at about the same levels of entropy. The result is a peculiar pattern of plateaus present in both panels of Fig. 8. (Let us stress, however, that these plateaus are only a visual effect appearing when all entropies are drawn in the same figure.) This hints at strong correlations in the structural changes of individual eigenstates after the passage through the shock-wave region.

The most distinguished steps of the patterns in Fig. 8 are the same for both seniorities. They correspond to the effective numbers of wave-function components equal approximately to

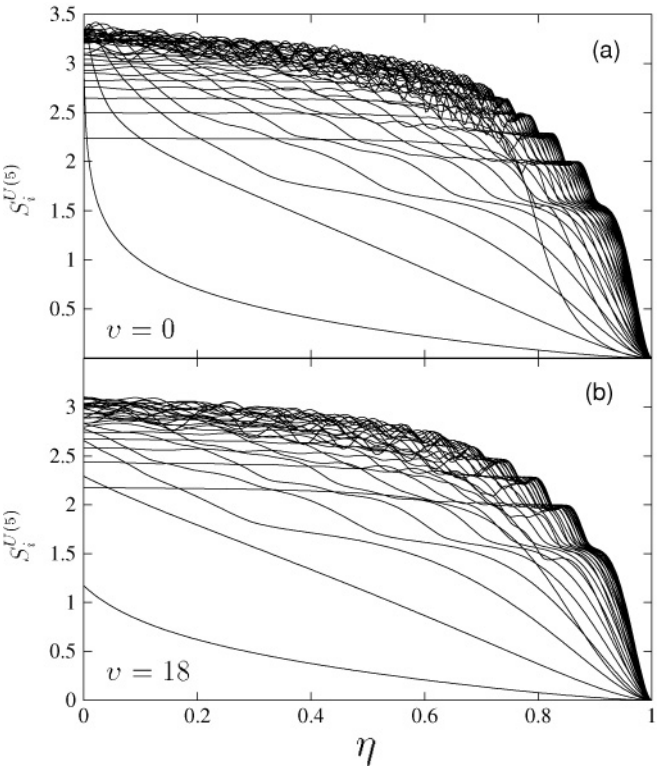

FIG. 8. U(5) wave-function entropy for all $v = 0$ and $v = 18$ eigenstates of Hamiltonian (1) with $l = 0$ and $N = 80$.

$n_i^{\rm eff} \approx 4.5, 7.5, 10$, and 12. Note that the average delocalization of a given state in a randomly chosen basis is for sufficiently high dimensions n given by $n_{\rm GOE}^{\rm eff} \approx 0.48\,n$ [20], which for the $v = 0$ and $v = 18$ subspaces yields typical saturation values of the wave-function entropy equal to $S_{\rm GOE} \approx 3$ and ≈ 2.7, respectively. [The largest U(5) entropies in the $\eta = 0$ limit slightly exceed the Gaussian-Orthogonal-Ensemble (GOE) values, but the latter provide reasonable estimates of averages if all states are taken into account.] We see that the system of plateaus in Fig. 8 disappear in noisy oscillations just below the respective GOE entropy values.

Let us stress that no steplike structures are observed in cumulative plots of the U(5) wave-function entropy of all $l = 0$ states for the SU(3)-U(5) and $\overline{\rm SU(3)}$-U(5) transitions. The present correlated behavior is therefore connected solely with the integrable $\chi = 0$ region.

V. CONCLUSIONS

We have studied dynamics of the $l = 0$ energy levels and the corresponding eigenstates along the [O(6)-U(5)] $\supset$ O(5) transition of the interacting boson model. Results of our numerical calculations were discussed in the framework of the Pechukas-Yukawa model, which describes the evolution of quantal spectra as one-dimensional motions of an ensemble of classical particles. Treated in this way, spectral attributes for all values of the control parameter—including possible phase transitions at some critical points—result just from a specific "initial condition," i.e., the set of energies and interaction matrix elements at a single *arbitrary* point η. (It needs to be stressed that this viewpoint does not, in fact, require the Pechukas-Yukawa equations, since the knowledge of energies and all matrix elements of $\hat{V}$ in the Hamiltonian eigenbasis at a single value of the control parameter clearly represent a complete determination of the Hamiltonian matrix for any η.) Of course, particularly tempting is to consider the whole spectral evolution along $\eta \in [0, 1]$ (and beyond) being predetermined by properties of the system in either of the two limiting dynamical symmetries.

We disclosed cooperative and highly coherent behaviors of the individual spectral constituents, i.e., level energies and wave functions corresponding to various seniorities. This may be generally linked to the integrability of the model in the present regime, namely, to the possibility to separate seniorities; but we have to admit that some of the findings remain just plain observations. Further studies may shed more light on how this all "comes about."

The most significant cooperative effect seems to rely on the shock-wave mechanism, which consists of an ordered sequence of avoided crossing of levels in the region around $E \approx 0$ and the accompanying changes of eigenstates (Secs. III C and IV). Triggered by an initial compression of the spectrum, the shock wave initiates in its densest upper part and propagates downward to the ground state. The passage of the wave through a given state starts the gradual transfiguration of the state structure into the U(5) form. This mechanism provides a deeper insight into the process that eventually leads to the ground-state phase transition of second order.

Among the other findings, we highlight the following: (a) approximate focal points of IBM spectra in transitions to the U(5) dynamical symmetry (Sec. III D), (b) possible finite-N prolate-oblate phase transitions along the whole [O(6)-U(5)] $\supset$ O(5) separatrix (Sec. III E), (c) extremes of spectral "bulk observables" in the region immediately preceding the phase transition (Sec. III F), (d) highly correlated changes of consecutive eigenstates leading to plateaus in the cumulative plot of U(5) wave-function entropies (Sec. IV).

In the following part of our article [19], we will focus on the interpretation of the $E \approx 0$ pattern of level bunchings (Sec. III B) within the semiclassical theory of quantal spectra.

ACKNOWLEDGMENTS

We acknowledge useful discussions with R. F. Casten and J. Dobes. This work was supported by the DFG Grant No. U36 TSE 17.2.04 and by the Czech Ministry of Education under Research Plan MSM 0021620834.

[1] F. Iachello and A. Arima, *The Interacting Boson Model* (Cambridge University, Cambridge, UK, 1987).
[2] R. Gilmore, *Catastrophe Theory for Scientists and Engineers* (Wiley, New York, 1981).
[3] D. H. Feng, R. Gilmore, and S. R. Deans, Phys. Rev. C **23**, 1254 (1981).
[4] A. E. L. Dieperink, O. Scholten, and F. Iachello, Phys. Rev. Lett. **44**, 1747 (1980).
[5] E. López-Moreno and O. Castaños, Phys. Rev. C **54**, 2374 (1996).
[6] J. Jolie, R. F. Casten, P. von Brentano, and V. Werner, Phys. Rev. Lett. **87**, 162501 (2001).
[7] J. Jolie, P. Cejnar, R. F. Casten, S. Heinze, A. Linnemann, and V. Werner, Phys. Rev. Lett. **89**, 182502 (2002).
[8] P. Cejnar, S. Heinze, and J. Jolie, Phys. Rev. C **68**, 034326 (2003).
[9] P. Cejnar, S. Heinze, and J. Dobes, Phys. Rev. C **71**, 011304(R) (2005); in *Workshop on Nuclei and Mesoscopic Physics*, AIP Conf. Proc. No. 777, edited by V. Zelevinsky (AIP, New York, 2005), p. 189.
[10] A. Leviatan, A. Novoselsky, and I. Talmi, Phys. Lett. **B172**, 144 (1986).
[11] Feng Pan and J. P. Draayer, Nucl. Phys. **A636**, 156 (1998).
[12] J. Dukelsky and S. Pittel, Phys. Rev. Lett. **86**, 4791 (2001).
[13] J. M. Arias, J. Dukelsky, and J. E. García-Ramos, Phys. Rev. Lett. **91**, 162502 (2003).
[14] F. Iachello, Phys. Rev. Lett. **85**, 3580 (2000).
[15] J. M. Arias, C. E. Alonso, A. Vitturi, J. E. García-Ramos, J. Dukelsky, and A. Frank, Phys. Rev. C **68**, 041302(R) (2003).
[16] D. J. Rowe, Phys. Rev. Lett. **93**, 122502 (2004); Nucl. Phys. **A745**, 47 (2004); D. J. Rowe, P. S. Turner, and G. Rosensteel, Phys. Rev. Lett. **93**, 232502 (2004).

[17] P. Pechukas, Phys. Rev. Lett. **51**, 943 (1983); T. Yukawa, *ibid.* **54**, 1883 (1985).
[18] M. C. Gutzwiller, J. Math. Phys. **12**, 343 (1971); M. V. Berry and M. Tabor, Proc. R. Soc. London, Sect. A **349**, 101 (1976).
[19] M. Macek, P. Cejnar, J. Jolie, and S. Heinze, Phys. Rev. C **73**, 014307 (2006), the following article, in this journal.
[20] P. Cejnar and J. Jolie, Phys. Rev. E **58**, 387 (1998).
[21] W. M. Zhang and D. H. Feng, Phys. Rep. **252**, 1 (1995).
[22] N. Whelan and Y. Alhassid, Nucl. Phys. **A556**, 42 (1993).
[23] R. L. Hatch and S. Levit, Phys. Rev. C **25**, 614 (1982).
[24] H.-J. Stöckmann, *Quantum Chaos. An Introduction* (Cambridge University, Cambridge, UK, 1999).
[25] W. D. Heiss, Phys. Rep. **242**, 443 (1994); I. Rotter, Phys. Rev. C **64**, 034301 (2001).
[26] T. Kato, *Perturbation Theory of Linear Operators* (Springer-Verlag, Berlin, 1966).

Evolution of spectral properties along the O(6)-U(5) transition in the interacting boson model. II. Classical trajectories

Michal Macek,[1] Pavel Cejnar,[1] Jan Jolie,[2] and Stefan Heinze[2]
[1]*Faculty of Mathematics and Physics, Charles University, V Holesovickách 2, CZ-180 00 Prague, Czech Republic*
[2]*Institute of Nuclear Physics, University of Cologne, Zülpicherstrasse 77, D-50937 Cologne, Germany*
(Received 5 April 2005; published 23 January 2006)

We continue our previous study of level dynamics in the [O(6)–U(5)]⊃O(5) transition of the interacting boson model [Phys. Rev. C **73**, 014306 (2006)] by using the semiclassical theory of spectral fluctuations. We find classical monodromy, related to a singular bundle of orbits with infinite period at energy $E = 0$, and bifurcations of numerous periodic orbits for $E > 0$. The spectrum of allowed ratios of periods associated with β and γ vibrations exhibits an abrupt change around zero energy. These findings explain anomalous bunching of quantum states in the $E \approx 0$ region, which is responsible for the redistribution of levels between O(6) and U(5) multiplets.

DOI: 10.1103/PhysRevC.73.014307 PACS number(s): 21.60.Ev, 21.60.Fw, 03.65.Sq

I. INTRODUCTION

In the first part of this work [1] (hereafter referred to as Part I), we discussed the evolution of level energies and wave functions along the [O(6)–U(5)]⊃O(5) transition in the interacting boson model (IBM) [2]. It is known that this transitional class is integrable—because of the O(5) underlying symmetry and the associated seniority quantum number ν—and exhibits a second-order ground-state phase transition from deformed γ-soft to spherical equilibrium shapes.

Remember that our family of model Hamiltonians is given by

$$\hat{H}(\eta) = a\left[-\frac{1-\eta}{N^2}(\hat{Q}\cdot\hat{Q}) + \frac{\eta}{N}\hat{n}_d\right], \qquad (1)$$

with $\eta \in [0, 1]$ denoting a dimensionless control parameter that drives the system between the O(6) ($\eta = 0$) and U(5) ($\eta = 1$) dynamical symmetries. The spectrum of $\hat{H}(\eta)$ at any point of the transitional path depends on the specific interplay of both terms in Eq. (1), where $\hat{Q} = [s^\dagger\tilde{d} + d^\dagger\tilde{s}]^{(2)}$ represents the quadrupole operator and $\hat{n}_d = (d^\dagger\cdot\tilde{d})$ is the d-boson number operator. Note that N is the total number of bosons, which in the classical limit tends to infinity (both terms in the above Hamiltonian are properly normalized by the N^k denominators to yield finite contributions in this limit), and $a = 1$ MeV is an arbitrary scaling factor (energy unit). The $N \to \infty$ ground-state shape-phase transition takes place at $\eta_c = 4/5$.

We have shown that one of the most significant features of spectra in the $\eta \in [0, 1]$ transitional regime of Hamiltonian (1) is the pattern of alternating compressions and dilutions of levels with angular momentum $l = 0$ around energy $E \approx 0$. This pattern spreads over a wide interval of the control parameter between $\eta \approx 0.3$ and 0.8; see Fig. 1 in Part I. After deconvoluting spectra with different seniorities, it transforms into a sequence of avoided crossings that constitute what we called the "shock-wave scenario" [1].

The level-bunching pattern represents basically a huge oscillation of the level density in the $E \approx 0$ region, not dissimilar to shell effects in single-particle spectra of some quantum-mechanical potentials. There exists a deep and far-reaching relation between fluctuations of the quantum level density and properties of periodic orbits in the classical counterpart of the given system [3,4]. While it is known that each periodic orbit brings one oscillatory term into the level density, with an amplitude related to the orbit's dimensionality and stability [5–7], the interference of several such terms gives rise to spectral *beating patterns* that underlie shell effects in nuclei, quantum dots, or metallic clusters [8]. Indeed, as follows from the analysis performed by Balian and Bloch [6], the inclusion of just the two the simplest periodic orbits in a spheroidal cavity explains the essentials of the shell structure in these systems.

The majority of semiclassical studies on level-density fluctuations was performed for hard-wall systems—two-dimensional billiards or three-dimensional cavities [3,4]. In these systems, the calculation is considerably simplified since each individual orbit exists with easily predictable properties for all energies of the particle bouncing between the walls and contributes by a well-defined term to the single-particle level density. Nevertheless, the influence of periodic orbits is equally important also in systems with "soft" potentials, in which the orbit analysis is much more involved. This is also the case of the IBM, in which the classical limit for $l = 0$ describes two-dimensional motions within a bounded (for each finite E) range of quadrupole deformation parameters, governed by a Hamiltonian containing specific kinetic and potential terms [9–12].

The purpose of the present part of our contribution is to show that the shell effects and the IBM level-bunching phenomenon are indeed of similar nature, both originating in some particular features of classical periodic trajectories. Nevertheless, our reasoning does not only point to ordinary beating patterns, known from hard-wall systems, but makes use of two concepts that in the context of nuclear models are somewhat less usual. The first one relies on *bifurcations* of periodic orbits [13], the second on *monodromy* in classical and quantum integrable systems [14]. Both these effects lead to singular contributions to semiclassical trace formulas that provide a simplified description of the level-density fluctuations. Therefore they can be potentially linked to anomalous effects in quantal spectra, such as the level bunching at $E \approx 0$. We want to emphasize that the conclusions of the present work are

mostly qualitative (because of large complexity of the rigorous theoretical description), but even with this limitation we hope to shed more light on the problems discussed.

The paper is organized as follows: In Sec. II we review the construction of the classical limit of the IBM Hamiltonian under study and describe basic features of the resulting classical dynamics. Subsection III A briefly recapitulates the Berry-Tabor trace formula and the role of singular orbits and bifurcations in the semiclassical theory of quantal spectra. Numerical analysis of orbits with $l = 0$, presented in Subsec. III B, shows that in the $E \approx 0$ region our system passes through a robust structural change of classical dynamics. This change is correlated with the occurrence of a singular bundle of $E = 0$ trajectories and triggers multiple bifurcations of orbits in the region $E > 0$. The relation of these findings to the concept of monodromy is discussed in Sec. IV. Finally, Sec. V contains concluding remarks.

II. CLASSICAL HAMILTONIAN

The classical limit of the IBM can be obtained by means of the well-known procedure, elaborated in detail by Hatch and Levit [9] and by Alhassid and Whelan [10–12]. The procedure makes use of Glauber coherent states $|\alpha\rangle \propto \exp(\alpha_s s^\dagger + \sum_\mu \alpha_\mu d_\mu^\dagger)|0\rangle$ with complex time-dependent coefficients $\alpha \equiv \{\alpha_s, \alpha_\mu\}_{\mu=-2,\ldots,+2}$ that define a set of 12 classicallike variables (both coordinates and momenta). The equations of motion for α are derived from the time-dependent variational principle, which results in the Hamilton function given by the coherent-state average $H_{\rm cl}(\eta;\alpha) = \langle\alpha|\hat{H}(\eta)|\alpha\rangle$. This function and analogous counterparts of other operators can be obtained by substitutions $s, d_\mu \mapsto \alpha_s, \alpha_\mu$ and $s^\dagger, d_\mu^\dagger \mapsto \alpha_s^*, \alpha_\mu^*$ in the respective normal-ordered quantal expressions.

Since Glauber coherent states do not fix the total number of bosons, an additional constraint must be required, namely that $\langle\alpha|\hat{N}|\alpha\rangle = |\alpha_s|^2 + \sum_\mu |\alpha_\mu|^2 = N$. This (plus an arbitrary choice of the overall phase, $\alpha_s = \sqrt{N - \sum_\mu |\alpha_\mu|^2}$) reduces the number of relevant degrees of freedom from 6 to 5. Naturally, the classicality of coherent states becomes more and more pronounced as N increases and the fully classical limit is obtained in the $N \to \infty$ limit. To prevent divergence of the corresponding averages, one has to scale all operators according to their order [see the $(1/N^k)$ factors in Hamiltonian (1)] and to absorb the respective factors into the definition of α's. This leads to the substitution $\alpha_\mu \mapsto \tilde{\alpha}_\mu = (\alpha_\mu/\sqrt{N})$ while, simultaneously, the $(1/N^k)$ factors drop out.

Final expressions for the classical-limit observables are obtained after the identification of real coordinates q_μ and momenta p_μ by means of relations $\sqrt{2}\tilde{\alpha}_\mu = (-)^\mu q_{-\mu} + i p_\mu$ and $\sqrt{2}\tilde{\alpha}_\mu^* = q_\mu - (-)^\mu i p_{-\mu}$. The coordinates q_μ are associated with the geometric variables describing an instantaneous quadrupole deformation of the nucleus and its orientation in the laboratory frame. Because of the fixed boson number average, the motion is constrained by the condition

$$\sum_\mu \left(p_\mu^2 + q_\mu^2\right) \leqslant 2 \tag{2}$$

to the interior of a sphere in the 10-dimensional phase space.

The calculation of classical observables is substantially simplified for zero angular momentum, $l = 0$ [12,15]. In this case, the intrinsic frame connected with the ellipsoid of deformation remains at rest, and one can fix $\mathrm{Re}\, q_0 \equiv x$ and $\mathrm{Re}\, q_{+2} = \mathrm{Re}\, q_{-2} \equiv y/\sqrt{2}$ (while $q_{\pm1} = \mathrm{Im}\, q_{\pm2} = \mathrm{Im}\, q_0 = 0$). The $l = 0$ classical limit of Hamiltonian (1) reads

$$H_{\rm cl} = \underbrace{\frac{\eta}{2}\pi^2 + (1-\eta)\beta^2\pi^2}_{T_{\rm cl}} + \underbrace{\frac{5\eta-4}{2}\beta^2 + (1-\eta)\beta^4}_{V_{\rm cl}} \tag{3}$$

(with $a = 1$), where $\beta^2 = x^2 + y^2$ is the squared radius in the $q_0 \times \sqrt{2}q_{\pm2}$ plane (the polar angle denoted as γ) and π^2 is the squared length of the associated vector of momenta:

$$\pi^2 = \pi_x^2 + \pi_y^2 = \pi_\beta^2 + \left(\frac{\pi_\gamma}{\beta}\right)^2. \tag{4}$$

Hamiltonian (3) can be thought of as describing planar motions of a particle with the position-dependent kinetic energy $T_{\rm cl}$ in potential $V_{\rm cl}$, which is for $\eta = 0$, 0.6, and 1, as shown in Fig. 1. Whereas for $\eta < \eta_c = 4/5$, the potential has the "Mexican-hat" (or "champagne-bottle") form, for $\eta \geqslant \eta_c$ it is just a well with a minimum at $\beta = 0$. To emphasize the rotational symmetry in the $x \times y$ plane, we show both positive and negative domains of β (the latter corresponding to the rotation by angle 180°). As follows from the form of the potential and from condition (2), the radius must satisfy

$$\beta \in [\beta_{\min}, \beta_{\max}] \subset [0, \sqrt{2}] \tag{5}$$

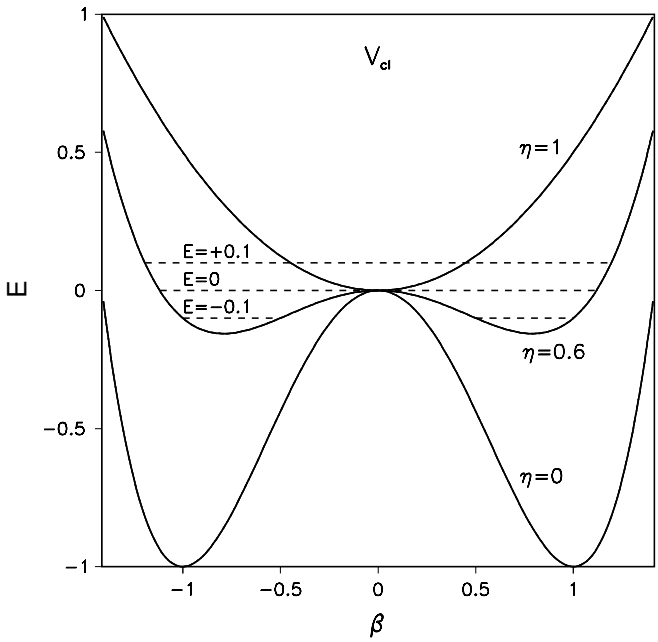

FIG. 1. Potential-energy term of Hamiltonian (3) for three values of parameter η. The lowermost ($\eta = 0$) and uppermost ($\eta = 1$) curves correspond to O(6) and U(5) limits, respectively. The middle curve ($\eta = 0.6$) represents an intermediate case, for which the accessible range of radii (for the three given energies) is shown by the dashed lines. Energy is given in units a from Eq. (1). "Negative radii" express the $(\beta, \gamma) \to (\beta, \gamma + 180^\circ) \equiv (-\beta, \gamma)$ transformation and are included just to emphasize the rotational symmetry.

and the total energy

$$E \in [E_{\min}, E_{\max}] \subset [-1, +1],$$
$$E_{\min} = \begin{cases} -\frac{(5\eta-4)^2}{16(1-\eta)} & \text{for } \eta < \frac{4}{5} \\ 0 & \text{for } \eta \geqslant \frac{4}{5} \end{cases}, \quad E_{\max} = \eta. \tag{6}$$

Remember that throughout this paper the energy is always expressed in units of the scaling constant a, see Eq. (1), so it is formally dimensionless.

Note that polar coordinates β and γ of x and y can be immediately associated with Bohr geometric variables, but in this case the deformation parameter is restricted to interval (5). To obtain $\tilde{\beta} \in [0, \infty)$, as is usual in nuclear structure, the coordinate plane would have to be radially stretched [16] according to $\beta \mapsto \tilde{\beta} = (\beta/\sqrt{2-\beta^2})$, together with the accompanying transformation of the radial momentum. In the following discussion, nevertheless, we use classical limit (3) with constraint (5).

It is immediately apparent that Hamiltonian (3) is "γ soft," invariant under rotations about the origin, so it conserves the "angular momentum":

$$\pi_\gamma = x\pi_y - y\pi_x. \tag{7}$$

Thus, since the number of degrees of freedom $f = 2$, the system must be integrable. This is in agreement with the arguments explaining the integrability of the [O(6)−U(5)]⊃O(5) Hamiltonians with arbitrary angular momenta, as outlined in Part I [1], since Eq. (7) is closely related to the integral of motion $\hat{C}_2[\mathrm{O}(5)] = \frac{1}{5}(\hat{L}\cdot\hat{L}) + 2(\hat{T}_3\cdot\hat{T}_3)$. Indeed, for $l = 0$, the classical limit of the O(5) Casimir invariant reads [9]

$$C_2[\mathrm{O}(5)]_{\mathrm{cl}}|_{l=0} = 2\pi_\gamma^2. \tag{8}$$

Note that since angular momentum (8) does not correspond to the ordinary O(2) algebra of two-dimensional rotations, its quantization yields eigenvalues $v(v+3)$, where, for $l = 0$, the seniority takes values $v = 0, 3, 6, \ldots$, in contrast to the m^2 formula with $m = 0, \pm1, \pm2, \ldots$, corresponding to O(2). Nevertheless, we realize that each value of $C_2[\mathrm{O}(5)]_{\mathrm{cl}}$ is associated with both signs of π_γ, i.e., with two opposite orientations of the motion in the γ direction. This intrinsic "degeneracy" (which does not affect physical results in the quantum case) will become important in Sec. IV.

The integrability of Hamiltonian (3) is illustrated in Fig. 2, where we show Poincaré phase-space sections for $\eta = 0.6$ at three different energies, (a) $E = -0.1$, (b) $E = 0$, and (c) $E = 0.1$. Each of the panels represents passages of 10–50 randomly selected trajectories with the given energy E through the $\beta \times \pi_\beta$ plane in four-dimensional phase space. Because of the rotational symmetry, the plane can have an arbitrary orientation in the $x \times y$ frame and the pattern of sections must be symmetric under the reflection of the β axis (we show both $\beta > 0$ and $\beta < 0$ halves).

All sections in Fig. 2 demonstrate fully regular dynamics, in agreement with the integrability of our system. As can be anticipated from Fig. 1, the $E < 0$ motions in panel (a) must be confined inside the annular region $\beta \in [\beta_{\min}, \beta_{\max}]$, while the $E > 0$ trajectories in panel (c) already range over the full disk $\beta \in [0, \beta_{\max}]$ (the values $\beta_{\min}$ and $\beta_{\max}$ depend on energy).

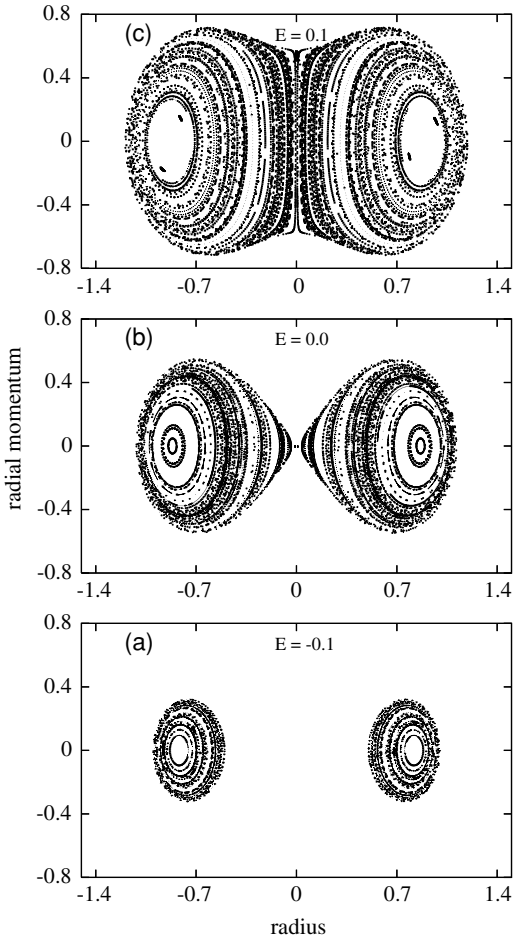

FIG. 2. Poincaré phase-space sections for Hamiltonian (3) with $\eta = 0.6$ at the three given values of energy. The sections show a finite number of crossings of (a) 10, (b) 30, and (c) 50 trajectories with the plane $\beta \times \pi_\beta$ for arbitrary γ.

Panel (b) shows just the singular $E = 0$ situation, when the central inaccessible (for $E < 0$) disk shrinks into a single point (which can be reached in infinite time). We return to this case in Sec. IV.

Let us stress that the Poincaré sections in Fig. 2 separate trajectories with different energies, but mix together those with various values of the angular momentum π_γ. Indeed, the outermost curves in all panels represent pure β vibrations with $\pi_\gamma = 0$, while the central points (not shown) correspond to "spinning" only in the γ direction with $\pi_\beta = 0$. The other trajectories correspond to various mixtures of β and γ vibrations. An interesting attribute of these intermediate cases is the spread $\Delta\beta$ of each individual trajectory in the β direction, which can be determined as the difference between radii corresponding to the outermost and the innermost points. This attribute is used in Sec. III to classify quasi-periodic orbits in our system.

III. PERIODIC ORBITS

A. Berry-Tabor formula, singular orbits, and bifurcations

Semiclassical analyses of quantal spectra are performed within the framework of so-called trace formulas that represent

the fluctuating part $\varrho_{\rm fl}(E)$ of the level density $\varrho_{\rm tot} = \varrho_{\rm sm} + \varrho_{\rm fl}$ in terms of purely classical quantities associated with periodic orbits, while the complementary smooth part $\varrho_{\rm sm}(E)$ is determined just as the classical phase-space volume available at a given energy E in units of $\hbar^f$ (where f is the number of the system's degrees of freedom). The best-known expression, derived by Gutzwiller [5], was obtained under the assumption that individual periodic orbits are isolated, which is not satisfied for integrable systems. In this case, periodic orbits come in continuous families characterized by arbitrary shifts of initial angles if the motion is described in the action-angle variables [13]. An adequate semiclassical approach to the level density of integrable systems was developed by Berry and Tabor [7].

In the following discussion, we consider a two-dimensional integrable system, $f = 2$, that applies in our case of Hamiltonian (3). In the action-angle representation, the Hamiltonian depends only on actions $H = H(I_1, I_2)$, and the angles evolve according to $\dot\theta_1 = \omega_1$ and $\dot\theta_2 = \omega_2$. All trajectories represent folded rotations on various tori determined by $\vec I = (I_1, I_2)$. Let us note that, in many integrable systems, including ours, the action-angle variables can be introduced only locally [14] (see Sec. IV). Therefore it is not possible to write analytic expressions for the corresponding canonical transformation from normal coordinates and momenta.

Any primitive periodic orbit on a given torus can be characterized by a pair of coprime integers $(\mu_1, \mu_2) \equiv \vec\mu$ such that the ratio of angular frequencies $\mathcal{R} = (\omega_1/\omega_2)$ coincides with the rational number μ_1/μ_2. The Berry-Tabor formula for the fluctuating part of the quantal state density [7] then reads

$$\varrho_{\rm fl}(E) = \frac{1}{\pi\hbar}\sum_{\vec\mu}\sum_{r=1}^{\infty}\frac{T_{\vec\mu}}{\sqrt{\hbar|g_E''|(r\mu_2)^3}} \times \cos\left[\frac{1}{\hbar}rS_{\vec\mu}(E) - \frac{\pi}{2}r\nu_{\vec\mu} - \frac{\pi}{4}\right], \qquad (9)$$

where the sum runs over all repetitions r of all primitive orbits $\vec\mu$ with period $T_{\vec\mu} = [(2\pi\mu_1)/\omega_1] = [(2\pi\mu_2)/\omega_2]$, Maslov index $\nu_{\vec\mu}$ [3], and action

$$S_{\vec\mu}(E) = 2\pi\vec I\cdot\vec\mu = \int_0^{T_{\vec\mu}}[\pi_\beta\dot\beta + \pi_\gamma\dot\gamma]\,dt. \qquad (10)$$

The meaning of the function g_E'' in Eq. (9) will be explained later.

Expression (10), which in the general case integrates the scalar product of momentum and velocity over the specific periodic trajectory $\vec\mu$, has a particularly simple form for billiards (or cavities), for which one can write $S_{\vec\mu} = 2ET_{\vec\mu} = pL_{\vec\mu}$, with $p = mv$ denoting the ordinary momentum and $L_{\vec\mu}$ the length of the given orbit. For "soft" systems, the dependence of $S_{\vec\mu}$ on energy is nonlinear and frequencies of individual cosine terms in Eq. (9) vary with E. Since in the latter case each oscillatory term in the Berry-Tabor formula contains also a nontrivial energy dependence of the amplitude, the semiclassical analysis of spectra in such cases is certainly much less intuitive than in the hard-wall systems.

In general, there may exist singular orbits with diverging contributions to the Berry-Tabor formula. This happens if either the period of the given orbit grows to infinity, $T_{\vec\mu}\to\infty$, or if the denominator of the prefactor in Eq. (9) vanishes, $g_E''\to 0$. The former case applies to the motions that for some energy become infinitely slow at a certain point, which can be associated with an unstable equilibrium of the system. We know from the discussion in Sec. II that our system contains such a point, namely the central maximum of the potential in Eq. (3) at $\beta = 0$ for $\eta \leqslant (4/5)$. For trajectories with $E = 0$, this maximum can be reached in only asymptotic times because the force vanishes there. Among the trajectories passing this point there are also various periodic orbits, whose contribution to Eq. (9) must diverge at $E = 0$ because of the period tending to infinity. This is essentially the classical mechanism responsible for the bunching of quantum levels in the region $E \approx 0$; see Fig. 1 in Part I [1]. It shows that the bunching pattern is not just a finite-N quantum fluctuation, but a robust effect deeply ingrained in the classical limit of the system. Theoretical foundations underlying the existence of the singular class of trajectories and another approach to understand their influence on the quantum spectrum will be discussed in Sec. IV.

The second possible source of infinite contributions to Berry-Tabor formula (9) is connected with the cases when $g_E''(I_1) \equiv [(\partial^2 g_E/\partial I_1^2)](I_1) = 0$. The function $g_E(I_1)$ is determined [17] from the implicit equation $H(I_1, I_2 = g_E) = E$, which after differentiation and the use of Hamilton equations yields

$$\dot\theta_1 + \dot\theta_2\frac{\partial g_E}{\partial I_1} = 0, \qquad (11)$$

so that $g_E' = -(\omega_1/\omega_2) = -\mathcal{R}$. In other words, the function g_E matches possible pairs of actions (I_1, I_2), i.e., selects the tori $\vec I$ relevant at a given energy, and its first derivative determines the corresponding frequency ratios. If $-g_E'$ is rational for a selected torus, the associated orbit is periodic and contributes to Eq. (9). The second derivative g_E'' measures the change of $\mathcal{R}$ as one steps to the tori in an infinitesimal vicinity of $\vec I$. If $g_E'' \neq 0$, the periodic orbit $\vec\mu$ on the torus $\vec I$ does not survive the transition to $\vec I + \delta\vec I$. If, however, $g_E'' = 0$, a family of periodic orbits with the same frequency ratio $\mathcal{R}$ exists in neighboring tori, which results in a diverging contribution to Berry-Tabor formula (9).

Note that the Gutzwiller formula [5], which is valid in nonintegrable systems with isolated periodic orbits, is formally similar to Eq. (9), but with the prefactor denominator replaced with $\sqrt{\det[(M_p)^r - 1]}$, where M_p stands for the so-called monodromy matrix of a given primitive periodic orbit p [3,4]. This matrix describes the stability of orbit p in terms of linearized deviations from the given phase-space trajectory under a perpendicular perturbation of its initial point. Thus $(M_p)^r - 1$ represents the deviation from the perturbed phase-space position after r repetitions. If one (or more) of the eigenvalues of this matrix is equal to zero, i.e., if $\det[(M_p)^r - 1] = 0$, there exists at least one direction in the phase space in which any deviation from the given orbit $r\cdot p$ results in another periodic orbit. The new orbits are detached from the primitive orbit p as its period r-tupling clones. Consequently p is not isolated and the corresponding term

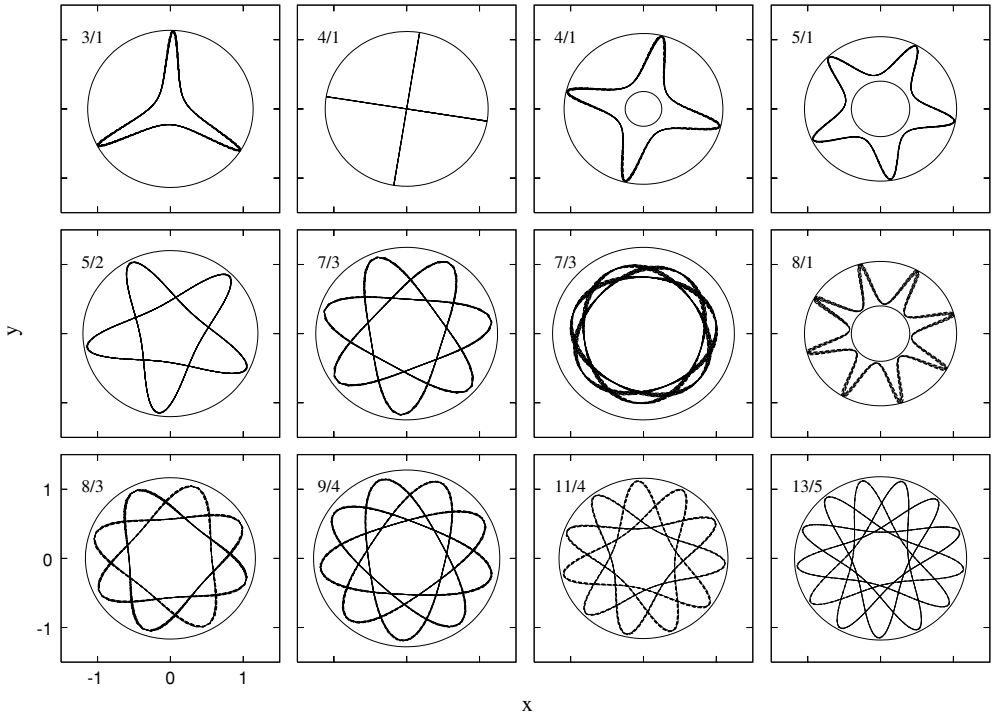

FIG. 3. Examples of various periodic orbits at different energies for Hamiltonian (3) with $\eta = 0.6$ and their classification by rational fractions $R = (\mu_\beta/\mu_\gamma)$.

in the Gutzwiller formula diverges. This situation is analogous to the one with $g''_E = 0$, as described above.

Both the above singular cases correspond to the same general phenomenon, called bifurcation [18]. In Hamilton systems of classical mechanics, bifurcations represent branching of periodic orbits at some critical values of energy or other parameters [13]. While periodic orbits existing below and above the given bifurcation energy E_b are isolated, either in the sense of $g''_E \neq 0$ or $\det[(M_p)^r - 1] \neq 0$, at $E = E_b$ two or more orbits merge together in the way described above, giving rise to zero denominators of the respective semiclassical level-density formulas. At the bifurcation energies E_b, the Berry-Tabor or Gutzwiller formula does not represent correct approximations of the fluctuating level density. Improved semiclassical methods were developed to treat these situations [19]. Intuitively one expects an enhancement of the level-density oscillations at the bifurcation points. In the following subsection we show that in our system numerous bifurcations of periodic orbits take place in the energy range $E > 0$.

B. Numerical results

We have performed a numerical analysis of classical motions corresponding to Hamiltonian (3) in the interval of energies $E \in [-0.1, +0.3]$ by using a sample of about 50 000 generated orbits. Individual trajectories were calculated with initial positions and momenta chosen randomly within the phase-space region accessible at a given energy and classified by the ratio

$$R = \frac{T_\gamma}{T_\beta} = \frac{\langle \omega_\beta \rangle}{\langle \omega_\gamma \rangle} \tag{12}$$

of periods T_γ and T_β associated with oscillations in both γ and β directions, respectively. Since $\omega_\gamma = \dot{\gamma}$ and the angular velocity ω_β connected with β vibrations are both time dependent, one has to use the corresponding average angular frequencies per period, $\langle \omega_\gamma \rangle = (2\pi/T_\gamma)$ and $\langle \omega_\beta \rangle = (2\pi/T_\beta)$. Their inverse ratio coincides with R and is analogous to the above-discussed ratio $\mathcal{R} = (\omega_1/\omega_2)$ of frequencies in the action-angle variables. In particular, rational values $R = (\mu_\beta/\mu_\gamma)$ correspond to periodic orbits with period $T_{\mu_\beta/\mu_\gamma} = \mu_\beta T_\beta = \mu_\gamma T_\gamma$.

Examples of periodic orbits with various rational values of ratio (12) are shown in Fig. 3. The rational fraction $R = (\mu_\beta/\mu_\gamma)$ classifying the given orbit has visual meaning as the number of outer return points of the β vibration over the number of rotations in the γ direction needed to close the orbit. Thus, for instance, the $5/2$ orbits look like stars with five outer "points" that close in two rotations, while the $5/1$ stars are similar, but close in only one rotation. The outer and in some panels also the inner circles in Fig. 3 demarcate the energetically accessible areas $\beta \in [\beta_{\min}, \beta_{\max}]$ in the $x \times y$ plane. As discussed in Sec. II, this area is a disk for $E > 0$, an annular ring for $E < 0$, and a disk minus the central point for $E = 0$. We see that although the orbits in Fig. 3 do not just trivially bounce between the outer (and inner) limits, as in the case of circular or annular infinite sharp wells, they still resemble to a large extent the trajectories in these simple systems [20].

Periodic orbits form a dense subset of all allowed motions, and we therefore need a more complete picture. A histogram showing the occurrence of trajectories with arbitrary (rational or irrational) values of the frequency ratio R within the whole sample of trajectories with $E \in [-0.1, +0.3]$ is presented in

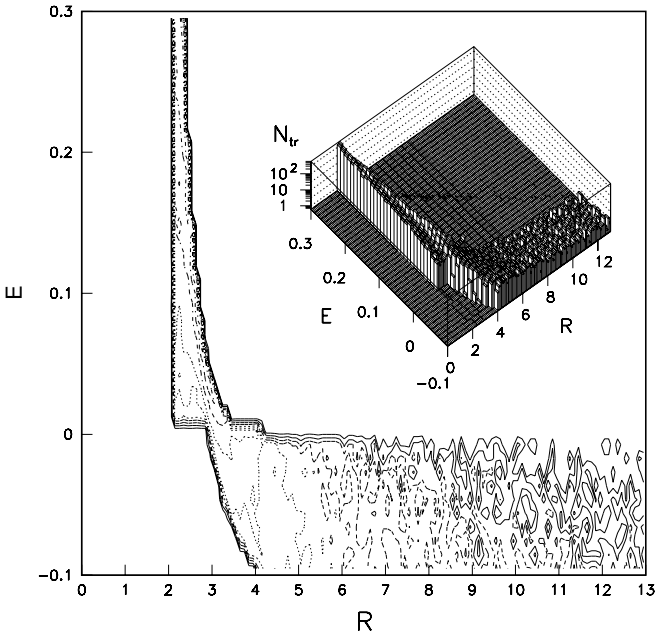

FIG. 4. Frequency of occurrence of trajectories with different ratios R for Hamiltonian (3), $\eta = 0.6$, in the reference sample of trajectories with different energies. For each value of E (step $\Delta E = 0.01$) there were 1200 generated trajectories, and the histogram (see the inset) shows their distribution in R (the bin width $\Delta R = 0.01$). The main diagram (contour plot of the logarithmic histogram) depicts the band structure of allowed R values; see expression (13) and below.

Fig. 4. For each value of energy within the given range (the energy step $\Delta E = 0.01$ was chosen), the sample contains $N_{\rm tot} = 1200$ trajectories, and Fig. 4 depicts their distribution (numbers $N_{\rm tr}$ of trajectories) into bins of size $\Delta R = 0.01$ along the R axis.

The structure shown in Fig. 4 discloses rather interesting features of classical motions. For each energy, the orbits occur within a band

$$R \in [R_{\rm min}(E), R_{\rm max}(E)] \tag{13}$$

of allowed frequency ratios. The lower bound $R_{\rm min}(E)$ gradually decreases with increasing energy for $E < 0$, but it is constant, $R_{\rm min} = 2$, for $E > 0$. Because of the limited precision inherent in our generated sample of trajectories (with nonzero values of the bin size ΔR and energy step ΔE) we cannot resolve whether the $R_{\rm min}(E)$ dependence is discontinuous or just nonanalytic at $E = 0$. In any case, the curve reaches the minimal value at this point. On the other hand, for energy approaching the minimum E_0 of the potential in Eq. (3) (this energy is below the range displayed in Fig. 4) we must have $R_{\rm min} \to \infty$. The upper bound of interval (13) is also a decreasing function of energy that passes the value $R_{\rm max} = 4$ at $E = 0$. The decrease of $R_{\rm max}(E)$ for $E < 0$ (and partly also just above $E = 0$) is so steep that it cannot be resolved with the present energy step, but we assume that it is a smooth curve. It is obvious that a very narrow energy interval around the point $E = 0$ carries the most substantial changes in the spectrum of orbits, where the trajectories pass between both negative and positive energy regions just through a bottleneck of values $R \in [3, 4)$. While for $E < 0$ the orbits look similar to those in the O(6) limit, for $E > 0$ they already resemble the U(5) limit.

The behavior demonstrated in Fig. 4 can be qualitatively understood from the change of the energetically accessible $x \times y$ area around $E \approx 0$. The form of an annular ring, valid for $E < 0$, does not support trajectories with $R < 3$ since these have to traverse through the central region. Consequently these trajectories can exist for only $E > -\varepsilon$, where $\varepsilon \approx 0.03$. On the other hand, the central reflecting disk is needed for trajectories with $R \geqslant 4$, which therefore appear only for $E < 0$. One can say that the $R \in [4, \infty)$ trajectories, which are "bouncing" between inner and outer circles inside the annular region for $E < 0$, transform to the straight $R \in [2, 3]$ trajectories at $E \approx 0$ where the central disk gradually disappears and the accessible domain of deformation parameters becomes simply connected. Note that the rapidity of changes of classical motions around zero energy is connected with the fact that for $E \to 0_-$ the radius of the central disk converges to zero with a rate increasing to infinity ($\beta_{\rm min} \propto \sqrt{-E}$), as directly follows from the form of the potential $V_{\rm cl}$ close to the $\beta = 0$ maximum.

It is evident from Fig. 4 that the 3/1 periodic orbit exists in only a very narrow interval around $E = 0$. A closer analysis of the term in the Berry-Tabor formula associated with this orbit may therefore enable one to estimate the width $\Delta E_{\rm bunch}$ of the bunching pattern in the quantum spectrum around $E \approx 0$. Since action (10) changes with energy faster for long periodic orbits than that for the short ones, the long orbits have a tendency to interfere destructively. This was verified by our schematic calculation, which shows that the dominant contribution to Eq. (9) in a broader vicinity of $E \approx 0$ is indeed practically only due to the 3/1 orbit. [As already mentioned above, a rigorous evaluation of the Berry-Tabor formula is very difficult in the present case, but we simplified the problem by considering only the main periodic orbits, those with $\mu_\gamma \leqslant 6$, and by estimating the weights of individual terms in Eq. (9) through the relative occurrence of the corresponding orbits in the generated sample.] Because the period of the cosine term associated with the 3/1 orbit is much longer than the width $\Delta E_{3/1}$ of the interval where this orbit exists, the latter should roughly coincide with the width $\Delta E_{\rm bunch}$ of the bunching pattern. Indeed, by comparing Fig. 4 above and Fig. 1 in Part I [1], we see that $\Delta E_{3/1} \approx \Delta E_{\rm bunch} \approx 0.05$. It should be stressed, however, that in spite of this approximate agreement the role of 3/1 orbits in explaning the bunching pattern must not be overestimated since the truly *singular* character of the value $E = 0$ results from the existence of $T_{\vec{\mu}} \to \infty$ trajectories, discussed in Subsec. III A. and Sec. IV.

Figure 5 shows the relative frequency of occurrence of several types of *periodic* orbits from Fig. 3 in our generated sample as a function of energy. The curves in Fig. 5 can be basically understood as energy cuts of the function $N_{\rm tr}$ in Fig. 4 at the respective rational values $R = (\mu_\beta/\mu_\gamma)$ of fraction (12), but with a variable precision ΔR. More specifically, Fig. 5 presents the relative fraction of all generated (at each energy) trajectories satisfying the condition that the μ_βth outer reflection after μ_γ revelations is shifted from the first outer reflection by an angle not exceeding (in absolute value) the

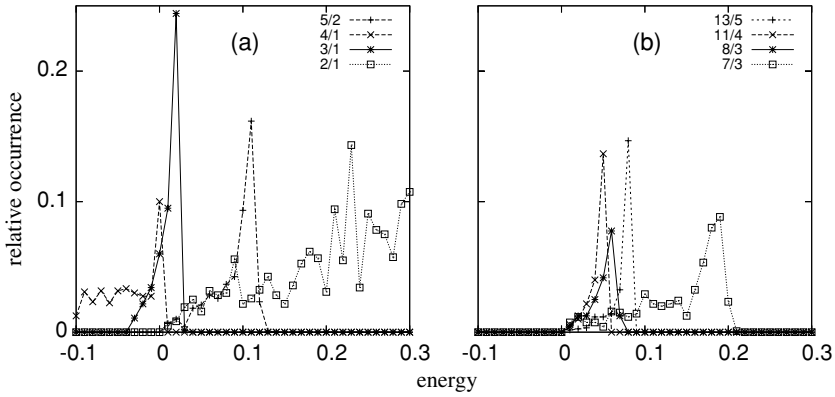

FIG. 5. Relative frequency of occurrence of several types of quasiperiodic orbits (see Fig. 3) for $\eta = 0.6$ as a function of energy. The scale on the vertical axis depends on the value $\Delta\gamma$ in condition (14), here equal to 5°.

selected precision $\Delta\gamma = 5^\circ$. This leads to the condition

$$\frac{\left|R - \frac{\mu_\beta}{\mu_\gamma}\right|}{R} \leqslant \frac{\Delta\gamma}{2\pi\mu_\gamma}. \tag{14}$$

Let us stress that the use of a smaller value of $\Delta\gamma$ decreases the yield of trajectories—implying a prolongation of the computation time—but does not change (as we checked for $\Delta\gamma = 1^\circ$) the shape of dependences in Fig. 5.

The most common type of behavior shown in Fig. 5 indicates that for many orbits the relative frequency of occurrence sharply culminates at a certain energy, just before this orbit totally disappears from the system. The sharpest peak of this kind is observed at $E = 0.02$ for the 3/1 orbits (see the discussion above), but there are also other well-pronounced peaks at higher energies, like the 5/2, 11/4, or 13/5 ones, and many others. All these maxima appear at positive energy, and one can trace their origin to the ridge of values $N_{\rm tr}$ visible for $E > 0$ at the upper bound $R_{\rm max}(E)$ in Fig. 4 (see the inset). The peak at $E = 0$ (the 4/1 "crosses") and also the one at $E = 0.02$ (the 3/1 "Mercedes-Benz stars", see Fig. 3) are located just on the upper edge of the major $E \approx 0$ level-bunching pattern in Fig. 1 of Part I [1].

Special attention should be paid to the 4/1 orbits that in our system take two different forms: For $E < 0$ they exist as stars, shown in the third uppermost panel of Fig. 3, but at $E \approx 0$ they can also look like crosses; see the second panel. (In fact, the latter case exemplifies the above-discussed critical $E = 0$ periodic trajectories with infinite period, as will be further elaborated in Sec. IV.) The contributions of these forms to the dependence in Fig. 5(a) can be decomposed into a constant steplike function equal to zero for $E > 0$ ("stars") and a sharp peak at $E = 0$ ("crosses").

We also see in Fig. 5(a) that the 2/1 orbits, which pass by means of the central maximum of the potential and correspond to the $E > 0$ edge $R_{\rm min}$ in Fig. 4, exhibit a different type of energy dependence than the others. The frequency of occurrence of these orbits is zero at $E \leqslant 0$ and gradually increases (if neglecting fluctuations) with energy $E > 0$.

It is not difficult to show that the peaks in Fig. 5 corresponding to the $R \in (2, 3]$ orbits are connected with bifurcations. To this end, we first characterize individual orbits by the radial width, defined as the difference $\Delta\beta$ between the outer and inner radii (see the end of Sec. II). The values of $\Delta\beta$ associated with various orbit types are shown in Fig. 6, where

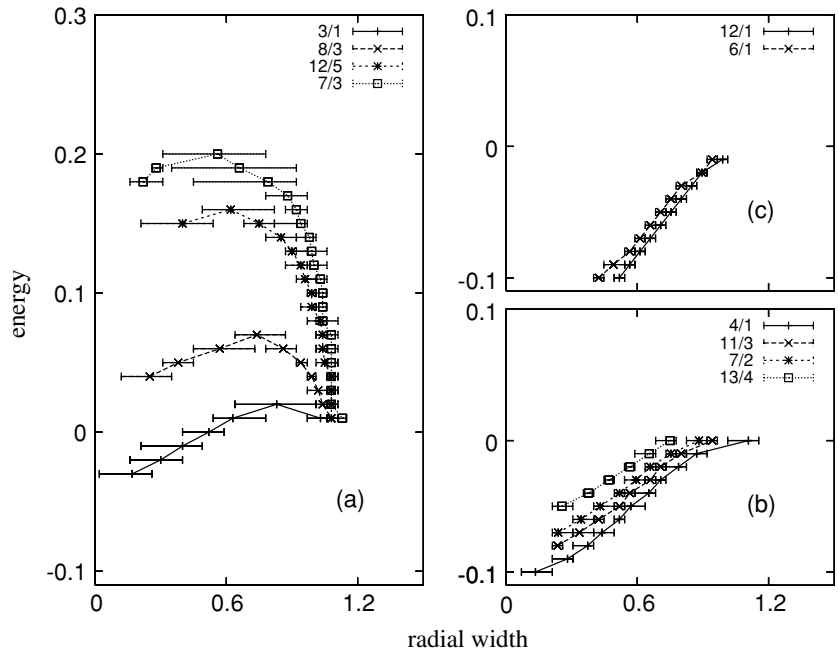

FIG. 6. The radial width $\Delta\beta$ of individual periodic orbits (μ_β/μ_γ) as a function of energy ($\eta = 0.6$). Horizontal bars at each energy demarcate intervals of $\Delta\beta$ where trajectories are detected within our sample, while points connected by curves represent statistical averages within each interval. The bifurcations of orbits in panel (a) explain the respective peaks in Fig. 5.

the horizontal bars demarcate intervals of the $\Delta\beta$ values that are populated (for energy given on the vertical axis) by some trajectories in our sample. The curves (used just to lead the eye) connect points that represent arithmetic averages of $\Delta\beta$ in neighboring intervals.

The three panels of Fig. 6 collect three types of qualitatively different behaviors: (a) For $R \in (2, 3]$, the populated domain of $\Delta\beta$ consists of two separate branches (see, e.g., the two 7/3 orbits in Fig. 3) that merge at a certain energy $E_b(R) > 0$, which can be determined from the condition $R_{\max}(E_b) = R$. Similarly, the lower endpoint energy (the termination of the longer branch of the respective curve) follows from the $R_{\min}(E)$ bound. (b) For $R \in (3, 4]$, the domains consist of only one band that shifts to larger $\Delta\beta$ values as the energy increases and terminates slightly above $E = 0$. The upper end-point energies can again be determined from $R_{\max}(E)$, but, as discussed above, this dependence is so steep in the given range of R that all end-point energies in Fig. 6(b) fall into the narrow interval $E \in [0, 0.01]$. Lower end-point energies again follow from $R_{\min}(E)$. A special case of this kind is the 4/1 orbit with the two above-discussed incarnations (see Fig. 3): The respective $\Delta\beta$ value at the end point $E = 0$ apparently deviates from the direction followed for $E < 0$. (c) For $R > 4$, the $\Delta\beta$ bands look similar, as in case (b), but terminate at energies just below $E = 0$, supposedly following the steep $E < 0$ branch of the curve $R_{\max}(E)$.

It becomes apparent that the $R \in (2, 3]$ peaks in Fig. 5 arise because of the merging of two different branches of $\Delta\beta$ values, as shown in Fig. 6(a). An increased frequency of occurrence of the orbit just before the end point is related to the flatness of the respective curve close to its maximum (a larger number of trajectories is concentrated in a smaller energy interval). At the end point $(\Delta\beta_b, E_b)$ of each of the curves in Fig. 6(a) the respective type of periodic orbit bifurcates, having infinitely close neighbors with different radial widths, and thus yields $g''_E = 0$, as discussed in Subsec. III A. Berry-Tabor formula (9) cannot be applied at these points [19]. In our case, the bifurcations seem to be of the pitchfork type, when two stable orbits join and produce an unstable one [18]. Unfortunately, the unstable orbits are not accessible to numerical studies, so they are not seen in Fig. 6. This problem may be further investigated analytically.

It follows from the above discussion that the bifurcations are connected with only the region of positive energies [there is a ridge of $N_{\rm tr}$ values, apparent in the inset of Fig. 4, that is located solely at the $R_{\max}(E)$ edge with $E > 0$]. This implies that divergences of the Berry-Tabor formula associated with bifurcations are not directly relevant in the explanation of the main level-bunching pattern in Fig. 1 of Part I [1] (except perhaps the 3/1 case with $E_b = 0.02$). Bifurcation energies for low-period orbits are not even correlated with the secondary less-pronounced bunchings of levels, observed in the region $E > 0$ [1]. Therefore it seems that the presence of various orbits in the same energy range and an interplay of their bifurcations result in interferences that wash out contributions of individual orbits.

On the other hand, highly organized behavior of levels at $E \approx 0$ perfectly coincides with the predicted existence of a singular torus of orbits with infinite period at zero energy and also with the observed abrupt redistribution of the spectrum of orbits in a narrow vicinity of this energy.

IV. CLASSICAL AND QUANTUM MONODROMY

The anomalous $E = 0$ bundle of orbits with infinite period, discussed in Subsec. III A, is related to a more general phenomenon, called monodromy. Classical monodromy in integrable Hamilton systems can be briefly introduced as the impossibility of defining global action-angle variables as being due to the existence of a singular, so-called "pinched" torus [14]. The name *Μονοδρομία* (*monodromia* or "once around") originates from a property similar to that of the Möbius strip: If one follows a closed loop in the space of regular tori around the singular torus and—loosely speaking—redefines the coordinate system on the consecutive tori continuously on the way along the loop, one returns back to the starting torus with a coordinate system that differs from the initial one.

Classical monodromy affects the quantum counterpart of the system by means of the Einstein-Brillouin-Kramers (EBK) quantization rules [3,4]. It turns out that quantum monodromy can be seen as a point defect in the lattice of quantum numbers corresponding to a complete set of commuting operators. This defect results in a transformation of the elementary quantum cell when a closed loop is completed around the singular point, in analogy with the above feature of phase-space tori. An overview of the mathematical background and various examples of monodromy can be found in Ref. [21].

Soon after its discovery in 1980 [22], it became clear that monodromy substantially affects global features of numerous integrable systems, which might have previously been considered too trivial for detailed analyses. The simplest system that exhibits monodromy is the spherical pendulum—particle moving on a sphere in a gravitational field. It can be shown [14,21] that the phase-space torus passing the unstable equilibrium position at the North pole, with the particle energy exactly equal to the critical value E_m needed to reach that point, is pinched, i.e., one of its basic circles is contracted to a single point (with appropriate initial conditions the particle is at rest). As a consequence, the lattice of quantum states, characterized by quantum numbers enumerating energy E and the projection L_z of angular momentum, has a point defect at $(E, L_z) = (E_m, 0)$. It was found that closely related to this simple observation is the realization of monodromy in vibrational and rotational spectra of some molecules [21,23].

Other examples of monodromy can be found in the following systems: Particle in quartic, sextic, and decatic potentials [24], hydrogen atom in orthogonal electric and magnetic fields [25], systems of two or three coupled angular momenta [26], particle bouncing between walls in a prolate elliptic cavity [27] or moving in a two-center attractive potential [28]. As in the spherical pendulum, monodromy in several of the latter systems is connected with the trajectories passing with the critical energy by means of the point of an unstable equilibrium [21,24,28]. We already know that a similar point, namely the top of the central maximum at $\beta = 0$, can be found in our classical Hamiltonian (3) for $\eta \leqslant \eta_c \equiv (4/5)$, with $E_m = 0$ being the minimal energy needed

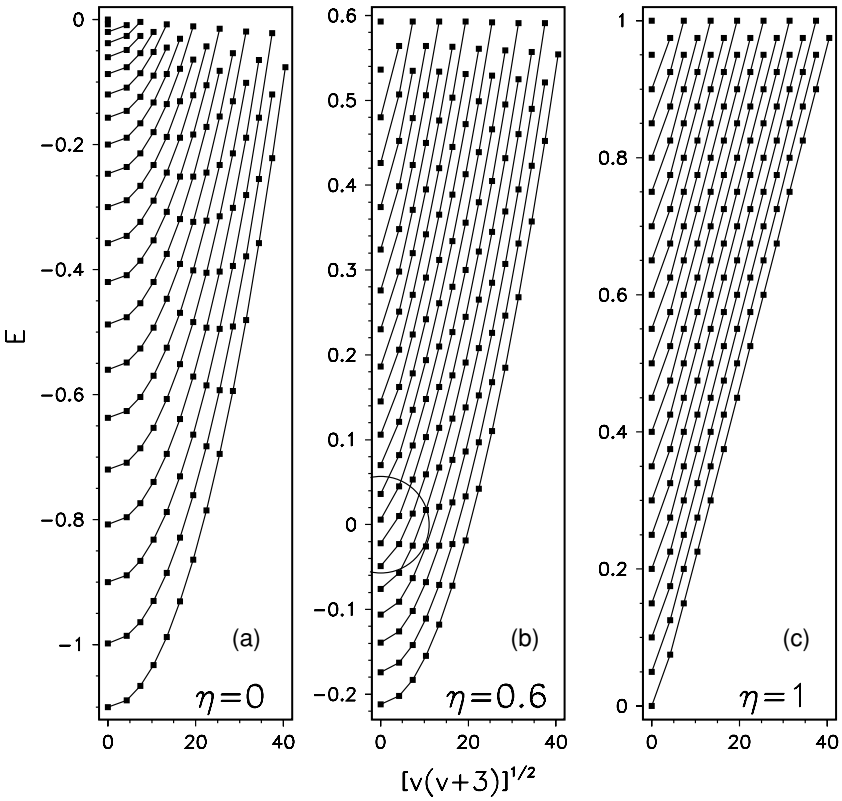

FIG. 7. The lattice of $l = 0$ eigenstates of Hamiltonian (1) with three given values of η and $N = 40$ in the plane $E\sqrt{v(v+3)}$ (where the seniority $v = 0, 3, 6, \ldots$). The curves connect states with the same radial quantum numbers n_β. The singular torus $(E, v) = (0, 0)$ is located in the center of the semicircle in panel (b).

to pass through this point. In fact, our Hamiltonian for $\eta \leqslant \eta_c$ is identical with the champagne-bottle Hamiltonian of Ref. [24], except the position-dependent kinetic term in Eq. (3), which, however, does not affect the presence of monodromy with the central point $(E, \pi_\gamma) = (0, 0)$.

Figure 7 shows the lattice of $l = 0$ eigenstates of quantum Hamiltonian (1) with the number of bosons $N = 40$ in the plane where the vertical axis represents energy E and the horizontal axis the momentum:

$$\pi_\gamma \equiv \sqrt{v(v+3)} = 3\sqrt{\tilde{v}(\tilde{v}+1)}. \tag{15}$$

Since for zero angular momentum the seniority takes values equal to multiples of 3, we defined above also the "reduced" seniority quantum number $\tilde{v} \equiv (v/3) = 0, 1, 2, \ldots$. The three panels in Fig. 7 correspond to various values of the control parameter: (a) $\eta = 0$, the O(6) case, (b) $\eta = 0.6$, a transitional case, and (c) $\eta = 1$, the U(5) case. Individual states (marked by dots) can be directly related to level energies at the respective values of η in Fig. 1 of Part I [1], which collects all states with different seniorities for the same boson number as that given here.

The sorting of states according to seniority in Fig. 7 helps identify the values of v that are involved in level bunchings at different points η. For instance, one immediately sees that the clustering of levels across the whole spectrum in the U(5) limit [panel (c)] is due to the multiple degeneracy of states with even or odd values of $\tilde{v}$ that correspond to the same value of the U(5) quantum number n_d (even or odd, respectively). For the highest states, this degeneracy remains approximately valid across the whole interval $\eta \in [0, 1]$; see panels (a)–(c). The seniority deconvolution of the spectrum for $\eta < (4/5)$ is exemplified by the $\eta = 0.6$ case in panel (b). We observe here that levels with all values of $\tilde{v}$ become nearly degenerate in the region around zero energy, which is a clear signature of the $E \approx 0$ bunching pattern [1].

The lattices in Fig. 7 represent quantum energy-momentum maps [21] of the classical phase space, with each dot being an image of a classical torus of trajectories that survived the semiclassical EBK quantization [17]. This is given by $I_i = 2\pi\hbar[n_i + (\nu_i/4)]$, where I_i (with $i = 1, 2$) are quantized actions and ν_i the respective Maslov indices [4]. The EBK tori should be determined by two quantum numbers n_1 and n_2, whose integer values increase by one. Good candidates for these numbers are the reduced seniority $\tilde{v}$ (connecting vertical columns of points in Fig. 7) and the radial quantum number $n_\beta = 0, 1, 2, \ldots$, which enumerates states with a fixed $\tilde{v}$ according to energy (in Fig. 7, the constant-n_β states are connected by curves). For $\eta = 0$, the radial quantum number is related to σ, which corresponds to the O(6) Casimir invariant [2], and the pair $(n_\beta, \tilde{v})$ represents the appropriate choice of the EBK quantum numbers. In the U(5)-like case, as shown below, yet another alternative pair of quantum numbers needs to be defined.

It follows from Eq. (3) that the $l = 0$ classical limit of the $\eta = 1$ Hamiltonian (1) is identical with an isotropic two-dimensional harmonic oscillator. Indeed, for the subset of states with the U(5) quantum number n_d equal to multiples of 3 (in this case $n_d = 2n_\beta + v$) the U(5) lattice coincides with the two-dimensional oscillator lattice of states (the energy in the latter case being enumerated by the oscillator quantum number $n_o = 2n_r + m$, where n_r and m stand for ordinary radial and angular-momentum quantum numbers,

respectively). In the entire U(5) lattice, however, the majority of states are located in "interstitial" positions with $n_d \neq 3k$; this is because the underlying angular-momentum algebra differs from that of the ordinary O(2). Apart from n_β and $\tilde{v}$, all U(5) states can be labeled by a pair of oscillatorlike quantum numbers $n_1 = n_\beta + \tilde{v}$ and $n_2 = n_\beta + 2\tilde{v}$. States with constant values $n_1 = 0, 1, 2, \ldots$, form upward-inclined rows of dots in Fig. 7(c), while the $n_2 = 0, 1, 2, \ldots$, quantum number connects states in the downward-inclined rows. The n_1 chains are clearly apparent also in both remaining panels (a) and (b) of Fig. 7.

For the purpose of the semiclassical analysis, the lattices in Fig. 7 must be extended to cover both positive and negative π_γ. Remember from Sec. II that, although the physical quantum states can be represented by nonnegative values of π_γ, the intrinsic degeneracy of classical motions in both γ directions results in the mirror imaging of all states with $v > 0$ into the $\pi_\gamma < 0$ half-plane (to guarantee a smooth continuation of quantum numbers, we assign values $\tilde{v} = -1, -2, \ldots$, to these "twin" states). In the absence of monodromy, one must be able to engage all states in the *extended* lattice into a "crystal" grid of continuous and *smooth* lines, corresponding to constant values of two compatible global quantum numbers, with "elementary cells" of the grid being topologically equivalent to squares. From Fig. 7(a) we see that a smooth grid, symmetric under the $\pi_\gamma \leftrightarrow -\pi_\gamma$ reflection, can be constructed in the O(6) case, by use of the pair of generating quantum numbers $(n_\beta, \tilde{v})$. In the U(5) case [panel (c)], this choice of quantum numbers produces a grid of lines that are broken at $\pi_\gamma = 0$, but a smooth global grid (a diagonal "chessboard") is generated by the pair (n_1, n_2). The latter structure can be extended to the whole interval $\eta \in [4/5, 1]$ where the U(5)-like spectrum exists.

In contrast, quantum monodromy implies the absence of a smooth *global* grid. This is the case in Fig. 7(b), in which a smooth grid for $E < 0$ would be generated by the pair of quantum numbers $(n_\beta, \tilde{v})$, but for $E > 0$ by the pair (n_1, n_2). Any attempt to define two global quantum numbers that behave smoothly in the entire lattice for $\eta \in (0, 4/5)$ fails at the point $(E, v) = (0, 0)$, which represents the singular torus of trajectories and, simultaneously, a "defect" in the quantum lattice of states [21,24,26]. It is clear that in the transition to the O(6) limit the defect is gradually pushed up to the upper edge of the lattice. For the whole interval $\eta \in (0, 4/5)$ the singular point indicates the place where the energy-momentum map passes between the O(6) and the U(5) types of elementary cells—tetragons with ordered $(n_\beta, \tilde{v})$, $(n_\beta, \tilde{v} + 1)$, $(n_\beta + 1, \tilde{v} + 1)$, and $(n_\beta + 1, \tilde{v})$ vertices and analogous tetragons in (n_1, n_2), respectively. Note that elementary cells of either type cannot be uniquely defined along a closed loop around the singular point since after one turn the cell gets distorted. This can be illustrated by a graphical construction in Fig. 7(b) and its mirror image, but the rigorous proof would require an infinite density of the lattice in the $N \to \infty$ limit. The last observation represents a common quantum signature of monodromy [21,23–28].

It should be stressed that monodromy in the present case is not a property of just a single Hamiltonian, but characterizes the whole $\eta \in (0, \eta_c)$ family (1) of transitional systems. Since—as shown in Part I [1]—the most substantial changes in quantum spectra of these systems take place in the $E \approx 0$ region, monodromy seems to play the key role in the process of redistribution of individual levels between the O(6) and U(5) multiplets. Related examples exist also in other parametric families of Hamiltonians, for instance, in transitions between uncoupled and coupled regimes of two quantum rotators [26] and between Zeeman and Stark limits of the hydrogen atom in crossed electric and magnetic fields [25]. Also in these examples, the crossover between the limiting spectral structures takes place at the point (or in the interval) of control parameters and energy where monodromy exists. These findings deserve further investigation.

V. CONCLUSIONS

In the present part of our work, devoted to the [O(6)−U(5)]⊃O(5) transition of the interacting boson model, we have studied the classical limit of Hamiltonian (1) with zero angular momentum. Results of the analysis of level dynamics, presented in Part I [1], were qualitatively discussed with the aid of the Berry-Tabor semiclassical trace formula, which describes fluctuations of quantum spectra in integrable systems in terms of families of periodic orbits existing at various energies. The transitional regime was exemplified by the choice of a single value of the control parameter, $\eta = 0.6$.

Both possible sources of diverging contributions to trace formula (9), namely, the existence of bifurcating ($g_E'' = 0$) and singular ($T_{\vec{\mu}} = \infty$) orbits, were identified in our system. While bifurcations of periodic orbits with ratios between γ- and β-vibration periods $R \in (2, 3]$ were shown to exist in the region $E > 0$, singular orbits with $\pi_\gamma = 0$ appeared at $E = 0$. The latter finding led to the identification of classical monodromy, which on the quantum level exhibits itself as a defect in the lattice of quantum states located at zero values of energy and seniority. This is related to the bunching of levels in the $E \approx 0$ region [1] and underlies the process of redistribution of states between O(6) and U(5) spectral structures, i.e., between the $(n_\beta, \tilde{v})$ and (n_1, n_2) types of elementary cells, and the respective multiplets of levels.

Also the numerical analysis of periodic and nonperiodic classical vibrations disclosed that the most substantial changes in the spectrum of allowed ratios R take place in a very narrow energy interval around $E \approx 0$. This interval represents a kind of demarcation line between the O(6) and U(5) types of classical motions. At $E \approx -0.03$, the inaccessible central disk in the plane of deformation parameters becomes sufficiently small to allow for vibrations with $R \in (2, 3]$, and at $E = 0$, when the disk vanishes, the oscillatorlike orbits with $R = 2$ arise. With the energy further growing to positive values, individual vibrations with $R > 2$ eventually disappear in bifurcations ("annihilations" of two separate $\Delta\beta$ branches of a given orbit). The 3/1 orbits, which exist only in a narrow interval around $E = 0$, determine the width $\Delta E_{\text{bunch}} \approx 0.05$ of the bunching pattern in the corresponding region of the quantum spectrum.

We believe that results of this analysis will have a concrete impact on the interpretation of data on collective vibrations in γ-soft nuclei. Collective 0^+ states in the nuclei between spherical and deformed equilibrium shapes have recently

received considerable attention (see Ref. [29], particularly the contribution by J. Jolie *et al*. therein). Our study (including the classical part) may help disclose the nature of these states, and it addresses the broadly discussed topic of coexisting shape structures found within the same nuclear species. In particular, the $E \approx 0$ bunching of levels, which for $\eta \in (0.5, 0.8)$ lies at reasonably low excitation energies, may turn out to serve as an observable signature of the transition between O(6)- and U(5)-like types of dynamics in the spectrum of a single nucleus. Relevant experimental work is in progress [29].

In a more general perspective, the $[\mathrm{O}(6)-\mathrm{U}(5)]\supset\mathrm{O}(5)$ transition of the interacting boson model represents a valuable theoretical laboratory for studying structural changes between incompatible dynamical symmetries in *integrable* quantum systems. It will be interesting to learn whether the $E = 0$ line separates (in the thermodynamic limit) the O(6)- and U(5)-like phases in the conventional sense of structural phase transitions involving excited states (finite temperatures).

ACKNOWLEDGMENTS

The authors acknowledge important discussions with P. Leboeuf and Z. Pluhar. This work was supported by Deutsche Forschungsgemeinschaft grant no. U36 TSE 17.2.04 and by the Czech Ministry of Education under Research Plan MSM 0021620834.

[1] S. Heinze, P. Cejnar, J. Jolie, and M. Macek, Phys. Rev. C **73**, 014306 (2006); companion paper to this paper.
[2] F. Iachello and A. Arima, *The Interacting Boson Model* (Cambridge University Press, Cambridge, UK, 1987).
[3] M. C. Gutzwiller, *Chaos in Classical and Quantum Mechanics* (Springer-Verlag, New York, 1990).
[4] H.-J. Stöckmann, *Quantum Chaos. An Introduction* (Cambridge University Press, Cambridge, UK, 1999).
[5] M. C. Gutzwiller, J. Math. Phys. **12**, 343 (1971).
[6] R. Balian and C. Bloch, Ann. Phys. (NY) **69**, 76 (1972).
[7] M. V. Berry and M. Tabor, Proc. R. Soc. London Ser. A **349**, 101 (1976).
[8] B. Mottelson, Nucl. Phys. **A574**, 365c (1994).
[9] R. L. Hatch and S. Levit, Phys. Rev. C **25**, 614 (1982).
[10] Y. Alhassid and N. Whelan, Phys. Rev. C **43**, 2637 (1991).
[11] N. Whelan and Y. Alhassid, Nucl. Phys. **A556**, 42 (1993).
[12] Y. Alhassid, in *Perspectives for the Interacting Boson Model*, edited by R. F. Casten, A. Vitturi, A. B. Balantekin, B. R. Barret, J. N. Ginocchio, G. Maino, and T. Otsuka (World Scientific, Singapore, 1994), p. 591.
[13] A. J. Lichtenberg and M. A. Lieberman, *Regular and Stochastic Motion* (Springer-Verlag, New York, 1983).
[14] R. H. Cushman and L. Bates, *Global Aspects of Classical Integrable Systems* (Birkhäuser, Basel, 1997).
[15] P. Cejnar and P. Stránský, Phys. Rev. Lett. **93**, 102502 (2004).
[16] A. Klein and M. Vallieres, Phys. Rev. Lett. **46**, 586 (1981).
[17] O. Bohigas, S. Tomsovic, and D. Ullmo, Phys. Rep. **223**, 43 (1993).
[18] G. Nicolis, *Introduction to Nonlinear Science* (Cambridge University Press, Cambridge, UK, 1995).
[19] M. Sieber, J. Phys. A **29**, 4715 (1996); H. Schomerus and M. Sieber, *ibid*. **30**, 4537 (1997); M. Sieber and H. Schomerus, *ibid*. **31**, 165 (1998).
[20] R. W. Robinett, Am. J. Phys. **67**, 67 (1999).
[21] K. Efstathiou, M. Joyeux, and D. A. Sadovskiĭ, Phys. Rev. A **69**, 032504 (2004).
[22] J. J. Duistermaat, Commun. Pure Appl. Math. **33**, 687 (1980).
[23] R. H. Cushman, H. R. Dullin, A. Giacobbe, D. D. Holm, M. Joyeux, P. Lynch, D. A. Sadovskiĭ, and B. I. Zhilinskiĭ, Phys. Rev. Lett. **93**, 024302 (2004).
[24] M. S. Child, J. Phys. A **31**, 657 (1998); M. S. Child, S. H. Dong, and X. G. Wang, *ibid*. **33**, 5653 (2000); S. H. Dong, Int. J. Theor. Phys. **41**, 89 (2002).
[25] R. H. Cushman and D. A. Sadovskiĭ, Europhys. Lett. **47**, 1 (1999); Physica D **142**, 166 (2000).
[26] D. A. Sadovskiĭ and B. I. Zhilinskiĭ, Phys. Lett. **A256**, 235 (1999); L. Grondin, D. A. Sadovskiĭ, and B. I. Zhilinskiĭ, Phys. Rev. A **65**, 012105 (2001).
[27] H. Waalkens and H. R. Dullin, Ann. Phys. (NY) **295**, 81 (2002).
[28] H. Waalkens, A. Junge, and H. R. Dullin, J. Phys. A **37**, L307 (2003); H. Waalkens, H. R. Dullin, and P. H. Richter, Physica D **196**, 265 (2004).
[29] *Proceedings of 12th International Conference on Capture Gamma-Ray Spectroscopy and Related Topics*, edited by A. Aprahamian (American Institute of Physics, New York, 2006), will be published.

A.2 Monodromy and excited-state quantum phase transitions in integrable systems: collective vibrations of nuclei

[*J. Phys. A: Math. Gen.* **39,** L515 (2006)] [**J3**]

The article identifies a non-analytic behavior of excited energy levels and eigenstates with zero seniority $v = 0$ along the completely integrable O(6)-U(5) transition of the interacting boson model (IBM) and recognizes it as a chain of continuous excited-state quantum phase transitions (ESQPT). The chain of observed ESQPT's starts at the ground state quantum phase transition (which is also continuous in this integrable case) at the critical point $\eta_{\rm crit} = 0.8$ and leads towards the vicinity of the O(6) limit ($\eta \to 0$), where it affects in the contrary the highest-lying excitations. In contrast to $v = 0$ states, the states with higher seniority $v > 0$ do not undergo ESQPT and evolve analytically.

The ESQPT's are found to be triggered here by a topological property of the phase space called the monodromy [Duis80, Sado06]. Classical monodromy is a generic property of systems which contain a singular pinched torus of classical trajectories with a diverging time period $T \to \infty$ in their phase space. The pinched tori can be found at a special value of energy $E = E_{\rm mon}$, which coincides with an unstable equilibrium of the potential. Quantum monodromy can be identified in joint spectra of two commuting operators, which provides a (2D crystal-like) lattice of points. In case that the monodromy is present, no primordial cell within the lattice can be circled around the monodromy point and brought to the original position and shape—it always becomes deformed, see e.g. Ref. [Sado06].

The link between the continuous non-analyticity in the evolution of energy levels and eigenstates (i.e. ESQPT) and the monodromy is in the IBM demonstrated by the breakdown of the shifted harmonic approximation (SHA) [Rowe04] precisely at the energy $E_{\rm mon}$. SHA provides an analytic transformation of the O(6) solutions to the whole interval $\eta \in [0, \eta_{\rm crit}]$. It however holds only for the eigenstates at energies $E < E_{\rm mon} = 0$, as we show. For $E > E_{\rm mon}$, the eigenstates seem to be linked analytically to the solutions at the U(5) limit, the link is however not yet known explicitly.

The results of the article lead to a generalization of the monodromy-ESQPT interconnection and its recognition in a wide class of systems with the Mexican-hat type of potential [Capr08].

Contribution of the author rests in the identification of the pinched torus resulting from his analysis of the properties of the classical trajectories shown in Ref. [**J2***]. He also performed the calculation of the phase space volume $\Omega(E)$ in Fig. 2 showing a non-analyticity at energy $E = 0$, which affects the smooth part of the energy level density and gives a first indication of the possibly ESQPT behavior.

INSTITUTE OF PHYSICS PUBLISHING JOURNAL OF PHYSICS A: MATHEMATICAL AND GENERAL

J. Phys. A: Math. Gen. **39** (2006) L515–L521 doi:10.1088/0305-4470/39/31/L01

LETTER TO THE EDITOR

Monodromy and excited-state quantum phase transitions in integrable systems: collective vibrations of nuclei

Pavel Cejnar[1], Michal Macek[1], Stefan Heinze[2], Jan Jolie[2] and Jan Dobeš[3]

[1] Faculty of Mathematics and Physics, Charles University, V Holešovičkách 2, 180 00 Prague, Czech Republic
[2] Institute of Nuclear Physics, University of Cologne, Zülpicherstrasse 77, 50937 Cologne, Germany
[3] Nuclear Physics Institute, Academy of Sciences of the Czech Republic, 250 68 Řež, Czech Republic

Received 26 April 2006, in final form 11 June 2006
Published 19 July 2006
Online at stacks.iop.org/JPhysA/39/L515

Abstract

Quantum phase transitions affecting the structure of ground and excited states of integrable systems with the Mexican-hat type potential are shown to be related to a singular torus of classical orbits passing the point of unstable equilibrium. As a specific example, we consider nuclear collective vibrations described by the $O(6)$–$U(5)$ transitional Hamiltonian of the interacting boson model. While all states with zero values of the $O(5)$ invariant undergo a continuous phase transition when crossing the energy of unstable equilibrium, the other states evolve in an analytic way.

PACS numbers: 21.60.Ev, 05.70.Fh, 02.30.Ik

Motions of a classical integrable system with n degrees of freedom in the phase space stick onto surfaces that are topologically equivalent to $2n$-dimensional tori. It is generally thought that this feature results in a fully analytic expressibility of observables for integrable systems. However, in some cases the analyticity cannot be maintained in the global sense. A common obstacle for $n = 2$ is monodromy [1], related to the existence of an anomalous, so-called pinched torus of orbits. Most usually, the pinched torus originates from a singular point of unstable equilibrium of the focus–focus type and is connected with a class of trajectories with period $\tau \to \infty$ if the energy crosses a certain critical value E_{mon}. The presence of such orbits in the phase space also affects the quantum spectrum, producing a 'crystal defect' in the joint spectrum of commuting operators [2].

One of the systems with monodromy is the spherical pendulum [3]. Here, the pinched torus is formed by orbits passing the upper point with just the energy needed for equilibration. Classical motions with zero value of the conserved angular momentum L_z undergo a qualitative

change and the corresponding quantum lattice in the joint spectrum has a defect at $E = E_{\rm mon}$ and the L_z quantum number $m = 0$. The parts of the lattice below and above $E_{\rm mon}$ are characterized by nearly degenerate multiplets of states with the same vibrational and rotational quantum numbers, respectively, and both types of multiplets fail to smoothly extend across the monodromy point to the other domain.

Another example of monodromy follows from the Mexican-hat potential $V \propto r^4 - r^2$ with $r^2 = x^2 + y^2$ [4]. The local maximum at $r = 0$ corresponds to an unstable equilibrium with $E_{\rm mon} = 0$, which results in a pinched torus of $L_z = 0$ orbits. Crossing the critical energy induces a transition between two types of $L_z = 0$ motions, the first type confined within the annulus $r \in [r_{\rm min}, r_{\rm max}]$, and the second one traversing across a compact region $r \in [0, r_{\rm max}]$. Also the joint spectrum shows a crossover between multiplets characterized by the radial quantum number $n_{\rm rad}$ (below $E_{\rm mon}$) and those labelled by the principal quantum number $2n_{\rm rad} + m$ (above $E_{\rm mon}$) [4].

These effects are reminiscent of another interesting class of phenomena—quantum phase transitions (QPTs). These are usually introduced as nonanalytic (in the thermodynamic limit) changes of system's ground-state properties with external parameters [5, 6]. Here, the concept will be extended also to excited states. The first-order or a continuous QPT, respectively, for the ith state is defined as the discontinuity of the first derivative or a more subtle nonanalyticity in the dependence of excitation energy E_i on a control parameter η. It is related to a nonanalytic evolution of the respective wavefunction $|\psi_i\rangle$. The aim of this letter is to show that monodromy and excited-state QPTs in integrable systems are closely related. This is exemplified by quadrupole vibrations of atomic nuclei in the so-called γ-soft regime [7, 8].

Recall that simplified models of nuclear collective motions take into account only the degrees of freedom corresponding to quadrupole deformations [7]. The quadrupole tensor α is characterized by five parameters, two of them describing the deformed shape and the other three its orientation. A pair of deformation parameters can be constructed from the only two independent scalar combinations of α, namely $[\alpha \times \alpha]^{(0)} = \beta^2/\sqrt{5}$ and $[[\alpha \times \alpha]^{(2)} \times \alpha]^{(0)} = -\sqrt{2/35}\beta^3 \cos 3\gamma$, where $[\bullet \times \bullet]^{(\lambda)}$ stands for coupling of the quantities involved to angular momentum λ. Variables $\beta \in [0, \infty)$ and $\gamma \in [0, 2\pi)$ represent Bohr deformation parameters [7], which can be visualized as polar coordinates in the plane $x \times y$. The radius β measures the overall deformation, while the angle γ characterizes the deformed shape type, orientation in the principal frame, and the degree of triaxiality.

The collective Hamiltonian can be written as

$$H = T_{\rm rot} + T_{\rm vib} + A\beta^2 + B\beta^3 \cos 3\gamma + C\beta^4 + \cdots, \tag{1}$$

where $T_{\rm rot}$ and $T_{\rm vib} = K\pi^2 + \cdots$ [with $\pi^2 = \pi_x^2 + \pi_y^2 = \pi_\beta^2 + (\pi_\gamma/\beta)^2$] stand for the rotational and vibrational kinetic energies (π_i denotes the momentum canonically conjugated to coordinate i). $\{K, A, B, C, \ldots\}$ is a set of external parameters ($K, C > 0$). Here, we included only the lowest order vibrational kinetic terms and the potential energy up to the quartic term.

If Hamiltonian (1) does not depend on γ (i.e., is 'γ-soft'), it is integrable. In the following, we will deal with motions at zero angular momentum J, thus $T_{\rm rot} = 0$, when the system has just two vibrational degrees of freedom and in the γ-soft case yields two commuting integrals of motions—energy E and momentum $\pi_\gamma = x\pi_y - y\pi_x$ (analogue of L_z). Without the higher order terms and for $B = 0$, $A < 0$ the potential energy in equation (1) represents the Mexican-hat potential that leads to monodromy at $E = \pi_\gamma = 0$.

It is known [9] that Hamiltonian (1) exhibits the ground-state QPT from deformed ($\beta_0 > 0$) to spherical ($\beta_0 = 0$) equilibrium shape at $A_{\rm c} = B^2/4C$. For $B = 0$ we have $A_{\rm c} = 0$ and the transition is continuous (of second order in the Ehrenfest classification). In this case, the

QPT is realized within an integrable domain with monodromy. Note that the $B = 0, A < 0$ half-line itself demarcates the first-order QPT between prolate ($\gamma_0 = 0, B < 0$) and oblate ($\gamma_0 = \pi/3, B > 0$) shapes, so the second-order transition lies in the intersection of three first-order phase separatrices [10].

Specific realization of Hamiltonian (1) can be achieved within the interacting boson model (IBM) [11]. The model, formulated in terms of s and d-bosons (with angular momenta 0 and 2), exploits the decompositions of dynamical algebra $U(6)$ into chains of subalgebras terminating at the symmetry algebra $O(3)$. Three such chains, called after the highest subalgebra $U(5)$, $O(6)$ and $SU(3)$ define dynamical symmetry limits (if the Hamiltonian is composed of invariants of the respective chain), while transitional Hamiltonians are located within a 'triangle' between these limits. In the dynamical-symmetry cases the model is integrable, and this property is preserved also along the transition between $O(6)$ and $U(5)$, where the underlying $O(5)$ symmetry results in conserved quantum number v called seniority [12].

In the following, we will consider a simplified $O(6)$–$U(5)$ transitional Hamiltonian given by

$$H^{(\eta)} = \eta \frac{n_d}{N} - (1-\eta)\frac{Q \cdot Q}{N^2}, \tag{2}$$

where N stands for the total number of bosons, $n_d = d^\dagger \cdot \tilde{d}$ for the d-boson number operator and $Q = d^\dagger s + s^\dagger \tilde{d}$ for the quadrupole operator. Note that the dot represents scalar coupling and $\tilde{d}_\mu = (-)^\mu d_{-\mu}$. For Hamiltonian (2) the $O(6)$ dynamical symmetry is located at $\eta = 0$ and $U(5)$ at $\eta = 1$. Using Glauber coherent states $|\alpha\rangle \propto \exp\left(\alpha_s s^\dagger + \sum_\mu \alpha_\mu d_\mu^\dagger\right)|0\rangle$ (where α_s can be eliminated by fixing the average of N and the global phase) [13], one can rewrite Hamiltonian (2) in the form (1) with $B = 0$:

$$H^{(\eta)}_{\text{clas}} = T^{(\eta)}_{\text{rot}} + \frac{\eta}{2}\pi^2 + (1-\eta)\beta^2\pi^2 + \frac{5\eta - 4}{2}\beta^2 + (1-\eta)\beta^4. \tag{3}$$

Since the role of $\hbar$ is played by N^{-1}, the classical limit is attained for $N \to \infty$. Moreover, in the $J = 0$ case ($T_{\text{rot}} = 0$), due to the coherent-state relation $C_2^{\text{O(5)}}/N^2 \mapsto \pi_\gamma^2$, where $C_2^{\text{O(5)}} = n_d(n_d + 3) - (d^\dagger \cdot d^\dagger)(\tilde{d} \cdot \tilde{d})$ is the $O(5)$ invariant with eigenvalues $v(v+3)$, the momentum π_γ can be (for $N \to \infty$) associated with relative seniority $\delta = v/N$ (where $v = 0, 3, 6, \ldots \leqslant N$ for $J = 0$).

It is clear from equation (3) that a continuous QPT between $O(6)$- and $U(5)$-like ground-state configurations happens at $\eta_c = 4/5$, where the potential changes from the Mexican-hat shape to a quartic oscillator. Note, however, that the IBM shows some specific differences from these standard potential systems: first, due to boundedness of Hamiltonian (2) the physical domain is restricted to $\beta \in [0, \sqrt{2}]$, $\pi_\beta \in [0, \sqrt{2}]$ and $\pi_\gamma \in [0, 1]$. Second, equation (3) also contains an unusual kinetic term $\propto \beta^2\pi^2$. Third, for $J = 0$ the quantum grid of states in E versus v differs from the standard E versus m grid associated with the given potential; this results from inherent differences between the $O(5)$- and $O(2)$-based angular momenta.

Figure 1 illustrates classical monodromy of Hamiltonian (3) at absolute energy $E_{\text{mon}} = 0$ for $\eta < 4/5$. The Poincaré phase-space section shows crossings of 30 orbits of $\pi_\gamma > 0$ with the plane $\beta \times \pi_\beta$. The $\pi_\gamma = 0$ orbits passing asymptotically the point $\beta = 0$ form the pinched torus, whose section corresponds to the cusped enveloping curve of the filled area. The surface of the pinched torus, nonanalytic at $\beta = 0$, interpolates between two distinct types of analytic $\pi_\gamma = 0$ tori at lower and higher energies. This results in a nonanalytic growth of the available phase-space volume $\Omega(E) = \int \delta(H - E)\,\mathrm{d}\pi_x\,\mathrm{d}\pi_y\,\mathrm{d}x\,\mathrm{d}y$ at $E = E_{\text{mon}}$. In particular,

$$\Omega(E) = 4\pi \int_{\beta_{\min}(E)}^{\beta_{\max}(E)} \pi_\beta(E, \beta, \pi_\gamma = 0)\beta\,\mathrm{d}\beta, \tag{4}$$

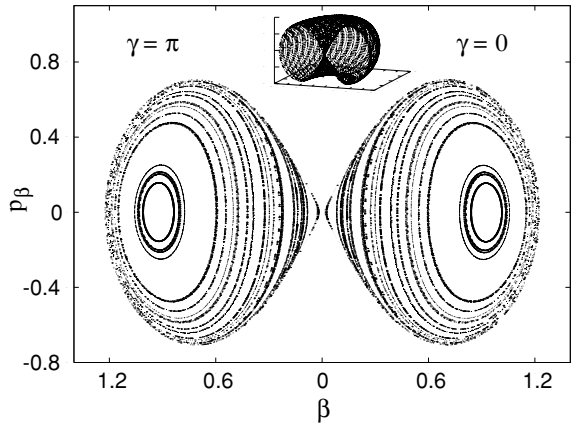

Figure 1. Poincaré phase-space section associated with Hamiltonian (3) at $E = 0$ and $\eta = 0.6$ and the enveloping pinched torus of $\pi_\gamma = 0$ orbits (inset).

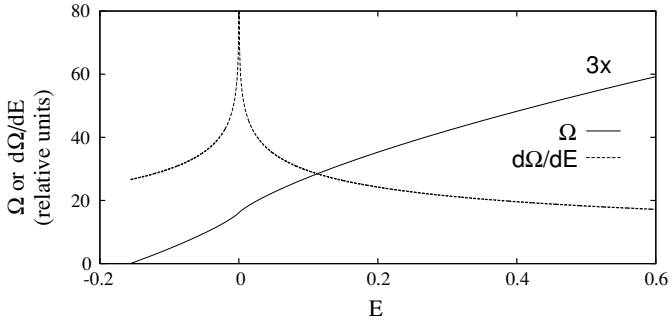

Figure 2. The available phase-space volume (4) and its first derivative at $\eta = 0.6$.

where π_β as well as $\beta_{\min}$ and $\beta_{\max}$ are evaluated from equation (3), has a singular tangent at zero energy, as shown in figure 2. Note that $\Omega(E)$ is related to the smooth part of the quantum density of states $\rho(E) = \mathrm{Tr}\,\delta(H - E)$; the oscillatory part depends on properties of periodic orbits (also singular at E_{mon} [8]) and is not discussed here.

Features of Hamiltonians (2) and (3) related to the anomalous behaviour at E_{mon} were recently analysed in [8]. It was shown that monodromy is correlated with two important dynamical effects: (i) on the classical level, trajectories with predominantly large values of the ratio $R = \tau_\gamma/\tau_\beta$ of β- and γ-vibration periods transform to those within a narrow band above $R = 2$. While values $R \gg 2$ observed for $E < E_{\mathrm{mon}}$ correspond to zig-zag orbits inside the accessible annular region in the $x \times y$ plane, the value $R \approx 2$ valid for $E > E_{\mathrm{mon}}$ is connected with 'bouncing-ball' orbits traversing through the central region. In particular, the $\pi_\gamma = 0$ trajectories undergo a discontinuous change from $R = \infty$ to $R = 2$. (ii) On the quantum level it was shown that $O(6)$- and $U(5)$-like types of elementary cells in the E versus v lattice of $J = 0$ quantum states exist in energy domains below and above E_{mon}, respectively, i.e., interchange at about the monodromy energy. This is accompanied by degeneracy of levels with different seniorities and by coherent patterns of avoided crossings of levels with the same seniority, both at energy $E \approx E_{\mathrm{mon}}$.

To show that these structures correspond to QPT evolutions of excited states with zero seniority, we invoke an oscillator approximation recently discussed by Rowe [14]. The method is valid on the $O(6)$ side of the transition for finite seniorities and asymptotic boson numbers, when $x = 2n_d/N - 1$ can be treated as a continuous variable. Eigenstates $|\psi_i\rangle$ are expressed as conventional wavefunctions $\psi_i(x) \equiv \langle n_d|\psi_i\rangle$ and the scaled Hamiltonian $H^{(\eta)}/(1-\eta)$ from equation (2) turns into a differential operator

$$-\frac{4}{N^2}\frac{\mathrm{d}}{\mathrm{d}x}(1-x^2)\frac{\mathrm{d}}{\mathrm{d}x} + \left[x - \frac{\eta}{4(\eta-1)}\right]^2 - \left[\frac{5\eta-4}{4(1-\eta)}\right]^2, \tag{5}$$

where the use is made [14] of the fact that Hamiltonian (2) only connects states with $\Delta n_d = 0 \pm 2$ and is therefore local in x for $N \to \infty$. The last expression, after neglecting $\mathcal{O}(N^{-1})$ and higher terms, reduces to a quantum oscillator with variable centroid position and energy shift, and with an x-dependent mass. (The latter feature was not discussed in [14] and can be neglected for $x \approx 0$.) Therefore, the $O(6)$ quasi-dynamical symmetry extends away from $\eta = 0$ through an analytic transformation of eigensolutions.

However, the analytic extension is limited to the range of η where the semiclassical wavefunction is located within the physical domain $n_d \in [0, N]$, thus $x \in [-1, +1] \equiv [x_{\min}, x_{\max}]$. Once the classical turning points of the oscillator particle reach these bounds, expression (5) is no longer applicable for the given state. This happens when the actual level energy E_i crosses the value of the oscillator potential energy at the lower edge, $V^{(\eta)}_{\mathrm{osc}}(x_{\min}) = 0$, i.e., just when $E_i = E_{\mathrm{mon}}$. At this point, the probability distribution $P(x) \propto \dot{x}^{-1}$ (where $\dot{x}$ stands for the velocity of the oscillator particle) becomes singular since the mass diverges for $x = \pm 1$ and the particle spends infinite time in an infinitesimal vicinity of $x_{\min}$. An equivalent conclusion follows from the classical Hamiltonian (3), which for $E = E_{\mathrm{mon}}$ yields a singular concentration of the probability distribution $P(\beta) \propto \dot{\beta}^{-1}$ at $\beta = 0$. As the analytic extension of $\eta = 0$ semiclassical wavefunction cannot pass over the singularity, the parameter range is split into two disconnected branches, which can be named quasi-$O(6)$ and quasi-$U(5)$.

The ground-state energy E_0 crosses E_{mon} at $\eta_{\mathrm{c}} = 4/5$. For the other $v = 0$ states with increasing excitation energy, the crossings form a descending sequence of points within the interval $\eta \in (0, \eta_{\mathrm{c}})$. These are positions of excited-state QPTs where individual eigenfunctions $|\psi_i\rangle$ and energies E_i evolve in a nonanalytic way. Note that for Hamiltonian (2), which has the form $H^{(0)} + \eta V$, the relation $\mathrm{d}E_i/\mathrm{d}\eta = \langle\psi_i|V|\psi_i\rangle$ transmits nonanalytic behaviours of wavefunctions to level energies. Since $\langle\psi_i|V|\psi_i\rangle$ itself changes in a continuous way, the QPT for excited states is—like the one for the ground state—continuous. The present analysis, however, does not allow one to specify the type of nonanalyticity for $i > 0$.

Finite-N precursors of excited-state QPT's are shown in figure 3, where we display $J = v = 0$ level dynamics and two examples of wavefunctions (n_d-distributions) for $N = 80$. Wavefunctions for $E_i < 0$ are approximate eigenstates of the oscillator Hamiltonian (5). They reach the $n_d = 0$ edge just when passing $E = 0$ (the region with multiple avoided crossings) where the validity of the quasi-$O(6)$ description for the given level ends. At the transition, the slope of individual energy curves tends to vanish, in agreement with the fact that $\langle\psi_i|V|\psi_i\rangle = 0$ at $E_i = E_{\mathrm{mon}}$ for $N \to \infty$. The $E_i > 0$ branch of wavefunction is analytically connected to the $U(5)$ limit.

Formula (5) is valid only if $\delta = v/N \to 0$ in the classical limit, i.e., for $v \approx 0$ in finite-N approximations. Therefore, a question appears what happens to states with $\delta \in [0, 1]$. The answer can be obtained from equation (3) that allows one to extract an effective potential corresponding to the fixed value $\pi_\gamma = \delta$:

$$V^{(\eta,\delta)}_{\mathrm{eff}}(\beta) = \frac{\eta\delta^2}{2}\frac{1}{\beta^2} + (1-\eta)\delta^2 + \frac{5\eta-4}{2}\beta^2 + (1-\eta)\beta^4. \tag{6}$$

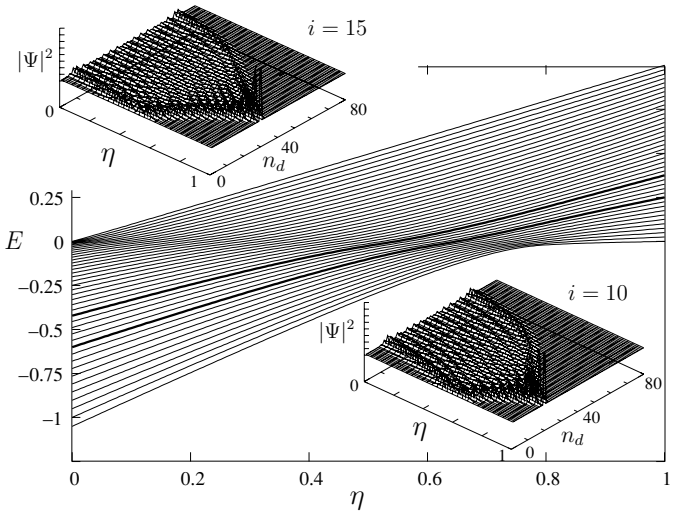

Figure 3. The evolution of $v = 0$ level energies between $O(6)$ and $U(5)$ limits and the n_d-distributions for the 10th and 15th excited states (thicker curves); $N = 80$.

This expression contains, besides the standard potential terms of Hamiltonian (3), also a constant shift and a centrifugal term $\propto\beta^{-2}$ resulting from the fixed value of π_γ. The centrifugal term keeps the solutions with $\delta \neq 0$ away from $\beta = 0$ (in agreement with the fact that minimal n_d for a given v is equal to v [11]) and destroys the Mexican-hat shape of the potential for states with nonzero seniority. Does the phase-transitional evolution survive under these circumstances?

The minimum β_0 of $V_{\rm eff}$ interpolates between $\beta_0 = 1$ at $\eta = 0$ and $\beta_0 = \sqrt{\delta}$ at $\eta = 1$. As we know, for $\delta = 0$ the minimum has a discontinuous derivative $\mathrm{d}\beta_0/\mathrm{d}\eta$ at $\eta_{\rm c} = 4/5$ which leads to a jump in the second derivative of the $V_{\rm eff}$ minimal value. On the other hand, for $\delta \neq 0$ the minimum evolves in a fully analytic way, as can be seen from the fact that within $\eta \in [0, 1]$ it does not cross the border where the sign of $\partial^2 V_{\rm eff}/\partial\beta^2$ changes (for $v = 0$ this happens at $\eta_{\rm c}$). Therefore, $V_{\rm eff}(\beta_0)$ is analytic for $\delta \neq 0$ implying that no phase transition occurs in the behaviour of the *lowest* state with $v \neq 0$. Although potential (6) itself does not allow us to predict properties of individual excited states, the above result and the absence of the central maximum in the $\delta \neq 0$ effective potential make one assume that critical behaviour dies out for *all* states with nonzero seniority. This conforms with numerical calculations of finite-N spectral properties [8] and also with classical considerations showing that only the $\pi_\gamma = 0$ trajectories change the form abruptly (at the monodromy point) as η and/or E vary. Of course, for very small v's one still obtains rapid, though analytic structural rearrangement in the $E \approx 0$ region.

In summary, we gave an example of integrable system where monodromy triggers continuous QPT evolutions of excited-state energies and wavefunctions. It shows that the critical value of interaction parameter may depend on the excitation and that some subsets of states may not undergo the phase transition at all. In the derivation, the key role was played by the oscillator approximation (5) (for $v = 0$ states) and by the effective potential (6) (for $v \neq 0$). Links of QPT phenomena to specific motions on the classical level were found crucial. It would be interesting to learn how the above-discussed properties extend to the nonintegrable regime with $B \neq 0$.

It can be anticipated that our conclusions, apart from having particular consequences for $J = 0$ collective states in γ-soft nuclei between deformed and spherical shapes, are generic for all quantum systems with the Mexican-hat potential. In particular, recent studies [15] of the Lipkin model disclosed very similar nonanalytic structures of quantum properties correlated with the top of a double-well potential. Since the fundamental Ginzburg–Landau model [16] of spontaneous symmetry breaking is based on the same type of potential, the present results might be relevant in rather broad context.

Acknowledgments

PC acknowledges useful discussions with D Rowe. This work was supported by Grant Agency of the Czech Republic (Project 202/06/0363), Czech Ministry of Education (Project MSM 0021620834) and by the German Research Foundation (Project TSE 17/1/06).

References

[1] Duirstermaat J J 1980 *Commun. Pure Appl. Math.* **33** 687
Cushman R H and Bates L 1997 *Global Aspects of Classical Integrable Systems* (Basel: Birkhäuser)
[2] Vu Ngoc S 1999 *Commun. Math. Phys.* **203** 465
[3] For a brief introduction, see Efstathiou K, Joyeux M and Sadovskii D A 2004 *Phys. Rev.* A **69** 032504
[4] Child M S 1998 *J. Phys. A: Math. Gen.* **31** 657
[5] Gilmore R 1981 *Catastrophe Theory for Scientists and Engineers* (New York: Wiley)
[6] Sachdev S 1999 *Quantum Phase Transitions* (Cambridge, UK: Cambridge University Press)
[7] Bohr A and Mottelson B 1975 *Nuclear Structure* vol II (Reading, MA: Benjamin)
[8] Heinze S, Cejnar P, Jolie J and Macek M 2006 *Phys. Rev.* C **73** 014306
Macek M, Cejnar P, Jolie J and Heinze S 2006 *Phys. Rev.* C **73** 014307
[9] For a recent review, see Cejnar P, Heinze S and Jolie J 2003 *Phys. Rev.* C **68** 034326
[10] Jolie J, Cejnar P, Casten R F, Heinze S, Linnemann A and Werner V 2002 *Phys. Rev. Lett.* **89** 182502
[11] Iachello F and Arima A 1987 *The Interacting Boson Model* (Cambridge, UK: Cambridge University Press)
[12] Leviatan A, Novoselsky A and Talmi I 1986 *Phys. Lett.* B **172** 144
[13] Hatch R L and Levit S 1982 *Phys. Rev.* C **25** 614
[14] Rowe D J 2004 *Phys. Rev. Lett.* **93** 122502
Rowe D J 2004 *Nucl. Phys.* A **745** 47
[15] Leyvraz F and Heiss W D 2005 *Phys. Rev. Lett.* **95** 050402
Heiss W D, Scholtz F G and Geyer H B 2005 *J. Phys. A: Math. Gen.* **38** 1843
[16] Ginzburg V L and Landau L D 1950 *J. Exptl. Theor. Phys. (USSR)* **20** 1064

A.3 Classical and quantum properties of the semiregular arc inside the Casten triangle

[*Phys. Rev. C* **75,** 064318 (2007)] [**J5***]

The article studies the dynamics of the interacting boson model in the non-integrable regime. Special emphasis is given to the dynamics at the so-called Alhassid-Whelan semiregular arc [Alha91b, Whel93]. Detailed properties of both quantum and classical solutions of the equations of motion are studied with the aim to understand the source of increased regularity in this region.

Firstly the results of Refs. [Alha91b, Whel93] are confirmed in the classical case by determining the relative fraction of regular trajectories in a sample with randomly generated initial conditions and by measuring the regular part of the Poincaré section area. Similarly for the quantum case, the Brody parameter of the nearest neighbor spacing distribution among eigenenergies is evaluated across the Casten triangle. All measures show significant increase of regularity in the Alhassid-Whelan arc.

An interesting bunching pattern (level density oscillation), markedly resembling the one found along the integrable O(6)–U(5) transition (cf. [**J1**, **J2***]), is found in the low angular momentum spectra slightly above $E = 0$ to be a characteristic feature of the semiregular arc. Its origin is found to be linked (through semiclassical trace formulas) with properties of three major families of classical regular trajectories grouped around three simple primitive orbits being stable in this domain of energy and control parameters. Two of these primitive orbits become degenerate in oscillation frequencies at the energy corresponding to the bunching within the quantum spectrum.

In the low lying spectrum, a degeneracy between simple β and γ vibrations (representing bandheads of β and γ rotational bands) is found along a line, which runs across the axially deformed region of the Casten triangle lying very close to the semiregular arc. The position of the line is determined analytically using the intrinsic coherent state formalism. This degeneracy line is also found to be closely correlated with a change of stability properties of low-energy classical β and γ vibrations.

In the last part of the paper, a particular region near to the deformed-to-spherical shape phase transition within the Casten triangle is disclosed, where the classical dynamics strongly resembles the dynamics of the geometric collective model, hence a link between these two models is obtained.

The author of this thesis developed the code for numerical solutions of the classical Hamilton equations of motion and performed extensive numerical calculations and analyses of the properties of the classical orbits. He recognized the periodic orbits substantially contributing to the semiclassical trace formulas and found the region linking the interacting boson model with the geometric collective model by comparison of the respective Poincaré sections. He also gave the analytical arguments for this correspondence.

Classical and quantum properties of the semiregular arc inside the Casten triangle

Michal Macek, Pavel Stránský, and Pavel Cejnar
Faculty of Mathematics and Physics, Charles University, V Holešovičkách 2, CZ-18000 Prague, Czech Republic

Stefan Heinze and Jan Jolie
Institute of Nuclear Physics, University of Cologne, Zülpicherstrasse 77, D-50937 Cologne, Germany

Jan Dobeš
Nuclear Physics Institute, Academy of Sciences of the Czech Republic, CZ-250 68 Rez, Czech Republic
(Received 23 November 2006; published 22 June 2007)

We investigate classical and quantum signatures of increased regularity in the Alhassid-Whelan semiregular arc inside the symmetry triangle of the interacting boson model. A significant bunching/antibunching pattern of quantum levels, similar to that observed along the O(6)-U(5) transition, is found in the 0^+ energy spectrum and related to a crossover of two specific families of classical regular orbits slightly above $E = 0$. We also discuss the degeneracy of β and γ bandheads in a region close to the arc and the relation to regularity in the geometric model.

DOI: 10.1103/PhysRevC.75.064318 PACS number(s): 21.60.Fw, 21.60.Ev, 05.45.Mt, 21.10.Re

I. INTRODUCTION

The interacting boson model (IBM) of nuclear collective motions, developed by Iachello and Arima [1] in the 1970's, displays a wide variety of interesting features. Apart from being successful in the description of low-lying collective states of even-even nuclei, it has also served as a useful "toy model" to study various general phenomena, such as quantum phase transitions [2–4] or order/chaos coexistence [5–16]. The interplay between regular and chaotic behaviors, observable on both the quantum and classical levels of the model, is surely one of the most intriguing properties. It seems to be a common feature of nuclear collective motions in general. The present paper contributes to this subject, extending our recent study [17,18] of fully regular dynamics in the IBM. Special attention is payed to the semiregular region of Alhassid and Whelan [8–10] lying within the parametric space of IBM.

The onset of chaos in a system is closely connected with the breakdown of symmetries [19–21]. The IBM is known [1] to possess three standard dynamical symmetries, namely, U(5), O(6), and SU(3), and two additional ones, $\overline{\mathrm{O}(6)}$ and $\overline{\mathrm{SU}(3)}$, following from gauge transformations [22]. They are related to the possible decompositions of the spectrum generating group U(6) into subgroup chains that contain the invariant-symmetry group O(3) of physical rotations. An important consequence of dynamical symmetries is the integrability of the corresponding Hamiltonians, guaranteed by the complete set of constants of motion provided by Casimir operators of respective subgroup chains [23]. The system in such cases exhibits completely regular dynamics.

Apart from the dynamical-symmetry limits, there exists a unique integrable transition path between O(6) and U(5) marked by conservation of the Casimir invariant of the common subgroup O(5) [24]. Away from these integrable regions, the IBM dynamics was expected to be chaotic until the study in Ref. [8] revealed surprisingly high degree of regularity along a particular path inside the model parameter space. This path forms a bent curve in between the SU(3) and U(5) vertices of the symmetry triangle and is called hereafter the "AW arc". Unlike the O(6)-U(5) path [15,17,18], the dynamics within the AW arc is not completely regular, indicating the existence of a kind of partial dynamical symmetry [25]. Interestingly, evolutions of energy spectra along the two regular paths display certain similarity, as we will show below.

Unknown nature of regularity along the AW arc stimulated research of the IBM properties from various perspectives. Originally, Alhassid and Whelan observed the dependence of both short- and long-range spectral correlations together with classical measures of chaos on the angular momentum l and two control parameters η, χ that change the amount of dynamical symmetries in the Hamiltonian. Significant rise of regularity in the arc was found using both quantum and classical measures [8–10]. Later, the analysis of wave function entropies [26] revealed an increased localisation of energy eigenstates in dynamical-symmetry bases within a region coinciding with the AW arc. Recently, several real nuclei were located very close to the arc, an approximate degeneracy of 0_2^+ and 2_2^+ states being pointed out as a characteristic feature of nuclei in this region [27]. Also a close relative of the IBM—the geometric collective model (GCM)—was found to show a similar increase of classical regularity away from integrable regimes [28–30].

The layout of this article is as follows. The IBM and its classical limit are briefly described in Sec. II. In Sec. III we demonstrate increased regularity of the dynamics within the AW arc using the nearest neighbor spacing distribution of 0^+ states and classical measures based on Poincaré sections [19] and so-called alignment indices [31]. Section IV presents an observation of strong level bunchings in the spectra of 0^+ states along the arc, slightly above zero absolute energy. The pattern shows great degree of similarity to the bunching found in spectra along the O(6)-U(5) transition [17]. In Sec. V, we search for related effects in the classical phase space, exploiting the connection of level density with periodic orbits.

In Sec. VI we apply the technique of intrinsic states to explain the approximate degeneracy of 0_2^+ and 2_2^+ states close to the arc. Section VII is devoted to the comparison of regular dynamics within IBM and GCM. Finally, Sec. VIII brings a summary and outlook.

II. HAMILTONIAN

The interacting boson model describes low-lying spectra of even-even nuclei in terms of an ensemble of N bosons s and d with angular momenta 0 and 2, respectively. Bilinear products of creation and annihilation operators $b_i^\dagger b_j$, where $i, j = s, 1, \ldots, 5$ stand for the s-boson and the five components of d-boson, form a set of U(6) generators. We limit our investigation to the simplest version of the model, the IBM-1, which does not distinguish neutron and proton types of bosons (we use nevertheless the common abbreviation IBM). Instead of the most general quantum Hamiltonian with all rotationally invariant one- and two-body terms we consider a simplified form

$$\hat{H} = a\left[\frac{\eta}{N}\hat{n}_d - \frac{1-\eta}{N^2}(\hat{Q}_\chi \cdot \hat{Q}_\chi)\right], \tag{1}$$

with $\hat{n}_d = (d^\dagger \cdot \tilde{d})$ denoting the d-boson number operator and $\hat{Q}_\chi = [s^\dagger \tilde{d} + d^\dagger \tilde{s}]^{(2)} + \chi[d^\dagger \tilde{d}]^{(2)}$ the quadrupole operator. The scaling factor a sets an effective energy unit in quantum spectra. In the figures below we use a numerical value $a = N/10$ in arbitrary units, thus the quantum energy is taken as an extensive quantity. Hamiltonian in Eq. (1) depends on two dimensionless parameters $\eta \in [0, 1]$ and $\chi \in [-\sqrt{7}/2, \sqrt{7}/2]$, that drive the system in between four dynamical-symmetry limits: U(5) for $(\eta, \chi) = (1, 0)$, O(6) for $(\eta, \chi) = (0, 0)$, SU(3) for $(\eta, \chi) = (0, -\sqrt{7}/2)$, and $\overline{\text{SU(3)}}$ for $(\eta, \chi) = (0, \sqrt{7}/2)$; the dynamical symmetry $\overline{\text{O(6)}}$ is not present in the parameter plane (so-called extended Casten triangle [32]).

The classical limit can be constructed by the method of Hatch and Levit [33] using Glauber coherent states. We have outlined the procedure in Ref. [18], where the special case $\chi = 0$ was studied for zero eigenvalue $l(l+1)$ of L^2, with the angular momentum defined as $L = \sqrt{10}[d^\dagger \tilde{d}]^{(1)}$. For general χ and $l = 0$ the Hamiltonian—with the quadrupole deformation parameters β, γ and their conjugate momenta p_β, p_γ as canonical coordinates—becomes

$$\begin{aligned} H_{\rm cl} = {} & \frac{1}{2}\left[\eta + 2(1-\eta)\beta^2\right](\beta^2 + T) - 2(1-\eta)\beta^2 \\ & - \frac{2}{\sqrt{7}}\chi(1-\eta)\sqrt{1 - \frac{1}{2}(\beta^2 + T)} \\ & \times \left[\left(p_\gamma^2/\beta - \beta p_\beta^2 - \beta^3\right)\cos 3\gamma + 2p_\beta p_\gamma \sin 3\gamma\right] \\ & - \frac{4}{7}\chi^2(1-\eta)\left[\frac{1}{8}(\beta^2 + T)^2 - \frac{1}{2}p_\gamma^2\right]. \end{aligned} \tag{2}$$

Here, $T \equiv p_\beta^2 + p_\gamma^2/\beta^2$ stands for the usual kinetic energy. The Hamiltonian (2) represents the "energy per boson". Coordinates and momenta are limited to intervals $\beta \in [0, \sqrt{2}]$, $p_\beta \in [0, \sqrt{2}]$, and $p_\gamma \in [0, 1]$ following from the boundedness of Hamiltonian (1). Note that classical energy from Eq. (2) is expressed in units of the numerical scaling parameter a, see Eq. (1). To distinguish energies obtained from Eqs. (1) and (2), we use hereafter symbols E and $E_{\rm cl}$, respectively.

In Sec. VII, the classical IBM dynamics will be compared with the dynamics of truncated geometric collective model with Hamiltonian [28–30,34]

$$H_{\rm GCM} = \frac{1}{2K}T + \underbrace{A\beta^2 + B\beta^3\cos 3\gamma + C\beta^4}_{V_{\rm GCM}}. \tag{3}$$

In contrast to GCM, the classical IBM Hamiltonian (2) is apparently not a sum of T and a potential V. The IBM potential

$$\begin{aligned} V(\beta, \gamma) = {} & \frac{1}{2}(5\eta - 4)\beta^2 + (1-\eta)\left(1 - \frac{1}{14}\chi^2\right)\beta^4 \\ & - \frac{2}{\sqrt{7}}\chi(1-\eta)\beta^3\sqrt{1 - \frac{1}{2}\beta^2}\,\cos 3\gamma\,, \end{aligned} \tag{4}$$

obtained by setting $p_\beta = p_\gamma = 0$ in Eq. (2), differs from $V_{\rm GCM}$ in Eq. (3) by the square-root factor. Variables β and γ can be treated as polar coordinates of the corresponding Cartesian variables x and y, thus

$$\begin{aligned} x &= \beta\cos\gamma\,, & p_x &= p_\beta\cos\gamma - (p_\gamma/\beta)\sin\gamma\,, \\ y &= \beta\sin\gamma\,, & p_y &= (p_\gamma/\beta)\cos\gamma + p_\beta\sin\gamma\,, \end{aligned} \tag{5}$$

with p_x and p_y denoting the associated momenta. This notation will be frequently used below.

Low-energy motions generated by potential (4) undergo essential changes when the first-order shape-phase separatrices are crossed [2–4]. These are located at $\chi = 0, \eta < 0.8$ (prolate-oblate ground-state transition) and $\eta = (4 + 2\chi^2/7)/(5 + 2\chi^2/7) \equiv \eta_c$ (deformed-spherical transition). In panel (b) of Fig. 1 we show a contour plot of the potential for $\eta = 0.5$, $\chi = -0.91$ in the plane $x \times y$, while panel (a) presents three sections in the plane $y = 0$ for the dynamical-symmetry limits. It is worth noting that the value of potential at $\beta = 0$ is always zero; for $\eta < 0.8$ it represents a local maximum while for $\eta > 0.8$ it is a minimum (which becomes global after η_c).

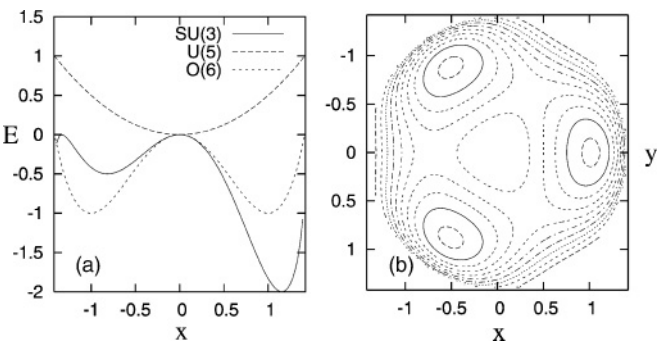

FIG. 1. Sections of potential (4) in the plane $y = 0$ for control parameters corresponding to dynamical symmetries (panel a) and a contourplot of the potential for $\eta = 0.5$ and $\chi = -0.91$ (panel b). Bohr coordinates β and γ are the radius and polar angle, respectively, in the plane $x \times y$. Energy unit is arbitrary.

III. ALHASSID-WHELAN SEMIREGULAR ARC

A. Linear fit of the arc

Location of the highly regular region inside the Casten triangle was determined in Ref. [9] by fitting the minimum of the fraction of chaotic classical phase space volume by a linear dependence. The other classical and quantum measures of chaos (average maximum Lyapunov exponents, spectral correlations, $E2$ strength distributions) showed very similar dependence. The linear fit can be approximated by [26]

$$\chi_{\rm reg}(\eta) \approx \pm\left[\frac{\sqrt{7}-1}{2}\,\eta - \frac{\sqrt{7}}{2}\right]. \qquad (6)$$

Note that the arc occurs symmetrically in both $\chi < 0$ and $\chi > 0$ halves of the extended Casten triangle (since the halves are dynamically equivalent, connected by a simple phase transformation). In the following, we will mostly use the convention with $\chi \leqslant 0$.

B. Classical measures of regularity

While the results of Refs. [5–9] comprehensively reflect the overall dependence of chaotic measures on the model control parameters η and χ, some peculiar features of motions related to the increase of regularity remain unaddressed. The present paper offers a closer view on the classical and quantum dynamics at zero angular momentum in the vicinity of the AW arc. In the classical part, the limitation to $l = 0$ admits us to use methods based on Poincaré sections [19] (since the system becomes effectively two-dimensional), which provide neat overall "snapshots" of the phase space at given energy E and allow us to consider stability properties of individual types of trajectories in a simple way. Let us note that Poincaré sections associated with Hamiltonian (1) at lower energies were for the first time studied in Ref. [10]. Here, we extend the study also to higher energies. Several examples of Poincaré sections at $E_{\rm cl} = 0$ can be seen in Fig. 2, where a line crossing the AW arc is followed at a fixed value of parameter η. The numerical procedure is described in Sec. V A.

To quantify the degree of regularity of a given Poincaré section, we determine the areal fraction $f_{\rm reg}^{\rm (P)}$ occupied by regular trajectories as described in Refs. [28,30]. This method, instead of evaluating the maximal Lyapounov exponent [6,9] associated with each orbit, makes use of the fact that regular orbits fill one-dimensional subsets of the section (topological circles), whereas chaotic orbits fill the available phase space ergodically [19]. The regular fraction is given as the ratio of the area $S_{\rm reg}$ filled with regular trajectories to the total area $S_{\rm tot}$ of the accessible phase space section,

$$f_{\rm reg}^{\rm (P)} = S_{\rm reg}/S_{\rm tot}. \qquad (7)$$

A different and faster method we use to determine regularity of the system is based on calculation of the so-called smaller alignment index (SALI) [31] for individual trajectories, randomly generated inside the whole accessible phase space. The regularity is now given as the ratio of the number of regular trajectories $N_{\rm reg}$ to the total number $N_{\rm tot}$ generated at a given

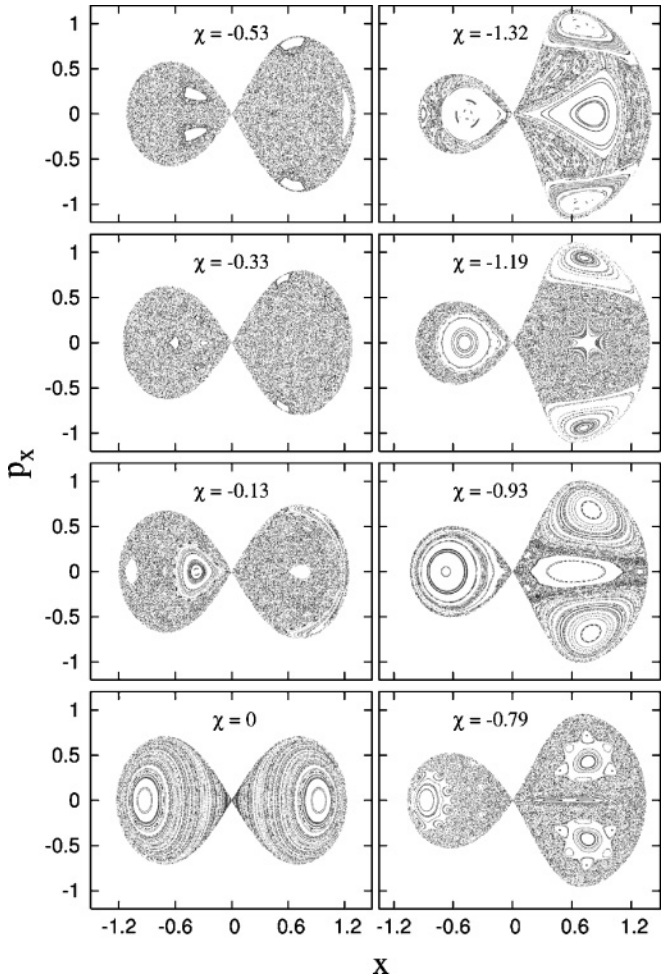

FIG. 2. Phase space portraits disclosed by $E_{\rm cl} = 0$ Poincaré sections at $\eta = 0.5$ and $\chi \in [0, -\sqrt{7}/2]$. Each panel contains $\sim 10^4$ passages of 120 trajectories with $E_{\rm cl} = l = 0$ and randomly generated initial condition through the plane defined by setting $y = 0$. The crossing of the AW arc can be noticed at $\chi \approx -0.9$.

values of control parameters and energy, hence

$$f_{\rm reg}^{\rm (S)} = N_{\rm reg}/N_{\rm tot}. \qquad (8)$$

Both measures attain values $f_{\rm reg} \in [0, 1]$ and provide an independent verification of increased regularity in the AW arc.

In Fig. 3, we present the dependence of regularity on χ at $\eta = 0.5$ and $E_{\rm cl} = 0$: both regular fractions decrease monotonously from $f_{\rm reg} = 1$ in the integrable regime $\chi = 0$ to values $f_{\rm reg} < 0.05$ for $\chi \approx -0.4$. Then they rise again to reach $f_{\rm reg} = 0.8$ at $\chi = -0.91$. Decreasing χ further, the fractions drop to $f_{\rm reg} \approx 0.3$ with a slight increase at $\chi = -\sqrt{7}/2$. In the more efficient SALI calculation, we chose a finer step in χ, which discloses some minor peaks in the interval $\chi \in [-0.8, -0.4]$. In the region of $\eta \approx 0.5$, these are however negligible in comparison with the main regularity increase around $\chi \approx -0.9$.

Poincaré sections in Fig. 2 corresponding to selected values of χ along the same line show, that in the most chaotic regions, $\chi \in [-0.8, -0.1]$, the phase space consists of a complicated pattern of minor regular regions emerging from

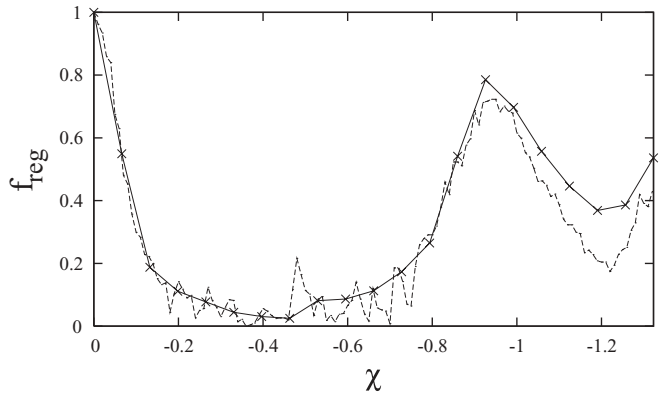

FIG. 3. Regularity of classical IBM for $\eta = 0.5$ and $E_{\rm cl} = 0$ as a function of χ determined by two methods: (i) the fraction of regular area in the Poincaré section (solid line) and (ii) the fraction of regular trajectories obtained by the SALI method (dashed line). The peak at $\chi \approx -0.9$ corresponds to AW arc. Oscillations on the dashed curve are caused by a finer step of the SALI evaluation.

the "background" of ergodic trajectories. On the other hand, the peak of regularity at $\chi \approx -0.9$ gives rise to a remarkably simple picture containing basically only four major regular islands. These correspond to two families of regular orbits, discussed further in Sec. V.

The degree of regularity is not uniform in energy and the relative regularity of the arc is most significant just around absolute energy $E_{\rm cl} = 0$. This is illustrated in Fig. 4, where we plot the regular fraction (8) for $\eta = 0.5$ and several values of χ as a function of energy. Our observations conform with the earlier results of Refs. [6–9]. The energy dependence will be studied in more detail in Sec. V.

C. Quantum measures of regularity

To check the signatures of classical regularity in the quantum spectrum, we fitted the Brody distribution of normalized spacings $S = (E_{i+1} - E_i)/\langle E_{i+1} - E_i \rangle$ between neighboring eigenvalues in the unfolded spectrum of 0^+ levels. The Brody

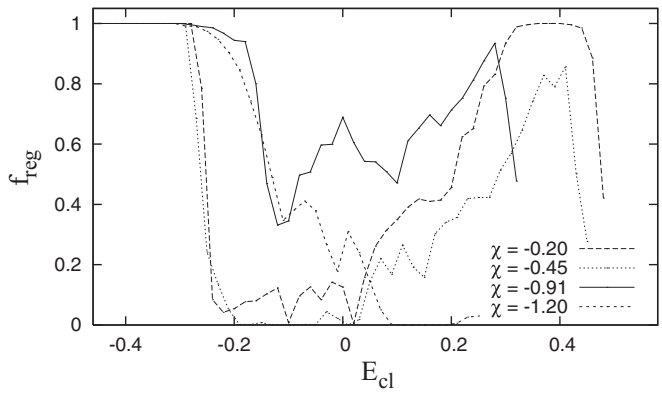

FIG. 4. Energy dependences of regularity in classical IBM for $\eta = 0.5$ at selected values of χ determined by the SALI method. Energy unit is arbitrary.

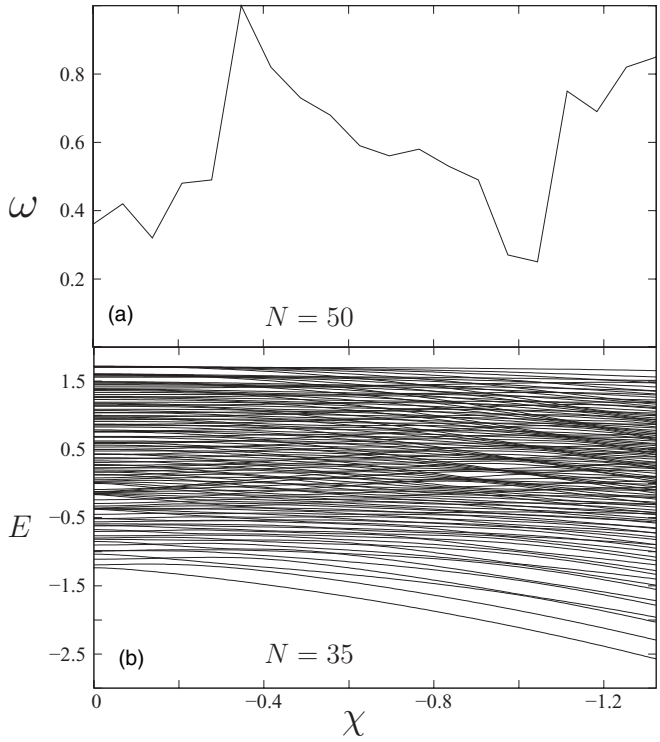

FIG. 5. The evolution of 0^+ energy levels (panel b) and the corresponding dependence of the Brody parameter ω on χ at $\eta = 0.5$ (panel a). The minimum of ω at $\chi \approx -1$ is connected with the bunching of $E \in [0, 1]$ levels. Energy unit is arbitrary. The boson numbers in each panel differ only to make panel (b) more legible.

distribution has the form [35]

$$\mathcal{P}_\omega(S) = \mathcal{N}_\omega S^\omega \exp(-\alpha_\omega S^{1+\omega}), \tag{9}$$

where ω is an adjustable parameter, $\alpha_\omega = \Gamma(\frac{2+\omega}{1+\omega})^{1+\omega}$, and $\mathcal{N}_\omega = (\omega + 1)\alpha_\omega$. It interpolates between Poisson distribution ($\omega = 0$) valid for generic integrable systems and Wigner distribution ($\omega = 1$) corresponding to chaotic systems [20,21]. The spectrum was obtained by numerical diagonalisation of Hamiltonian (1) and the subsequent unfolding was performed by methods described in Ref. [36].

In Fig. 5 we show values of the Brody parameter ω (panel a) and the evolution of 0^+ energies (panel b) as χ is varied at $\eta = 0.5$. The dependence of $\omega(\chi)$ has again a clear minimum $\omega \approx 0.25$ corresponding to a Poisson-like distribution (hence quasiregular dynamics) at $\chi \approx -1$. Note that the nonzero value of ω in the integrable region $\chi = 0$ results from nongeneric spectral fluctuations [9].

We can conclude that both classical and quantum measures $f_{\rm reg}$ and ω show significant increase of regularity for values close to curve Eq. (6) that predicts $\chi_{\rm reg} \approx 0.91$ for $\eta = 0.5$. However, it should be stressed again that the picture depends very much on energy. Although the increase of regularity can be clearly observed in energy-averaged measures [8,9], the greatest contribution comes from the region around $E \approx 0$ (cf. Fig. 2 of Ref. [8]). If repeating the above classical analysis for another energy value, the AW arc might remain unnoticed.

IV. BUNCHING OF 0^+ STATES

In this section, we study the evolution of energy spectra of Hamiltonian (1) with variable η, following the path along the AW arc. We try to trace out a pattern of multiple bunchings and antibunchings of levels, noticeable already in Fig. 5(b) at $\chi \approx -0.9$, and discuss its relation to a similar structure in the O(6)-U(5) transition [17,18]. We claim that this pattern, for the first time noticed in the analysis of unfolded spectra in Ref. [4] and also reported in Ref. [37], constitutes the most distinctive characteristic of the AW arc.

The pattern can be clearly observed when looking at η-dependent spectral evolution along the path $\chi_{\rm reg}(\eta)$, Eq. (6). The relevant part of the 0^+ spectrum for $N = 40$ bosons is plotted in the middle panel [$k = 3$, see Eq. (10) below] of Fig. 6. Note that in this subsection we use a numerical scaling factor $a = N/10$ of quantum Hamiltonian (1), i.e., $a = 4$ energy units for $N = 40$. As seen, the bunching pattern resides slightly above $E = 0$; it starts at $\eta \approx 0.1$, $E \in [0.2, 0.6]$ and spans roughly the whole region of deformed ground-state shapes until it runs off the spectrum at $\eta \approx 0.8$, $E \in [-0.2, 0.2]$.

The question arises whether such bunchings may be observed also in neighboring parameter regions. To find the answer, we chose several paths "parallel" with the AW arc, see Fig. 7, and look at the associated spectra in various panels

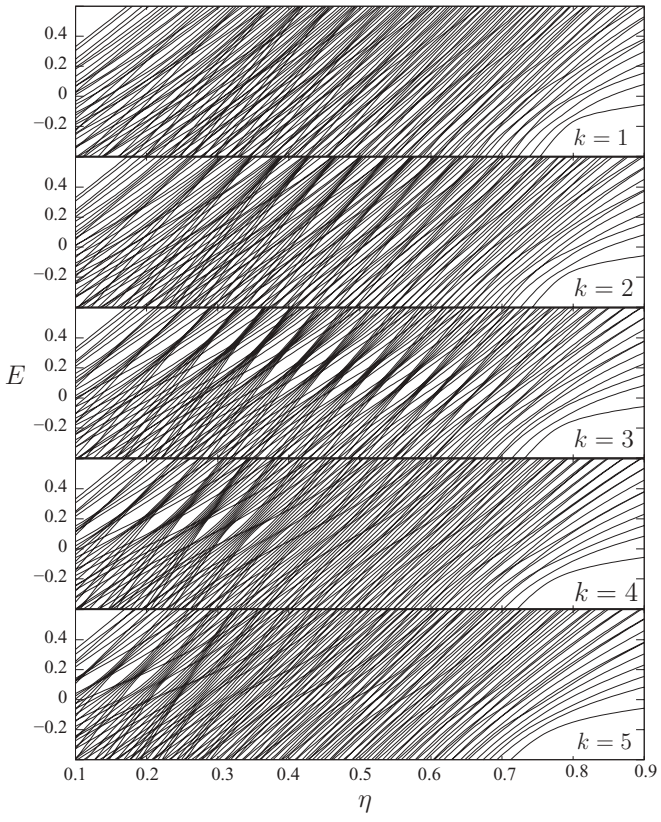

FIG. 6. Evolutions of 0^+ spectra for $N = 40$ [Hamiltonian (1) with $a = 4$] along paths shown in Fig. 7. Energy unit is arbitrary. A bunching pattern slightly above $E = 0$ is observed in the AW arc (panel $k = 3$) and gradually disappears as the path deviates from the arc (panels with $k \neq 3$).

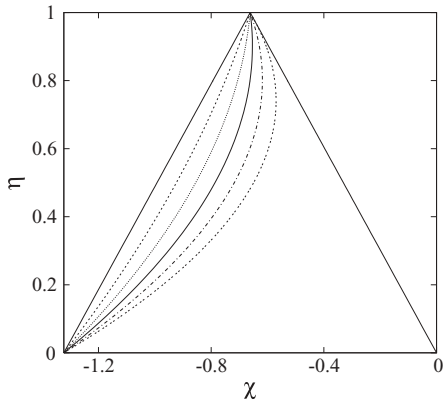

FIG. 7. A set of paths (10) "parallel" to the AW arc (6). The paths are labeled by $k = 0, 1, \ldots, 5$, with $k = 0$ corresponding to the SU(3)-U(5) edge and $k = 3$ representing the arc (solid curve). Only the $\chi \leqslant 0$ half of the extended Casten triangle is shown.

of Fig. 6. The paths are labeled by integer k in the following parametrization:

$$\chi_k = \pm\left[k\frac{\sqrt{7}-1}{6}\,\eta - \frac{\sqrt{7}}{2}\right], \tag{10}$$

where $k = 0$ corresponds to the SU(3)-U(5) [or $\overline{\rm SU(3)} - {\rm U(5)}$] edge of the Casten triangle while $k = 3$ to the fit (6) of the arc. Apparently, the bunching fades away as we depart from the arc. Since, as mentioned in Sec. III, the regularity within the AW arc for low spins is mostly connected with the region around and just above zero absolute energy (cf. Fig. 4 above and Fig. 2 of Ref. [8]), we anticipate that the bunching (present in the same range) is intimately related to the source of regularity.

Another immediate question is whether the bunching survives an increase of angular momentum. Figure 8 shows that when increasing the angular momentum eigenvalue l, the gaps in the spectrum become less pronounced due to repulsion among increased numbers of levels. For low spins a tendency to bunch is still observable in the same range of energies, but the effect is practically gone for $l \geqslant 8$.

Figure 9 offers a comparison of the bunching pattern in the AW arc (lower panel) with a similar pattern along the integrable O(6)-U(5) transition [17,18,38] (upper panel). It is clear that both structures exist at $l = 0$ in very close (although not identical) energy domains, $E \approx 0$, and exhibit great deal of similarity. On the other hand, while in the O(6)-U(5) transition the bunching involves real crossings of levels with different seniority quantum numbers, all crossings along the AW arc are presumably avoided (though to prove this numerically is, in some cases, practically impossible). It can be noticed that if proceeding along the bunching from the right ($\eta \approx 0.8$) to the left, the numbers of states involved form a sequence 1, 2, 3, 4, 5, . . ., in the O(6)-U(5) case and 1, 1, 2, 2, 3, 3, . . ., in the AW case.

With increasing η, the center of the bunching in both O(6)-U(5) and AW cases travels toward the kink of the ground-state energy at $\eta = \eta_c$ which separates the deformed and spherical phases [2–4]. As shown recently [38], the $E = 0$ bunching along the O(6)-U(5) path demarcates the $N \to \infty$

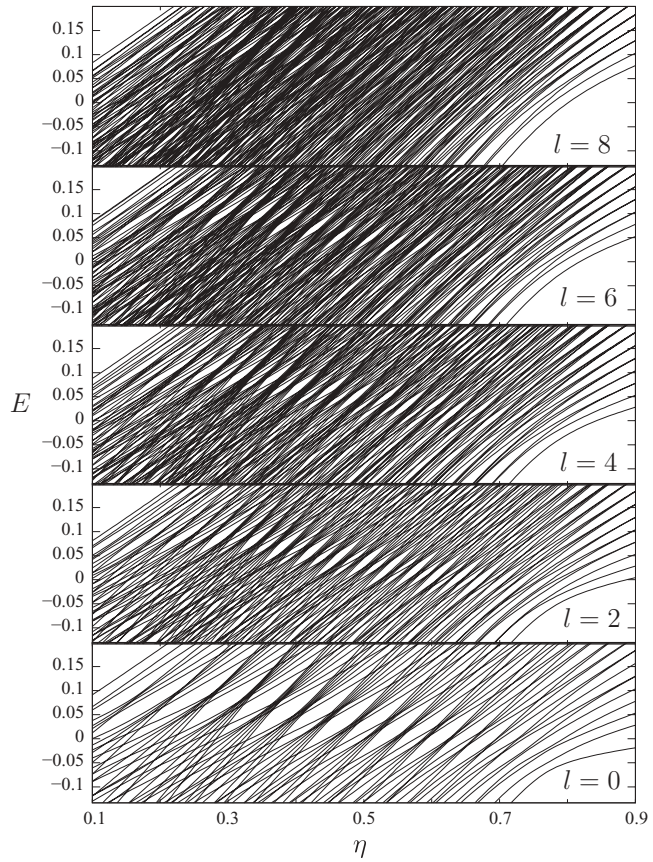

FIG. 8. Washing out of the bunching pattern at $\chi_{\rm reg}(\eta)$ ($k = 3$) with increasing angular momentum l for $N = 30$. (Energy unit is arbitrary.)

phase transition of excited states with zero seniority. It would be interesting to learn whether the pattern in the AW arc has a similar consequence (although seniority is not defined in this case).

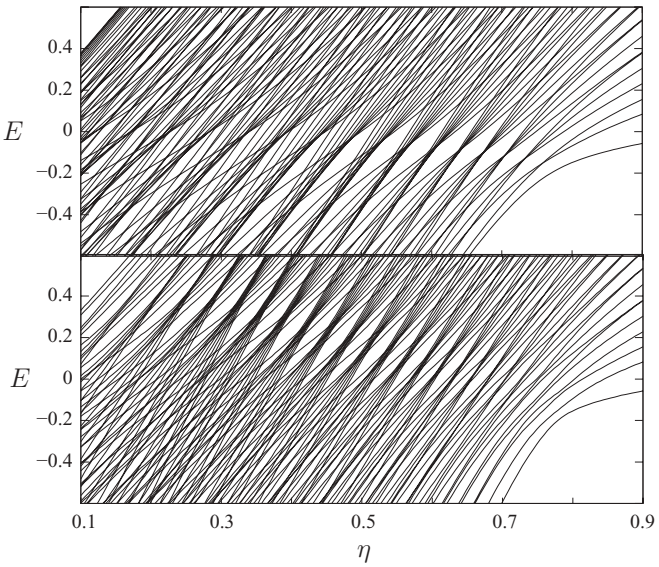

FIG. 9. Comparison of the bunching of 0^+ states in O(6)-U(5) transition (upper panel) and along the AW arc (lower panel); both spectra calculated for $N = 40$. (Energy unit is arbitrary.)

V. CLASSICAL EFFECTS

A. Numerical procedure

In the following, we discuss classical phase-space structures arising from Hamiltonian (2) that uncover various types of regular motions in different parts of the Casten triangle. We focus in particular on classical motions within the AW arc.

To make a detailed image of the IBM phase space, a sufficient number of trajectories must be launched, covering the whole plane of the Poincaré section, and each of them must be traced for sufficiently long time. In our calculations, we generated 120 trajectories with random initial conditions (satisfying the constraint $l = 0$) for every set of η, χ, and $E_{\rm cl}$. The classical equations of motions corresponding to Hamiltonian (2) were solved numerically, using the fourth-order Runge-Kutta method, and the calculation was stopped after 3×10^4 passages of each trajectory through the $x \times p_x$ plane with $y = 0$.

The method of evaluating the areal fraction $f_{\rm reg}^{\rm (P)}$ from Eq. (7) was described in Ref. [30]. Finite resolution of the Poincaré section division leads to some systematic errors which are most significant when $f_{\rm reg}^{\rm (P)} \approx 1$ but do not exceed cca 5%. The implementation of the SALI method (for details, see Ref. [31]) in the evaluation of $f_{\rm reg}^{\rm (S)}$ from Eq. (8) induces statistical errors connected with the finite numbers of generated trajectories. In our case ($N_{\rm tot} = 500$ for each point of $f_{\rm reg}^{\rm (S)}$) the error is estimated by the expression $\Delta f_{\rm reg}/f_{\rm reg} \approx 0.04\, f_{\rm reg}^{-1/2}$.

The energy dependence of the degree of chaos at selected values of η and χ is explored with a sample of ten equidistant levels

$$E_i = V_{\rm min} + \frac{i}{11}\,(V_{\rm lim} - V_{\rm min})\,, \qquad (11)$$

$i = 1, \ldots, 10$, covering the whole energy range between the global minimum $V_{\rm min} = V(\beta = \beta_{\rm min})$ of the potential for given η, χ and the value $V_{\rm lim} \equiv V(\beta = \sqrt{2})$, which represents the uppermost energy for the classical motion to be finite (since $\beta = \sqrt{2}$ is the maximal physical value of the deformation parameter). Remind that energies $E_{\rm cl}$ obtained from classical Hamiltonian (2) are scale-free, i.e., given in units of a (in contrast to quantum energies E analyzed in Sec. IV). We point out two important intermediate energy values: (i) Energy $E_{\rm sad} < 0$ of the saddle points between three degenerate global $\beta > 0$ minima of potential (4) at $\gamma = 0, 2\pi/3$, and $4\pi/3$. Below $E_{\rm sad}$, the energetically accessible region in the plane $x \times y$ consists of three separate areas surrounding the global minima; at $E_{\rm cl} = E_{\rm sad}$ these areas touch and merge. (ii) The energy $E_{\rm cl} = 0$ coinciding with the local maximum $V(\beta = 0)$. For $E_{\rm cl} > 0$ the accessible region in the $x \times y$ plane is a simply connected area.

B. Poincaré sections

Poincaré sections corresponding to $E_{\rm cl} = E_1, \ldots, E_{10}$ from Eq. (11) were generated at 35 points lying on paths χ_k, Eq. (10), with $k = 0, 1, \ldots, 5, 7$ and $\eta \in [0.3, 0.7]$. The results show a sensitive dependence of the dynamics on χ,

with particularly distinct structural changes of trajectories in the vicinity of the AW arc ($k = 3$), for all values of η. On the other hand, varying η for a fixed k affects the motions mostly via shifting both energy limits $V_{\min}$ and $V_{\lim}$ upward (thus energies $E_{\rm cl} < 0$ become unattainable for $\eta > \eta_{\rm c} \approx 0.8$), but the shape of the main phase space structures far enough from $\eta_{\rm c}$ remains visually intact.

A complete collection of Poincaré sections may be found on our website [39]. Here we will illustrate the dependence of the dynamics on χ at $\eta = 0.5$, by selecting three values χ_k with $k = 2, 3, 4$, that represent the regions of $|\chi| > |\chi_{\rm reg}|$, $\chi = \chi_{\rm reg}$, and $|\chi| < |\chi_{\rm reg}|$, respectively. The corresponding Poincaré sections are arranged in three columns of Fig. 10. Rows from bottom to top correspond to increasing energies from Eq. (11). Note that values of E_i differ for the three columns (because the shape of potential depends on η and χ), but energy ranges below and above the above-specified benchmarks $E_{\rm cl} = 0$ and $E_{\rm sad}$ can be easily recognized from the topology of the respective section: While for $E_{\rm cl} < E_{\rm sad}$ (no pass between three degenerate global minima) the crossings form a single compact area around $x \approx \beta_{\min} > 0$, $p_x = 0$, for $E_{\rm cl} > E_{\rm sad}$ we observe two separate areas of crossings (with $x > 0$ and $x < 0$) that merge at $E_{\rm cl} = 0$. For $E_{\rm cl} > 0$, the crossings fill in a single area around the origin.

Regular trajectories contributing to Poincaré sections in Fig. 10 form islands of concentric "circles" enfolding some simple periodic orbits in their centers. Examples are given in Fig. 11. The central orbits represent *elliptic* fixed points of the associated Poincaré mapping [19] and can be used to classify the enveloping islands. We distinguish the following principal families of orbits:

(i) Trajectories forming a regular island centered at a point $x > 0$ and $p_x = 0$. These constitute a family of "γ-vibrations" since the central orbit (see orbit 1 in both panels of Fig. 11) oscillates with $\beta \approx \beta_{\min}$ around the potential minimum. (To avoid confusion we note that in the present case angular momentum $l = 0$, which is in contrast to the lowest γ-vibrational quantum state with $l = 2$.)

(ii) Trajectories forming two symmetric regular islands with central points at $x > 0$ and $p_x > 0$, $p_x < 0$ and for $E_{\rm cl} > E_{\rm sad}$ also an additional island at $x < 0$ and $p_x = 0$. These are mixed "$\beta\gamma$-vibrations" that for $E_{\rm cl} < E_{\rm sad}$ oscillate around one potential minimum [see both orbits 2 in panel (a) of Fig. 11] and for $E_{\rm cl} > E_{\rm sad}$ migrate over the saddle points between the pairs of neighboring minima [orbits $2_{\rm a}$ and $2_{\rm b}$ in panel (b) of Fig. 11 connecting the $\gamma = 2\pi/3$ and $4\pi/3$ minima; analogous orbits exist also for the other pairs of minima].

We observe (cf. Figs. 4 and 10) that the degree of chaos varies with χ most significantly at intermediate energies, especially around $E_{\rm cl} \approx 0$ (cf. Sec. IV). At low energies, $E_{\rm cl} < E_{\rm sad}$, but also at very high energies, $E_{\rm cl} \approx V_{\lim}$, the dynamics is mostly regular—this being understood from the prevailing harmonic and pure quartic character of collective oscillations in the respective regimes [30]. In the following,

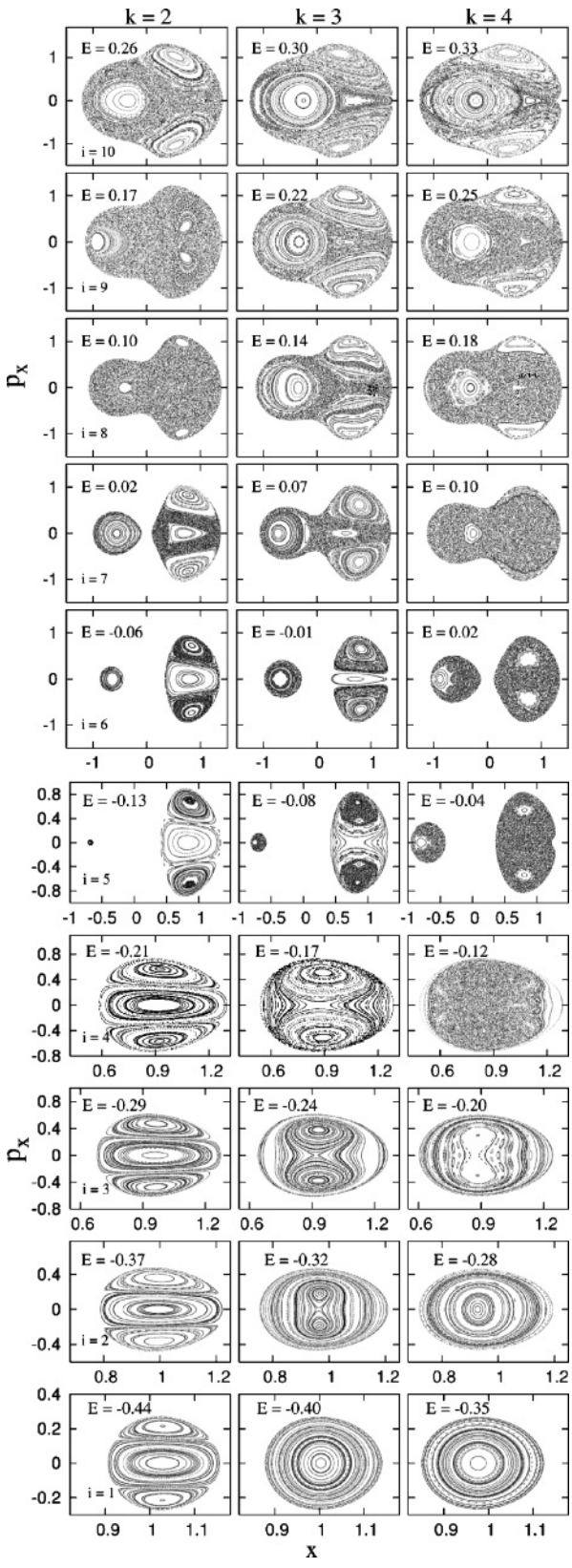

FIG. 10. Poincaré sections $y = 0$ for $\eta = 0.5$ and χ_k, $k = 2, 3, 4$ (columns) at energies $E_{\rm cl} = E_1, \ldots, E_{10}$ (rows). The middle column corresponds to the AW arc. Notice that sections for $E_{\rm cl} < E_{\rm sad}$ are expanded compared to those for $E_{\rm cl} \geqslant E_{\rm sad}$.

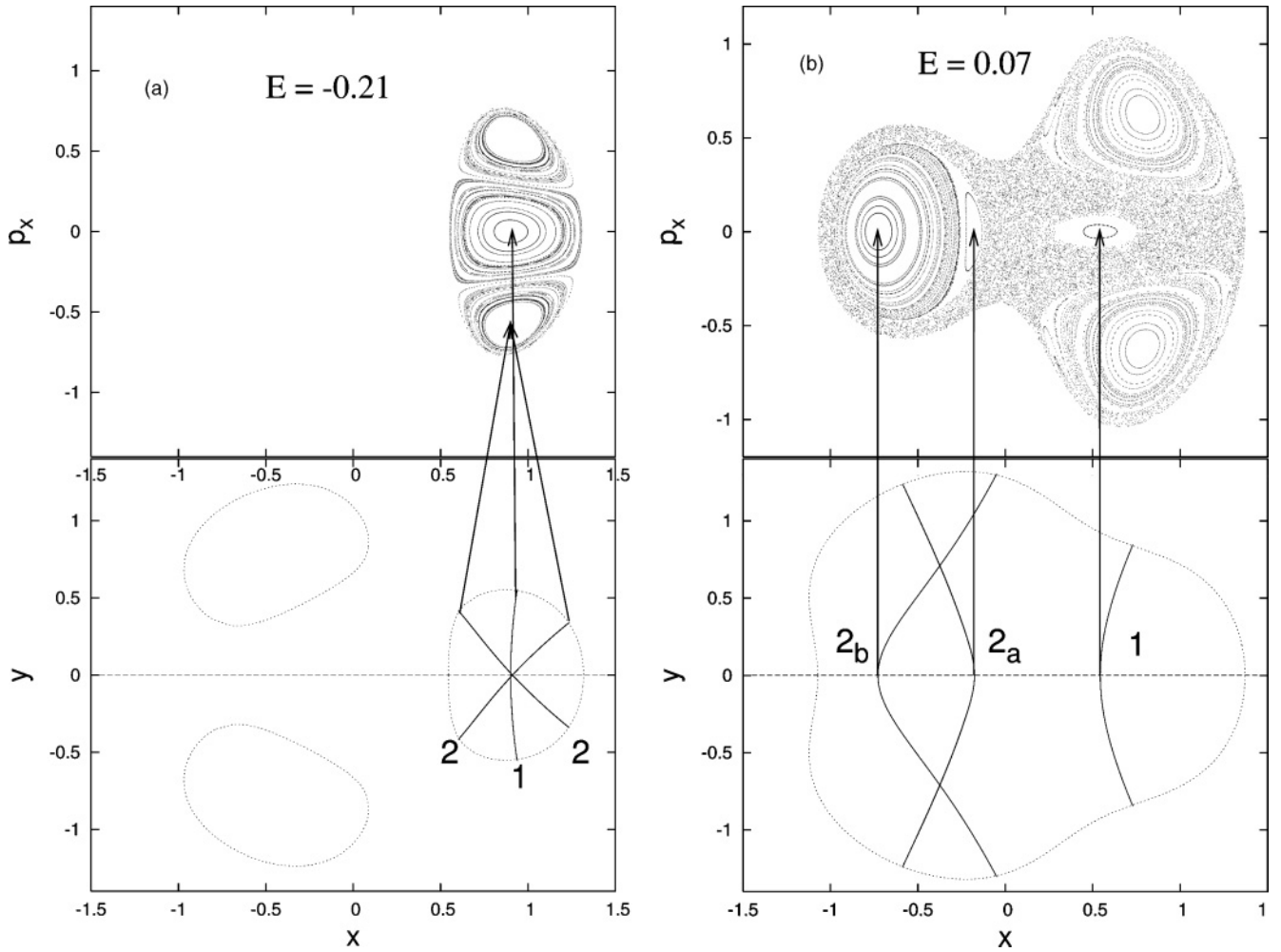

FIG. 11. Poincaré sections and the central periodic orbits corresponding to the principal regular islands in the vicinity of the AW arc. In both panels $\eta = 0.5$. Panel (a) corresponds to $E_{\rm cl} = E_4 < E_{\rm sad}$, $\chi = \chi_2$, panel (b) to $E_{\rm cl} = E_7 > 0$, $\chi = \chi_3$ (cf. the respective sections of Fig. 10). The dashed lines at $y = 0$ demarcate the plane of section and the arrows show the position of individual orbits in the Poincaré sections.

we describe features of motions characteristic for the three regions with respect to the regular arc.

$|\chi| > |\chi_{\rm reg}|$ ($k = 2$ column of Fig. 10): The low-energy behavior below $E_{\rm sad}$ ($E_1, \ldots, E_4$) is completely regular, dominated by γ and $\beta\gamma$ vibrations (types 1 and 2). The Poincaré section at E_5 reflects merging of the hitherto separate accessible regions. The rims of the regular islands get chaotic around E_6, E_7. Increasing the energy further, chaos prevails destroying the regular family around the type 1 and only tiny regular areas roughly in the previous position of the three regular islands of type 2 are left. At the highest energies, around E_{10}, the regular islands of the type-2 vibrations spread significantly, increasing $f_{\rm reg}$ to ≈ 0.5.

$\chi = \chi_{\rm reg}$ ($k = 3$ column of Fig. 10): The single island of type-1 γ-vibrations present at the lowest energies (E_1) splits in its center into two smaller islands corresponding to vibrations of type 2 (see panels $E_2, \ldots, E_5$). Unlike in the previous case, the γ-vibration now constitutes a *hyperbolic* fixed point [19]. Interestingly, it becomes elliptic again around $E_{\rm cl} \approx 0$ [(see regular islands around $x > 0$, $p_x = 0$ in panels E_6 and E_7 of Fig. 10 and panel (b) of Fig. 11] and subsequently "disappears" in a sea of chaos at E_8. Another distinctive fact is a *crossover* of the $2_{\rm a}$ and $2_{\rm b}$ types of $\beta\gamma$-vibrations slightly above $E_{\rm cl} = 0$ (see E_7): one of the outermost tori of mixed vibrations (with central orbit of type $2_{\rm b}$) disintegrates to produce a new island of regular trajectories (type $2_{\rm a}$), which with increasing energy "expels" the original island of type $2_{\rm b}$ orbits toward the boundary of the accessible region. At E_9 and E_{10}, a new family or regular orbits appears: these circle around the whole accessible region giving rise to two new islands. It is worth noting that the regular islands corresponding to $\beta\gamma$-vibrations (types 2 or $2_{\rm a}$, $2_{\rm b}$) exist in the whole energy range between E_2 and E_{10} and that the low-energy form of these trajectories (type 2) reminds strongly the trajectories of the SU(3) limit.

$|\chi| < |\chi_{\rm reg}|$ ($k = 4$ column of Fig. 10): The process starts in a similar way as for $\chi = \chi_{\rm reg}$, with the γ-vibration becoming hyperbolic around E_3, but the enveloping "circles" disintegrate into complicated Poincaré-Birkhoff chains of alternating elliptic and hyperbolic fixed points [19] which usher in strong chaos resident at higher energies, $E_4, \ldots, E_7$.

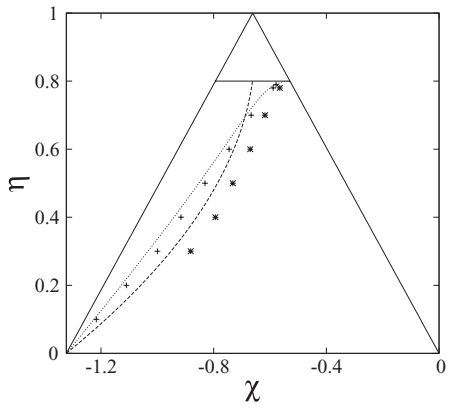

FIG. 12. The AW arc [Eq. (6), the dashed curve] and the locus of degeneracy of β and γ bandheads [Sec. VI, the dotted curve] inside the Casten triangle. The points mark the change of stability of γ-vibrations (orbits of type 1 in Fig. 11) at $E_{\rm cl} = -|V_{\rm min}|/2$ (crosses) and at $E_{\rm cl} = 0$ (asterisks), see Subsec. V B. Numerical errorbars are smaller than the pointsize.

At the highest energies the regularity rises again; the Poincaré section at E_{10} yields $f_{\rm reg} \approx 0.8$.

The scenarios described above hold for the whole region $\eta < 0.6$. As already pointed out in Refs. [10,11], the vicinity of AW arc can be recognized as a place where the γ-vibrations (type-1 orbits) change their character from elliptic ($|\chi| > |\chi_{\rm reg}|$) to hyperbolic ($|\chi| < |\chi_{\rm reg}|$) fixed points. Note that at *low energies* ($E_{\rm cl} < 0$), the change of stability of the central γ-vibration is always accompanied by stability changes of the outermost enveloping "circles" in Poincaré sections, which in turn represent almost pure β-vibrations (for our choice of the phase space section, $y = 0$, these do not represent fixed points). The stability properties of β-vibrations are opposite to those of γ-vibrations: they are stable in the region where γ-vibrations are unstable and vice versa. This happens very close to $\chi_{\rm reg}$ on the SU(3)-U(5) side of the triangle. On the other hand, at *higher energies* ($E_{\rm cl} \approx 0$), the γ-vibrations change stability on the other side of $\chi_{\rm reg}$. This may be seen in Fig. 12, where the stability changes at $E_{\rm cl} = -|V_{\rm min}|/2$ and at $E_{\rm cl} = 0$ are marked by crosses and asterisks, respectively.

When approaching the phase transition, for $0.6 < \eta < 0.8$, the loci of $E_{\rm cl} < 0$ and $E_{\rm cl} \approx 0$ stability changes discussed above deviate from the curve $\chi_{\rm reg}(\eta)$ from Eq. (6). In fact, the linear fit of the regular arc becomes inaccurate in this region and changes in classical dynamics follow rather the curve $\chi_{\rm deg}(\eta)$ of the β- and γ-bandhead degeneracy (dot-dashed curve in the Fig. 12), which will be discussed further in Sec. VI.

As a final remark we point out that crossing of the SU(3)-U(5) edge of the Casten triangle, in contrast to crossing of the AW arc, does not bring about any significant change in dynamics.

C. Periodic orbits

In this subsection, we will discuss a possible relation of stability changes in classical dynamics (as described in Sec. V B) to the $E \approx 0$ bunching pattern in quantum spectra (Sec. IV). In particular, we focus on the crossover between the two types of $\beta\gamma$-vibrations (orbits $2_{\rm a}$ and $2_{\rm b}$ in Fig. 11) and on the temporal resurrection of γ-vibrations (orbit 1 therein), both these phenomena taking place in the relevant energy and parameter domains (cf. panels E_6 and E_7 of Fig. 10).

The influence of classical dynamics on quantized energy spectra is described in the framework of semiclassical periodic orbit theory [19–21]. The oscillating part $\rho_{\rm osc}(E)$ of the quantum level density can be be expressed via so-called trace formulas, which depend on properties of classical periodic trajectories and have the following generic form:

$$\rho_{\rm osc}(E) = \frac{1}{\pi\hbar} \sum_p \sum_{r=1}^{\infty} \frac{r T_p}{A_p} \cos\left[\frac{r S_p(E)}{\hbar} - r\mu_p \frac{\pi}{2}\right]. \quad (12)$$

The sum is running over all primitive orbits p with period T_p together with their multiple retracings $r = 1, 2, 3, \ldots$. The argument of the cosine is determined by the action

$$S_p(E) = \oint \vec{p} \cdot d\vec{q} = \int_0^{T_p} \vec{p} \cdot \dot{\vec{q}} dt \quad (13)$$

along the primitive orbit and the number of caustics μ_p (Maslow index) encountered there. Inverse amplitude A_p reflects the stability properties of the orbit and depends on the nature of dynamics. The explicit form of A_p is known only for completely regular or chaotic systems, respectively, given by the Berry-Tabor formula for contributions of tori [40] and Gutzwiller formula for contributions of isolated orbits [41].

The level bunching described in Sec. IV constitutes a significant fluctuation in level density. We may therefore expect that it is connected, through Eq. (12), with changes in properties of classical periodic orbits. In Sec. V B, the increased regularity of $l = 0$ motions in the AW arc was shown to be basically due to regular trajectories surrounding the vibrations of types 1 and 2 (see Fig. 11). Although we are not able to perform the semiclassical calculation of the level density for a mixed regular/chaotic system such as the IBM (the formula is not known), we will show that stability intervals of the above types of motions and crossover energies are strongly correlated with the bunching pattern.

For this purpose, we calculated actions (13) of orbits from Fig. 11 using a numerical approximation $S_p = \sum(p_x \Delta x + p_y \Delta y)$ in variables (5), where the sum runs over all calculated points until the orbit closes. The energy dependences of $\cos S_p$ for the three types of orbits are presented in Fig. 13 for $\chi = \chi_{\rm reg}$ and $\eta = 0.35$ (panel a), $\eta = 0.5$ (panel b), and $\eta = 0.65$ (panel c). Individual curves end at the values of energy, where the respective trajectories turn unstable and the surrounding regular islands disappear. The classical energy $E_{\rm cl}$ from Hamiltonian (2) is related to quantum energy E scaled by $a = N/10$ via $E = 4E_{\rm cl}$ (for $N = 40$, see Figs. 6 and 9). The energy interval where the bunching of quantum spectrum resides for the given value of η is demarcated by the shaded area in the respective panel of Fig. 13.

As we observe, the upper edge of the energy gap demarcating the bunching pattern coincides almost precisely with the endpoint of $2_{\rm b}$ orbits, while the crossover energy of $2_{\rm a}$ and $2_{\rm b}$ orbits takes place within the gap. This is so for all selected values of η (panels a–c of Fig. 13). It also turns out that both orbits $2_{\rm a}$ and $2_{\rm b}$ match their periods just above the crossover

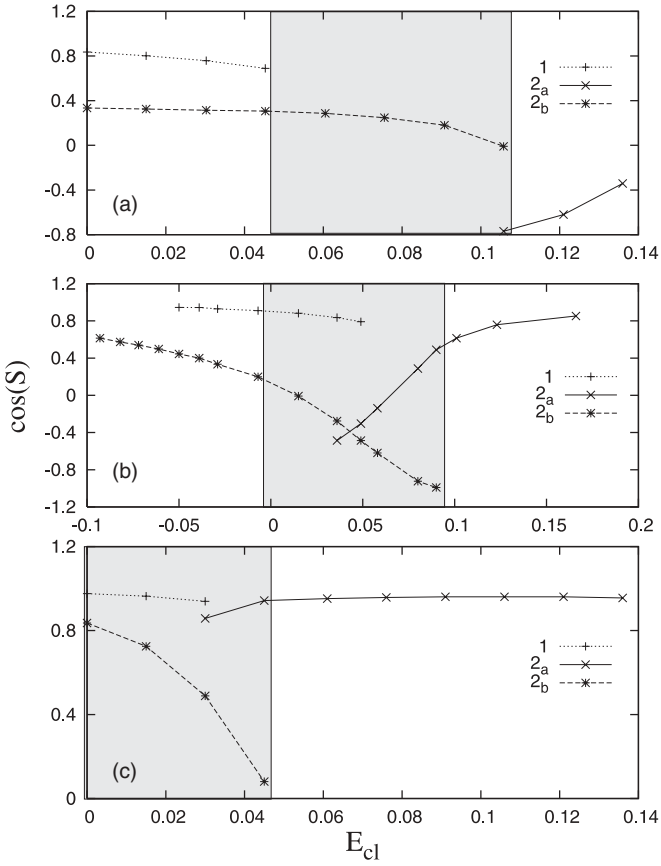

FIG. 13. Oscillating contributions to the state density calculated for the central periodic orbits from Fig. 11 at $\chi = \chi_{\rm reg}$ and $\eta = 0.35$ (a), 0.5 (b), 0.65 (c). Maslow index $\mu_p = 4$ for all orbits makes no change of the cosine. Grey zones indicate the regions corresponding to the bunching of quantum levels. (Energy unit is arbitrary.)

energy, within the shaded area. The stability changes of type-1 orbits are also correlated with the bunching, although in this case the energy match does not behave in a systematic way.

These findings provide a strong support to the hypothesis that the quantum bunching pattern discussed in Sec. IV is closely connected with the stability changes of the above orbits, in particular with the crossover between $2_{\rm a}$ and $2_{\rm b}$ vibrations. Whether this is just an interplay of accidents or a deeper effect resulting from internal symmetries of the system remains an open question.

VI. β AND γ BANDHEAD DEGENERACY

In attempts to fit nuclear spectra with the simplified Hamiltonian (1), an approximate degeneracy of 0_2^+ and 2_2^+ states (belonging to so-called β and γ bands, respectively) was found to be a useful tool for identification of nuclei close to the AW arc [27]. Here we estimate the locus of the 0_2^+-2_2^+ degeneracy region in the Casten triangle analytically, by means of the intrinsic-state formalism [42]. It will turn out that the curve $\chi_{\rm deg}(\eta)$ expressing the locus lies indeed very close to the AW arc $\chi_{\rm reg}(\eta)$.

In the intrinsic-state formalism, the unprojected wave functions for the ground-state band, β-band, and γ-band are up to a combinatorial factor given by

$$|K=0,\mathrm{gs}\rangle \propto \Gamma_0^{\dagger N}|0\rangle\,, \quad |K=0,\beta\rangle \propto \Gamma_\beta^\dagger \Gamma_0^{\dagger N-1}|0\rangle, \quad |K=2,\gamma\rangle \propto \Gamma_\gamma^\dagger\, \Gamma_0^{\dagger N-1}|0\rangle \tag{14}$$

with

$$\Gamma_0^\dagger = \frac{1}{\sqrt{1+\beta^2}}[s^\dagger + \beta d_0^\dagger], \quad \Gamma_\beta^\dagger = \frac{1}{\sqrt{1+\beta^2}}[-\beta s^\dagger + d_0^\dagger] \tag{15}$$

$$\Gamma_\gamma^\dagger = \frac{1}{\sqrt{2}}[d_2^\dagger + d_{-2}^\dagger].$$

The deformation parameter β is determined by minimizing the ground state energy

$$E_{\rm g.s.} = \langle K=0,\,\mathrm{g.s.}|H|K=0,\,\mathrm{g.s.}\rangle \tag{16}$$

while the excitation energies of the β and γ bandheads consequently follow from

$$E_\beta^* = \langle K=0,\beta|H|K=0,\beta\rangle - E_{\rm g.s.}, \tag{17}$$

$$E_\gamma^* = \langle K=2,\gamma|H|K=2,\gamma\rangle - E_{\rm g.s.}. \tag{18}$$

The minimization of the ground-state energy (16) and equality of expressions (17) and (18) lead—after taking the $N\to\infty$ limit—to two simultaneous equations in η, χ, and β. Elimination of β gives the dependence $\chi_{\rm deg}(\eta)$, which is shown in Fig. 12 together with the linear fit $\chi_{\rm reg}(\eta)$ of the AW arc, Eq. (6).

We see in Fig. 12 that both curves $\chi_{\rm deg}(\eta)$ and $\chi_{\rm reg}(\eta)$ are relatively close to each other for $\eta < 0.7$. The agreement even slightly improves if we compare $\chi_{\rm deg}(\eta)$ directly with the points in Fig. 13 of Ref. [9] without the fit (6). As η approaches 0.8 both curves diverge. Indeed, since at $\eta = \eta_{\rm c} \approx 0.8$ the spherical configuration of the ground state is reached, the notion of β and γ bands looses its sense. Note, however, that the whole spherical region with $\eta > \eta_{\rm c}$ behaves rather regularly and the concept of the semiregular arc is not well defined here. Notably, both loci of classical-orbit changes discussed in Sec. V apparently follow the $\chi_{\rm deg}(\eta)$ curve instead of $\chi_{\rm reg}(\eta)$.

Note that the present procedure equating the bandhead energies of the β and γ vibrational bands differs somewhat from that of Ref. [27] where energies of the 0_2^+ and 2_2^+ states are compared. Namely, the rotational energy shifts up the position of the 2_2^+ state from the γ bandhead energy. For the near rotor nuclei discussed in Ref. [27] this does not make a substantial difference as the rotational energy is small as compared to the excitation energy of the γ bandhead. In some cases inspected in Ref. [27], the 2_2^+ state even belongs to the β-band, then however γ-band is still close to the β-band. For the near vibrator nuclei, the comparison is less straightforward. Here, however, the comment of the previous paragraph applies.

A rotational $L\cdot L$ term can remove the degeneracy of states of different spins but does not change eigenfunctions and the extent of regularity. Then a link of the regular region to the 2_2^+-0_2^+ degeneracy may somewhat be hidden. On the other hand, the $L\cdot L$ term shifts also the relative position of the β and γ bands. This shift is, however, of the order of $1/N$ as compared to the effect of all other two-body terms of the

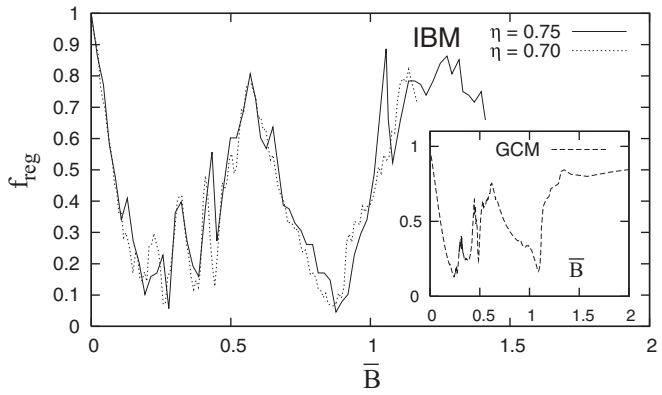

FIG. 14. Regularity $f_{\rm reg}^{(S)}$ at $E_{\rm cl} = 0$ as a function of $\bar{B} = B/\sqrt{|AC|}$ and $\bar{B}(\eta, \chi)$ in the GCM and IBM, respectively, determined by the SALI method.

general IBM Hamiltonian. Of course, the latter deficiency of the $L \cdot L$ term could be balanced by coefficient $\sim N$ of that term. Then the unprojected version of the intrinsic-state formalism ceases to be valid and the angular momentum projection should be considered [43].

VII. RELATION TO GEOMETRIC MODEL

Recent analyses [28–30] of the classical GCM displayed an unexpectedly complicated dependence of chaoticity on the control parameters and energy. It is certainly interesting to find out whether at least some of the distinctive features of GCM phase space can be "mapped" onto the more realistic IBM. We are going to set focus on the energy $E_{\rm cl} \approx 0$, connected with the most dramatic changes of regularity in the GCM as well as in the IBM case.

We start with an expansion of the square root in the IBM Hamiltonian (2), which up to first order in $(\beta^2 + T)/2$ gives

$$\begin{aligned} H'_{\rm cl} = {} & \frac{1}{2K'}T + A'\beta^2 + B'\beta^3\cos 3\gamma + C'\beta^4 \\ & + \frac{B'}{4}\left(2p_\beta p_\gamma + p_\gamma^2/\beta - \beta p_\beta^2\right)(\beta^2 + T - 4)\sin 3\gamma \\ & - \frac{B'}{4}(\beta^3 T\cos 3\gamma + \beta^5) + D'\beta^2 T + E'\left(\frac{1}{2}p_\gamma^2 - \frac{1}{8}T^2\right) \\ \equiv {} & H'_{\rm GCM} + H'_{\rm res}. \end{aligned} \tag{19}$$

We may immediately identify the GCM-like Hamiltonian (3) in the first line. The residual terms $H'_{\rm res}$ in the next two lines contain a correction $\propto \beta^5$ in the potential and a collection of rather complicated kinetic terms. The coefficients $A', \ldots, E'$ are functions of η, χ: A', B', C' being equal to respective factors in Eq. (4), while $K' = 1/\eta$, $D' = (1-\eta)(1-\chi^2/7)$, $E' = 4\chi^2(1-\eta)/7$. The expansion (19) is justified only for small amplitude vibrations around an equilibrium deformation satisfying $\beta_0^2 \ll 1$, which is for $E_{\rm cl} \approx 0$ fulfilled in a region near to the phase transition, $\eta \in [0.7, 0.8]$. It needs to be stressed that even in this region $H'_{\rm res}$ contains kinetic terms of the same order as T. One therefore cannot expect a perfect match with the GCM results. Nevertheless, as shown below, the similarity is appreciable.

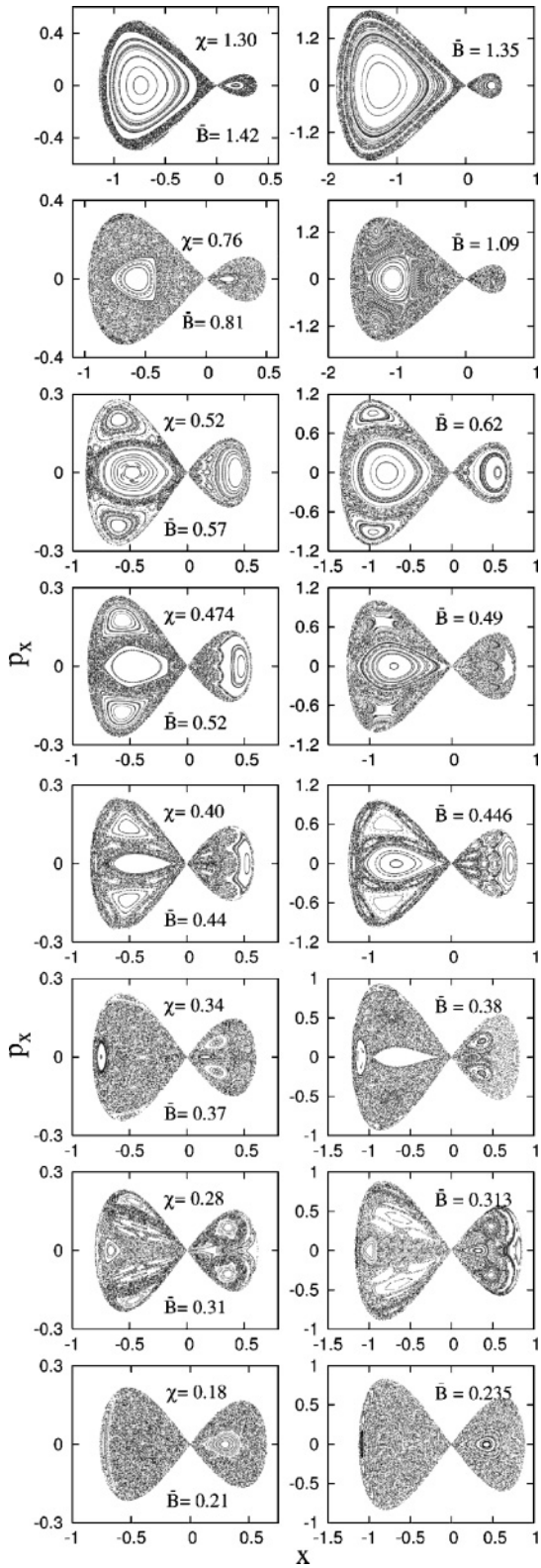

FIG. 15. Comparison of $E_{\rm cl} = 0$ Poincaré sections $y = 0$ in the IBM at $\eta = 0.75$ (lefthand column) and GCM (righthand column) at the most pronounced minima and maxima of $f_{\rm reg}(\bar{B})$ from Fig. 14.

To obtain a mapping between IBM and GCM parameters, we use scaling properties of the classical GCM Hamiltonian, see Ref. [30]. In this way, $H'_{\rm GCM}$ is transformed so that only the coefficient $\bar{B}$ in front of the term $\propto \beta^3$ remains variable while $\bar{A} = -\bar{C} = -1$ are fixed. The expression for the rescaled control parameter then reads $\bar{B}(\eta, \chi) = B'/\sqrt{|A'C'|}$. This provides the desired correspondence $(\eta, \chi) \leftrightarrow \bar{B}$ for small-amplitude vibrations (wrong scaling of the noninvariant part $H'_{\rm res}$ may then be neglected).

In Sec. III we saw that in the "middle" of the Casten triangle ($\eta = 0.5$, cf. Fig. 3) the zero-energy dependence of $f_{\rm reg}$ on χ in the IBM has the only well pronounced peak at the AW arc, quite in contrast with the corresponding fine structured $f_{\rm reg}(\bar{B})$ dependence in GCM [28] at $E_{\rm cl} = 0$ (see the inset of Fig. 14). However, as we approach the deformed-to-spherical phase transition, some significant peaks of regularity develop in the region between $\chi = 0$ and the AW arc. As the validity of approximation (19) improves in this part of the Casten triangle, the $f_{\rm reg}$ dependences start to resemble that of the GCM, see Fig. 14.

The similarity is evident also from the Poincaré sections shown in Fig. 15, where the lefthand and righthand columns correspond to the IBM and GCM, respectively. The adjacent pairs of sections belonging to the most pronounced maxima and minima of $f_{\rm reg}$ in the GCM and IBM at $\eta = 0.75$ are visually almost identical (here we use $\chi > 0$ to be consistent with the choice $B > 0$ of Refs. [28,30]). The differences must be attributed to the residual part $H'_{\rm res}$ of Hamiltonian (19), which is not obviously small.

We can conclude that the GCM peak of regularity at $\bar{B} \approx 0.6$ is closely related to the AW arc in the region $\eta \in [0.7, 0.8]$. Note, however, that the most regular IBM Poincaré section, observed at $|\chi| = 0.52$ (associated with the GCM section at $\bar{B} = 0.62$), is already deviated from the linear fit (6) of the AW arc, which predicts $|\chi_{\rm reg}| = 0.71$ for $\eta = 0.75$. This is in agreement with results of Secs. V B and VI (see Fig. 12).

VIII. SUMMARY AND OUTLOOK

In this paper, we studied quantum and classical effects associated with a partial increase of regularity in nuclear collective dynamics away from integrable regimes. This increase seems to be a common feature of both the interacting boson model and the geometric model, but so far lacks unambiguous theoretical evidence. Below we list our most important findings together with the questions they induce:

(i) The increase of regularity, localized mainly in the absolute-energy region around $E \approx 0$, coincides with the "macroscopic" bunching of the IBM quantum states, most clearly observed in the 0^+ spectrum. This bunching is visually similar to that observed in the O(6)-U(5) transition (see Fig. 9 and Ref. [17]), but cannot have the same origin (monodromy [18,38]) as there is no local potential maximum with the corresponding energy. More sophisticated concepts, like generalized forms of monodromy [44] or Hamiltonian fixed points [45] may turn relevant in future studies. Since the O(6)-U(5) bunching was recently related to excited-state quantum phase transitions [38], the question rises whether the present bunching induces analogous effects in the SU(3)-U(5) case.

(ii) At the classical level, the bunching pattern seems to be related to changes in stability of some specific orbits. In particular, we disclosed the crossover between orbits of types $2_{\rm a}$ and $2_{\rm b}$ from Fig. 11 and equalizing of their periods taking place in the relevant energy and parameter domains, see Fig. 13.

(iii) Proximity of the AW arc to the locus of 0_2^+-2_2^+ degeneracy, previously noticed in Ref. [27], was related to the the degeneracy of β and γ bandheads. It remains unclear whether it is accidental or systematic. The exchange of stability of low-energy γ-vibrations [type-1 orbits from Fig. 11(a)] and β-vibrations was found to be correlated with the locus of degeneracy (see Fig. 12). It is known that no ground-state phase transition occurs in between γ-soft and γ-rigid sides of the Casten triangle, but the present observations suggest that a kind of sharp change of low-energy collective modes appears very close to the AW arc.

(iv) The relation of the AW arc to the increase of regularity observed at $E_{\rm cl} \approx 0$ in the geometric model [28] was demonstrated in the region $\eta \in [0.7, 0.8]$, i.e., close to the deformed-to-spherical transition. Even in this region, however, the IBM corrections to the GCM kinetic energy cannot be fully neglected and lead to some rescaling of the fine structure of $f_{\rm reg}$ in parameter $\bar{B}$ (see Fig. 14).

Note that findings summarized under (iii) and (iv) indicate that the semiregular arc is in fact well defined only on the deformed side of the Casten triangle [a kind of partial SU(3) dynamical symmetry being a potential explanation] and that close to the phase transition it deviates significantly from the linear fit (6).

We hope that results presented in this paper will help to eventually disclose microscopic origins of regularity in nuclear collective dynamics. This is an important fundamental task in itself, but in view of the recent revival of interest in statistical analyses of nuclear 0^+ spectra [46] it may also turn relevant from the experimentalists' viewpoint.

ACKNOWLEDGMENTS

M.M., P.S., and P.C. wish to thank F. Iachello for stimulating discussions and A. Frank and J. Barea for drawing the attention to the SALI method. ECT* in Trento and IKP in Cologne are acknowledged for hospitality and support. This work was funded by the Grant Agency of the Czech Republic (Project 202/06/0363), Czech Ministry of Education (Projects MSM 0021620834 and LA 080), and by German Research Foundation (Project TSE 17/1/06).

[1] F. Iachello and A. Arima, *The Interacting Boson Model* (Cambridge University Press, Cambridge, UK, 1987).
[2] A. E. L. Dieperink, O. Scholten, and F. Iachello, Phys. Rev. Lett. **44**, 1747 (1980); D. H. Feng, R. Gilmore, and S. R. Deans, Phys. Rev. C **23**, 1254 (1981).
[3] E. López-Moreno and O. Castaños, Phys. Rev. C **54**, 2374 (1996); R. F. Casten, D. Kusnezov, and N. V. Zamfir, Phys. Rev. Lett. **82**, 5000 (1999).
[4] P. Cejnar and J. Jolie, Phys. Rev. E **61**, 6237 (2000).
[5] Y. Alhassid, A. Novoselsky, and N. Whelan, Phys. Rev. Lett. **65**, 2971 (1990).
[6] Y. Alhassid and N. Whelan, Phys. Rev. C **43**, 2637 (1991).
[7] Y. Alhassid and A. Novoselsky, Phys. Rev. C **45**, 1677 (1992).
[8] Y. Alhassid and N. Whelan, Phys. Rev. Lett. **67**, 816 (1991).
[9] N. Whelan and Y. Alhassid, Nucl. Phys. **A556**, 42 (1993).
[10] N. Whelan, Ph.D. thesis, Yale University (1993).
[11] Y. Alhassid, in *Perspectives for the Interacting Boson Model*, edited by R. F. Casten *et al*. (World Scientific, Singapore, 1994), p. 591.
[12] Y. Alhassid and D. Vretenar, Phys. Rev. C **46**, 1334 (1992).
[13] V. Paar and D. Vorkapić, Phys. Lett. **B205**, 7 (1988); Phys. Rev. C **41**, 2397 (1990).
[14] V. Paar, D. Vorkapić, and A. E. L. Dieperink, Phys. Rev. Lett. **69**, 2184 (1992).
[15] T. Mizusaki, N. Yoshinaga, T. Shigehara, and T. Cheon, Phys. Lett. **B269**, 6 (1991).
[16] E. Canetta and G. Maino, Phys. Lett. **B483**, 55 (2000).
[17] S. Heinze, P. Cejnar, J. Jolie, and M. Macek, Phys. Rev. C **73**, 014306 (2006).
[18] M. Macek, P. Cejnar, J. Jolie, and S. Heinze, Phys. Rev. C **73**, 014307 (2006).
[19] M. C. Gutzwiller, *Chaos in Classical and Quantum Mechanics* (Springer, New York, 1990).
[20] H.-J. Stöckmann, *Quantum Chaos. An Introduction* (Cambridge Universty Press, Cambridge, UK, 1999).
[21] F. Haake, *Quantum Signatures of Chaos* (Springer, Berlin, 1991).
[22] P. Van Isacker, A. Frank, and J. Dukelsky, Phys. Rev. C **31**, 671 (1985); D. Kusnezov, Phys. Rev. Lett. **79**, 537 (1997); A. M. Shirokov, N. A. Smirnova, and Yu. F. Smirnov, Phys. Lett. **B434**, 237 (1998).
[23] W. M. Zhang and D. H. Feng, Phys. Rep. **252**, 1 (1995).
[24] A. Leviatan, A. Novoselsky, and I. Talmi, Phys. Lett. **B172**, 144 (1986).
[25] Y. Alhassid and A. Leviatan, J. Phys. A: Math. Gen. **25**, L1265 (1992).
[26] P. Cejnar and J. Jolie, Phys. Lett. **B420**, 241 (1998); Phys. Rev. E **58**, 387 (1998).
[27] J. Jolie, R. F. Casten, P. Cejnar, S. Heinze, E. A. McCutchan, and N. V. Zamfir, Phys. Rev. Lett. **93**, 132501 (2004).
[28] P. Cejnar and P. Stránský, Phys. Rev. Lett. **93**, 102502 (2004).
[29] P. Cejnar, M. Macek, P. Stránský, and M. Kurian, in *Capture Gamma-Ray Spectroscopy and Related Topics*, edited by A. Woehr and A. Aprahamian, AIP Conf. Proc. No. 819 (AIP, Melville, NY, 2006), p. 487.
[30] P. Stránský, M. Kurian, and P. Cejnar, Phys. Rev. C **74**, 014306 (2006).
[31] Ch. Skokos, J. Phys. A: Math. Gen. **34**, 10029 (2001); Ch. Skokos, Ch. Antonopoulos, T. C. Bountis, and M. V. Vrahatis, *ibid*. **37**, 6269 (2004).
[32] J. Jolie, R. F. Casten, P. von Brentano, and V. Werner, Phys. Rev. Lett. **87**, 162501 (2001).
[33] R. L. Hatch and S. Levit, Phys. Rev. C **25**, 614 (1982).
[34] A. Bohr and B. R. Mottelson, *Nuclear Structure*, Vol. II (Benjamin, Reading, MA, 1975).
[35] T. A. Brody, Lett. Nuovo Cimento **7**, 482 (1973).
[36] T. Guhr, J. Z. Ma, S. Meyer, and T. Wilke, Phys. Rev. D **59**, 054501 (1999).
[37] J. Jolie and S. Heinze, in [29], p. 331; M. Macek and P. Cejnar, *ibid*., p. 570.
[38] P. Cejnar, M. Macek, S. Heinze, J. Jolie, and J. Dobeš, J. Phys. A: Math. Gen. **39**, L515 (2006).
[39] http://www-ucjf.troja.mff.cuni.cz/∼geometric.
[40] M. V. Berry and M. Tabor, Proc. R. Soc. Lond. A **349**, 101 (1976).
[41] M. C. Gutzwiller, J. Math. Phys. **12**, 34 (1971).
[42] A. Leviatan, Ann. Phys. (NY) **179**, 201 (1987).
[43] J. Dobeš, Phys. Rev. C **42**, 2023 (1990).
[44] D. A. Sadovskii and B. I. Zhilinskii, Mol. Phys. **104**, 2595 (2006).
[45] P. Leboeuf and M. Saraceno, Phys. Rev. A **41**, 4614 (1990).
[46] D. Bucurescu *et al*., Phys. Rev. C **73**, 064309 (2006); D. Bucurescu *et al*. (unpublished).

A.4 Peres lattices in nuclear structure
[*Int. J. Mod. Phys. E*, **18,** 1058 (2009)] [**P5***]

This short article applies the visual lattice method of distinguishing between quantum integrable and quantum chaotic systems originally introduced by Peres, see Ref. [Pere84a], to study the mixed regular/chaotic dynamics of the interacting boson model. The method may be considered as a quantum analog of the Poincaré section method in classical mechanics. Here, it is used for the first time in the IBM, following its previous application in the geometric collective model [Stra09b].

IBM provides an especially good environment to test the Peres' proposal, which states that if a quantum system is integrable, the lattices corresponding to practically arbitrary operators (even those non-commuting with the Hamiltonian) should display visually regular patterns [Pere84a]. The Casimir operators connected to mutually incompatible dynamical symmetries of the IBM may be easily taken as the Peres operators and their lattices be evaluated in some of the integrable domains within the parametric space of IBM. We select here in particular the U(5) limit and plot the lattices corresponding to the operators related to the incompatible O(6) and SU(3) symmetries and indeed confirm the intuitively rather surprising statement about the regularity of all lattices.

We also investigate the mixed regular/chaotic interior of the Casten triangle plotting the Peres lattices corresponding to various incompatible quantities in several points inside the triangle. The results allow to observe an interesting combination of regular and chaotic regions within the lattices and in particular enable to select "regular states", which belong to regular sublattices within the lattices corresponding to each individual quantity. The quantum regularity, as revealed by the lattices, is found to correspond very well to the classical regularity determined by the relative volume of the regular phase space, cf. the preceding paper, Ref. [**J5***].

The author of this thesis initiated the simultaneous study of different Peres lattices and performed the classical as well as quantum numerical calculations necessary to plot the figures 1 and 2.

International Journal of Modern Physics E

PERES LATTICES IN NUCLEAR STRUCTURE

Michal Macek, Pavel Stránský, Pavel Cejnar
Faculty of Mathematics and Physics, Charles University, V Holešovičkách 2, 180 00 Prague, Czech Republic

Received (received date)
Revised (revised date)

A method by Peres is used to represent spectra of the interacting boson model as lattices in the plane of energy versus an arbitrary observable average (or variance). Ordered (disordered) lattices are signatures of regularity (chaos) in both quantum and classical dynamics. The method is also apt to disclose exact or approximate dynamical symmetry.

We use a method by Asher Peres[1] to study order and chaos within the spectra of collective nuclear models. The method allows to distinguish order/chaos in a quantum system by visual inspection, which is in a way similar to the well-known Poincaré section method used in classical mechanics. In contrast to the conventional approaches to study of quantum chaotic systems based mostly on statistical properties of energy eigenvalues found in a certain interval, the lattice method enables one to assign regular or chaotic type of dynamics to *individual* states.

Within every quantum-mechanical model, we can construct trivial integrals of motion—we call them Peres invariants $\hat{P}(\hat{O})$—by taking the time average of an arbitrary "well-behaved" operator $\hat{O}$:

$$\hat{P}(\hat{O}) = \lim_{T\to\infty} \frac{1}{T} \int_0^T \hat{O}(t) dt \,, \tag{1}$$

where $\hat{O}(t)$ is the Heisenberg image of $\hat{O}$. By plotting the expectation values $P_i(\hat{O}) = \langle\psi_i|\hat{P}(\hat{O})|\psi_i\rangle$ versus the energy $E_i = \langle\psi_i|\hat{H}|\psi_i\rangle$ for an arbitrary set of states $|\psi_i\rangle$, we obtain what we call Peres lattices. If $|\psi_i\rangle$ are eigenstates of the Hamiltonian $\hat{H}$, the expression $\langle\psi_i|\hat{P}(\hat{O})|\psi_i\rangle$ can be simply replaced by $\langle\psi_i|\hat{O}|\psi_i\rangle$.

A regular lattice of points can be expected, if the system is integrable.[1] The supporting arguments are based on semiclassical Einstein-Brillouin-Keller (EBK) quantisation: For a classically integrable system in d dimensions, the phase space trajectories are bound to d-dimensional tori. A complete set of motion integrals can be formed by the action variables $J_k = \oint_{C_k} p_i dx^i$, where $i, k = 1, .., d$ and C_k are topologically non-equivalent curves on the torus surfaces. From the EBK quantisation we obtain $J_k = \hbar n_k + a_k$, where a_k are constants and $n_k = 0, 1, 2, ..$integers. Any other integral of motion—including energy E and the Peres invariant $\hat{P}(\hat{O})$—can

be expressed as a smooth function of J_k. The lattice of $P(\hat{O})$ versus E is therefore a smooth transform of the regular lattice J_k versus E and should in most cases be visually regular.

Adding a perturbation to an integrable system brings about formation of irregular patterns in the Peres lattices. For weak perturbations, the regular lattice usually does not break down "uniformly". On the contrary, chaos develops in localised segments of the lattice, while the rest may remain untouched, as seen from the studies within the geometric collective model and interacting boson model of nuclei.[2,3] The method allows to select the states most affected by the perturbation and is thus appealing for studies of the onset of quantum chaos.

To demonstrate the essence of the method, we consider the interacting boson model (IBM) Hamiltonian[4] in the simple form which incorporates all standard dynamical symmetries of IBM:

$$H = \eta\, \hat{n}_d - (1-\eta)\, N^{-1}\, \hat{Q}^{\chi} \cdot \hat{Q}^{\chi}, \tag{2}$$

with $n_d = d^{\dagger} \cdot \tilde{d}$ the d-boson number operator, $\hat{Q}^{\chi}_{\mu} = d^{\dagger}_{\mu} s + s^{\dagger} \tilde{d}_{\mu} + \chi [d^{\dagger} \tilde{d}]^{(2)}_{\mu}$ the quadrupole operator, N the total number of bosons being conserved and (η, χ) two external parameters defining the Casten triangle. Its vertices $(\eta, \chi) = (1, 0)$, $(0, 0)$, and $(0, -\sqrt{7}/2)$ correspond to the U(5), O(6), and SU(3) dynamical symmetries, respectively.

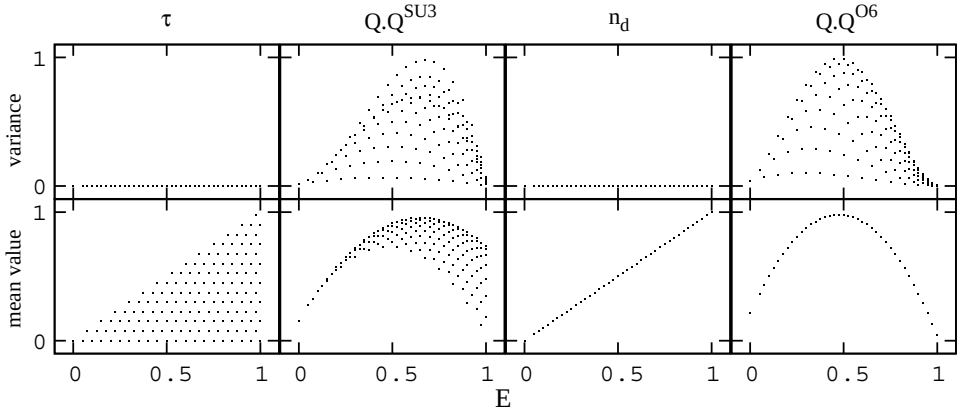

Fig. 1. Peres lattices—the mean values of selected invariants indicated above the corresponding columns—calculated in the integrable U(5) limit of IBM for $L = 0$ states and $N = 40$ bosons are arranged in the bottom-row panels. Notice that all lattices are regular despite non-commutativity of $\hat{Q}{\cdot}\hat{Q}^{\chi}$ with the Hamiltonian $\hat{H}^{U5} = \hat{n}_d$. The corresponding variance lattices (top row) show non-zero values for $\hat{Q}.\hat{Q}^{\rm SU3}$ and $\hat{Q}.\hat{Q}^{\rm O6}$ and zero for the good quantum numbers τ, n_d. All quantities are scaled by their maximum value to fit in the interval $[0, 1]$.

The striking property of the Peres method—the arbitrariness of choice of $\hat{O}$ in Eq. (1)—is demonstrated here in the completely integrable U(5) limit of (2).

In the bottom row of Fig. 1, we plot the Peres lattices related to the Casimir operators of groups O(5), SU(3), U(5) and O(6). Notably, *all* quantities display completely regular lattices despite the fact that only τ (O(5) label) and n_d (U(5) label) are indeed exact quantum numbers. Non-existence of quantum numbers related to $\hat{Q}.\hat{Q}^{\mathrm{SU(3)}}$ and $\hat{Q}.\hat{Q}^{\mathrm{O(6)}}$ is evident from the variance lattices shown above the corresponding Peres invariants—all eigenstates display non-zero value of the variance $\mathrm{var}(\hat{O}) = \langle\hat{O}^2\rangle - \langle\hat{O}\rangle^2$.

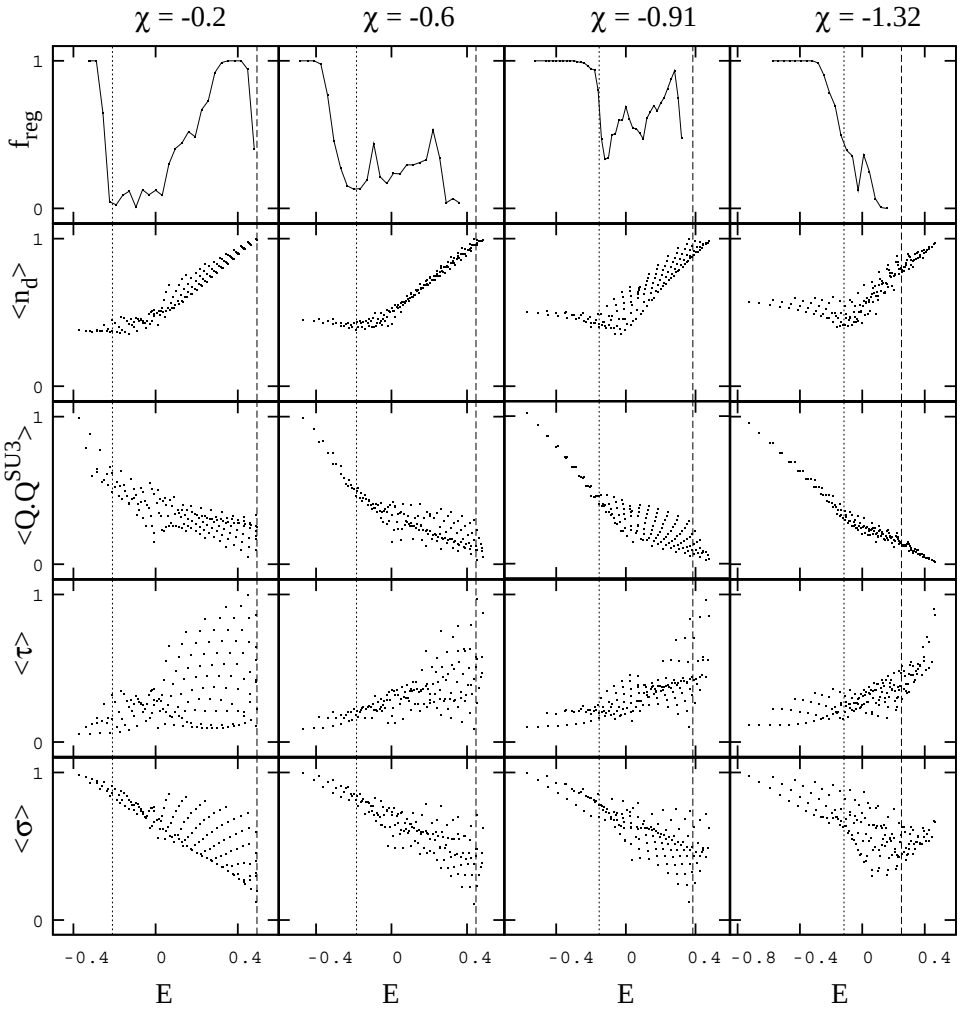

Fig. 2. Peres lattices of $L = 0$ eigenstates of the IBM Hamiltonian (2) for U(5) and SU(3) Casimir invariants and O(6) and O(5) labels σ, τ and the corresponding classical regular fraction f_{reg} calculated inside the Casten triangle for $N = 40$ bosons. The parameter $\eta = 0.5$ and χ is indicated on the top of individual columns. The dotted and dashed lines mark respectively E_{sad} and E_{lim} of the classical IBM potential. Each invariant is scaled to fit in the interval $[0, 1]$.

Having tested the Peres' proposal in one of the integrable cases, we can explore the interior of the Casten triangle, which is known to display mixed regular/chaotic dynamics.[5,6] Figure 2 illustrates the evolution of various Peres invariants—n_d, $\hat{Q}.\hat{Q}^{\mathrm{SU}(3)}$, τ and σ (O(6) label)—for selected values of χ changing across the Casten triangle at $\eta = 0.5$. Panels devoted to a particular invariant are arranged in rows, while the columns correspond to a given value of χ. In the top row, we show the classical regularity expressed by the regular fraction f_{reg} of the phase space (see Ref.[6] for details).

Peaks of f_{reg} correspond to distinct regular areas in the lattices of all the Peres invariants considered. In the energy intervals of mixed dynamics, we may point out states belonging to the regular lattices. A thorough analysis shows that for every Peres invariant the "regular" states form a completely regular lattice if plotted separately without the remaining "chaotic" states. The regular states correspond to resilient classical tori.[3]

As the energy E increases, we observe changes of the form and pattern in the lattices. Major changes in the overall form are noticeably triggered by stationary points of the classical IBM potential (see Ref.[6])—the saddle point energy E_{sad}(dotted vertical lines in Fig. 2), the local maximum at $E = 0$ and the limiting energy for the system to be bound E_{lim}(dashed lines). Probably the most significant overall feature is the "linear" dependence of $\langle \hat{Q}.\hat{Q}^{\mathrm{SU}(3)} \rangle$ on E below E_{sad} roughly in the range of $\chi < -0.8$, which is connected with the quasi SU(3) dynamical symmetry.[3]

The lattice method is applicable for any quantum model, possibly beyond nuclear structure physics. It is in particular well suited to disclose approximate symmetries of the model, like quasi dynamical symmetry[7] and partial dynamical symmetry,[8] especially using the variance lattices. More results concerning the dynamics of both the interacting boson model and the geometric collective model are accessible in an interactive way at our web site[9] and will be described in deeper detail in our prepared publications.[3]

This work was supported by the Czech Science Foundation (202/06/0363) and by the Czech Ministry of Education (MSM 0021620859 and LA 314).

References

1. A. Peres, *Phys. Rev. Lett.* **53**, 1711 (1984).
2. P. Stránský, M. Macek, P. Cejnar, J. Dobeš, in Proc. of *13th International Symposium on Capture Gamma-Ray Spectroscopy*, Cologne, 2008, to be published.
3. P. Stránský *et al.*, submitted to *Phys. Rev.* E; M. Macek *et al.*, in preparation
4. F. Iachello, A. Arima, *The Interacting Boson Model* (Cambridge University Press, Cambridge, UK, 1987).
5. N. Whelan, Y. Alhassid, *Nucl. Phys.* **A556**, (1993) 42.
6. M. Macek, P. Stránský, P. Cejnar, S. Heinze, J. Jolie, J. Dobeš, *Phys. Rev.* C **75** 064318 (2007).
7. D. J. Rowe, P. Rochford, *J. Math. Phys.* **29**, (1988) 3.
8. Y. Alhassid, A. Leviatan, *J. Phys. A: Math. Gen.* **25** (1992) L1265-L1271.
9. `http://www-ucjf.troja.mff.cuni.cz/~geometric/`.

A.5 Transition from gamma-rigid to gamma-soft dynamics in the interacting boson model: Quasicriticality and quasidynamical symmetry [*Phys. Rev. C* **80,** 014319 (2009)] [**J6***]

This article presents a detailed study of the low-energy dynamics in the axially deformed region of the Casten triangle. The numerical results are compared and physically interpreted using the bosonic mean-field (BMF) approximation utilizing extensively the intrinsic coherent state formalism.

We find out that the BMF states approximate the low-lying exact spectrum of IBM very well throughout the axially deformed part of the Casten triangle. The upper limit of their applicability is found to be closely related to the saddle point energy $E_{\rm sad}$ of the potential energy surface. Below $E_{\rm sad}$, the plain BMF approximation becomes inadequate also near to the degeneracies of individual intrinsic BMF excitations, some features of the spectrum can be however even here reproduced, if we consider the mixing of equal-K BMF states. The location of the degeneracies within the Casten triangle is studied systematically in the article.

The main points of the article involve the observation of a (i) novel type of critical behavior (called here "quasicriticallity") which affects already the lowest vibrational excitations (β and γ band, as well as higher excitations lying below the saddle point $E_{\rm sad}$) above the ground state band and (ii) observation of SU(3) quasi dynamical symmetry in the interior of the Casten triangle. The SU(3) QDS can be understood using the BMF states and its locus coincides with the applicability of the BMF approximation.

We also illustrate that the quasi-SU(3) rotational bands can be neatly disclosed by the Peres lattice method [Pere84a, **P5***]. The Peres method indeed turns out to be a powerful indicator of rotational band structures within the spectrum. It points out to the occurrence of some very high lying rotational bands, which cannot be explained by the simple BMF approximation. The rotational character of these states was actually proven in subsequent Refs. [**J7***, **J8***].

The author of this thesis used the IBM codes from Pavel Cejnar and the transition code provided by Francesco Iachello to calculate the exact spectra and $B(E2)$ transition rates and adapted these codes for calculation of Peres lattices and the SU(3) decompositions of the wave functions. He noticed the overlapping patterns in the Peres lattices corresponding to different angular momentum l states, which lead Jan Dobeš to suggest the mean-field interpretation of the low-energy spectra. The author subsequently performed the corresponding calculations using the BMF approximation determining also the exact positions of various BMF degeneracies inside the Casten triangle.

Transition from γ-rigid to γ-soft dynamics in the interacting boson model: Quasicriticality and quasidynamical symmetry

Michal Macek,[1] Jan Dobeš,[2] and Pavel Cejnar[1]

[1]*Institute of Particle and Nuclear Physics, Faculty of Mathematics and Physics, Charles University, V Holešovičkách 2, CZ-18000 Prague, Czech Republic*

[2]*Nuclear Physics Institute, Academy of Sciences of the Czech Republic, CZ-25068 Řež, Czech Republic*

(Received 23 March 2009; revised manuscript received 8 June 2009; published 23 July 2009)

We study the transition from the γ-rigid to γ-soft collective nuclear dynamics across the Casten triangle of the interacting boson model using mean-field techniques and confront the description with the exact diagonalization. We inspect the domain of validity of the SU(3) quasidynamical symmetry inside the Casten triangle and reveal critical behavior within the low-lying excited spectrum due to a degeneracy of β and γ vibrations.

DOI: 10.1103/PhysRevC.80.014319 PACS number(s): 21.60.Fw, 21.60.Ev, 21.10.Re, 05.45.Mt

I. INTRODUCTION

As known from the maritime history, nautical navigation began as cruises along coastal lines and only much later continued with the first successful passages across the open sea [1]. The study of nuclear structure between various types of collective dynamics has taken a similar route. Within the models taking into account quadrupole degrees of freedom, (a) an (anharmonic) spherical vibrator, (b) an axially symmetric (γ-rigid) deformed rotor, and (c) a deformed rotor unstable against the onset of triaxiality (γ-soft) represent the basic structural archetypes of collectivity. In the interacting boson model (IBM) [2], the above three cases are represented by three distinct dynamical symmetries: (a) U(5), (b) SU(3), and (c) O(6), which form vertices of the so-called Casten triangle [3–5]. It is not surprising that numerical studies of the transitions between the IBM dynamical symmetries were first performed along the sides of the Casten triangle, avoiding the "turmoil of the elements" inside the triangle, i.e., taking into account the interplay between only two selected symmetries and neglecting the contribution of the remaining symmetry.

A large number of analyses within the IBM have been focused on the so-called transitional classes A and C, i.e., the U(5)-SU(3) and U(5)-O(6) sides of the Casten triangle, respectively [2]. In the limit of infinite boson numbers, both these paths exhibit a spherical-deformed shape-phase transition, which according to the Ehrenfest classification are of the first order in case A and of the second order in case C [6,7]. On the other hand, the transitional class B, i.e., the SU(3)-O(6) side of the triangle, exhibits no phase transition on the ground-state level [2].

At present, a competition of all three dynamical symmetries (a)–(c) is considered when nuclei are placed in the Casten triangle [8]. Empirical signatures of the spherical-deformed phase transition, which is of the first order except for the U(5)-O(6) line, are commonly searched using the IBM Hamiltonians of transitional class D [9]. The investigations of the triangle interior led to interesting and sometimes even surprising findings. It was so when Alhassid and Whelan [10,11] disclosed therein a rather unexpected region of semiregular dynamics, the so-called arc of regularity [12,13]. This is in contrast to the most disordered area of the triangle, which appears to be centered close to the middle of the SU(3)-O(6) side.

While the transitions between spherical and deformed shapes have a critical character, the transition between γ-rigid and γ-soft deformed shapes is known to be just a crossover everywhere in the Casten triangle [2,6,7]. Nevertheless, the question concerning the mechanism of this transition is very interesting. In critical shape-phase transitions, the restructuralization of the low-lying spectra between the forms corresponding to the limiting dynamical symmetries appears to be rather abrupt, supporting the concept of quasidynamical symmetries associated with individual "phases" of the system [14,15]. It is not so clear, however, how the restructuralization proceeds in the crossover case. Because the main attention has been on the IBM quantum phase transitions, this question has not been studied much in the past.

In this work, we attempt to perform a detailed theoretical analysis of the transition between the U(5)-SU(3) (γ-rigid) and U(5)-O(6) (γ-soft) sides of the Casten triangle. This transition has been recently partly addressed in Ref. [16], but here we focus on its different aspects. In particular, we identify the critical behavior in the spectrum of excited states and demonstrate the range of applicability of the SU(3) quasidynamical symmetry in an extensive domain inside the Casten triangle. We remark that the SU(3)-O(6) transition has been recently studied also in the context of the shell model [17].

In Sec. II, the simplified IBM Hamiltonian and the intrinsic mean-field states suitable for the description of the γ-rigid to γ-soft transition are introduced. Properties and evolution of the energy spectrum throughout the transition are discussed in Sec. III by the mean-field approximation (Sec. III A) and by exact diagonalization (Secs. III B and III C). In Sec. IV, the critical behavior caused by degeneracy of β and γ vibrations is revealed in electromagnetic transitions. In Sec. V, the rotational quasidynamical symmetry and the related regularity of the spectrum are studied by decomposition of the wave functions into the SU(3) basis (Sec. V A) and by spectral lattices showing global characteristics of the spectra (Sec. V B). Finally, Sec. VI presents the summary and conclusions.

II. BOSONIC MEAN-FIELD BASIS IN THE IBM

A. Model

We consider the IBM-1 version of the interacting boson model, which approximates the coupled pairs of nucleons in the nucleus by the s and d bosons of the total angular momentum 0 and 2, respectively. We take the simplified form of the Hamiltonian [11,18,19]

$$\hat{H}(\eta,\chi) = \frac{\eta}{N}\hat{n}_d - \frac{1-\eta}{N^2}\hat{Q}(\chi)\cdot\hat{Q}(\chi), \tag{1}$$

which incorporates all three basic dynamical symmetries (DS) of the model. The Hamiltonian in Eq. (1) is composed of the d-boson number operator $\hat{n}_d = d^\dagger\cdot\tilde{d}$ and the quadrupole operator $\hat{Q}_m(\chi) = d_m^\dagger s + s^\dagger\tilde{d}_m + \chi[d^\dagger\tilde{d}]_m^{(2)}$. Scaling by the total number of bosons N ensures that the bounds of the energy spectrum do not change for asymptotic values of N. Two control parameters $\eta\in[0,1]$ and $\chi\in[-\sqrt{7}/2,0]$ drive the transitions of the system between the individual DS limits and span the Casten triangle. We neglect the overall scaling coefficient of the Hamiltonian, i.e., we express energy in units of this coefficient.

The U(5), SU(3), and O(6) limits are reached setting (η,χ) to $(1,\chi)$, $(0,-\sqrt{7}/2)$, and $(0,0)$, respectively. The SU(3) can also be obtained with $(\eta,\chi)=(0,+\sqrt{7}/2)$, but since the $\chi>0$ domain is just a mirror image of the $\chi<0$ one, see Ref. [20], we do not discuss it explicitly in this paper. Eigenstates of Eq. (1) are for general (η,χ) labeled by the U(6)-label N and the O(3)-label l corresponding to the angular momentum operator $\hat{L}_m = \sqrt{10}[d^\dagger\tilde{d}]_m^{(1)}$. The usual convention $\tilde{d}_\mu \equiv (-)^\mu d_{-\mu}$ and the scalar product notation related to the standard tensor coupling via $\hat{A}^{(l)}\cdot\hat{B}^{(l)} \equiv (-)^l\sqrt{2l+1}[\hat{A}^{(l)}\hat{B}^{(l)}]_0^{(0)}$ are utilized.

For the $E2$-transition calculations, we take the quadrupole operator

$$\hat{T}^{E2}(\chi) = q\,\hat{Q}(\chi), \tag{2}$$

consistently with Eq. (1). In all the following calculations, we set the effective charge to $q=1$.

B. Bosonic condensate

The geometrical interpretation and phase-transitional behavior can be deduced from a variational calculation performed on the condensate state [6,21]

$$|\mathrm{gs};N\rangle = \frac{1}{\sqrt{N!}}\Gamma_0^{\dagger N}|0\rangle, \tag{3}$$

composed of N general intrinsic bosons [22]

$$\Gamma_0^\dagger = \frac{1}{\sqrt{1+\beta^2}}\left[s^\dagger + \beta\cos\gamma\, d_0^\dagger + \beta\sin\gamma\,\frac{d_2^\dagger + d_{-2}^\dagger}{\sqrt{2}}\right]. \tag{4}$$

Here, $|0\rangle$ is the boson vacuum, and the parameters $\beta\geqslant 0$ and $\gamma\in[0,2\pi)$ are connected with the Bohr deformation variables of the geometric collective model via an N-dependent relation [6,23]. Condensate (3) with $\beta=\beta_{\min}$ and $\gamma=\gamma_{\min}$ corresponding to the minimum $E_{\min}$ of the potential energy surface

$$V(\beta,\gamma,N) \equiv \langle\mathrm{gs};N|\hat{H}|\mathrm{gs};N\rangle, \tag{5}$$

approaches the exact ground state of Eq. (1) as $N\to\infty$.

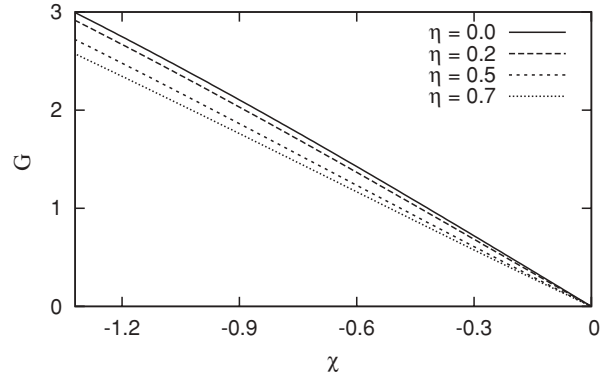

FIG. 1. Relative γ rigidity G from Eq. (6) of the semiclassical $N\to\infty$ potential in the deformed part of the Casten triangle.

The γ rigidity of the system may be suitably characterized by a quantity

$$G = \left[\frac{1}{\beta^2}\left(\frac{\partial^2 V}{\partial\gamma^2}\right)\Big/\left(\frac{\partial^2 V}{\partial\beta^2}\right)\right]_{\min} \tag{6}$$

evaluated at the minimum point $\beta_{\min},\gamma_{\min}$. Figure 1 shows the dependences $G(\chi)$ for a few values of η in the deformed part of the Casten triangle. All the curves show a monotoneous decrease to zero as $\chi\to 0$.

In the Casten triangle, the spherical ($\beta_{\min}=0$) and deformed ($\beta_{\min}>0$) shapes are separated by the critical line $\eta_{\mathrm{crit}} = (4+2\chi^2/7)/(5+2\chi^2/7)+O(1/N)$ [24], which in the semiclassical limit $N\to\infty$ corresponds for $\chi\neq 0$ to a first-order quantum phase transition (QPT), while for $\chi=0$ the phase transition is of the second order [6].

In the deformed part of the triangle, $\beta_{\min}\in(0,\sqrt{2}]$. For $\chi<0$, the angle $\gamma_{\min}=0$ (or equivalently $2\pi/3$ or $4\pi/3$; the latter two, however, make all the expressions cumbersome) and the γ rigidity $G>0$. Finally, for $\chi=0$, the potential energy surface of Eq. (5) becomes independent of the angle γ and $G=0$.

Thus the Casten triangle splits into the spherical part ($\eta\in[\eta_{\mathrm{crit}},1]$), the axially symmetric prolate-deformed γ-rigid part ($\eta\in[0,\eta_{\mathrm{crit}}]$, $\chi<0$), and the γ-soft part ($\eta\in[0,\eta_{\mathrm{crit}}]$, $\chi=0$), in which the nuclei are unstable against the onset of triaxiality. The oblate-deformed γ-rigid shapes are obtained with $\chi>0$ and will not be discussed in the current paper. A schematic phase diagram is depicted in Fig. 2.

In the γ-rigid prolate-deformed part of the Casten triangle, the potential energy surfaces [Eq. (5)] have a three-fold symmetry with respect to rotations by the angle γ and display three degenerate saddle points at $\gamma_{\mathrm{sad}}\in\{\pi/3,\pi,5\pi/3\}$, $\beta_{\mathrm{sad}}>0$, located between the three minima at $\gamma_{\min}\in\{0,2\pi/3,4\pi/3\}$ with $\beta_{\min}>0$. The saddle point energy E_{sad} will be shown to set an upper bound to the applicability of the SU(3) quasidynamical symmetry. In Fig. 2, we show the elevation of E_{sad} above $E_{\min}$ across the Casten triangle by contours of the ratio

$$R_{\mathrm{sad}} = \frac{E_{\mathrm{sad}}}{E_{\min}}, \tag{7}$$

measuring the fraction of the $E<0$ spectrum that is above E_{sad}. As $\chi\to 0$ the saddle point energy falls down so that

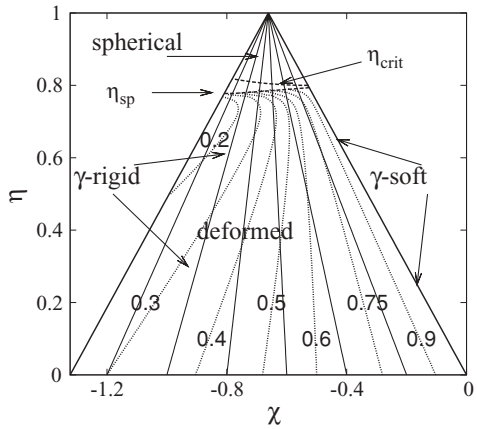

FIG. 2. Casten triangle with the regions of different ground-state shapes separated by the line of the spherical-to-deformed phase transition η_{crit}. We indicate the contours of the ratio R_{sad} from Eq. (7) throughout the deformed region together with the spinodal line η_{sp} for $N = 100$.

$R \to 1$. Precisely at $\chi = 0$, the saddle point melts away into the degenerate γ-independent minimum of the potential, which obtains the Mexican hat form here. Note that in the SU(3) limit, $R_{sad} = 0.25$ for $N \to \infty$. At the spinodal line $\eta_{sp}(\chi)$ of the spherical-to-deformed phase transition, the three saddle points merge to form a spherical minimum with $\beta_{min} = 0$. The spinodal line $\eta_{sp}(\chi)$ is drawn in Fig. 2 for $N = 100$.

C. Mean-field excitations

The Hamiltonian (1) is frequently diagonalized numerically in the U(5) basis (we perform it using an adaptation of the PHINT code [25]). Alternatively, the low-energy states can be inspected in a mean-field approximation using an orthogonal set of the general nonspherical bosons [22] that contains the ground-state boson from Eq. (4) and specific mutually orthogonal excitations. For a general account of this method, see Ref. [26]. A thorough study of general IBM-1 Hamiltonians by diagonalization within the intrinsic mean-field states up to two-phonon excitations has been performed in Ref. [27]. In our analysis, we use the mean-field techniques to interpret the critical behavior and SU(3) quasidynamical symmetry within the spectrum of the simple Hamiltonian (1) lying below the saddle point energy E_{sad}.

The excitations can be separated into the part related to vibrations in the intrinsic frame (usually called "phonons")

$$\Gamma^\dagger_\beta = \frac{1}{\sqrt{1+\beta^2}}\left[-\beta s^\dagger + \cos\gamma\, d^\dagger_0 + \sin\gamma\,\frac{d^\dagger_2 + d^\dagger_{-2}}{\sqrt{2}}\right],$$
$$\Gamma^\dagger_\gamma = -\sin\gamma\, d^\dagger_0 + \cos\gamma\,\frac{d^\dagger_2 + d^\dagger_{-2}}{\sqrt{2}}, \tag{8}$$

and collective rotations

$$\Gamma^\dagger_x = \frac{d^\dagger_1 + d^\dagger_{-1}}{\sqrt{2}}, \quad \Gamma^\dagger_y = \frac{d^\dagger_1 - d^\dagger_{-1}}{\sqrt{2}}, \quad \Gamma^\dagger_z = \frac{d^\dagger_2 - d^\dagger_{-2}}{\sqrt{2}}. \tag{9}$$

In the U(5) limit, all excitations (8) and (9) are physical. Away from U(5), the rotations (9) turn into Goldstone modes in the semiclassical limit $N \to \infty$. The same holds additionally for $\Gamma^\dagger_\gamma$ along the γ-soft $\chi = 0$ leg of the Casten triangle.

In the current paper, we will try to capture the essential features of the low-energy dynamics inside the Casten triangle using the set of bosonic mean-field (BMF) states, which we compose in a simple way only of the condensate in Eq. (3) and the vibrational phonons, that is,

$$\begin{aligned} |1,0;N\rangle &\propto \Gamma^\dagger_\beta \Gamma^{\dagger N-1}_0 |0\rangle, \\ |0,1;N\rangle &\propto \Gamma^\dagger_\gamma \Gamma^{\dagger N-1}_0 |0\rangle, \\ &\vdots \\ |n_\beta,n_\gamma;N\rangle &\propto \Gamma^{\dagger n_\beta}_\beta \Gamma^{\dagger n_\gamma}_\gamma \Gamma^{\dagger N-n_\beta-n_\gamma}_0 |0\rangle, \end{aligned} \tag{10}$$

with the normalization $\mathcal{N} = 1/\sqrt{n_\beta! n_\gamma! (N-n_\beta-n_\gamma)!}$. The set of many-body states in Eq. (10) is orthogonal because of the orthogonality of states in Eqs. (4) and (8); but of course it is incomplete because of the omission of the rotations in Eq. (9). For the sake of brevity, we will nevertheless call it a basis hereafter. Further on, we will sometimes use the shorthand notation $|n_\beta, n_\gamma\rangle \equiv |n_\beta, n_\gamma; N\rangle$ taking N implicitly.

It is quite natural to anticipate that the low-energy excitations in the γ-rigid region sufficiently far from $\chi = 0$ will display a structure similar the SU(3) limit, differing expectedly only by the deformation value $\beta \neq \beta_{SU(3)} = \sqrt{2}$ found by variation of the condensate in Eq. (3). Similarly, the eigenstates in the deformed γ-soft region near $\chi = 0$ should reflect the structure of the O(6) basis with only β corresponding to the minimum of Eq. (5). The expectation is supported by the observed SU(3)- and O(6)-quasidynamical symmetries along the SU(3)-U(5) and O(6)-U(5) legs of the Casten triangle [14,15,28], respectively, for $\eta < \eta_{crit}$. We ask what is the detailed mechanism of transition between these two regimes.

D. Dynamical symmetry limits and beyond

As a starting point, we describe briefly the structure of eigenstates at the dynamical symmetry limits SU(3) and O(6) and along the two legs of the Casten triangle leading from them toward the U(5) limit. The description is based on studies in Refs. [29,30], which the reader may consult for details.

The SU(3) basis can be constructed using the BMF states of Eqs. (3) and (10) with $\beta = \sqrt{2}$, $\gamma = 0$. The construction is *exact* in the $N \to \infty$ limit, in which the contribution of the rotations in Eq. (9) vanishes [29]. With $\gamma = 0$, the BMF states are endowed with a definite projection of the angular momentum onto the symmetry axis, labeled by K (we use the convention in which $K \geqslant 0$). Among the lowest excitations, the ground-state and β bands have $K = 0$, and the γ band has $K = 2$. For the higher excitations, K may take the values $0 \leqslant K \leqslant 2n_\gamma$, with $K/2$ being even (odd) for n_γ even (odd).

The β and γ excitations are *degenerate* in the SU(3) limit, so the diagonal energy of the individual excited BMF bands depends merely on the total number of excitation phonons $n \equiv n_\beta + n_\gamma$. Hence, the only peculiarity of the

otherwise simple construction is that all β and γ combinations coupled to identical K quantum numbers for given n are mixed in order to fit the BMF states into definite SU(3) irreducible representations (irreps), which are labeled by two quantum numbers (λ, μ) associated with the SU(3) Casimir operator [27,29]. The SU(3) ground band belongs to the irrep $(\lambda, \mu) = (2N, 0)$, the one-phonon β and γ bands ($K = 0, 2$, respectively) to $(2N-4, 2)$, two-phonon $\gamma^2, \beta\gamma$ and the mixed $\sqrt{2/3}\beta^2 + \sqrt{1/3}\gamma^2$ ($K = 4, 2, 0$, respectively) to $(2N-8, 4)$, and the second mixed band $\sqrt{1/3}\beta^2 - \sqrt{2/3}\gamma^2$ ($K = 0$) to the $(2N-6, 0)$. The individual band members are obtained applying an angular momentum projection being expressed formally by an operator $\hat{\mathcal{P}}_l$, with $l = 0, 2, 3, 4, \ldots$.

Throughout the whole prolate-deformed region of the Casten triangle ($\chi < 0$, $\eta < \eta_{\text{crit}}$), i.e., also away from SU(3), the energy minimizing value of γ is *zero*. Consequently the BMF states may be labeled by K in a similar way as in the SU(3) limit. The only difference is the changing value of $\beta = \beta_{\min}(\eta, \chi)$.

The O(6) basis is labeled by σ, which is the quantum number associated with the O(6) Casimir operator, and consists of states of the form

$$|\sigma; N\rangle = \frac{1}{\sqrt{\sigma![(N-\sigma)/2]!}} \hat{A}^{\dagger(N-\sigma)/2} \Gamma_0^{\dagger\sigma} |0\rangle. \qquad (11)$$

They can be obtained from the condensate in Eq. (3) with $\beta = 1$ by successively replacing the ground-state bosons in pairs by $\hat{A}^\dagger = d^\dagger \cdot d^\dagger - s^\dagger s^\dagger$. The band members are now obtained applying at first the seniority projection (involving integration over γ) and then the angular momentum projection (involving integration over Euler angles). For example, the ground state is given by

$$|\text{gs, O(6)}\rangle_{\text{proj}} = \hat{\mathcal{P}}_{l=0} \int_0^{\pi/3} d\gamma \, \sin 3\gamma \, |\text{gs}; N\rangle_{\beta=1}, \qquad (12)$$

where the integral over γ represents the projection onto the seniority $v = 0$ and is followed by angular momentum projection onto $l = 0$ (see Ref. [31]).

The ground-state condensate of Eq. (3) with $\beta = \beta_{\min}(\eta)$ while γ remains free applies to the O(6) limit as well as along the O(6)-U(5) leg. The seniority projection leads then to analytical expressions for the expansion coefficients $\zeta^N_{n_d,v}$ of the condensate state in the U(5) basis (i.e., in powers of the $d^\dagger$ operator) [30,32]. For example, the $v = 0$ states are up to normalization given by

$$\zeta^N_{n_d,0} = \beta^{n_d} \sqrt{\frac{N!}{(N-n_d)!} \frac{3}{(n_d+3)(n_d+1)!}}, \qquad (13)$$

where only even n_d are present.

To conclude the section, we would like to stress the significance of the saddle point energy E_{sad} of the potential in Eq. (5) for the dynamics in the prolate-deformed part of the Casten triangle. Above E_{sad}, the eigenstates of Eq. (1) are no longer localized around the potential minima, and the dynamics becomes in a way "γ-soft" and sometimes chaotic; see, e.g., Ref. [13]. Therefore we cannot expect much accuracy from Eq. (10) with $\gamma = 0$ here. The eigenstates above E_{sad} display in general quite complicated structures unless a dynamical symmetry is present. We shall demonstrate this in Sec. V B.

III. EVOLUTION OF ENERGY SPECTRA FROM γ-RIGID TO γ-SOFT DYNAMICS

The dynamics in the interior of the Casten triangle is known to be of intricately mixed, regular/chaotic nature [10,11,13]. One thus tends to be naturally skeptical about the sufficiency of the simple basis construction algorithm (10). Nevertheless, it turns out that the BMF states of Eq. (10) can describe some essential features of the exact spectrum despite the fact that they do not form a complete basis [the bosons from Eq. (9) are omitted]. In particular, evolution of the energies of the individual BMF states sheds light on the evolution of the low-lying rotational bands coming from the exact diagonalization of Hamiltonian in Eq. (1) throughout the deformed part of the Casten triangle. The asymptotic behavior of the mixing matrix elements among different BMF states, moreover, influences the onset of chaotic dynamics within the triangle, as will be argued in Sec. V B.

Apart from the results of the complete numerical diagonalization, we present BMF calculations that are twofold: either we show most simply the diagonal matrix elements of the Hamiltonian (1) in the BMF states of Eq. (10) or we perform a highly restricted diagonalization within equal-K BMF subspaces of a small dimension d (typically $d = 2$), see also Ref. [27]. In the rest of the paper, we will often use the terms "diagonal BMF" and "mixed BMF" to distinguish the latter two approximations from the *exact* numerical diagonalization.

It should be stressed that both of the above BMF approaches lose their sense at $\chi = 0$. The description along this line would require a proper treatment of the spurious γ excitations by either (a) restoring the O(5) symmetry or (b) considering spontaneously broken O(5) through resolution of the Hamiltonian into intrinsic and collective parts, see Ref. [22]. This we do not perform here, since we focus on the $\chi \neq 0$ case.

The results shown in the current paper are mostly calculated along the line $\eta = 0.5$, $\chi \in [-\sqrt{7}/2, 0)$. Note, nevertheless, that we performed the calculations also at $\eta = 0.0, 0.2, 0.7$ and found that all essential properties being discussed for the deformed region of the Casten triangle are well represented by the $\eta = 0.5$ line.

A. Mean-field spectrum and degeneracies

Let us first discuss the evolution of diagonal BMF energies in the prolate-deformed region without the possible mixing being considered. The general trend is such that all multiple γ excitations fall toward the ground state as χ approaches zero [remember the potential of Eq. (5) being γ flat and the γ excitations hence spurious]. On the contrary, the energies of the β excitations evolve "in parallel" with the ground-state energy, so their excitation energies remain approximately constant. This leads to a considerable number of level crossings among the β and γ bands of various excitation degree $n = n_\beta + n_\gamma$. We recall that above the saddle point energy E_{sad}, the BMF energies (especially the diagonal ones) should not be considered to have a straightforward physical relevance; see discussion in Secs. II and V B.

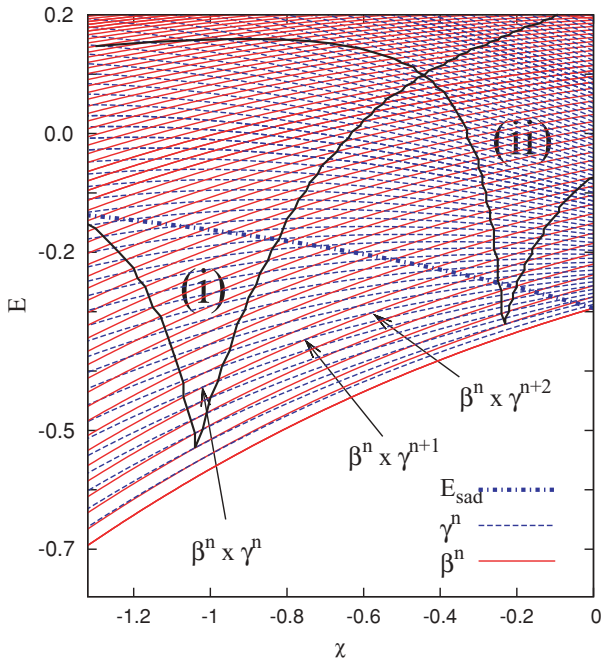

FIG. 3. (Color online) Diagonal BMF energies (in arbitrary units) of β^n-(solid red lines) and γ^n-(dashed blue lines) phonon excitations for $\eta = 0.5$ and $N = 100$ bosons with $n = 0, \ldots, 30$. Selected series of degeneracies among the mean-field states are indicated by arrows. Additionally, the saddle point energy $E_{\rm sad}$ is indicated by the dot-dashed blue line roughly delimiting the region of applicability ($E \lesssim E_{\rm sad}$) of the BMF method. The solid black lines delimit the wedge-shaped mixing regions of BMF states listed in rows (i) and (ii) of Table I.

Figure 3 shows the evolution of diagonal BMF energies for $N = 100$ along the line $\eta = 0.5$. Since the complete spectrum would be highly overabundant, we plot only the energies of n-tuple pure β and pure γ excitations $|n_\beta = n, n_\gamma = 0\rangle$ and $|n_\beta = 0, n_\gamma = n\rangle$ with $n = 0, 1, 2, \ldots, \approx 30$. The energies of combined excitations $|n_\beta, n - n_\beta\rangle, n_\beta = 1, \ldots, n-1$ (not shown in Fig. 3) spread in between the latter two extreme cases except (for high enough N) of the near vicinities of the $\beta^n \times \gamma^n$ degeneracy points, denoted as $\chi_{\rm deg}(\beta^n, \gamma^n)$, where the ordering of the levels may differ [an example can be seen in Fig. 5(a)].

Degeneracies of diagonal BMF energies appear systematically throughout the spectrum and create an "interference-like" pattern in Fig. 3. The $\beta^n \times \gamma^n$ ($n = 1, 2, 3, \ldots$) degeneracies form an almost vertical sequence at $\chi \approx -1$. The sequences of $\beta^n \times \gamma^{n+i}$ ($i = 1, 2, 3, \ldots$) degeneracies form neighboring "interference fringes" in the figure.

The diagonal BMF treatment as shown in Fig. 3 is of course incomplete. In the mixed BMF approach, the character of level crossings is modified by the level repulsion among interacting states, and the levels may become *avoided*. The Hamiltonian (1) in general mixes only BMF states of equal angular momentum projection (K, if $\gamma_{\rm min} = 0$). Moreover, the crossings may be avoided only if the BMF states under consideration differ by at most two excitations due to one- and two-body interactions present in the Hamiltonian (1).

TABLE I. Asymptotic behavior of nonzero matrix elements mixing the BMF states of Eq. (10) coupled to equal K. Rows (i)–(iii) contain states differing by two γ excitations, while the rows (iv)–(vi) contain states with equal n_γ. The bottom row—behavior of the diagonal matrix elements—reflects the energy-per-boson scaling of Hamiltonian (1).

(i)	$\langle n_\beta, n_\gamma + 2\|\hat{H}\|n_\beta + 2, n_\gamma\rangle$	$O(N^{-2})$
(ii)	$\langle n_\beta, n_\gamma + 2\|\hat{H}\|n_\beta + 1, n_\gamma\rangle$	$O(N^{-3/2})$
(iii)	$\langle n_\beta, n_\gamma + 2\|\hat{H}\|n_\beta, n_\gamma\rangle$	$O(N^{-1})$
(iv)	$\langle n_\beta + 2, n_\gamma\|\hat{H}\|n_\beta, n_\gamma\rangle$	$O(N^{-1})$
(v)	$\langle n_\beta + 1, n_\gamma\|\hat{H}\|n_\beta, n_\gamma\rangle$	$O(N^{-1/2})$
(vi)	$\langle n_\beta, n_\gamma\|\hat{H}\|n_\beta, n_\gamma\rangle$	$O(1)$

Let us point out that *direct* level crossings appear throughout the whole spectrum and represent a vast majority of the BMF degeneracies. On the contrary, the *avoided* BMF crossings inhabit only certain limited parts of the spectrum, which we shall specify below.

Interesting clues can be obtained from the asymptotic behavior of the mixing matrix elements of the equal-K BMF states $\langle n_\beta, n_\gamma|\hat{H}|n'_\beta, n'_\gamma\rangle$. We summarize all possible nonzero elements in Table I. For the BMF states mixed according to the table, the degeneracies of the diagonal BMF energies with consequent level repulsion occur *only* among the cases labeled (i) and (ii), if we stay inside the Casten triangle. In the $N \to \infty$ limit, the degeneracies are recovered, as the off-diagonal matrix elements vanish.

As χ approaches 0, the spectrum of the BMF states with multiple γ excitations in Fig. 3 gets compressed, as expected from the fact that γ excitations become spurious, hence carrying zero energy. The remnant splitting among these states seen in the $\chi \approx 0$ region of Fig. 3 is due to different number $N - n_\gamma$ of ground-state bosons $\Gamma_0^\dagger$. Because the energy of the saddle point of the potential (5) converges to the ground-state energy for $\chi \to 0$, as the potential becomes γ flat, the BMF description of the spectrum is invalid at $\chi \approx 0$.

Energies of the states differing only by n_β, as in the cases (iv) and (v), evolve visually in "parallel," as evident from Fig. 3. Hence their mixing, despite being for finite N strong, does not introduce any observable level repulsion. The strong interactions just reflect the fact that the Hamiltonian (1) is in general not a mean-field operator.

Let us now specify the regions where the avoided crossings (i) and (ii) appear. For convenience, we actually spot the points of direct crossings of diagonal BMF energies, which are followed by the corresponding avoided crossing points and provide reasonable distinction of the regions (i) and (ii).

In case (i), the crossings correspond to BMF states that differ by two excitations—β^2 in one state and γ^2 in the other—while they have *additional* $n_\beta - 2, n_\gamma - 2$ excitations in common. Taking states of a definite excitation degree $n = n_\beta + n_\gamma$, the individual avoided crossings take place within specific *bounded* χ domains. The crossings are ordered so that increasing the number of the additional γ excitations against the number of β excitations increases the χ value of the degeneracy point. As shown in Fig. 3, region (i) is limited from below in the energy by a line connecting degeneracy points

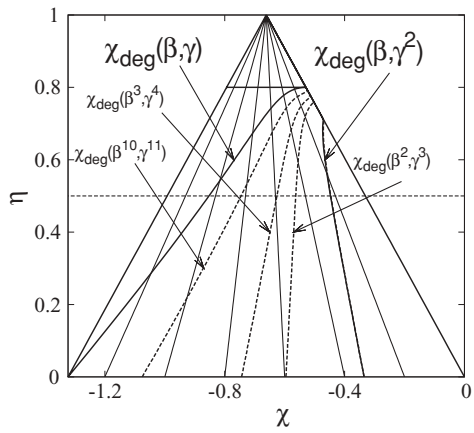

FIG. 4. Casten triangle with selected $\beta^{n_\beta} \times \gamma^{n_\gamma}$ BMF degeneracy lines. The $\beta \times \gamma$ and $\beta \times \gamma^2$ lines are valid in the $N \to \infty$ limit (solid lines), while $\beta^2 \times \gamma^3$, $\beta^3 \times \gamma^4$, and $\beta^{10} \times \gamma^{11}$ lines correspond to $N = 100$ (dashed lines). The $\eta = 0.5$ line, where the most calculations in the present paper have been performed, is also indicated.

for which the additional excitations are either purely β^{n-2} or purely γ^{n-2}. The minimum energy point of this boundary line is the degeneracy point $\chi_{\rm deg}(\beta^2, \gamma^2)$. The left wing of the line for $\chi < \chi_{\rm deg}(\beta^2, \gamma^2)$ connects the degeneracy points $\chi_{\rm deg}(\beta^2\beta^{n-2}, \gamma^2\beta^{n-2})$, whereas the right wing connects for $\chi > \chi_{\rm deg}(\beta^2, \gamma^2)$ the points $\chi_{\rm deg}(\beta^2\gamma^{n-2}, \gamma^2\gamma^{n-2})$.

In case (ii), the crossings correspond to a single-β state on one side and a γ^2 state on the other, while both states have additional $n_\beta - 2, n_\gamma - 2$ excitations in common (there is moreover one extra ground-state boson in the β state compared to the γ^2 state). In complete analogy with case (i), region (ii) is limited from below by a line with the minimum point $\chi_{\rm deg}(\beta, \gamma^2)$, the left wing for $\chi < \chi_{\rm deg}(\beta, \gamma^2)$ connecting the degeneracy points $\chi_{\rm deg}(\beta\beta^{n-2}, \gamma^2\beta^{n-2})$ and the right wing for $\chi > \chi_{\rm deg}(\beta, \gamma^2)$ connecting the points $\chi_{\rm deg}(\beta\gamma^{n-2}, \gamma^2\gamma^{n-2})$.

The boundary lines demarcate two wedge-shaped regions inside the spectrum, as shown in Fig. 3 for $N = 100$. At low energies, the regions are distinct, while at higher energies $E > 0$, they overlap. We remark that the shape of the regions relative to the upper and lower bounds of the spectrum $E_{\rm max}(\chi)$, $E_{\rm min}(\chi)$ is practically independent of N.

The structure of the BMF spectrum just described for $\eta = 0.5$ smoothly changes across the whole prolate-deformed part of the Casten triangle. What differs, are the precise positions of the degeneracies for particular values of η. They shift along the lines indicated in Fig. 4, where we plot $\chi_{\rm deg}(\beta, \gamma)$ and a few other selected degeneracies. These curves, together with those from Fig. 2, provide a set of guidelines on the "sailing map" leading our voyage from the γ-rigid to the γ-soft "coast."

B. Exact spectrum

Let us now compare the BMF approximation (10) with the exact spectra. Figure 5 shows the evolution of energies of low-lying states along $\eta = 0.5$ for $N = 20$ bosons for both diagonal and mixed BMF in Fig. 5(a) and for the exact $l = 0, 2$ states in Fig. 5(b). Among the BMF energies, we show the diagonal matrix elements calculated within the $n \leqslant 3$ BMF subspace supplemented by levels coming from a simple diagonalization of Eq. (1) in the $n \leqslant 2$ $K = 0$ BMF subspace consisting of $\{{\rm gs}, \beta, \beta^2, \gamma^2\}$. Comparing the spectra in panels Figs. 5(a) and 5(b), we come to several observations:

(1) The BMF spectra are obviously lifted up in energy compared to the exact spectra. The correspondence can be improved by angular momentum projection. In Fig. 5(b), we show the effect of the approximate projection after variation

$$E'_{\rm min} = \langle {\rm gs}; N | \hat{H} - \frac{\hat{L} \cdot \hat{L}}{2\mathcal{J}_{\rm c}} | {\rm gs}; N \rangle \tag{14}$$

using the cranking moment of inertia

$$\mathcal{J}_{\rm c} = \frac{3N\beta^2}{(1+\beta^2)(E_1 - E_{\rm min})}, \tag{15}$$

with $E_1 = \langle {\rm gs}; N-1 | \Gamma_x \hat{H} \Gamma_x^\dagger | {\rm gs}; N-1 \rangle$. $E_{\rm min}$ and $E'_{\rm min}$ stand for the unprojected minimum of Eq. (5) and the projected $l = 0$ energy, respectively. This approximate projection provides a reasonable agreement with the exact rotational-band levels (excitation energies given by $l(l+1)/2\mathcal{J}_{\rm c}$), as apparent from the detail shown in the inset of Fig. 5(b). Note that this approximate projection (in contrast to the exact projection) may locate the state slightly *below* the actual eigenstate.

(2) To reproduce the level repulsion between exact β^2 and γ^2 bands in the $\chi \approx \chi_{\rm deg}(\beta^2, \gamma^2) = -1.0$ region, it is sufficient to consider the mixing of just the nearest equal-K BMF states [this holds in general for equal-K states in the mixing region (i) described in Sec. III A]. On the other hand, the mixing strength of the order $O(N^{-3/2})$ between β and γ^2 excitations requires for $N = 20$ a diagonalization in a more extended equal-K subspace, and the method loses its appeal [similarly in the whole mixing region (ii)]. Moreover, the spectrum in the latter case gets complicated because of the falling saddle point energy $E_{\rm sad}$—the approximate limit of BMF applicability (see Secs. II and V B)—as $\chi \to 0$.

(3) Another notable effect seen in Fig. 5(b) is the increasing deviation of the exact ground state from the approximate $l = 0$ projected state as χ converges to zero. Indeed, at $\chi = 0$, the seniority $v = 0$ projection is needed to obtain a correct estimate of the ground-state energy. Interestingly, the deviation can be very well reproduced by considering the mixing of the BMF ground state with γ^2 excitation; see Fig. 5(a). [The difference between mixed and diagonal BMF g.s. energies in Fig. 5(a) is about the same as the difference between the exact and the approximately projected $l = 0$ state.] This can be understood from Eq. (13), which for $\eta = 0.5, N = 20$ shows the $\hat{n}_d = 2$ component to be dominant in the seniority $v = 0$ projected ground state. The BMF ground state and $\gamma^2(K = 0)$ excitation are then sufficient to cover this $\hat{n}_d = 2, K = 0$ component, since the $\beta^2(K = 0)$ excitation lies at significantly higher energy, which makes its contribution less important. So the mixing of these two

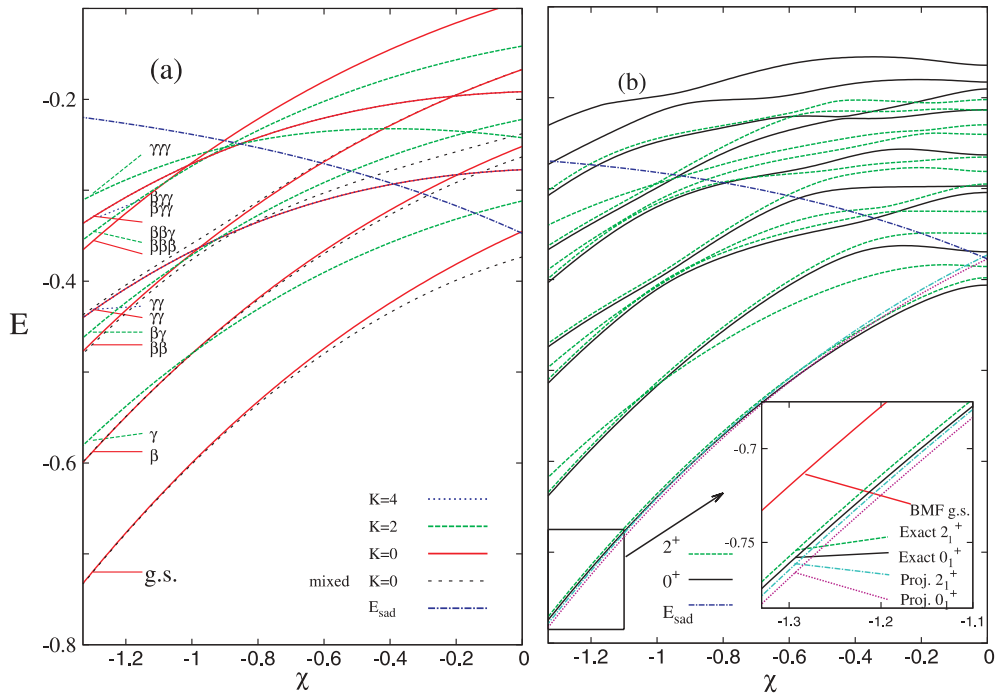

FIG. 5. (Color online) Evolution of energy spectra (in arbitrary units) calculated for $\eta = 0.5$ and $N = 20$ bosons. (a) BMF spectra both with and without mixing of $K = 0$ states [Eq. (10)]. (b) Corresponding exact spectrum of a few lowest $l = 0$ and $l = 2$ states; inset shows the effect of the angular momentum projection (14)—the exact spectrum is supplemented by the 0_1^+ and 2_1^+ levels projected from the BMF condensate. $E_{\rm sad}$ is indicated by decreasing dot-dashed blue lines in both panels.

states simulates the effect of the seniority projection in this case.

(4) A more subtle effect, uncaptured by the BMF basis of Eq. (10), is the breaking of the K quantum number away from the SU(3) limit. As noted above, the scalar Hamiltonian (1) cannot mix the BMF states differing in the K quantum number. However, this restriction does not hold for the states being angular momentum projected from the BMF basis. Similarly, K is not applicable for states from the exact diagonalization. Nevertheless, it can be inferred that the mixing of states developing from the BMF states with the same K is much stronger than the mixing of those coming from BMF states of different K. The repulsion for the equal-K case is obvious in Fig. 5(b), whereas it is indistinguishable for the bands differing in K. Under close inspection, the crossings of individual l states in different-K bands, e.g., in the β and γ band, are found to be avoided. This effect reflects the actual absence of the dynamical symmetry inside the triangle, although the resilience of K in contrast to the O(6) "missing label" n_Δ is rather strong, as was pointed out already in Ref. [33].

C. Rotational bands

The rotational character of the bands can be tested by suitable excitation energy ratios, such as

$$R(4_i/2_i) \equiv \frac{E(4_i) - E(0_i)}{E(2_i) - E(0_i)}, \tag{16}$$

$$R(4_i/3_i) \equiv \frac{E(4_i) - E(2_i)}{E(3_i) - E(2_i)}, \tag{17}$$

$$R(6_i/4_i) \equiv \frac{E(6_i) - E(2_i)}{E(4_i) - E(2_i)}, \tag{18}$$

plotted in Fig. 6 for $i = 1, 2, 3$. The indices $i = 1, 2, 3$ correspond on the γ-rigid side for $\chi < \chi_{\rm deg}(\beta, \gamma)$ to the ground, β, and γ bands, respectively. Some care has to be taken because of the band crossings and consequent reordering of the levels: for $\chi > \chi_{\rm deg}(\beta, \gamma)$, we have $i = 1, 3, 2$ for the same bands. Note also that $R(4_i/2_i)$ obviously cannot be applied to the $K = 2$ γ band, so we employ $R(4_i/3_1)$ here.

As we may observe from Fig. 6, all the bands are rotational at $\chi = -\sqrt{7}/2$, showing the $l(l+1)$ excitation energy dependence with high accuracy. The ground band remains such almost up to the completely γ-soft regime and starts to deviate from the SU(3) values $R(4_i/2_i) = 4/3$ and $R(6_i/4_i) = 18/7$ noticeably only for $\chi > -0.4$, where it interacts significantly with γ^2, as we have noted above. In the excited bands, deviations from the SU(3) values set on noticeably for $\chi > -0.6$, with the exception of the *staggering* around $\chi_{\rm deg}(\beta, \gamma) = -1.04$. The staggering is caused by the fact that individual even-l states from β and γ bands cross for slightly different χ. Moreover the odd-l states from the γ band of course do not undergo any crossings, since the β band with $K = 0$ contains only even spins. As a consequence, distinction of the β and γ bands is meaningless in the small vicinity of $\chi_{\rm deg}(\beta, \gamma)$.

Validity and breakdown of the rotational bands can also be observed as the "parallel" evolution of the $l = 0$ and

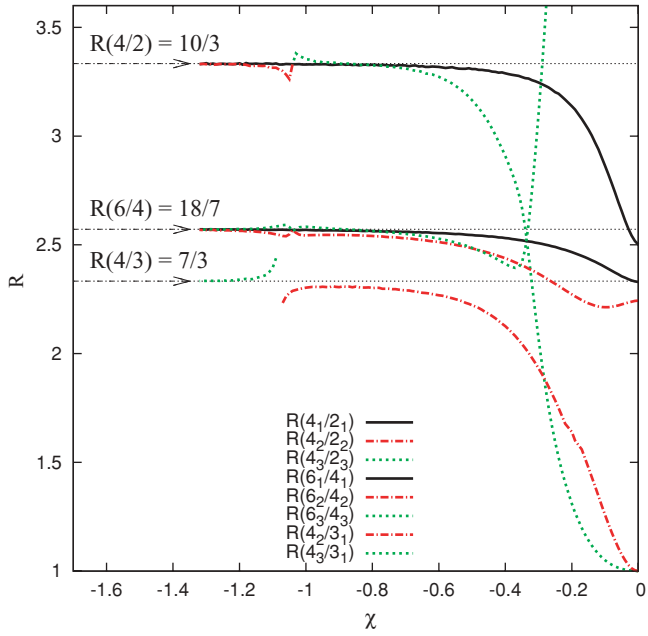

FIG. 6. (Color online) Exact excitation energy ratios $R(4_i/2_i)$, $R(6_i/4_i)$ plotted for $i = 1, 2, 3$, and $R(4_i/3_1)$ for $i = 2, 3$ along the $\eta = 0.5$ line with $N = 20$. The "rotational" SU(3) values are indicated by arrows. Staggering of the ratios due to the crossing of β and γ bands is observable at $\chi \approx -1.04$. We plot $R(4/2)$ for the ground and β bands; $R(6/4)$ for the ground, β, and γ bands; and $R(4/3)$ for the γ band. For $\chi > -0.6$, the spectrum evidently undergoes a transformation from the rotational to the seniority directed pattern.

$l = 2$ states on the γ-rigid side of the transition, which can be followed in Fig. 5(b). This corresponds to only a very gentle variation of the moments of inertia with χ on this side. The parallel evolution is evidently disrupted as the levels approach the saddle point energy $E_{\rm sad}$, close to which the $l = 0$ and $l = 2$ levels split to obey gradually the seniority directed pattern at $\chi = 0$. In Fig. 7, we plot the moments of inertia $\mathcal{J}$ calculated for the ground-state and β ($K = 0$) bands as $\mathcal{J} = 3/(E(2^+) - E(0^+))$, while for the γ ($K = 2$) band as $\mathcal{J} = 3/(E(3^+) - E(2^+))$ for $\eta = 0.5$ and $N = 20$ in the main panel and for $N = 40$ in the inset. We may notice that with increasing boson number N, the moments of inertia $\mathcal{J}$ approach each other for $\chi < -0.6$.

A strong evidence for rotational bands is provided by electromagnetic transitions, in particular the reduced $E2$ transition rates should be well described by the Alaga rule

$$B(E2; l, K \to l', K') = \langle K'|\hat{T}^{E2}(\chi)|K\rangle^2 (lK2m|l'K')^2, \tag{19}$$

where $(lK2m|l'K')$ is the relevant Clebsch-Gordan coefficient with $m \equiv K' - K$, and $|K\rangle$ denotes a BMF state of given K.

For relative intraband $B(E2)$ transition rates, the Alaga rule of Eq. (19) predicts values given simply by ratios of squared Clebsch-Gordan coefficients. In Figs. 8(a), 8(b), and 8(c), we show the relative intraband rates within the ground-state, β, and γ bands, respectively, obtained by exact IBM calculations

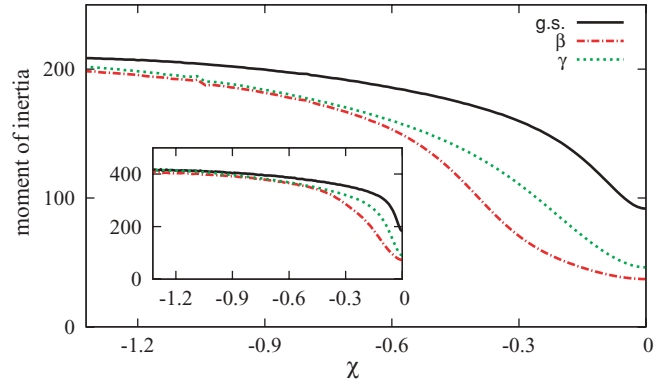

FIG. 7. (Color online) Moments of inertia (in arbitrary units) for the ground-state band and excited β and γ bands for $\eta = 0.5$ and $N = 20$ (exact calculation). The disturbance of the smooth dependence at $\chi \approx -1.04$ is due to $\beta \times \gamma$ degeneracy. The inset shows the same for $N = 40$, which demonstrates mutual convergence of all three curves for high N.

for $N = 20$ bosons at $\eta = 0.5$ together with the Alaga values indicated by thin lines. The transition rates are divided by $B(E2; 2^+ \to 0^+)$ for the ground-state band and β band and by $B(E2; 4^+ \to 2^+)$ for the γ band. The agreement with the Alaga rule is good for $\chi < -0.4$, especially for $l \leqslant 6$. Strong deviations from the Alaga rule for $\chi > -0.4$ are due to mixing with higher excited bands.

The spikes seen in Figs. 8(b) and 8(c) at $\chi \approx -1.04$ result from ambiguous assignments of the $2^+, 4^+, 6^+, 8^+$ states to

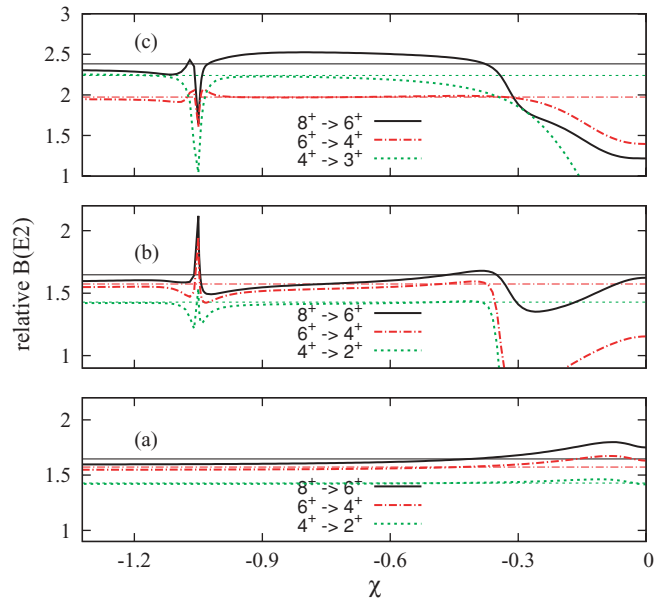

FIG. 8. (Color online) Relative intraband $B(E2)$ transition rates (exact calculation) for the (a) ground-state, (b) β, and (c) γ bands for $\eta = 0.5$ and $N = 20$. The transitions indicated in the legend are divided by $B(E2; 2^+ \to 0^+)$ for the ground-state and β bands and by $B(E2; 4^+ \to 2^+)$ for the γ band. For each transition, the values predicted by the Alaga rule are indicated by thin lines of corresponding type and color. The spikes at $\chi \approx -1.04$ originate from the $\beta \times \gamma$ crossing (see text).

the β and γ bands in the region where the individual members of these bands cross. Close to each crossing, the distinction of the β and γ excitations with the same spin is washed out because of strong effects of mixing, which makes the concept of β and γ bands invalid. In Fig. 8, the notation based on these bands is used just for brevity, while in a detailed study of the transitional region one should look at individual $B(E2)$ values organized according to the order of the levels involved. Rapid changes of the relevant $E2$ strengths represent a significant indicator of the $\beta \times \gamma$ crossing (see the discussion of Fig. 6).

IV. QUASICRITICALITY OF THE γ-RIGID TO γ-SOFT TRANSITION

In the IBM framework, the phase transitions in nuclear shapes involving the γ degree of freedom have been identified between the prolate and oblate shapes [Hamiltonian (1) extended to negative and positive values of χ] [20] and between the axially symmetric and triaxial γ-rigid shapes (IBM with three-body interactions) [34]. In contrast, the transition from the γ-rigid (either prolate or oblate) to the γ-soft dynamics is a noncritical crossover—the ground-state properties evolve analytically as the γ dependence of the deformation energy surface disappears [6].

The crossings of the diagonal BMF energies described in Sec. III, especially the $\beta \times \gamma$ degeneracy pointed out already in Refs. [12,13], are nevertheless connected with the nonanalytic behavior of low-lying excited states and display significant finite-N precursors of the criticality, as we shall show in this section. The effect is actually very similar to a quantum phase transition, because although not the ground band itself, already the lowest excited bands experience the crossings of energy levels, which is the mechanism responsible for the *first-order* phase transition [35]. The nonanalyticities can be studied by calculating specific electromagnetic transitions, which may also represent an interesting observable from the experimental point of view.

In Fig. 9, we show the χ dependence of $B(E2)$ values between the lowest excited two-phonon $l = 0$ and one-phonon $l = 2$ states for $\eta = 0.5$ and $N = 20$ bosons. In the γ-rigid region, the two-phonon $l = 0$ states belong in a good approximation to two orthogonal combinations of $K = 0$ bands [27]:

$$|\beta^2 + \gamma^2\rangle = A|2, 0\rangle + B|0, 2\rangle,$$
$$|\beta^2 - \gamma^2\rangle = B|2, 0\rangle - A|0, 2\rangle. \quad (20)$$

The mixing amplitudes A, B are obtained by diagonalization of $\hat{H}$ within this two-dimensional $K = 0, n = 2$ BMF subspace. On the contrary, the one-phonon $l = 2$ states belong to the single β and γ bands. The observed agreement between the mixed BMF and the exact $B(E2)$ values is very good in the γ-rigid region for $\chi < -0.6$, but it breaks down as $E_{\rm sad}$ falls toward the energy of the two-phonon BMF states, as described in Sec III A—see Figs. 5(a) and 5(b).

In Fig. 10 we may observe that the $\beta \times \gamma$ crossing is in a similar way responsible also for the singular behavior of transitions from one-phonon bands to the ground-state band.

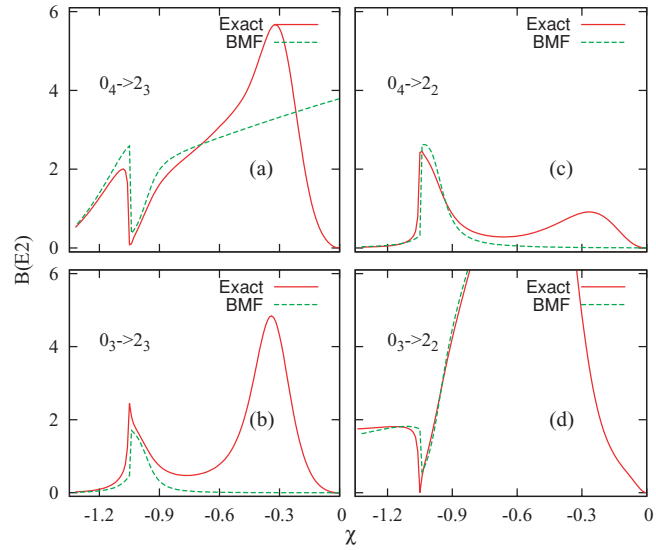

FIG. 9. (Color online) $B(E2)$ values for transitions between two-phonon $K = 0$ and one-phonon bands (states indicated in each panel) obtained by both the intrinsic BMF formalism and exact numerical diagonalization for $\eta = 0.5$ and $N = 20$ bosons. The BMF calculation takes into account the mixing of two-phonon $K = 0$ bands. The mixing of bands with different phonon number n is not included, which leads to significant discrepancies for $\chi > -0.6$.

Precursors of nonanalytic jumps at $\chi = -1.04$ may be clearly noticed in all panels of Fig. 9. The jumps themselves originate in the direct crossings among one-phonon BMF ("nearly direct" among the exact) β and γ bands, while the abruptly changing, but still smooth behavior near the jumps [see the "peaks" in Figs. 9(b) and 9(c) and "trenches" in Figs. 9(a) and 9(d)] is caused by the variation of the deformation parameter β and the mixing amplitudes A, B from Eq. (20) among the avoided-crossing two-phonon bands. The variation of $A(\chi)$ and $B(\chi)$ is shown in the inset of Fig. 11 for $\eta = 0.5$ and $N = 20$ bosons.

If we define the width of the mixing region Δ_χ as the distance between the extremes of $\partial^2 A/\partial\chi^2$ and $\partial^2 B/\partial\chi^2$ (see

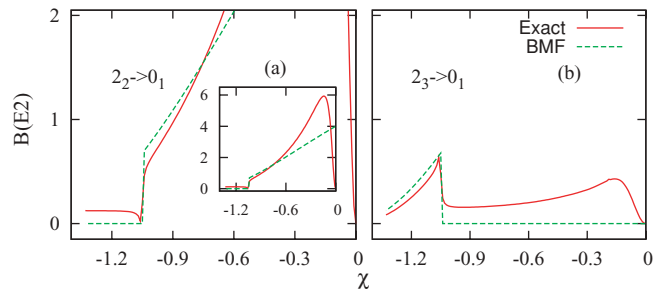

FIG. 10. (Color online) $B(E2)$ values of transitions from the $l = 2$ states belonging to the one-phonon β and γ bands to the $l = 0$ ground state for $N = 20$ bosons calculated by both BMF approximation and exact diagonalization. The range of axes is set to allow direct comparison between panels (a) and (b) in the region $\chi_{\rm deg}(\beta, \gamma) \approx -1.04$. The inset inside panel (a) displays the complete curves using a different scaling of the y axis.

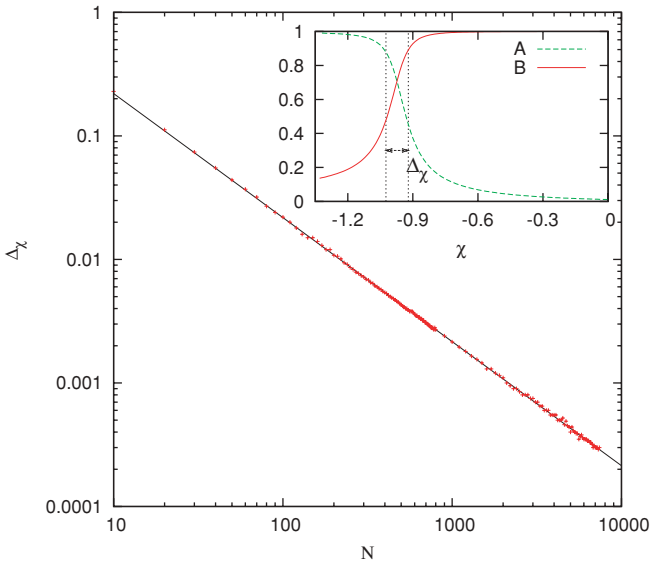

FIG. 11. (Color online) Behavior of the mixing amplitudes A, B of the two-phonon β^2 and γ^2 $K = 0$ bands for $\eta = 0.5$ as a function of χ for $N = 20$ bosons is shown in the inset, while the width of the mixing region Δ_χ, decreasing roughly as $O(1/N)$, is in the main panel. The line represents a linear fit yielding $\Delta_\chi \propto N^{-1.004}$.

the inset in Fig. 11), we may observe that the mixing region calculated within the BMF scales as $\Delta_\chi \propto N^{-\alpha}$, with $\alpha \doteq 1$, as found by fitting the points in the main panel of Fig. 11. The amplitudes $A(\chi)$ and $B(\chi)$ consequently converge to step functions for $N \to \infty$. The BMF approximation gives for the transition strengths

$$\begin{aligned} &B(E2;\beta^2 \to \gamma) = 0, \quad B(E2;\gamma^2 \to \beta) = 0, \\ &B(E2;\beta^2 \to \beta) \propto N, \quad B(E2;\gamma^2 \to \gamma) \propto N, \end{aligned} \tag{21}$$

so the peaks and trenches consequently become asymptotically high and deep, respectively, as well as infinitesimally narrow because of the step-like shape of $A(\chi)$ and $B(\chi)$ in the limit $N \to \infty$. It would be interesting to verify the scaling of Δ_χ also within the exact calculations using an IBM code able to work with high enough N. Since the amplitudes $A(\chi)$ and $B(\chi)$ are defined only for BMF, in the exact calculations, one could alternatively consider, for example, the scaling of width of the above-discussed $B(E2)$ peaks at the half-maximum.

We remark that the exact position of the degeneracy point $\chi_{\rm deg}$ is usually very sensitive to the energies of the levels involved, because of the acute angle of crossing. Actually, the position of the nonanalytic jump in the $B(E2)$ strengths described above in exact and BMF results agrees to the extent shown in Fig. 9 only after the angular momentum projection of Eq. (14). It means that the proper energies and the crossing point of projected 2^+_β and 2^+_γ states must be considered instead of the unprojected BMF. The degeneracy of unprojected β and γ BMF states for $N = 20$ occurs at $\chi = -1.00$ compared to the exact $\chi_{\rm deg}(\beta,\gamma) = -1.04$.

V. QUASIDYNAMICAL SYMMETRY, ORDER, AND CHAOS INSIDE CASTEN TRIANGLE

A. Wave functions

An interesting behavior of wave functions inside the Casten triangle is revealed when we decompose the β-dependent BMF states into the SU(3)-BMF basis ($\beta_{\rm min} = \sqrt{2}$, $\gamma_{\rm min} = 0$) and compare them with the SU(3) decomposition of the exact eigenstates of individual spins l.

To obtain the transformation coefficients between the general and the SU(3) BMF bases, we introduce a shorthand notation for the SU(3) ground-state and β bosons, i.e.,

$$g^\dagger \equiv \frac{s^\dagger + \sqrt{2}d^\dagger_0}{\sqrt{3}}, \quad \beta^\dagger \equiv \frac{-\sqrt{2}s^\dagger + d^\dagger_0}{\sqrt{3}}, \tag{22}$$

whence for $\Gamma^\dagger_0$, $\Gamma^\dagger_\beta$ given by Eqs. (4) and (8) follows

$$\begin{aligned} &\Gamma^\dagger_0 = C_1 g^\dagger + C_2 \beta^\dagger, \quad \Gamma^\dagger_\beta = -C_2 g^\dagger + C_1 \beta^\dagger, \\ &C_1 \equiv \frac{1+\sqrt{2}\beta}{\sqrt{3}\sqrt{1+\beta^2}}, \quad C_2 \equiv \frac{\beta - \sqrt{2}}{\sqrt{3}\sqrt{1+\beta^2}}. \end{aligned} \tag{23}$$

Consequently, we just substitute Eq. (23) into Eqs. (3) and (10). The results of the transformation for $\eta = 0.5$ and $\chi = -1.3, -1.04, -0.7$ are displayed in Fig. 12. The BMF wave functions are being compared with the exact numerical wave functions for $l = 0, 2, 4, 6, 8$ (arranged in bars from left to right beside the BMF bar). We show the components in the four lowest SU(3) irreps, namely, $(\lambda,\mu) = (2N, 0), (2N-4, 2), (2N-8, 4)$, and $(2N-6, 0)$, in absolute values for greater legibility. The two-phonon $K = 0$ bands are approximated by two orthogonal BMF combinations from Eq. (20).

All excited bands corresponding to $\chi = -1.3$ (left-hand column) show a remarkable *coherence* among the different low-l states—the decomposition amplitudes are practically identical. Moreover, the BMF calculation predicts the amplitudes with deviations less than 2%. This is true until we reach the $\beta \times \gamma$ degeneracy line $\chi_{\rm deg}(\beta,\gamma) \approx -1.04$, which is the locus of the strongest mixing of higher l states among different-K bands, see Sec. III B. Departing slightly from the degeneracy with $\chi > \chi_{\rm deg}(\beta,\gamma)$, the coherence is restored to a certain extent, as seen in the right-hand column corresponding to $\chi = -0.7$. It does not, however, reach the precision of the $\chi < \chi_{\rm deg}(\beta,\gamma)$ side mainly because of the $\beta \times \gamma^2$ interaction, and it disintegrates finally as the rotational bands approach the saddle point energy $E_{\rm sad}$ with $\chi \to 0$. The ground band, in contrast, shows undisturbed coherence much farther toward $\chi = 0$. It is not affected by any crossings at $\chi = \chi_{\rm deg}(\beta,\gamma)$, but only by the interaction with γ^2 near $\chi = 0$, as described in Sec. III B. In general we observe that the band coherence is connected with the validity of the "rotational values" of the ratios in Eq. (16) shown in Fig. 6.

The coherent behavior of wave function components of different (here spin) states may indicate the presence of the so-called quasidynamical symmetry (QDS). The concept was introduced and discussed in Refs. [14,15,28,36–38] and describes the peculiar situations when a dynamical system does *not* possess any dynamical symmetry (the eigenstates

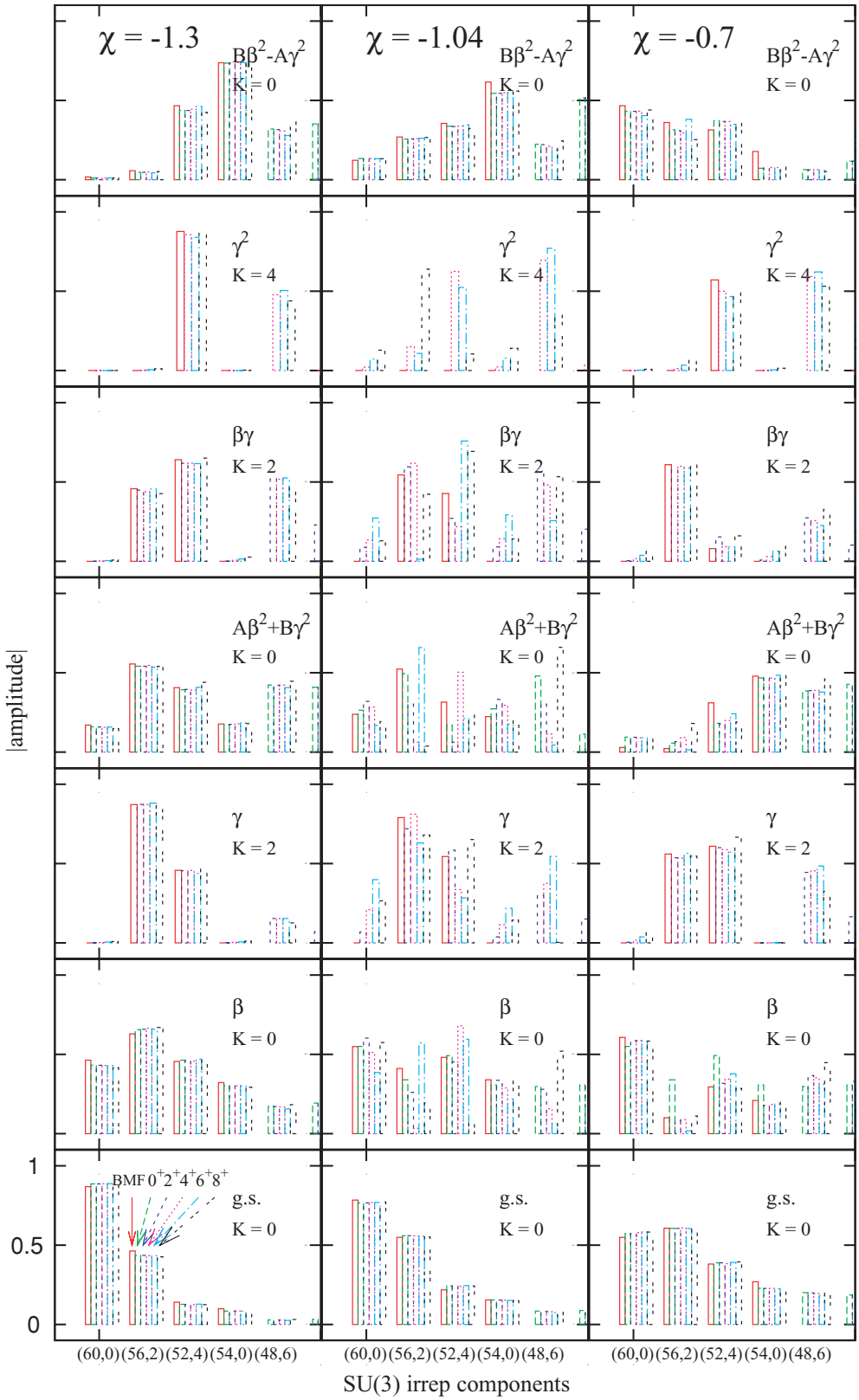

FIG. 12. (Color online) Wave function components in the SU(3) basis for $N = 30$, $\eta = 0.5$, and $\chi = -1.3, -1.04, -0.7$ in the left, middle, and right columns, respectively. The amplitudes of the BMF states and individual exact states with different l are arranged as indicated in the left-most bottom panel. The SU(3) quasidynamical symmetry is disclosed by approximate equality of the amplitudes among the rotational band members. Evidently, it is present for $\chi = -1.3$, gets disrupted by the degeneracy of β and γ excitations around $\chi_{\rm deg}(\beta, \gamma) \approx -1.04$, and is restored (although not perfectly) for $\chi = -0.7$ (especially in γ, $\beta\gamma$, and $A\beta^2 + B\gamma^2$ bands).

are mixtures of irreps of the symmetry group); however, the observable quantities (such as the energy spectrum and transition strengths) within a particular subset of eigenstates behave as if the symmetry were present. Very often, a QDS based on a group G is reflected by a coherent mixing of basis states associated with different irreps of G. This was found in several specific realizations of the quasi-SU(3) symmetry in various nuclear models [28,37,38] and turns out to hold in the IBM case as well [15].

The presence of an SU(3)-based QDS in our case is verified by direct spectroscopic observables. In Figs. 6–8, we have studied the rotational character of the lowest bands. For energies lower than $E_{\rm sad}$, we observe the $l(l+1)$ dependence of the excitation energies on spin within the bands, equality of the moments of inertia among the bands (for high enough N), and good fulfillment of the Alaga rule for the intraband $B(E2)$ transition rates. The latter ones are even in better agreement with the SU(3) predictions that bring the finite N corrections to the Alaga rule [2]. The interband $B(E2)$ transitions (Figs. 9 and 10) are also well described by the Alaga rule. Moreover, in the $N \to \infty$ limit, the interband $B(E2)$ transitions vanish when compared to the intraband transition rates. All of these features are characteristic of the SU(3) dynamical symmetry and suggest the existence of the SU(3) QDS.

Figure 12 shows that the states exhibiting the SU(3) QDS are spread across numerous SU(3) irreps with the mixing being practically independent of the spin. As shown in Refs. [15,28,36], this effect can be interpreted in terms of embedded (also called adiabatic) representations of SU(3). The observed agreement of the mixing amplitudes with the BMF predictions shows that the mechanism forming the embedded representations is well understood in terms of the angular momentum projection from a common intrinsic BMF state.

So far, QDS in IBM has been detected along the O(6)-U(5) and SU(3)-U(5) legs of the Casten triangle, in the spectral evolutions of the low-lying states. The ground-state bands have been identified as being formed by embedded representations [36] of the corresponding dynamical groups. Particularly, the character of SU(3) QDS is discussed extensively in Ref. [15].

Now, we observe that the SU(3) QDS is not limited to the $\chi = -\sqrt{7}/2$ line, but it reaches rather far into the interior of the Casten triangle. It may be attributed to the low-lying rotational bands localized below the saddle-point energy $E_{\rm sad}$ of the potential energy surface [Eq. (5)]. Degeneracies of the BMF states, predominantly the $\beta \times \gamma$ degeneracy, represent *local disturbances* to the coherent behavior of the angular momentum multiplets in the rotational bands.

B. Spectral lattices and quantum chaos

In the last part of this paper, we apply an approach inspired by a visual method of Peres [39]. The method was primarily developed to disclose regularity/chaoticity of quantum systems on the basis of the ordered/disordered character of particular lattices, deduced from and reflecting the structure of individual eigenstates. Recent studies that focused on order/chaos in collective nuclear dynamics using the lattice method can be found in Refs. [40–42].

The lattices are formed by the expectation values $\langle\psi_i|\hat{O}|\psi_i\rangle$ of an arbitrary operator $\hat{O}$ plotted against the energies $E_i = \langle\psi_i|\hat{H}|\psi_i\rangle$ of the Hamiltonian eigenstates $|\psi_i\rangle$. We extend the Peres method slightly and investigate also the variances of the operators $\mathrm{var}[\hat{O}] = \langle\psi_i|\hat{O}^2|\psi_i\rangle - \langle\psi_i|\hat{O}|\psi_i\rangle^2$, which bring additional information on the dynamical symmetry content of $|\psi_i\rangle$. The method allows us to spot individual eigenstates possessing dynamical symmetry almost in "one glimpse" while looking at the whole spectrum. A more detailed theoretical explanation of the method can be found in Ref. [41], as well as in the original paper [39].

First, let us look at the structure formed by the *low-energy* states already considered in previous sections. As the operator $\hat{O}$, we take the linear Casimir operator $C_1[\mathrm{U}(5)] = \hat{n}_d$. In Fig. 13, we plot the mean values and variances of $\hat{n}_d$ in the eigenstates corresponding to $\chi = -1.3, -1.04, -0.7, -0.4$ and $l = 0, 2, 4, 6, 8$ along the $\eta = 0.5$ line (in accord with all previous sections) and $N = 30$ bosons. The exact diagonalization results are supplemented by the BMF values corresponding to the ground-state band and one- and two-phonon

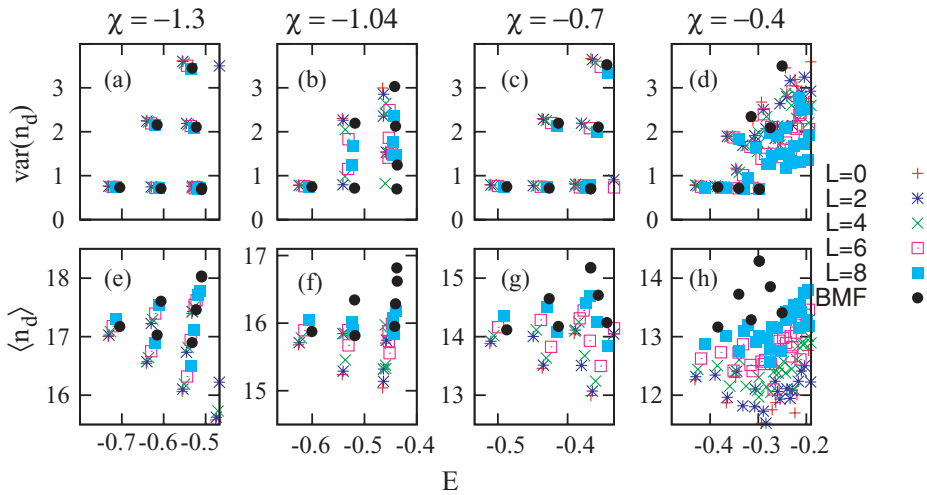

FIG. 13. (Color online) Low-energy part of the $\langle\hat{n}_d\rangle$ and $\mathrm{var}(\hat{n}_d)$ spectral lattices for $\eta = 0.5$ and $N = 30$ bosons (quantities are dimensionless). The numerical eigenstates of Eq. (1) with angular momenta $l = 0, 2, 4, 6, 8$ (crosses and squares) are supplemented by the BMF approximation (dots).

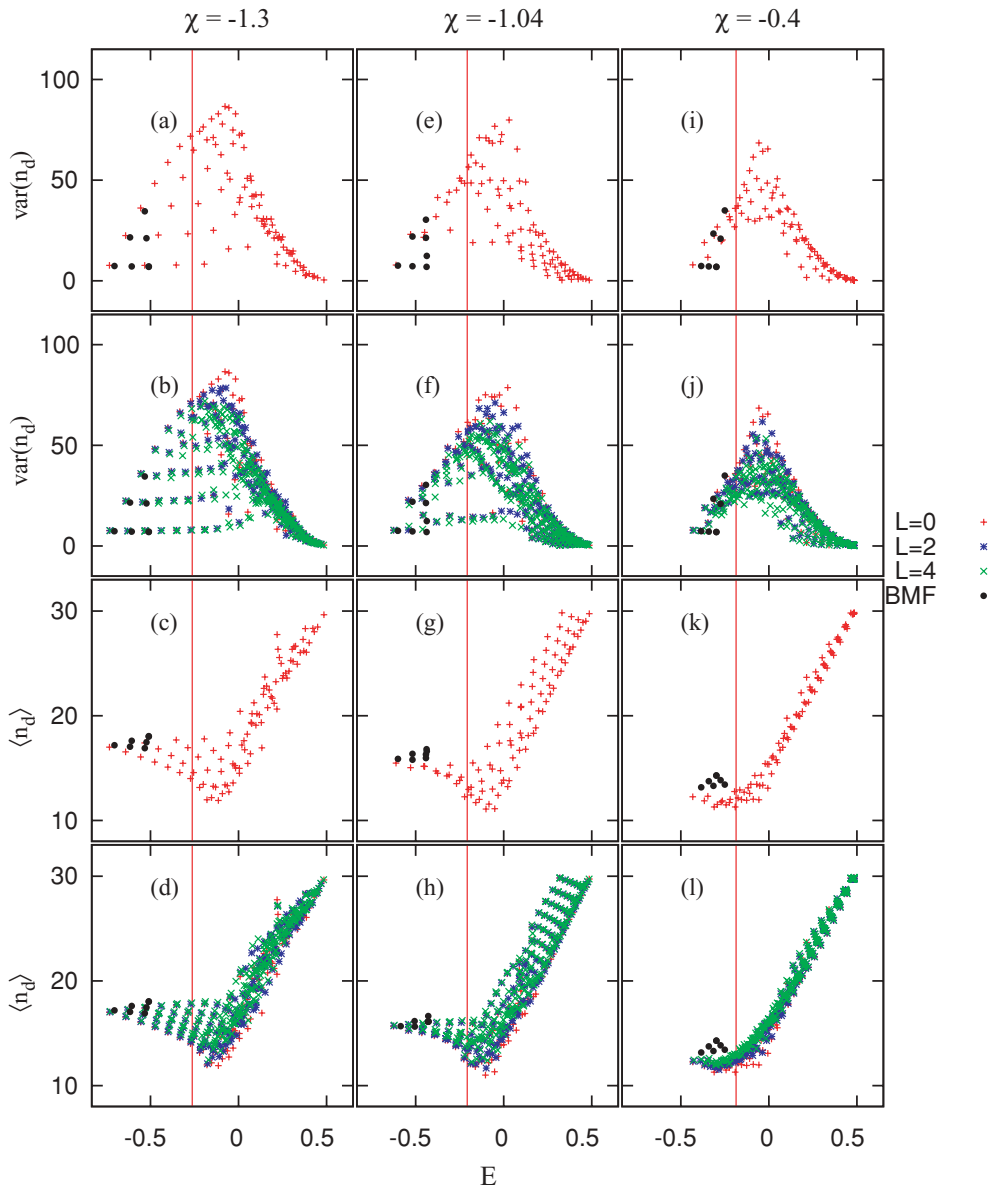

FIG. 14. (Color online) $\langle \hat{n}_d \rangle$ and var$(\hat{n}_d)$ lattices of the whole spectrum of numerical eigenstates for $\eta = 0.5$ and $N = 30$ bosons (quantities are dimensionless). Panels (a)–(d) correspond to $\chi = -1.3$, (e)–(h) to $\chi = -1.04$, and (i)–(l) to $\chi = -0.4$. The panels in the first and third row display the $l = 0$ spectrum separately, while those in the second and fourth row show a synoptical view upon the $l = 0, 2, 4$ lattices. The solid vertical lines correspond to E_{sad} for $N = 30$. For comparison, black dots corresponding to a few lowest BMF states (10) are inserted, see Fig. 13.

excitations. The two-phonon bands are mixed according to Eq. (20).

The points corresponding to numerical states with $l = 0, 2, 4, 6, 8$ bunch for $\chi \leqslant -0.7$ into sequences which represent the rotational bands. We may distinguish between bands of different K on the basis of the actual spin values being present. We observe, that the BMF states give very good prediction (especially for the variances) for $\chi = -1.3, -1.04, -0.7$ and that they start to deviate considerably for $\chi = -0.4$ because of the already discussed breakdown of the rotational band structure.

The *whole spectrum* is displayed in Fig. 14 by means of spectral lattices and variances corresponding again to $\hat{n}_d$. The values of N and η are the same as in Fig. 13. Panels in the first and third rows from the top display the separate $l = 0$ spectra, while those in the second and fourth rows each show a combined plot of spins $l = 0, 2, 4$.

The variances in Figs. 14(a) and 14(b) corresponding to $\chi = -1.3$ display notable "plateaux" at low E and reveal a series of states with distinct symmetry content, which may have been noticed already in Fig. 13. The structure can be explained well by BMF. The bottom plateau is formed

by the ground band followed by pure n-tuple γ bands as E increases, so the number of β excitations $n_\beta = 0$. The following plateaux differ by additional β excitations; hence, e.g., in the first $n_\beta = 1$ plateau, we have $\beta, \beta\gamma, \beta\gamma^2, \ldots$; in the second $\beta^2, \beta^2\gamma, \beta^2\gamma^2, \ldots$, etc. Notice that the individual low-spin states reside near each other. This creates "spots" corresponding to the low-energy rotational bands in this part of the spectral lattices, in contrast to the "chaos" for $E > E_{\rm sad}$, where the different spin lattices start to overlap without any obvious correlation.

The plateaux at $\chi = -1.3$ exist below $E_{\rm sad}$, as we may roughly say. This supports the expectation that $E_{\rm sad}$ represents a reasonable terminating point of applicability of the BMF approximation and of validity of the closely related quasi-SU(3) symmetry. The mixing of $\beta^2 \times \gamma^2$ and other equal-K bands evidently disturbs the plateau pattern at $\chi_{\rm deg}(\beta, \gamma) = -1.04$ [mixing region (i)]. Notice that all spectral lattices change dramatically at $E \approx E_{\rm sad}$ for any value of χ. A similarly pronounced change in the overall shape of lattices happens also at the local maximum of the potential of Eq. (5) at $\beta = 0$ with $E \approx 0$ (exactly zero for $N \to \infty$).

As found in Refs. [11,13], regions of appreciable regularity of the system—here observed as regular "sublattices" within the entire lattice—are *not* restricted to low energies. It is interesting to observe that the regular sublattices of states with different angular momenta l display similar patterns and often almost overlap in some energy intervals, creating the spots like in the low-energy domain. This suggests a link of the observed regularity with some (so far unknown) intrinsic states, from which the individual l states could be projected. We point out that the regularity at high energies is most pronounced around $\chi = -1.04$ (for $\eta = 0.5$), i.e., around the Alhassid-Whelan arc of regularity [10,11]—see Figs. 14(d), 14(h), and 14(l).

An important clue to understanding Poisson (regular) and Wigner (chaotic) types of level statistics inside the Casten triangle [10,11,13] is provided by the asymptotic behavior of matrix elements in Table I. The matrix elements reveal stronger repulsion among $\beta \times \gamma^2$ states [case (ii)] than between $\beta^2 \times \gamma^2$ states [case (i)]. Recall that the avoided crossings take place approximately within two wedge-shaped regions in the spectrum, as shown in Fig. 3.

We suppose that the strong repulsion in case (ii) is reflected in the prevalence of quantum chaos in a broad region of the Casten triangle located between the O(6)-U(5) and SU(3)-O(6) legs and the semiregular arc [11]. On the other hand, the relatively closely approaching levels in case (i) lead to spectral statistics similar to that of regular systems [10] in the vicinity of $\chi_{\rm deg}(\beta, \gamma)$, i.e., close to the Alhassid-Whelan semiregular arc [13].

This observation sheds light on one aspect of the increased regularity of the Alhassid-Whelan arc, namely, on its overall increase evident from the behavior of energy-averaged measures [10,11]. The BMF states of Eq. (10) may represent a subset of the Hilbert space, which shifts the overall nearest neighbor spacing distribution among energy levels more toward the Poisson distribution for any energy E in the wedge-shaped region around $\chi_{\rm deg}(\beta, \gamma)$ because of the relatively very narrowly-avoided crossings among the states (i). We stress, however, that the β and γ excitations of the type in Eq. (10) approximate the spectrum of exact eigenstates adequately at low energies $E < E_{\rm sad}$. Above $E_{\rm sad}$, the spectrum becomes more complicated with the so-far omitted modes of Eq. (9) presumably also coming into play. So the second aspect of the Alhassid-Whelan arc—namely, the intricate energy dependence of the measures of regularity at high energies $E > 0$ (connected to some more peculiar modes of motion [13] and observed also in Fig. 14)—seems to be unexplainable by merely the behavior of the BMF states.

VI. SUMMARY AND CONCLUSIONS

This paper presents a detailed study of nuclear collective dynamics at the transition from the γ-rigid to the γ-soft side of the Casten triangle. The effects connected to the transition are studied by both exact diagonalization and a mean-field approximation using intrinsic states [Eq. (10)]. The results map the locus of validity of the SU(3) quasidynamical symmetry inside the Casten triangle and reveal a novel type of critical behavior within the low-lying spectrum. Also one aspect contributing to the increase of regularity in the Alhassid-Whelan regular arc is pointed out.

We found that the SU(3) quasidynamical symmetry (and the consequent presence of rotational bands in the low-lying spectrum) is not limited to only the line $\chi = -\sqrt{7}/2$ and the ground band [15], but rather it affects the low-lying states throughout the prolate-deformed part of the Casten triangle. We observed that SU(3) QDS has an upper bound, which is set by the saddle point energy $E_{\rm sad}$ of the potential energy surface [Eq. (5)]. Basically the QDS applies to states residing inside the potential wells around the tree equivalent minima of Eq. (5). Above $E_{\rm sad}$, the structure of the eigenstates becomes radically different, which is well demonstrated by the spectral lattices. As the γ-soft regime at $\chi = 0$ is approached, the fraction of quasi-SU(3) symmetric states among the eigenstates vanishes, since $E_{\rm sad} \to E_{\rm min}$.

We can reconstruct the quasi (or "embedded") representations of SU(3) using the intrinsic mean-field states of Eq. (10) with $\gamma = 0$. Local disturbances to SU(3) QDS below $E = E_{\rm sad}$ in certain regions of the Casten triangle can be interpreted as a consequence of degeneracies and consequent mixing among the intrinsic states [Eq. (10)], most significantly by the degeneracy of the single β and γ bands and their multiphonon analogs.

We observe critical behavior of excited states around the $\chi_{\rm deg}(\beta, \gamma)$ line, although the ground-state energy and deformation evolve analytically between the γ-rigid and γ-soft dynamical regimes. The criticality affects already the lowest excited bands and is caused by the degeneracy of β and γ vibrations. Its finite-N precursors are well expressed in the interband electromagnetic transitions. The abrupt changes in the $B(E2)$ values as well as the staggering in β and γ bands may represent a suitable experimental signature of this quasicritical region, in addition to the (approximate) degeneracy of the 0_2^+ and 2_2^+ levels already pointed out in Ref. [12].

We also show how the $\beta \times \gamma$ degeneracy proliferates into the BMF spectrum at high excitation energies. It causes level

crossings among equal-K BMF states which are narrowly-avoided in comparison with the crossings due $\beta \times \gamma^2$ degeneracy resident in the most chaotic regions of the Casten triangle. We suggest this is an important source of the nearly Poisson spectral statistics observed in the exact spectra around the Alhassid-Whelan regular arc [10,11].

ACKNOWLEDGMENTS

The authors thank Pavel Stránský for useful advice. This work was supported by the Czech Science Foundation (Grant Nos. 202/06/0363 and 202/09/0084) and by the Czech Ministry of Education (under Project Nos. MSM 0021620859 and LA 314).

[1] J. B. Hattendorf, *Oxford Encyclopedia of Maritime History* (Oxford University Press, Oxford, UK, 2007).
[2] F. Iachello and A. Arima, *The Interacting Boson Model* (Cambridge University Press, Cambridge, UK, 1987).
[3] R. F. Casten and D. D. Warner, Rev. Mod. Phys. **60**, 389 (1988).
[4] R. F. Casten, in *Interacting Bose-Fermi Systems in Nuclei*, edited by F. Iachello (Plenum, New York, 1981).
[5] *Mapping the Triangle: International Conference on Nuclear Structure*, edited by A. Aprahamian, S. Pittel, J. A. Cizewski, and N. V. Zamfir, AIP Conference Proceedings Series (Springer-Verlag, New York, 2002).
[6] A. E. L. Dieperink, O. Scholten, and F. Iachello, Phys. Rev. Lett. **44**, 1747 (1980).
[7] D. H. Feng, R. Gilmore, and S. R. Deans, Phys. Rev. C **23**, 1254 (1981).
[8] E. A. McCutchan, N. V. Zamfir, and R. F. Casten, Phys. Rev. C **69**, 064306 (2004); E. A. McCutchan and R. F. Casten, Phys. Rev. C **74**, 057302 (2006).
[9] R. F. Casten, Prog. Part. Nucl. Phys. **62**, 183 (2009).
[10] Y. Alhassid and N. Whelan, Phys. Rev. Lett. **67**, 816 (1991).
[11] N. Whelan and Y. Alhassid, Nucl. Phys. **A556**, 42 (1993).
[12] J. Jolie, R. F. Casten, P. Cejnar, S. Heinze, E. A. McCutchan, and N. V. Zamfir, Phys. Rev. Lett. **93**, 132501 (2004).
[13] M. Macek, P. Stránský, P. Cejnar, S. Heinze, J. Jolie, and J. Dobeš, Phys. Rev. C **75**, 064318 (2007).
[14] D. J. Rowe, Nucl. Phys. **A745**, 47 (2004).
[15] G. Rosensteel and D. J. Rowe, Nucl. Phys. **A759**, 92 (2005).
[16] F. Pan, T. Wang, Y.-S. Huo, and J. P. Draayer, J. Phys. G: Nucl. Part. Phys. **35**, 125105 (2008).
[17] G. Rosensteel and D. J. Rowe, Nucl. Phys. **A797**, 94 (2007).
[18] P. O. Lipas, P. Toivonen, and D. D. Warner, Phys. Lett. **B155**, 295 (1985).
[19] D. D. Warner and R. F. Casten, Phys. Rev. Lett. **48**, 1385 (1982).
[20] J. Jolie, R. F. Casten, P. von Brentano, and V. Werner, Phys. Rev. Lett. **87**, 162501 (2001).
[21] J. N. Ginocchio and M. W. Kirson, Nucl. Phys. **A350**, 31 (1980).
[22] A. Leviatan, Ann. Phys. (NY) **179**, 201 (1987).
[23] J. N. Ginocchio and M. W. Kirson, Phys. Rev. Lett. **44**, 1744 (1980).
[24] J. Jolie, P. Cejnar, R. F. Casten, S. Heinze, A. Linnemann, and V. Werner, Phys. Rev. Lett. **89**, 182502 (2002).
[25] O. Scholten, in *Computational Nuclear Physics 1, Nuclear Structure*, edited by K. Langanke, J. A. Maruhn, and S. E. Koonin (Springer-Verlag, Berlin, Heidelberg, 1991).
[26] M. Caprio, J. Phys. A: Gen. Phys. **38**, 6385 (2005).
[27] J. E. García-Ramos, C. E. Alonso, J. M. Arias, P. Van Isacker, and A. Vitturi, Nucl. Phys. **A637**, 529 (1998).
[28] C. Bahri and D. J. Rowe, Nucl. Phys. **A662**, 125 (2000).
[29] H. C. Wu, A. E. L. Dieperink, and S. Pittel, Phys. Rev. C **34**, 703 (1986).
[30] A. E. L. Dieperink and O. Scholten, Nucl. Phys. **A346**, 125 (1980).
[31] J. Dobeš, Phys. Rev. C **42**, 2023 (1990).
[32] A. Arima and I. Iachello, Ann. Phys. (NY) **123**, 468 (1979).
[33] Y. Alhassid, A. Novoselsky, and N. Whelan, Phys. Rev. Lett. **65**, 2971 (1990).
[34] R. V. Jolos, Phys. At. Nucl. **67**, 931 (2004).
[35] J. M. Arias, J. Dukelsky, and J. E. García-Ramos, Phys. Rev. Lett. **91**, 162502 (2003).
[36] D. J. Rowe, P. Rochford, and J. Repka, J. Math. Phys. **29**, 572 (1988).
[37] D. J. Rowe, in *Computational and Group-Theoretical Methods in Nuclear Physics*, edited by J. Escher, O. Castaños, J. G. Hirsch, S. Pittel, and G. Stoitcheva (World Scientific, Singapore, 2004), p. 165.
[38] C. Bahri, D. J. Rowe, and W. Wijesundera, Phys. Rev. C **58**, 1539 (1998).
[39] A. Peres, Phys. Rev. Lett. **53**, 1711 (1984).
[40] P. Stránský, M. Macek, P. Cejnar, and J. Dobeš, AIP Conf. Proc. **1090**, 174 (2009); M. Macek, P. Stránský, and P. Cejnar, Int. J. Mod. Phys. E **18**, 1058 (2009).
[41] P. Stránský, P. Hruška, and P. Cejnar, Phys. Rev. E **79**, 046202 (2009); **79**, 066201 (2009).
[42] M. Macek, P. Stránský, P. Cejnar, and J. Dobeš (in preparation).

A.6 Regularity-induced separation of intrinsic and collective dynamics

[recently submitted to *Phys. Rev. Lett.*] [**J7***]

This Letter is closely related to the more detailed article [**J8***] about the observation of very high lying rotational bands in the IBM (this article follows on the subsequent pages of this thesis). The Letter brings a rather general conjecture about the influence of the regularity/chaoticity of intrinsic dynamics in many-body systems on the adiabatic separation of the intrinsic and collective motions, while the details interesting specifically for the nuclear structure audience are reserved for Ref. [**J8***].

We support the conjecture by the observations made in the IBM dynamics corresponding to the axially-deformed ground state shape. We observe that the regular non-rotating $l = 0$ states are accompanied by states with $l > 0$, that have (approximately) the same intrinsic structure as the $l = 0$ states, which is demonstrated by their (approximately) equal decompositions in the SU(3) basis.

The regularity of the quantum $l = 0$ states is determined by the Peres lattice method [Pere84a] (see the detailed elaboration of this in Ref. [**J8***]), while regularity of the classical trajectories is determined by the method of alignment indices [Skok01], and used to calculate the regular fraction f_{reg} of the classical $l = 0$ phase space. We observe a clear correlation between the regularity of the non-rotating $l = 0$ states and the occurrence frequency of the rotational bands in the whole accessible range of energies.

The author of this thesis discovered the high-lying rotational bands in the IBM on the basis of the coherent SU(3) decomposition of some states identified with the help of Peres lattices and coded an algorithm for automatic identification of the rotational bands, which is described in detail in Ref. [**J8***].

Regularity-Induced Separation of Intrinsic and Collective Dynamics

Michal Macek[1], Jan Dobeš[2], Pavel Stránský[1,3], Pavel Cejnar[1]
[1] *Institute of Particle and Nuclear Physics, Faculty of Mathematics and Physics, Charles University, V Holešovičkách 2, Prague, 18000, Czech Republic*
[2] *Nuclear Physics Institute, ASCR, Řež, 25068, Czech Republic*
[3] *Institute of Nuclear Sciences, UNAM, Mexico City, 04510, Mexico*
(Dated: March 30, 2010)

We propose that the adiabatic separation of collective and intrinsic motions in many-body systems is related to increased regularity of the intrinsic dynamics. The surmise is verified on the separation of rotations from intrinsic vibrations in the interacting boson model of nuclear structure.

PACS numbers: 21.10.Re, 21.60.Ev, 33.20.Vq, 05.45.Mt

One of the most significant effects in the dynamics of quantum many-body systems is the adiabatic separation of the intrinsic and collective motions, *e.g.*, electronic and nuclear motions in molecules [1, 2] or single-particle and collective motions in atomic nuclei [3]. This phenomenon results from the fact that the collective dynamics is typically much slower than the intrinsic one and therefore can be approximated by a gradual, nearly adiabatic variation of the intrinsic Hamiltonian. In such a situation, the mixing between intrinsic states is strongly suppressed, implying that rather similar sequences of collective excitations are built on any intrinsic state. Abundant examples of rotational and vibrational bands are known from nuclei and molecules [2, 3]. Similar physics seems to be relevant also at higher energies, where collective vibrations corresponding to nuclear giant resonances [3] are often found to be well separated from the nucleonic motions [4].

Of course, the adiabatic separation is only an approximation. It fails at high collective energies for which the intrinsic and collective time scales converge, but sometimes it is not good enough even at low energies. The degree of validity of the adiabatic approximation is not only a question of the time scales, but depends also on the susceptibility of intrinsic states to external perturbations. If the susceptibility is large, even a slow collective motion affects the intrinsic dynamics, which results in mixing up of various intrinsic states in an amount strongly depending on the collective quantum number. The collective bands loose their characteristic shape and uniformity, and eventually disappear.

In this Letter, we offer a very simple tentative criterion to assess the prevailing validity or invalidity of the adiabatic separation. It is based on the distinction between regular and chaotic dynamics as it follows from the study of classical and quantum chaos [5]. One consequence of chaos on the quantum level concerns the generic forms of high-lying (semiclassical) energy eigenstates. While an overwhelming majority of wave functions from chaotic parts of the spectrum are spread over the whole kinematically accessible domain of the configuration space [6] (with exceptions known as quantum scars [5]), the ones corresponding to regular parts usually cover much smaller regions along stable classical orbits [7]. This has an immediate consequence that a typical 'chaotic' wave function can be mixed very easily with another wave function of the same kind as there should be a considerable overlap (perturbation matrix element) between both states. On the other hand, a 'regular' wave function is likely to be more rigid since the overlap is much smaller.

Guided by these intuitive considerations, one may anticipate that states from regular parts of the intrinsic spectrum are better candidates to support adiabatically separated sequences of collective excitations than states from chaotic domains, which are prone to loose their identity under collective perturbations. Clearly, the efficiency of any perturbation depends on many circumstances, of which the most substantial is perhaps the energy separation of unperturbed states. Nevertheless, the above conclusion should hold in a statistical sense for regular and chaotic domains of comparable level densities.

To support this surmise, we employ the interacting boson model (IBM) of atomic nuclei [8]. This model describes nuclear collective dynamics in terms of a finite number N (a half of the valence particle or hole number) of mutually interacting s and d-bosons with angular momentum $l = 0$ and 2, respectively. The bosons represent pairs of valence particles (holes) and simultaneously stem from the quantization of the most relevant collective degrees of freedom in nuclei. The geometric interpretation of these motions in terms of (i) two shape variables $\{\beta, \gamma\}$ describing the intrinsic quadrupole shape of the nucleus (the degree of deformation and axial asymmetry, respectively [3]) and (ii) three Euler angles $\{\theta_i\}_{i=1}^3$ yielding its orientation in space can be obtained via the method of coherent states [9]. These two sets of variables define for us the (i) intrinsic (vibrational) and (ii) collective (rotational) degrees of freedom, on which the above-outlined idea of adiabatic separation will be probed. Note that a more general approach to intrinsic and collective dynamics in the IBM (including also collective modes in β and γ) is introduced in Ref. [10].

The IBM has a symmetry-dictated structure following from the fact that its finite Hilbert space (for a fixed N) coincides with the space of irreducible representation (irrep) of the algebra U(6) generated by $b_i^\dagger b_j$ combinations of boson creation and annihilation operators [11]. This dynamical algebra can be further decomposed into some subalgebras ending at the rotation

algebra O(3), generated by angular momentum operators $L^{(1)}_m = \sqrt{10}[d^\dagger \tilde{d}]^{(1)}_m$, where $\tilde{d}_m = (-)^m d_{-m}$ and $[A\,B]^{(l)}_m = \sum_{m',m''}(l'm'l''m''|lm)A^{(l')}_{m'}B^{(l'')}_{m''}$ (coupling of rank-l' and l'' tensors into a product with rank l and projection m). The decomposition leads to three alternative dynamical symmetries of the model, for which the spectrum is given analytically since the Hamiltonian is written in terms of commuting Casimir invariants of the algebras in one particular chain U(6)$\supset\,\cdots\,\supset$O(3) [8]. These symmetries are called U(5), SU(3), and O(6) after the first algebra in the decomposition.

The IBM Hamiltonian typically contains only one- and two-body terms. Here we employ a simplified form

$$H = \eta\frac{1}{N}n_d - (1-\eta)\frac{\sqrt{5}}{N^2}[Q^{(2)}(\chi)\,Q^{(2)}(\chi)]^{(0)}\,, \qquad (1)$$

with $\eta \in [0,1]$ and $\chi \in [-\sqrt{7}/2, 0]$ being control parameters, $n_d = \sqrt{5}[d^\dagger \tilde{d}]^{(0)}$ the d-boson number operator, and $Q^{(2)}_m(\chi) = d^\dagger_m s + s^\dagger \tilde{d}_m + \chi[d^\dagger \tilde{d}]^{(2)}_m$ the quadrupole operator. The classical phase-space dynamics and the equilibrium shape associated with the ground state can be obtained for $N \to \infty$ from the coherent-state technique. Based on the ground-state shape, the model exhibits three distinct quantum phases: spherical (for $\eta \gtrsim 4/5$), deformed axially symmetric ($\eta < 4/5, \chi \neq 0$), and deformed axially unstable ($\eta < 4/5, \chi = 0$). Associated with these are the three dynamical symmetries U(5), SU(3), and O(6), achieved for $(\eta,\chi) = (1, \text{arbitrary})$, $(0, -\sqrt{7}/2)$, and $(0,0)$, respectively. At these places and for $\chi = 0$ the Hamiltonian is integrable, hence fully regular. For the other parameter values, the system exhibits a complicated mixture of regular and chaotic features [12]. It is therefore a good environment to study effects of regularity on the adiabatic separation.

The dynamical symmetry SU(3), based on the embedding U(6)$\supset$SU(3)$\supset$O(3), exhibits perfect separation of rotational and vibrational modes [13]. Intrinsic excitations (connected with the β, γ degrees of freedom) are classified by quantum numbers λ, μ, parameterizing the eigenvalues of the SU(3) invariant, and by index K, that represents a missing label of the SU(3)$\supset$O(3) reduction and is interpreted as the angular momentum projection to the shape symmetry axis. Members of rotational bands (connected with the $\{\theta_i\}_{i=1}^3$ degrees of freedom) are classified by the O(3) quantum number l (total angular momentum), which takes the values $l = K, K+1, \ldots, K+\max(\lambda,\mu)$. In the following, we consider the sequences built on $l = 0$ states, hence $K = 0$.

Quite surprisingly, characteristic features of the SU(3) dynamical symmetry survive in a vast parameter domain within the axially deformed ground-state phase. This is a concrete implementation of a more general phenomenon named quasidynamical (effective) symmetry [14]. It turns out, in particular, that the SU(3) dynamical symmetry breaking happens in such a way that the decomposition of the actual Hamiltonian eigenstates in the (λ,μ)-basis yields very similar patterns of amplitudes for a number of states from the original rotational band. Hence, although a strong mixing among the SU(3) irreps takes place, the concept of the intrinsic state—here a common structure present in several l-members of a given sequence of states—is still applicable.

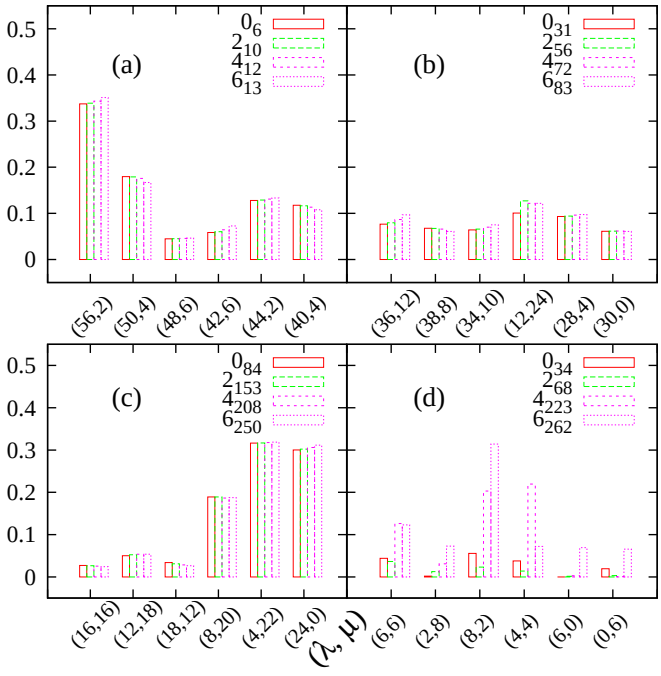

FIG. 1: Squared amplitudes from the decomposition of some eigenstates of Hamiltonian (1) with $(\eta,\chi) = (0.5, -0.9)$, $N = 30$ in the SU(3) basis (only the most important components shown). Gathered in each panel are the l_j states maximally correlated with the respective 0_i state.

As shown in Ref. [15], the rotational band structure remains intact at low energies, where the intrinsic shape is not yet completely smeared by vibrational fluctuations, *i.e.*, roughly below the energy $E_{\rm sad}$ corresponding to the saddle point of the potential energy surface $V(\beta,\gamma)$. The intrinsic dynamics in this energy domain is almost fully regular. In this Letter we show that also for excitations above $E_{\rm sad}$ the band structure is preserved at those places where the prevailing character of the intrinsic dynamics is regular. This is so despite the spread of high-energy wave functions over the space of shape variables makes the intrinsic shape indefinite.

The coherence of the (λ,μ)-mixing amplitudes for states with different angular momenta far away from the SU(3) limit is illustrated in panels (a)-(c) of Fig. 1. Here we show squared amplitudes from the expansion of individual members of several rotational bands in the SU(3) basis. Note that the bandheads of these sequences belong to different parts of the spectrum (consisting altogether of 91 $l = 0$ states for $N = 30$), panel (a) corresponding to an excited band below the saddle-point energy $E_{\rm sad}$, panels (b) and (c) to highly excited bands well above $E_{\rm sad}$. Panel (d) shows an example of a non-rotational sequence of states with a negligible overlap of intrinsic structures.

The states in each panel of Fig. 1 were grouped together by a numerical procedure, which connects states with increasing values of l on the basis of maximal correlation in their (λ,μ)-decomposition. We use the Pearson coefficient $\pi(\vec{x},\vec{y})$ measuring the amount of linear correlation between the respective components of two vectors. For asymptotic dimensions the values of π are bounded between $+1$ and -1 demarcating a perfect linear correlation and anticorrelation, respectively, while medium values indicate a weak (vanishing for $\pi = 0$) correlation. In our case, the vectors $\vec{x}$ and $\vec{y}$ are identified with probability distributions of a given pair of states in the (λ,μ)-basis. For the $K = 0$ sequences built on a presumptive $l = 0$ bandhead state 0_i the correlation coefficient $\pi(0_i, l_j)$ is evaluated for all $l = 2, 4, 6, \ldots$ states l_j (the subscript distinguishes individual states with a given angular momentum l). The sets of states in Fig. 1 are those with a maximal correlation. In the following, we will use the product $C(2,4)_i = \max_j[\pi(0_i, 2_j)]\max_k[\pi(0_i, 4_k)]$, which takes into account only the correlation of $l = 0, 2$ and $l = 0, 4$ pairs of states.

It turns out that a high correlation $\pi(0_i, l_j)$ is not a sufficient condition for states with increasing l to form a rotational band. Relative excitation energies $\Delta E(l)_i = E(l_j) - E(0_i)$ of individual band members l_j with respect to the given bandhead state 0_i should follow the law of a rotator, *i.e.*, $\Delta E(l)_i = l(l+1)/2\mathcal{J}_i$, where $\mathcal{J}_i$ stands for the moment of inertia. This means, in particular, that the ratio $R(4/2)_i = \Delta E(4)_i/\Delta E(2)_i$ should be close to 10/3. Another signature of rotational bands concerns the rates of electromagnetic transitions. In the IBM, these can be evaluated using the electric quadrupole (E2) transition operator $T^{\mathrm{E2}}(\chi) = q\,Q^{(2)}(\chi)$, where $Q^{(2)}(\chi)$ is the operator from Eq. (1) and q an effective charge. For large values of N, the intra- and inter-band E2 transitions for low-lying rotational sequences in the SU(3) limit and nearby follow the Alaga rule: the transition rate from a state with quantum numbers l and K to a state with l' and K' factorizes into a 'dynamical' part depending on both intrinsic structures and a 'kinematical' part given by $(lK2m|l'K')^2$ with $m = K' - K$ [3]. The first part cancels out if considering only ratios of transition rates between members of fixed bands. Note that absolute rates of the interband transitions are usually considerably suppressed with respect to the intraband ones.

We have performed an extensive search for the rotational bands within the IBM spectrum in the plain of control parameters η and χ. A detailed description of the procedure, which takes into account all the criteria mentioned above, is given in a parallel publication [16]. Two examples of our results are depicted in Figs. 2 and 3, corresponding to two places in the parameter plane. We show (a) the behavior of $C(2,4)_i$ for individual 0_i-based sequences throughout the whole spectrum and (b) the corresponding energy ratios $R(4/2)_i$. Electromagnetic transition rates are not shown, but they were evaluated as well, disclosing a very high coincidence degree for state sequences satisfying simultaneously (i) $C(2,4)_i$ close to 1, (ii) $R(4/2)_i$ close to 10/3, and (iii) E2 ratios following the Alaga rule. Vertical lines demarcate the energies corresponding to stationary points of the potential $V(\beta,\gamma)$, specifically, the minimum E_{min}, saddle point E_{sad}, local maximum E_{lmax}, asymptotic value E_{lim}, and global maximum E_{max} [15].

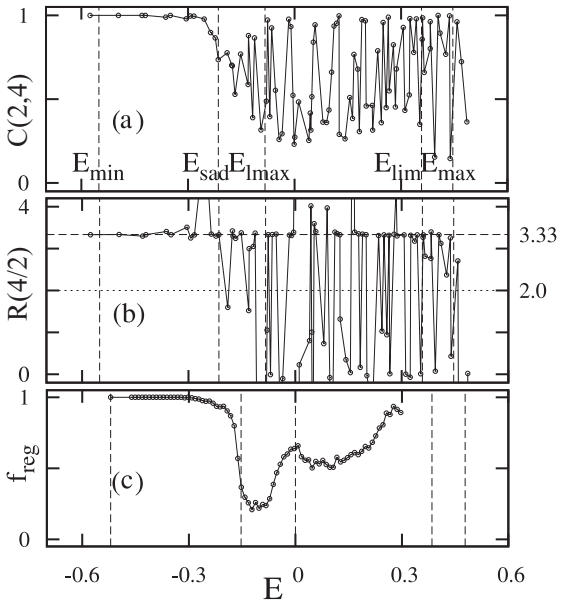

FIG. 2: $C(2,4)_i$ and $R(4/2)_i$ for rotational-like sequences at energy $E(0_i)$ (arb. units) for $(\eta,\chi) = (0.5, -0.9)$, $N = 30$, and the corresponding classical regular fraction f_{reg}. Vertical lines mark energies of stationary points.

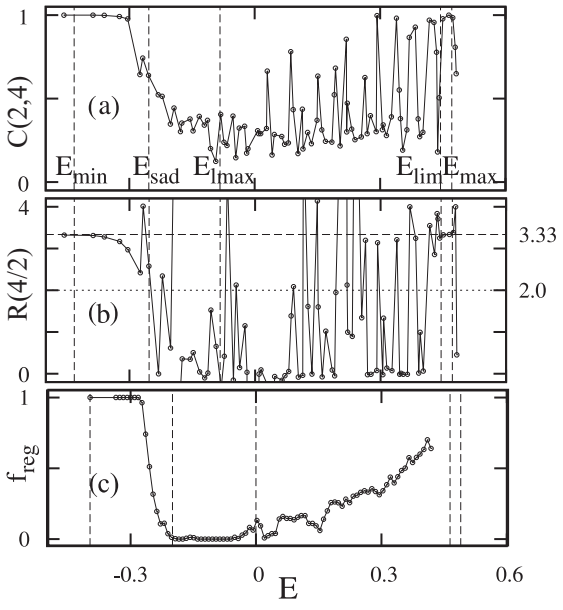

FIG. 3: The same as in Fig. 2 but for $(\eta,\chi) = (0.5, -0.5)$.

From these results it is obvious that rotational bands occur abundantly at low excitation energies, below E_{sad}. This is so in a broad territory within the axially deformed

phase, in the domain of the SU(3) quasidynamical symmetry [14, 15]. In addition, well distinguished sequences of states with increasing l satisfying criteria (i)–(iii) exist also at much higher energies, well above $E_{\rm sad}$ and sometimes up to the maximal energy of the spectrum. The occurrence of these bands is limited only to some parameter and energy domains, but even so it is rather surprising because there is no definite shape for such highly excited states. In particular, our calculations indicate that each of the high-energy bands has a common intrinsic structure, see Fig. 1(b,c), but this structure deviates substantially from that of the low-energy bands (*e.g.*, the moments of inertia in the high-energy case are larger by a factor of ≈ 3, and other observables differ as well [16]).

We find that the occurrence rate of the high-energy rotational-like bands is strongly correlated with the degree of regularity. In panels (c) of Figs. 2 and 3 we show the regularity measure $f_{\rm reg}(E)$ of the intrinsic classical dynamics. This quantity, defined as a fraction of the phase-space volume containing regular trajectories over the total volume available at energy E, was evaluated by the method of so-called alignment indices [17] on a sample of trajectories generated with randomly chosen initial conditions. The calculation was done in the nonrotating regime (considering only the shape variables β, γ and their momenta, with the Euler angles frozen) and therefore corresponds to the intrinsic dynamics. Note that in the classical limit, $N \to \infty$, we obtain slightly different values of stationary-point energies (vertical lines) than for $N = 30$. Also, the $f_{\rm reg}$ curve cannot be calculated (because of stability problems) above the asymptotic energy of the potential, thus it ends below the maximal energy. It needs to be stressed that qualitatively the same results would be obtained from the other classical or quantal measures of chaos, as follows from their detailed comparisons in Ref. [12].

Confrontation of the three panels in each of Figs. 2 and 3 (taking into account the finite-N energy shift) discloses that the regions with an increased degree $f_{\rm reg}$ of intrinsic regularity coincide with the regions showing a higher statistical occurrence of $l = 0$ bandheads of rotational-like sequences. This is in agreement with our initial surmise on the applicability of the adiabatic separation. Similar pictures can be obtained also in other places of the parameter plane (η, χ).

To summarize, we report on rotational-like bands of excitations occurring in the interacting boson model of nuclei far away from the SU(3) dynamical symmetry, where the band structure is anchored analytically. A considerable fraction of the non-SU(3) bands resides at low energies, below the saddle point of the potential, where the nucleus still has a well defined axially deformed shape and conforms to a quasi-SU(3) description [14, 15]. However, a large amount of rotational bands was identified at much higher energies, where the intrinsic structure is completely different [16]. In all cases, a positive correlation between the band occurrence rate and the degree of intrinsic regularity is observed, in agreement with the intuition of higher susceptibility of chaotic wave functions to external perturbations. These observations hint at a new tentative criterion for the statistical validity of the adiabatic approximation for collective dynamics.

This work was supported by the Czech Science Foundation (202/09/0084) and by the Czech Ministry of Education (MSM 0021620859).

[1] M. Born, J. Oppenheimer, Ann. Phys. 84, 457 (1927).
[2] H. Haken, H.C. Wolf, *Molecular Physics and Elements of Quantum Chemistry* (Springer, Berlin, 1995).
[3] J.M. Eisenberg, W. Greiner, *Nuclear Theory*, Vol. 1, Nuclear Models (North Holland, Amsterdam, 1970).
[4] D. Brink, Oxford Univ. Thesis, 1955; P. Axel, Phys. Rev. 126, 671 (1962); J.O. Newton *et al.*, Phys. Rev. Lett. 46, 1383 (1981); M. Krtička *et al.*, Phys. Rev. Lett. 92, 172501 (2004)
[5] M.C. Gutzwiller, *Chaos in Classical and Quantum Mechanics* (Springer, New York, 1990).
[6] J. Reichl, Europhys. Lett. 6, 669 (1988); B. Li, M. Robnik, J. Phys. A: Math. Gen. 27, 5509 (1994); A. Bäcker, R. Schubert, P. Stifter, Phys. Rev. E 57, 5425 (1998).
[7] P. Stránský, P. Hruška, P. Cejnar, Phys. Rev. E 79, 046202; 066201 (2009).
[8] F. Iachello, A. Arima, *The Interacting Boson Model* (Cambridge Univ. Press, Cambridge, 1987).
[9] A.E.L. Dieperink, O. Scholten, F. Iachello, Phys. Rev. Lett. 44, 1747 (1980); J.N. Ginocchio, M.W. Kirson, Nucl. Phys. A 350, 31 (1980).
[10] A. Leviatan, Ann. Phys. 179, 201 (1987).
[11] F. Iachello, *Lie Algebras and Applications*, Lecture Notes in Physics, Vol. 708 (Springer, Berlin, 2006).
[12] Y. Alhassid, N. Whelan, Phys. Rev. Lett. 67, 816 (1991); N. Whelan, Y. Alhassid, Nucl. Phys. A 556, 42 (1993); M. Macek *et al.*, Phys. Rev. C 75, 064318 (2007).
[13] H. C. Wu, A. E. L. Dieperink, S. Pittel, Phys. Rev. C 34, 703 (1986).
[14] D.J. Rowe, P. Rochford, J. Repka, J. Math. Phys. 29, 572 (1988); D.J. Rowe, Nucl. Phys. A 745, 47 (2004); G. Rosensteel, D.J. Rowe, Nucl. Phys. A 759, 92 (2005).
[15] M. Macek, J. Dobeš, P. Cejnar, Phys. Rev. C 80, 014319 (2009).
[16] M. Macek, J. Dobeš, P. Cejnar (submitted).
[17] Ch. Skokos, J. Phys. A: Math. Gen. 34, 10029 (2001).

A.7 Occurrence of high-lying rotational bands in the interacting boson model

[recently submitted to *Phys. Rev. C*] [**J8***]

This article brings a more detailed discussion of the properties of the high-lying rotational bands in IBM shown in the Letter [**J7***] and also describes the procedure for the identification of the rotational bands.

To complement the brief Letter [**J7***], this article additionally:

(i) Discusses the behavior of the SU(3) correlation coefficient, which sets the basis for the identification procedure.

(ii) Shows the Peres lattices demonstrating the quantum regularity/chaoticity of the eigenstates.

(iii) Describes the electric quadrupole $B(E2)$ transition rates within and in between the high-lying rotational bands; in particular it demonstrates the validity of the Alaga rule and reveals the structure of allowed, suppressed and forbidden inter-band transitions among the high-lying bands.

(iv) Apart from the $K = 0$ bands, it considers also the properties of bands with $K > 0$ by stydying the Peres lattices and $B(E2)$ transition rates.

Occurrence of high-lying rotational bands in the interacting boson model

Michal Macek[1], Jan Dobeš[2], Pavel Cejnar[1]
[1] *Institute of Particle and Nuclear Physics, Faculty of Mathematics and Physics, Charles University, V Holešovičkách 2, 180 00 Prague, Czech Rep.*
[2] *Nuclear Physics Institute, Academy of Sciences of the Czech Republic, 250 68 Řež, Czech Rep.*
(Dated: May 7, 2010)

We observe an adiabatic separation of collective rotations built upon a subset of intrinsic vibrational states within the interacting boson model (IBM) in the parameter domains corresponding to axially deformed ground state. The effect is not limited only to the low-lying states and closely follows the variation of quantum and classical measures of regularity. It leads to the existence of rotational bands even close to the highest accessible energies in specific regions within the IBM symmetry triangle. We conjecture a more general effect of regular intrinsic dynamics on the adiabatic separation of intrinsic and collective motion.

PACS numbers: 21.60.Ev, 21.10.Re, 21.60.Fw, 24.60.Lz, 05.45.Mt

I. INTRODUCTION

Rotational bands represent a widely observed characteristic of various mesoscopic systems ranging from molecules and atomic clusters to atomic nuclei. Their appearance signifies a decoupling of intrinsic degrees of freedom from the collective rotation of the entire body, which gives rise to characteristic $l(l+1)$ excitation energy sequences for states with different angular momentum l being built upon intrinsic bandhead states.

Apart from the rotational bands, the mesoscopic systems display numerous other regular patterns arising from different types of collective motion. In collective dynamics of nuclei, these include prominently vibrational and seniority directed energy spectra and transition probabilities [1–3]. Such highly regular properties used to be originally attributed only to exact or very slightly broken dynamical symmetries (DS) of the systems [4, 5].

Only later it was noticed, that the symmetry-like properties of observables may persist even when very strong symmetry breaking interactions occur in the Hamiltonian. This gave rise to a novel concept named quasi dynamical symmetry (QDS) [6–9] or effective symmetry [10]. Rotational bands resulting from the separation of intrinsic vibrational and collective rotational motions may be caused also by some specific forms of QDS; the one based on the SU(3) dynamical symmetry being a simple example.

In the context of nuclear dynamics, QDS of various kinds have been studied mainly in connection with the experimentally relevant *low*-energy states using various models (shell model, geometric collective model, interacting boson model) [11]. In the present paper, we take instead a more general perspective onto the particular case of the quasi SU(3) symmetry, with its separation of collective rotations and intrinsic vibrations: We ask how the adiabatic separation depends on the regular/chaotic nature of the intrinsic vibrational dynamics while looking at the *entire* range of accessible energies.

Taking the interacting boson model of the nucleus (IBM) [4], we study the rate of occurrence of the rotational bands in connection with the changing degree of regularity/chaos of the non-rotating $l = 0$ modes throughout the accessible energy domain in the axially-deformed part of the IBM symmetry triangle. The observation is made especially interesting by the very non-trivial dependence of the measures of regularity on the energy and control parameters of the model [12–14].

Recently, the low-energy rotational bands resident in IBM were explained analytically using specific SU(3)-like intrinsic β and γ excitations built upon the intrinsic boson condensates in Ref. [15]. A conjecture about the rotational character of some peculiar high-energy states was made therein. In this paper, we prove that these states indeed form rotational bands of definite angular momentum projection on the symmetry axis K and compare the occurrence rate of the $K = 0$ rotational bands with the classical and quantum measures of regularity of the non-rotating $l = 0$ modes throughout the whole energy spectrum.

The paper is organized as follows: Sec. II briefly describes the interacting boson model Hamiltonian, Sec. III presents the methods used to distinguish and visualize the regular/chaotic modes in the quantum as well as in the classical cases, Sec. IV specifies the selection algorithm for identification of rotational bands, Sec. V presents the results of the numerical calculations, which map the occurrence of rotational bands and put them in correlation with the previously observed regular regions in the parameter and energy domains, and finally Sec. VI brings the summary and conclusions.

II. INTERACTING BOSON MODEL

We consider the IBM-1 version of the interacting boson model [4], which approximates the coupled pairs of nucleons of the same type by the s- and d-bosons of total angular momentum 0 and 2, respectively, not distinguishing between proton and neutron bosons. We take

the simplified form of the Hamiltonian [13, 16, 17]:

$$\hat{H}(\eta,\chi)=\frac{\eta}{N}\hat{n}_d-\frac{1-\eta}{N^2}\hat{Q}(\chi)\cdot\hat{Q}(\chi), \tag{1}$$

which incorporates all three basic dynamical symmetries of the model. The Hamiltonian in Eq. (1) is composed of the d-boson number operator $\hat{n}_d = d^\dagger\cdot\tilde{d}$ and the quadrupole operator $\hat{Q}_m(\chi) = d^\dagger_m s + s^\dagger\tilde{d}_m + \chi[d^\dagger\tilde{d}]^{(2)}_m$. The usual convention $\tilde{d}_\mu \equiv (-)^\mu d_{-\mu}$ and the scalar product notation related to the standard tensor coupling via $\hat{A}^{(l)}\cdot\hat{B}^{(l)} \equiv (-)^l\sqrt{2l+1}[\hat{A}^{(l)}\hat{B}^{(l)}]^{(0)}_0$ are utilized. Scaling by the total number of bosons N ensures that the bounds of energy spectrum do not change for large values of N as approaching the classical limit with $N\to\infty$. We neglect the overall scaling coefficient of the Hamiltonian, i.e. we express the energy in units of this coefficient.

Two control parameters $\eta\in[0,1]$ and $\chi\in[-\sqrt{7}/2,0]$ drive the transitions of the system between the individual dynamical symmetry limits and span the symmetry (Casten) triangle of IBM [see the inset in panel (a) of Fig. 1]. The U(5), SU(3) and O(6) limits are reached setting (η,χ) to $(1,\chi)$, $(0,-\sqrt{7}/2)$ and $(0,0)$, respectively. Eigenstates of (1) are for general (η,χ) labeled by the U(6)-label N and the O(3)-label l corresponding to the angular momentum operator $\hat{L}_m = \sqrt{10}[d^\dagger\tilde{d}]^{(1)}_m$.

For the E2-transition calculations we take the quadrupole operator

$$\hat{T}^{E2}(\chi)=q\hat{Q}(\chi), \tag{2}$$

consistently with Eq. (1). In following calculations, we set the effective charge to $q=1$.

The rotational bands flaunt naturally, if we express the eigenstates in the SU(3) basis [6, 7, 15]. Therefore we briefly describe the basis here: The SU(3) representations are labeled by two non-negative quantum numbers (λ,μ), so that for a fixed number of bosons N, they form subspaces $(\lambda,\mu) = (2N,0)\oplus(2N-4,2)\oplus(2N-8,4)\oplus\cdots\oplus(2N-6,0)\oplus(2N-10,2)\oplus(2N-14,4)\oplus\ldots$. The transition from SU(3) to the O(3) subgroup is not fully reducible, i.e. there may appear more than one state of given O(3) quantum number l within a single (λ,μ) SU(3) irrep. Hence an additional quantum number (a "missing label") K is introduced to distinguish the states. K can be linked to the projection of the angular momentum on the symmetry axis of the nucleus and may take the values $K = \min\{\lambda,\mu\},\min\{\lambda,\mu\}-2,...,2,0$. The angular momentum values contained in a band with given K are $l = K, K+1, K+2, ..., K+\max\{\lambda,\mu\}$ with the exception of the $K=0$ band, where only even values $l = 0,2,4,...,\max\{\lambda,\mu\}$ are present, see Refs. [4, 5]. In the SU(3) limit, obtained setting $(\eta,\chi) = (0,-\sqrt{7}/2)$, the Hamiltonian (1) reduces to a weighted sum of the quadratic Casimir operators of SU(3) and its subgroup O(3), since $\hat{Q}(-\frac{\sqrt{7}}{2})\cdot\hat{Q}(-\frac{\sqrt{7}}{2}) = \frac{1}{2}C_2^{\mathrm{SU3}} - \frac{3}{8}C_2^{\mathrm{O3}} = \frac{1}{2}(\lambda^2+\mu^2+\lambda\mu+3\lambda+3\mu) - \frac{3}{8}l(l+1)$.

It is known [18, 19] that in the limit $N\to\infty$, equivalent to $\hbar\to\infty$, the IBM can be related to the geometrical model of nuclear collectivity [20]. The link is obtained through the N-boson condensate states

$$|\Theta,\beta,\gamma;N\rangle = \hat{R}(\Theta)\frac{1}{\sqrt{N!}}\Gamma_0^{\dagger N}|0\rangle\,, \tag{3}$$

where

$$\Gamma_0^\dagger = \frac{1}{\sqrt{1+\beta^2}}\left[s^\dagger+\beta\cos\gamma d_0^\dagger+\beta\sin\gamma\frac{d_2^\dagger+d_{-2}^\dagger}{\sqrt{2}}\right] \tag{4}$$

represents an intrinsic boson with parameters $\beta\geq 0$ and $\gamma\in[0,2\pi)$, and $\hat{R}(\Theta)$ stands for a rotation in space by the Euler angles $\Theta\equiv\{\theta_1,\theta_2,\theta_3\}$. The parameters β and γ are connected with the Bohr quadrupole deformation variables of the geometric collective model via an N-dependent relation [18]. Expanding the IBM state vectors in terms of the condensates (3) one can obtain a coordinate representation of an arbitrary operators acting on the IBM Hilbert space. For instance, the Hamiltonian turns into a differential operator

$$\hat{H} = \hat{H}(\beta,\frac{\partial}{\partial\beta},\gamma,\frac{\partial}{\partial\gamma},\Theta,\frac{\partial}{\partial\Theta})\,, \tag{5}$$

see Ref. [18], which describes the intrinsic dynamics of deformation variables β, γ, as well as the rotations of the body-fixed frame with respect to the laboratory frame.

A general procedure to specify the intrinsic and collective dynamics contained within any IBM-1 Hamiltonian was described in detail in Ref. [21]. The procedure leads to a separation $\hat{H} = \hat{H}_{\mathrm{int}} + \hat{H}_{\mathrm{coll}}$, where the collective part $\hat{H}_{\mathrm{coll}}$ may in special cases incorporate—apart from the O(3) rotations involving the Euler angles Θ—also generalized rotations involving the γ and β degrees of freedom [21]. However, if we consider only the axially deformed regime [$\chi\neq 0$, $\eta<0.8$ in the Hamilotnian (1)] far enough from the γ-soft case ($\chi=0$, $\eta<0.8$), the intrinsic and collective modes should essentially retain the intuitive meaning: the intrinsic modes corresponding to vibrations in β, γ, while the collective modes being connected with the Θ-rotations.

In particular, for the regular part of the $l=0$ spectrum, we observe that numerous $l>0$ states share a common structure within the decomposition into the SU(3) basis (λ,μ) with the non-rotating $l=0$ states. This indicates that the rotational (Θ-dependent) part of the wave function separates from the vibrational one (depending on β,γ).

III. SIGNATURES OF INTRINSIC REGULARITY

The rich regular/chaotic properties of the interacting boson model have been studied using numerous methods and from various perspectives in both the quantum and the classical cases. The key question about the degree of regularity/chaos of the dynamics has been addressed in Refs. [12, 13, 22] by inspecting statistical properties of energy spectra and transition-strengths as well

as by classical Lyapounov exponents. The content of dynamical symmetries within the mixed regular/chaotic regions of the symmetry triangle was tested by measuring wave function entropies in the decomposition of eigenstates in all relevant dynamical symmetry bases in Refs. [23]. Detailed properties of the classical trajectories within the symmetry triangle and their possible influence on fluctuations in energy spectra have been studied in Refs. [14, 24, 25].

To gain more insight into the structure of the various regular and chaotic modes in the quantum dynamics, we take a different approach here—a visual method originally proposed by Peres [26]. The method is not rigorously quantitative, but—rather in analogy to the Poincaré section method in classical mechanics [27]—it enables a qualitative distinction between regular and chaotic motion. Regular/chaotic dynamics is inferred from the regular/chaotic form of particular spectral lattices [26, 28–30]. The method was recently applied in the geometric collective model, which is closely related to the IBM, see Ref. [31], where a more detailed discussion of the relevant general background is contained.

The lattices are formed by the expectation values $O_i = \langle\psi_i|\hat{O}|\psi_i\rangle$ of an arbitrary operator $\hat{O}$ plotted against the energies $E_i = \langle\psi_i|\hat{H}|\psi_i\rangle$ of the Hamiltonian eigenstates $|\psi_i\rangle$, $i = 1, 2, 3, ...$ Due to arguments based on semiclassical quantization, the lattices of points (E_i, O_i), $i = 1, 2, 3, ...$ show regular patterns in integrable systems. In chaotic systems on the other hand, the Peres spectral lattices are formed by visually disordered collections of points. In partially regular systems, which are neither completely integrable nor fully chaotic, the lattices show a combination of ordered and disordered patterns. In addition to the identification of regularities, an ordered pile-up of states with various values of angular momentum on the same place of the lattice indicates a common intrinsic wave function and therefore hints at a band structure.

In Sec.V, we describe in particular the lattices of $\hat{O} = \hat{n}_d$ corresponding to the eigenstates of (1) with different angular momenta l. Note that other operators, as for example the Casimir operators related to the remaining symmetries of the symmetry triangle besides U(5)—namely the SU(3) and O(6) symmetries, show different lattice shapes. The identification of regularity/chaos with them is nevertheless in the cases we consider here practically equivalent to the U(5) Casimir $\hat{n}_d$. We display the lattices of $\hat{n}_d$ just because of its simple interpretation and elaborate the different operator lattices elsewhere [32, 33].

Classical limit of the Hamiltonian (1) describing the dynamics of vibrational modes with $l = 0$ has been described in detail in Refs. [12–14]. The Hamiltonian corresponding to $l = 0$ modes effectively represents a system with two degrees of freedom, which can be identified with the quadrupole deformation parameters β and γ. The individual regular trajectories are confined to two-dimensional torus-like manifolds within the four-dimensional phase space and their separation from neighboring regular trajectories changes at most polynomially in time. In contrast, the chaotic trajectories show locally an exponential mutual divergence governed by the Lyapounov exponents and cover a subset of the energy manifold of a dimension $2 < d \leq 3$, see Ref. [27].

We will be interested in the fraction of the phase-space volume showing a flow of regular trajectories $\Omega_{\rm reg}(E)$ with respect to the total volume of the phase space manifold $\Omega_{\rm tot}(E)$ corresponding to energy E for given values of η and χ in (1). This fraction, defined as $f_{\rm reg}(E) = \Omega_{\rm reg}(E)/\Omega_{\rm tot}(E)$, is numerically approximated by the fraction of regular trajectories $N_{\rm reg}$ generated within a sample of $N_{\rm tot}$ trajectories with random initial conditions spread over the whole energy manifold, cf. Ref. [34]. The regularity of individual trajectories is determined by the method of the alignment indices, [35]. Hence we obtain $f_{\rm reg} \approx N_{\rm reg}/N_{\rm tot}$, keeping always a fixed size of the sample $N_{\rm tot} = 500$.

We note that our classical calculations encounter a numerical instability of solutions of the Hamilton equations at highest energies near to and above the asymptotic value $E_{\rm lim}$ of the classical potential [14], hence we are forced to end the $f_{\rm reg}(E)$ curves slightly below the maximum potential energy.

IV. IDENTIFICATION OF ROTATIONAL BANDS

The intricately mixed, regular/chaotic spectrum of the Hamiltonian (1) may easily hide regular structures like the rotational bands for general η, χ in Eq. (1). The spectral lattice method described in Sec. III provides a heuristical first indicator of their existence, as the lattices corresponding to different angular momenta l show mutually similar regular patterns and overlap, if the states belong to rotational bands. This was pointed out in Ref. [15] and will be discussed further in Sec. V. If we however want to find and classify all rotational states into the individual bands, it is desirable to develop an automatic procedure. We propose one based on the SU(3)-decomposition of the rotational band states.

It was shown in Refs. [6, 7, 15] that the states $|i, l; N\rangle$ belonging to rotational bands with given symmetry-axis projection K do not necessarily fit into a single SU(3) irrep and can actually be strongly mixed. The mixing is however systematic, as the angular momentum multiplets show remarkable *coherence* when decomposed in the SU(3) basis $|(\lambda, \mu), K, l; N\rangle$. More precisely, the member states with particular $l = l_1, l_2, \ldots$ and ordinal numbers $i = i_1, i_2, \ldots$ within the bands display SU(3)-decompositions

$$|i, l; N\rangle = \sum_{(\lambda,\mu),K} A^{i,l}_{(\lambda,\mu),K} |(\lambda, \mu), K, l; N\rangle \,, \qquad (6)$$

in which the amplitudes $A^{i,l}_{(\lambda,\mu),K}$ are approximately constant within the multiplet, so that $A^{i_1,l_1}_{(\lambda,\mu),K} \approx A^{i_2,l_2}_{(\lambda,\mu),K} \approx$

... holds for every $(\lambda, \mu), K$.

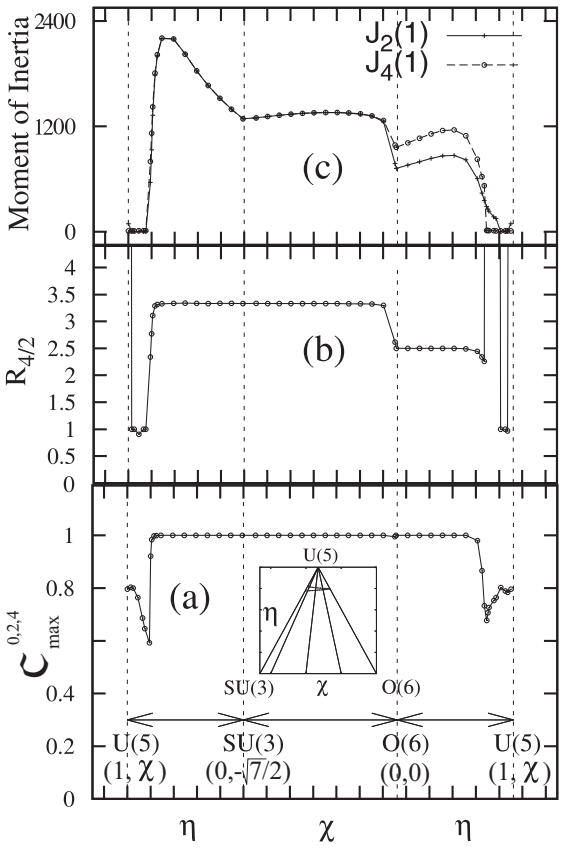

FIG. 1: Behavior of the SU(3) correlation coefficient $\mathcal{C}^{0,2,4}_{\max}$ (panel a) with the corresponding $R_{4/2}$ ratios (panel b) and the moments of inertia $\mathcal{J}_2(1)$, $\mathcal{J}_4(1)$ (in arbitrary units) calculated along the edges of the symmetry triangle for the *ground state* 0^+_1. The parameters on the x-axis measure the perimeter of the symmetry triangle [see the inset in panel (a)] and the vertical dashed lines indicate the dynamical symmetry points having the (η, χ) values as indicated in panel (a). The number of bosons $N = 32$. Notice the spherical/deformed phase transitions at $\eta_{\rm crit} \approx 0.8$ and the fact that in the spherical part near U(5), the $2^+, 4^+$ states having the maximal SU(3) correlation with 0^+_1 do *not* actually belong to the ground state band (hence the strange $R_{4/2} \neq 2$), see Fig.2.

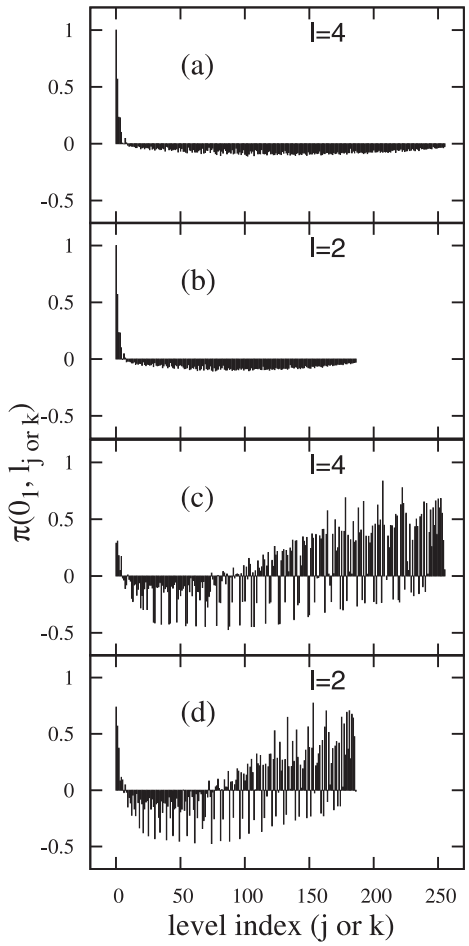

FIG. 2: Pearson correlation coefficients $\pi(0_1, 2_j)$ and $\pi(0_1, 4_k)$ showing the SU(3) correlations of the 0_1 ground state with the complete spectra of $l = 2, 4$ states for $N = 32$, $\chi = -1.32$ and two values of $\eta = 0.51$ (panels a,b), $\eta = 0.85$ (panels c,d). Notice that while in the deformed case $\eta = 0.51$, the correlations show clear preference of the ground state band members 2_1 and 4_1, in the spherical case $\eta = 0.85$ the correlations are rather evenly distributed with maxima located among the high-lying $l = 2, 4$ states.

The coherent SU(3)-decomposition suggests that the states can be obtained by angular momentum projection from a common intrinsic state [15]. Note however, that this fact alone does not imply rotational character and quasi SU(3) symmetry of the band, but only its common intrinsic origin—the pattern of excitation energies may be completely different from the $l(l+1)$ dependence, as in the case of the O(6) ground state band, which also shows a perfect SU(3) coherence. (The intrinsic ground states in both the SU(3) and the O(6) cases attain in fact the same form and differ only by the deformation $\beta_{\rm SU(3)} = \sqrt{2}$, while $\beta_{\rm O(6)} = 1$, see e.g. Ref. [21], if the O(6) intrinsic state—which spontaneously breaks the O(5) symmetry, related to γ—is chosen with $\gamma = 0$.) We will discuss this in more detail in Sec. V.

Inspired by these observations, we utilize an algorithm based on correlations between the wave functions of different-l eigenstates expressed in the SU(3) basis, followed by detailed investigation of excitation energy ratios, moments of inertia and the behavior of electromagnetic transitions. We describe the algorithm in the following steps:

(a) To measure the correlation of the wave functions, we make use of the standard Pearson correlation coefficient defined for two n-dimensional vectors X, Y as

$$\pi(X,Y) = \frac{1}{n-1} \sum_{m=1}^{n} \frac{(X_m - \bar{X})}{s_X} \frac{(Y_m - \bar{Y})}{s_Y}\,, \qquad (7)$$

where $\bar{X}$, $\bar{Y}$ and s_X, s_Y are the mean values and stan-

dard deviations of the vector components, respectively. The Pearson coefficient measures the validity of a linear dependence between X, Y and its values lie within $\pi(X,Y) \in [-1,1]$. Specifically $\pi(X,Y) = 1$, $\pi(X,Y) = -1$ and $\pi(X,Y) = 0$ indicate a perfect correlation, perfect anticorrelation and no linear correlation, respectively. The eigenvectors $|i,l;N\rangle$ of (1) with different l differ in the number of components, therefore we introduce the probability distributions $P^{i,l}_{(\lambda,\mu)}$, where we sum over the missing label K:

$$P^{i,l}_{(\lambda,\mu)} = \sum_K \left| A^{i,l}_{(\lambda,\mu),K} \right|^2 . \qquad (8)$$

Now we can link the multiindex (λ,μ) with m in Eq. (7). To simplify the notation, we introduce the symbol $\pi(l_i, l'_j) \equiv \pi(P^{i,l}, P^{j,l'})$ for the correlations between the probability distributions $P^{i,l}$, $P^{j,l'}$ corresponding to the eigenstates l_i, l'_j, where the subscripts i,j now indicate the ordinal number of the respective state in the spectrum with given l, l'.

(b) Let's proceed with the actual search of the bands throughout the spectra. Focusing our attention first to prospective $K = 0$ bands (containing sequences $l = 0, 2, 4, 6, ...$), we correlate each $l = 0$ eigenstate with the whole spectrum of $l = 2, 4, 6 \ldots$ eigenstates and for each l select the states l_j, which show the *maximum* correlation $\max_j\{\pi(0_i, l_j)\}$ for each given 0_i. These will represent the candidates for the band-members. Next, we define the product of the maximum correlation coefficients between $l = 0$, $l = 2$ and $l = 0$, $l = 4$ states

$$\mathcal{C}^{0,2,4}_{\max}(i) \equiv \max_j\{\pi(0_i, 2_j)\} \max_k\{\pi(0_i, 4_k)\} , \qquad (9)$$

to characterize the degree of correlation between the i-th $l = 0$ state and the lowest members of the prospective $K = 0$ bands with $l = 2, 4$.

(c) Having in mind the expected rotational dependence of excitation energies $E(l) - E(0) = l(l+1)/2\mathcal{J}$ within the bands, we take the prospective bandhead 0_i and calculate the "moments of inertia"

$$\mathcal{J}_2(i) \equiv \frac{3}{E(2_j) - E(0_i)} , \quad \mathcal{J}_4(i) \equiv \frac{10}{E(4_k) - E(0_i)} , \quad (10)$$

and the excitation energy ratio

$$R_{4/2}(i) = \frac{E(4_k) - E(0_i)}{E(2_j) - E(0_i)} = \frac{10}{3}\frac{\mathcal{J}_2(i)}{\mathcal{J}_4(i)} , \qquad (11)$$

for the prospective band members, with j, k in Eqs. (10), (11) being the same as in Eq. (9). It needs to be stressed that the Hamiltonian (1) contains an inherent scaling factor, which obscures a direct physical interpretation of moments of inertia if the parameters η, χ are varied. The absolute values of $\mathcal{J}_2(i)$, $\mathcal{J}_4(i)$ are meaningful therefore only for mutual comparison of individual excited bands at *fixed* values of η and χ in Eq.(1).

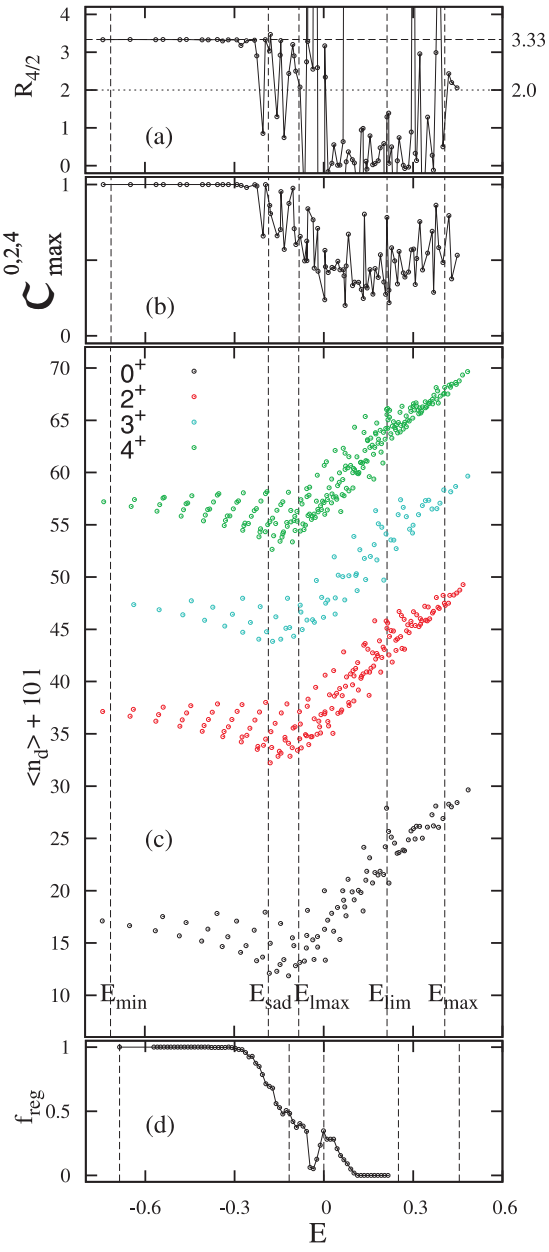

FIG. 3: (color online) IBM dynamics at $\chi = -1.32$ and $\eta = 0.5$ displays complete regularity at low energies roughly for $E < E_{\rm sad}$ (vertical dashed lines) while it becomes chaotic for $E > E_{\rm sad}$ in both quantum and classical cases. The regular part of the quantum spectrum is inhabited by SU(3)-like rotational bands, while the classical phase space by regular SU(3)-like trajectories. We show simultaneously: (panel a) excitation energy ratio $R_{4/2}$, (panel b) SU(3) correlation coefficient $\mathcal{C}^{0,2,4}_{\max}$, (panel c) the spectral lattices of the $\hat{n}_d$ operator, (panel d) the classical fraction of the phase space $f_{\rm reg}$ occupied by regular trajectories. $R_{4/2}$ and $\mathcal{C}^{0,2,4}_{\max}$ are plotted against the bandhead energies. The vertical dashed lines indicate values of the potential energy surface at stationary or asymptotic points, as indicated in panel (b), for both quantum (panels a-c) and classical cases (panel d). $N = 30$ bosons in panels (a)–(c), while $N \to \infty$ in panel (d). Energy units are arbitrary.

(d) If the rotational dynamics separates adiabatically from the intrinsic dynamics, the reduced $E2$ transition rates (both inter- and intra-band) should for $l \ll N$ be well described by the Alaga rule [36]

$$B(E2; l, K \to l', K') = \langle K'|\hat{T}^{E2}(\chi)|K\rangle^2 (lK2m|l'K')^2, \tag{12}$$

where $(lK2m|l'K')$ is the relevant Clebsch-Gordan coefficient with $m \equiv K' - K$ and $|K\rangle$ denotes an intrinsic state of given K. Calculating the relative $B(E2)$ values, we may test the Alaga rule (12) even in case that the structure of $|K\rangle$ is unknown (often relevant in our following investigations). The intrinsic matrix element $\langle K'|\hat{T}^{E2}(\chi)|K\rangle$ then drops out to leave a mere ratio of squared Clebsch-Gordan coefficients, for which only the projection values K, K' are needed—these can be deduced from the sequence of l-values within the prospective band obtained in steps (a)–(c).

(e) We say that the states 0_i, 2_j and 4_k belong to a $K = 0$ rotational band, if they satisfy simultaneously:

$$\mathcal{C}^{0,2,4}_{\max}(i) \approx 1\,, \tag{13}$$

$$\mathcal{J}_2(i) \approx \mathcal{J}_4(i)\,, \tag{14}$$

$$\frac{B(E2; 4_k \to 2_j)}{B(E2; 2_j \to 0_i)} \approx \frac{(4,0,2,0|2,0)^2}{(2,0,2,0|0,0)^2}\,. \tag{15}$$

The condition (14) may be eventually replaced by $R_{4/2}(i) \approx 10/3$, according to Eq. (11).

The procedure (a–e) may be generalized considering bands of different K and angular momenta $l > 4$ in a straightforward way. We only take the i-th bandheads with $l_i = K$ and define the correlations $\mathcal{C}^{l_i,l'_j,l''_k}_{\max}(i)$, excitation energy ratios $R_{l''_k/l'_j}(i)$ and the moments of inertia $\mathcal{J}_{l'_j}(i)$, for the excited states l'_j, l''_k in analogy with the previous paragraphs. For example the moments of inertia become

$$\mathcal{J}_{l'_j}(i) = \frac{1}{2(E_{l'_j} - E_{l_i})}\left[l'(l'+1) - l(l+1)\right]\,. \tag{16}$$

We note that alternatively to the selection (a–e) based on the SU(3) correlations, the band members may be selected naturally also on the basis of $B(E2)$ transition rates. To consider the states l_i to form a rotational band, we require in this case that the $B[E2; l_i \to (l+2)_j]$ rates have to dominate the other (interband) rates $B[E2; l_i \to (l+2)_{j'}]$, $j' \neq j$, while the sequence has to show a well defined moment of inertia $\mathcal{J}_l(i) \approx \mathcal{J}_{l+2}(i)$. In Sec. V B, we utilize a recursive tracing of the chains of states $l_i \to (l+2)_j$ starting from the bandheads to show, that the rotational bands often reach up to very high angular momenta $l \approx N/2$, where the moment of inertia changes abruptly. We have checked, that both methods indeed lead to the same identification of the SU(3)-like rotational bands.

V. NUMERICAL RESULTS

A. Edges of the symmetry triangle

We diagonalize the Hamiltonian (1) numerically in the U(5) basis using an adaptation of the PHINT code [37] for different η, χ and N and consequently decompose the eigenstates into the SU(3) basis obtained for $\eta = 0$ and $\chi = -\sqrt{7}/2$. Then we apply the selection algorithm of Sec. IV and also plot the spectral lattices as described in Sec. III. Finally, we supplement the quantum calculations by evaluating the classical regular fractions $f_{\rm reg}(E)$ described at the end of Sec. III.

To get a feeling for the behavior of the quantities introduced in Sec. IV, we inspect them at first for the ground state along the well understood perimeter of the symmetry triangle. In Fig. 1, the panel (a) displays the correlation $\mathcal{C}^{0,2,4}_{\max}(1)$, panel (b) the ratio $R_{4/2}(1)$ and panel (c) the moments of inertia $\mathcal{J}_2(1)$, $\mathcal{J}_4(1)$ corresponding to 0_1 and its maximally correlated $l = 2$ and 4 counterparts for $N = 32$. In all panels, the x-axis is split into parts corresponding to the respective parameter driving the transitions along the three edges of the symmetry triangle. For the U(5)-SU(3) edge it is η changing from 1 to 0 with fixed $\chi = -\sqrt{(}7)/2$, for the SU(3)-O(6) edge it is χ changing from $-\sqrt{7}/2$ to 0 with fixed $\eta = 0$, and finally for the O(6)-U(5) edge it is again η changing now from 0 to 1 with $\chi = 0$, as indicated in panel (a). The dynamical symmetry points are denoted by vertical dashed lines.

The panel (a) in Fig. 1 illustrates that the ground state 0_1 shows perfect SU(3) correlations with the yrast states 2_1, 4_1 throughout the deformed part of the symmetry triangle—quite surprisingly even in the O(6) limit and along the deformed part of the O(6)-U(5) edge. This might be a consequence of the non-standard $\ddot{\rm SU}(3)$ subgroup present in the subgroup chain O(6) $\supset$ $\ddot{\rm SU}(3)$ $\supset$ SU(2) $\times$ U(1) within the O(6) limit, and a related quasi $\ddot{\rm SU}(3)$ symmetry further along the O(6)-U(5) edge (we do not however inspect it here). This chain is not considered usually in IBM, since it does not conserve the rotational O(3) symmetry, it is however relevant for the intrinsic dynamics, see Ref. [21].

In order to distinguish the rotational bands, we therefore need to employ the ratio $R_{4/2}$ of Eq. (11), or eventually the moments of inertia $\mathcal{J}$ of Eq. (10) in addition to $\mathcal{C}^{0,2,4}_{\max}$. Indeed, panels (b) and (c) of Fig. 1 show that these characteristics abruptly change in the vicinity of the O(6) limit: the excitation energy ratio changes from the rotational values $R_{4/2} \approx 10/3$ to the seniority-based values $R_{4/2} \approx 2.5$ and the band simultaneously loses a well defined moment of inertia ($\mathcal{J}_2$ and $\mathcal{J}_4$ clearly differ). The SU(3) correlations, on the other hand, start to deviate from $\mathcal{C}^{0,2,4}_{\max}(1) \approx 1$ only near to the deformed-to-spherical phase transition at $\eta_{\rm crit} \approx 0.8$.

We point out one "artifact" of our SU(3)-focused method: In the spherical region near the U(5), the $l = 2, 4$ states showing maximum SU(3) correlations with

0_1 actually belong to a rather high lying spectrum, *not* to the ground state band (vibrational in this case). It leads to the fluctuating values of $R_{4/2}$ near U(5) in panel (b) Fig. 1, which are obviously different from the vibrational value $R_{4/2} = 2$. We illustrate it in Fig. 2, where we plot the Pearson coefficients $\pi(0_1, 2_j)$, $\pi(0_1, 4_k)$ correlating the ground state 0_1 with the whole spectra of $l = 2, 4$ eigenstates for $\chi = -1.32$ and two values of η: a prolate-deformed $\eta = 0.51$ (panels a,b) and a spherical $\eta = 0.85$ (panels c,d). Notice that in the deformed part—in contrast to the spherical part—the SU(3) correlations clearly prefer the lowest-energy 2_1 and 4_1 (panels a,b), while in the spherical part, the maxima are located "randomly" among high-lying excitations (panels c,d).

Note also that the decreasing moment of inertia toward the SU(3) point in panel (c) of Fig. 1 (which is in contrast to physical expectations) results from an inherent scaling factor of the Hamiltonian in the parametrization (1) and has no experimental consequences.

B. Interior of the symmetry triangle

Having understood the behavior of the SU(3) correlation coefficient $\mathcal{C}^{0,2,4}_{\max}$, we may start to explore the interior of the symmetry triangle. In Figs. 3, 4, 5, we display the SU(3) correlations $\mathcal{C}^{0,2,4}_{\max}$ (panels a), the ratios $R_{4/2}$ (panels b), spectral lattices of $\hat{n}_d$ (panels c) and the classical regular fraction of the phase space $f_{\rm reg}$ (panels d) corresponding to three different values of $\chi = -1.32$, -0.9 and -0.5, respectively, always lying within the prolate-deformed part of the triangle with $\eta = 0.5$ and $N = 30$ (except panels d, where $N \to \infty$). These points make a suitable representative sample of the dynamics in the prolate-deformed part, see also [15, 33]. We discuss these cases separately in the blocks (i), (ii) and (iii) below.

The panels of Figs. 3–5 are arranged vertically with the same energy scale on the horizontal axis to facilitate a direct comparison. The vertical dashed lines in panels (a–c) correspond to the stationary points or the asymptotic value of the potential energy surface $V(\beta, \gamma) = \langle {\rm gs}; N|\hat{H}|{\rm gs}; N\rangle$, derived using the intrinsic condensate from Eq. (3) for the respective value of N: in order of increasing energy, they denote the global potential minimum $E_{\rm min}$, the saddle point $E_{\rm sad}$, the local maximum $E_{\rm lmax}$ corresponding to the potential energy at zero quadrupole deformation $\beta = 0$, the asymptotic value $E_{\rm lim}$ at $\beta \to \infty$ and finally the global maximum $E_{\rm max}$, see Fig. 6. In panels (d), the lines denote the corresponding points of the classical potential obtained for $N \to \infty$, in analogy.

(i) At $\chi = -1.32$, $\eta = 0.5$ (see Fig. 3), lying at the SU(3)-U(5) edge of the symmetry triangle, we observe perfect SU(3) correlations accompanied by $R_{4/2} \approx 10/3$ for the low-lying states roughly up to the saddle point $E_{\rm sad}$, while for $E > E_{\rm sad}$ the ordered behavior breaks down.

The qualitative difference in the quantum spectrum for

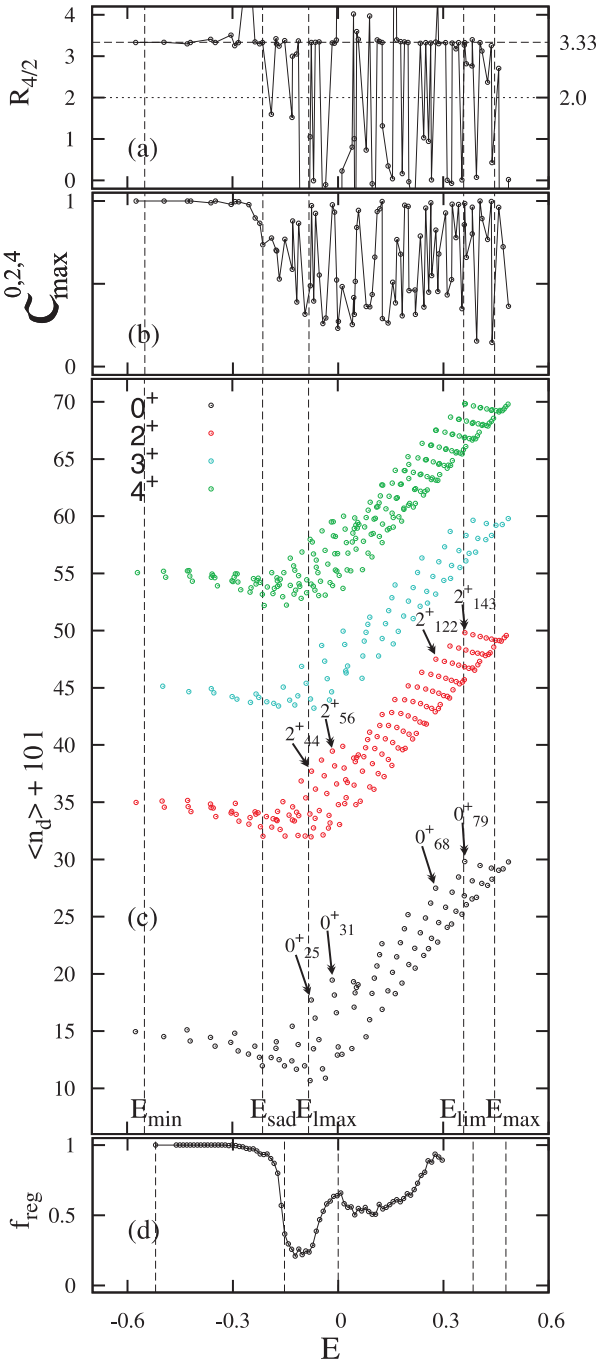

FIG. 4: (color online) The same quantities as in Fig. 3 show that at $\chi = -0.9$, significant regularity appears at intermediate energy $E \approx 0$ as well as in a broad high-energy interval reaching up to the maximum energy $E_{\rm max}$ in addition to the omnipresent regularity for $E < E_{\rm sad}$ (vertical dashed lines). In the regular regions, most states show characteristics of rotational bands (panels a,b). The values of N and η are the same as in Fig. 3.

$E < E_{\rm sad}$ and $E > E_{\rm sad}$ is illustrated by the spectral lattices of $\hat{n}_d$ in panel (c): the lattices for $l = 0, 2, 3$ and 4 (relatively shifted here by $\Delta n_d = 10l$ for clear visual separation of the lattices corresponding to the states with different angular momenta l) display mutually very similar pattern at low E, while they become disordered at high E. The lattice-points of different l form bunches, lying close in E and $\langle \hat{n}_d \rangle$ and inspecting them closely, we may identify sequences $l = 0, 2, 4$ and $l = 2, 3, 4$ corresponding to $K = 0$ and $K = 2$ bands, respectively. It means, that if the artificial l-dependent shift of the lattices with different angular momenta were removed, the states with sequential values of l belonging to the same rotational band would be located very near to each other (they would nearly overlap, cf. Fig. 7). In Ref. [15], these structures were identified as rotational bands built upon intrinsic quasi SU(3) β and γ excitations.

In parallel to the quantum measures, the classical measure $f_{\rm reg}$ shows complete regularity of $l = 0$ modes for $E < E_{\rm sad}$, with a gradual decrease to $f_{\rm reg} \approx 0$ at high energies. The regular trajectories at $E < E_{\rm sad}$ vibrate within the potential well around the minimum and very much resemble the β and γ vibrations found in the SU(3) limit.

(ii) At $\chi = -0.9$, $\eta = 0.5$ (see Fig. 4), which corresponds to the Alhassid-Whelan semiregular arc inside the symmetry triangle [12–14], the dynamics at $E > E_{\rm sad}$ changes quite dramatically. In both the classical $f_{\rm reg}$ as well as in the $\hat{n}_d$ spectral lattices, we may notice two novel distinct regular regions to appear—one at $E \approx 0$ and second reaching to the highest accessible energies $E \approx E_{\rm max}$—in addition to the always present regularity at $E < E_{\rm sad}$.

Looking at the SU(3) correlations and $R_{4/2}$, we immediately see that a substantial fraction of the $l = 0$ states at $E \approx 0$ and even more significantly at $E \approx E_{\rm max}$ represent bandheads of $K = 0$ bands. Zoom into the high energy part of the lattice around $E \approx E_{\rm max}$ in Fig. 7 (now without the l-dependent shift) shows, that the $K = 0$ bands are accompanied by $K = 2$ bands sitting in the "vacancies" of the $K = 0$ lattice, as can be seen from the alternating pattern of $l = 0$ or $l = 3$ states nearly overlapping with the lattice of $l = 2$ states. For sake of clarity, we show only the positions of $K = 0, 2, 3$ bands, the alternating pattern however extends to higher values of K with $K = 4$ bands resident in near vicinities of $K = 0$ bands, $K = 6$ bands near $K = 2$, etc... In fact, the neighboring $K = 0, 4$ bands can be identified in the high-energy part of the $l = 4$ lattice in panel (c), Fig. 4, under close inspection. This reveals a picture indicating a successive composition of multiple γ-like vibrational modes.

The moments of inertia (see Fig. 8) provide an alternative aspect, which illustrates further the rotational character of the regular states. The three regular regions at low, intermediate and high energy, corresponding to $K = 0$ bandheads 0_i can be identified by $\mathcal{J}_2(i) \approx \mathcal{J}_4(i)$. Notice that the moments of inertia of the low-energy family of rotational bands found below $E < E_{\rm sad}$ decrease with energy, while for the other families—resident at $E \approx 0$ as well as in the highest part of the spectrum—they grow with E, attaining about 3-times greater values for the highest-lying bands compared to the ground-state band. The values of $\mathcal{J}_l(i) \approx 0$, $l = 2, 4, ...$ are typical for chaotic $l = 0$ states, in contrast. Notice that the regular bands may actually retain well defined moments of inertia up to very high angular momenta, as exemplified in the inset of Fig. 8.

(iii) At $\chi = -0.5$, $\eta = 0.5$ (see Fig. 5), the spectral lattices in contrast to the previous case are apparently much more chaotic and do not show very clear regular patterns apart from the low-energy interval $E < E_{\rm sad}$. In particular, the regular region at $E \approx 0$ disappears. The lattices in the highest part of the spectrum seem to be a superposition of regular and chaotic sublattices. The classical $f_{\rm reg}$ (panel d) supports this interpretation, as it shows regularity for $E < E_{\rm sad}$, a complete chaos at intermediate energy $E \approx 0$ and a slight increase of regularity at high energies. The regularities may be again identified with the rotational bands on the basis of SU(3) correlations and $R_{4/2}$ (panels a,b).

To demonstrate further the rotational character of states found in the regular parts of spectrum, we analyze the $B(E2)$ transition strengths both within and in between the bands. In Fig. 9 we plot the relative $B(E2; l \to l + 2)$ calculated for $K = 0$ and $K = 2$ bands from the intermediate $E \approx 0$ energy spectrum at $\chi = -0.9$, $\eta = 0.5$ and $N = 30$ and compare them with the ratios of squared Clebsch-Gordan coefficients given by Eq. (15). Apparently, a very good agreement is observed. Similarly, Fig. 10 shows the relative $B(E2; l \to l + 2)$ values in the high energy $E \approx E_{\rm max}$ region. Location of the latter bands within the high-energy section of the $\hat{n}_d$ spectral lattices is shown in detail in Fig. 7. Again, the Alaga rule is well preserved (with the accuracy demonstrated in Fig. 10) in the upper-left part of the lattice, where we indicate the directions of "allowed" transitions by heavy arrows. Apart from this very regular region, there is a thin rather chaotic strip in the lower-right part of the lattice, where the states no longer fit into rotational band sequences [cf. panels (a–c) in Fig. 4].

The structure of the "allowed", "suppressed" and "forbidden" interband transitions in the upper-left part of Fig. 7 is remarkable (the same pattern holds in the $E \approx 0$ regular region), since it follows the pattern of quasi SU(3) bands resident at low-energies $E < E_{\rm sad}$, cf. Ref. [15]. Firstly, the transitions between different bands of equal K as well as those between the bands differing by $\Delta K \geq 4$ vanish (are suppressed by a factor less than 10^{-6}, more precisely). We observe non-vanishing transitions only in between neighboring bands differing by $\Delta K = 2$, which are $5 - 10$ times weaker in comparison with the intraband rates for $N = 30$. (We note that in the vicinity of the ground state band, this suppression factor is much greater—about 300, in contrast.) In particular, the interband transitions occurring

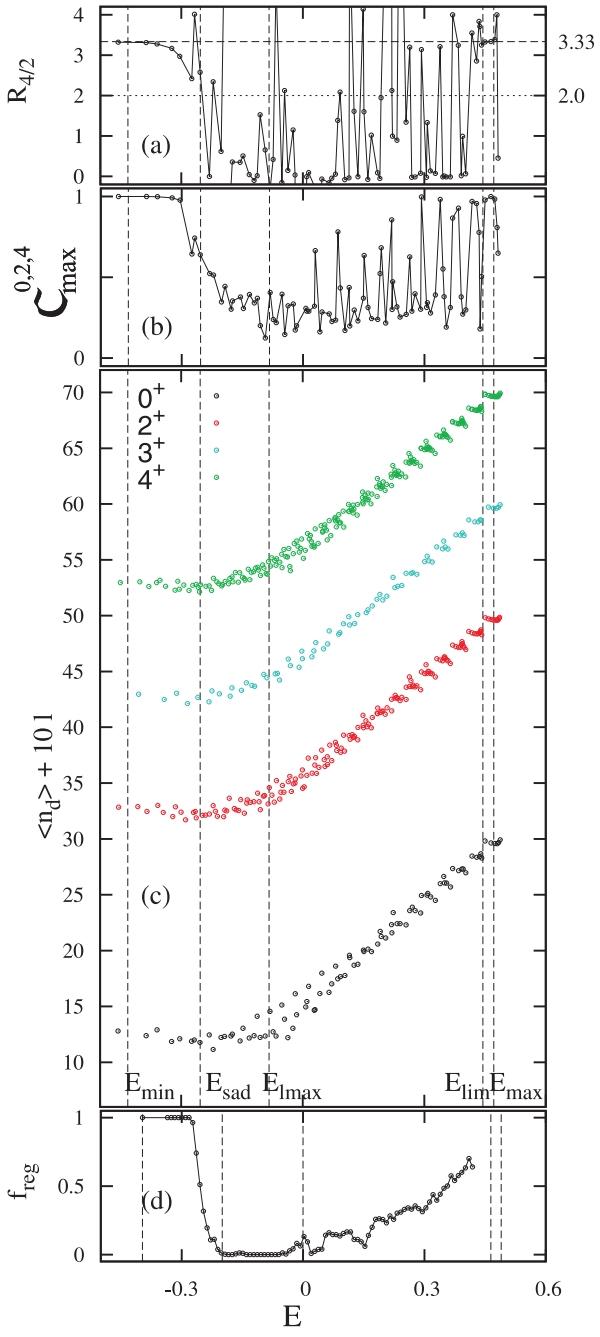

FIG. 5: (color online) The same quantities as in Figs. 3, 4 show that at $\chi = -0.5$, the dynamics is mostly chaotic apart from $E < E_{\rm sad}$ (vertical dashed lines) and a narrow region near to $E_{\rm max}$, where we may see a few rotational bands (panels a,b). The values of N and η are the same as in Figs. 3, 4.

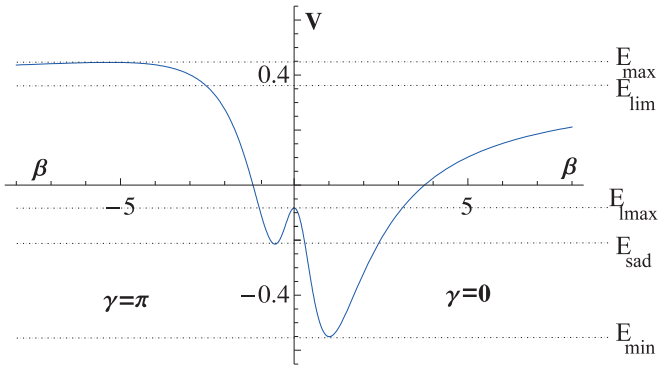

FIG. 6: Stationary and asymptotic values (horizontal dot-dashed lines) of the potential energy surface $V(\beta, \gamma)$ plotted here for $(\eta, \chi) = (0.5, -0.9)$ and $N = 30$ bosons. This particular point corresponds to the situation plotted in Fig. 4, the shape of the potential however essentially represents the potentials throughout the whole prolate deformed part of the Casten triangle.

in the directions indicated by heavy arrows in Fig. 7 are two orders of magnitude stronger than those in the perpendicular direction (thin dashed arrows). This resembles the structure among the multiple β, γ excitations at low energies [15], where $\Delta K = 2$ transitions between bands differing by the number of β-excitations n_β are suppressed in comparison with those differing only by the number of γ-excitations n_γ, while having $\Delta n_\beta = 0$ at the same time. However, the intrinsic states underlying the high-energy rotational bands should have a different form than the mean field excitations used in Ref. [15], since the exact and mean-field spectral lattices are completely different at high E. We remark finally, that a few of the high-energy states belonging to the "chaotic strip" in the lower-right part of the lattice in Fig. 7 form U(5)-like sequences with $R_{4/2} \approx 2$, as revealed by tracing the dominant $B(E2)$ transition rates.

VI. SUMMARY AND CONCLUSIONS

We have revealed families of high-energy rotational bands in the spectrum of the interacting boson model in parameter domains corresponding to the nuclei with axially symmetric ground state deformation. The bands show signatures of SU(3) quasi dynamical symmetry in the $l(l+1)$ excitation energy pattern, in the inter- and intra-band $E2$ transition rates and within the decomposition of eigenstates in the SU(3) basis.

Let us stress that the results discussed here differ substantially from those of Ref. [38], where the SU(3)-like degeneracies were identified along the Alhassid-Whelan (AW) arc in the low-energy part of the spectrum, which occur here below or close to the saddle point energy $E_{\rm sad}$. The rotational bands that we bring to attention in the present paper lie much higher in energy. Indeed, as it was shown already by Alhassid and Whelan [12, 13], the partially increased regularity of the AW arc (relative to the neighboring regions) is brought about essentially by the regular high-lying modes, not the low-energy dynamics, which is almost completely regular in the entire symmetry triangle.

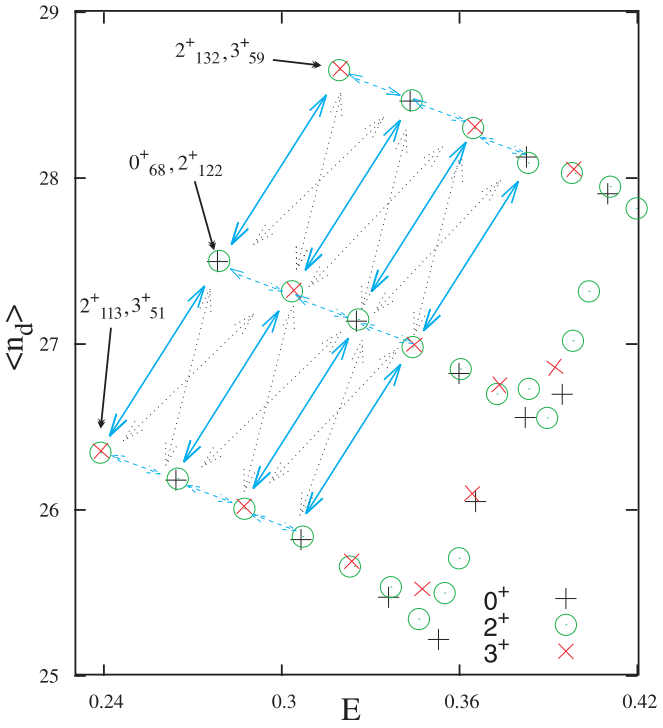

FIG. 7: (color online) Zoom into the high-energy part of the $\hat{n}_d$ lattice at $\chi = -0.9$ from Fig. 4 for $l = 0, 2, 3$ states. Allowed, suppressed and forbidden interband $E2$ transitions are schematically marked by heavy, dashed and dotted arrows, respectively. Allowed transitions (heavy arrows) among $K = 0$ and $K = 2$ rotational bands follow the Alaga rule considerably, as do the intraband transitions, cf. Fig. 10. Interband transitions in the "perpendicular" directions (thin dashed arrows) are suppressed by $\approx 10^{-2}$, while those marked by dotted arrows are forbidden. The intraband $B(E2)$ values are 5-10 times higher than the allowed interband values in this energy interval for $N = 30$. Note that the positions of $l = 0$ and $l = 3$ states distinguish $K = 0$ and $K = 2$ bands in the regular part of the lattice.

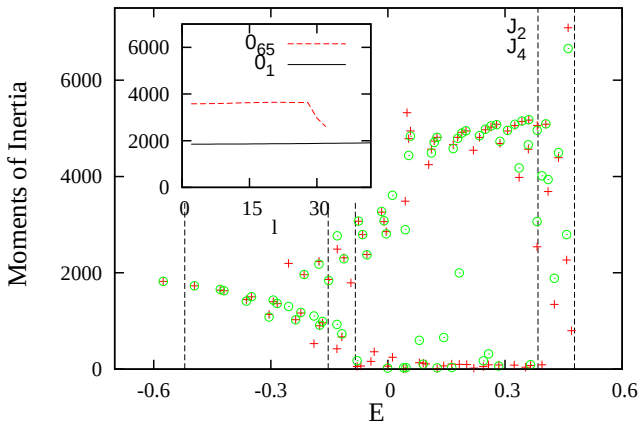

FIG. 8: (color online) The moments of inertia $\mathcal{J}_2(E)$ and $\mathcal{J}_4(E)$, Eq.(10), plotted against the energy of the $l = 0$ states in the most regular region (Alhassid-Whelan arc) at $\eta = 0.5$, $\chi = -0.9$ and $N = 30$. Values of $\mathcal{J}_2(E) \approx \mathcal{J}_4(E)$ correspond to the $l = 0$ bandheads of the $K = 0$ rotational bands. Similarly to Fig. 4, the plot reveals three distinct families of regular rotational bands resident at low, intermediate and high energies, respectively. The quantities are shown in arbitrary units, related to an overall scaling of the Hamiltonian (1) and the vertical lines indicate the stationary and asymptotic values of the potential energy surface as in Figs. 3-5. The inset shows the l-dependence of the moments of inertia of the i-th band $\mathcal{J}_l(i)$ through high values of l for two $K = 0$ bands with $i = 1$ and $i = 65$ at $\eta = 0.5$, $\chi = -1.04$ and $N = 30$. The band headed by 0_{65} sharply terminates at $l = 28$.

Our findings cannot be interpreted as an explanation of the increased regularity in the AW arc. Instead we suggest a sort of an inverse optics: We do not try to explain the origin of regular or chaotic character of the intrinsic modes in specific parameter and energy domains. Rather in contrast, we accept it and look for possible consequences upon the separation of intrinsic and collective degrees of freedom.

Within our results, we observe a strong correlation between the occurrence rate of the rotational bands and the variation of classical and quantum degree of regularity of the intrinsic dynamics, as signified by the regularity of the $l = 0$ motions. This is remarkable especially if we appreciate the complicated dependence of the measures of regularity on energy. The low-energy dynamics, bounded from above roughly by the saddle point energy $E_{\rm sad}$, is regular throughout the axially-deformed part of the symmetry triangle and in this entire domain it displays rotational characteristics, as demonstrated in Figs. 3-5. As it was shown in Ref. [15], the rotational quasi SU(3) behavior (in the sense of coherent SU(3) decompositions of band-member eigenstates, inter- and intra-band $B(E2)$ values and the excitation energy ratios within the bands) is here slightly disturbed only in the vicinities of band crossings, which cause mixing of eigenstates between the crossing bands.

Above the saddle point energy $E_{\rm sad}$, the rotational bands with well-defined projection on the symmetry axis K appear quite surprisingly also in the intermediate- and high-energy domains, precisely in the regions showing increased classical and quantum regularity. The highest occurrence of rotational bands is observed in the semiregular Alhassid-Whelan arc. However, it is not the sole locus of their existence, since they occur also—apart from the above-mentioned $E < E_{\rm sad}$ energies—in a broad region between the AW arc and the O(6)-U(5) edge; in this region, they reside only within a more narrow interval at the very high energies close to $E \approx E_{\rm max}$ (see Sec. V).

Our observation suggests, that the chaotic non-rotational $l = 0$ states are more prone to mixing, if rotation of the whole nucleus comes into play, while the regular states are protected by their symmetry and retain their properties. This may be intuitively understood from the phenomenology of semiclassical regular/chaotic wave functions in generic quantum-chaotic systems: the

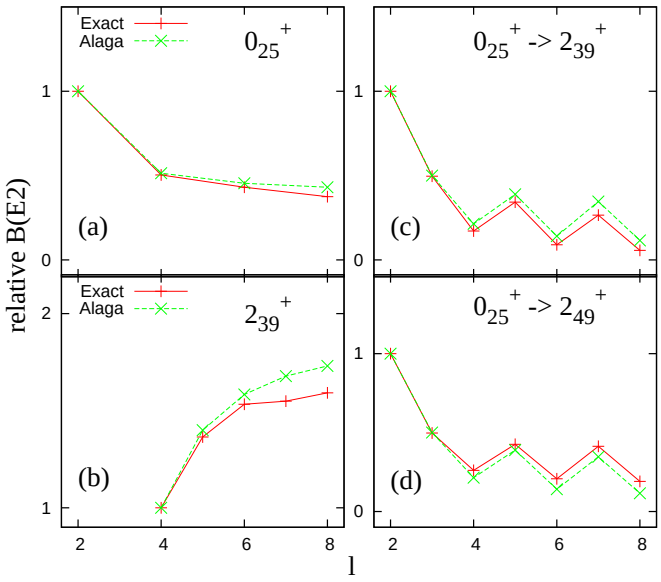

FIG. 9: Separation of intrinsic and collective rotational motion is demonstrated by significant accuracy of the Alaga rule for relative $B(E2; l-2 \to l)$ transitions. Panels (a) and (b) show relative intra-band transitions, while panels (c), (d) show relative inter-band transitions between the bands headed by the states indicated in each panel, while $\eta = 0.5$, $\chi = -0.9$ and $N = 30$. The interband $B(E2; l-2 \to l)$ transitions are supplemented by $B(E2; l-1 \to l)$ in cases of odd l. The bands reside in the predominantly regular interval of intermediate energies around $E \approx 0$ (see Fig. 4).

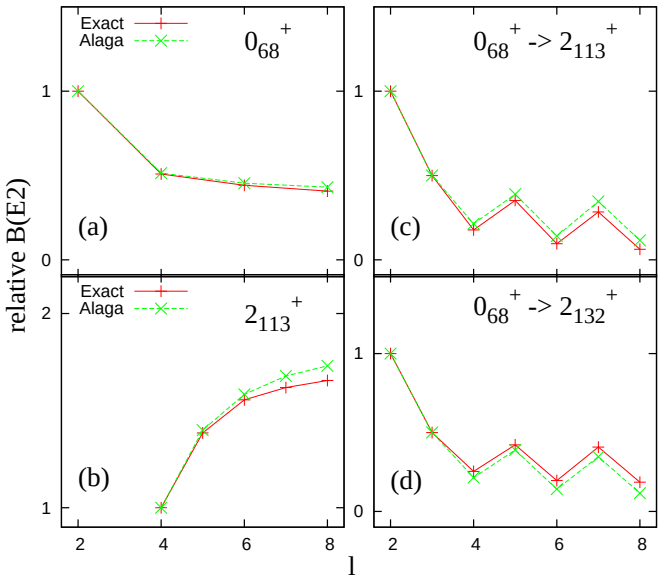

FIG. 10: The relative $B(E2; l-2 \to l)$ transitions as in Fig. 9, but now for bands selected from the highest-energy spectrum near to $E \approx E_{\max}$. The interband $B(E2; l-2 \to l)$ transitions are supplemented by $B(E2; l-1 \to l)$ in cases of odd l. The detailed position of the bands within the $\hat{n}_d$ spectral lattice is indicated in Fig. 7.

"chaotic" wave functions fill the classically accessible configuration space more or less homogeneously with very complicated nodal patterns, while the "regular" wave functions show a distinct pattern of nodes and antinodes approximately following the paths of classical regular trajectories, see Refs. [27, 31, 39]. A perturbation—in this case the external rotation added—is then more likely to mix the chaotic wave functions rather than the regular ones among one another.

VII. ACKNOWLEDGEMENT

The authors appreciate the encouragement and fruitful discussions on the quasi dynamical symmetries with D. J. Rowe, A. Leviatan and F. Iachello and the help of P. Stránský with the classical numerical calculations. This work was supported by the Czech Science Foundation (grant no. 202/09/0084) and by the Czech Ministry of Education (under projects MSM 0021620859).

[1] R. F. Casten, *Nuclear Structure from a Simple Perspective*, (Oxford University Press, New York, 1990).

[2] I. Talmi, *Simple Models of Complex Nuclei*, (Harwood Academic Publishers, Chur, Switzerland, 1993).

[3] A. Frank, J. Jolie, P. Van Isacker, *Symmetries in Atomic Nuclei: from Isospin to Supersymmetry*, (Springer Science+Business Media, New York, 2009).

[4] F. Iachello, A. Arima, *The Interacting Boson Model* (Cambridge University Press, Cambridge, UK, 1987).

[5] A. Frank, P. Van Isacker, *Symmetry Methods in Molecules and Nuclei* (S y G Editores, Mexico, D.F., 2005).

[6] D. J. Rowe, *Nucl. Phys.* **A745**, 47 (2004).

[7] G. Rosensteel, D. J. Rowe, *Nucl. Phys.* **A759**, 92 (2005).

[8] D. J. Rowe, in *Computational and Group-Theoretical Methods in Nuclear Physics*, ed. by J. Escher, O. Castaños, J. G. Hirsch, S. Pittel and G. Stoitcheva (World Scientific, Singapore, 2004), p.165.

[9] D. J. Rowe, P. Rochford, J. Repka, *J. Math. Phys.* **29**, 572 (1988).

[10] P. O. Hess, A. Algora, M. Hunyadi and J. Cseh, *Eur. Phys. J. A* **15**, 449454 (2002).

[11] M. Jarrio, J. L. Wood, D. J. Rowe, *Nucl. Phys.* **A528**, 409 (1991); D. Turner, D.J. Rowe, *Nucl. Phys.* **A756**, 333 (2005); J. Cseh, A. Algora, J. Darai, P. O. Hess, *Phys. Rev. C* **70** 034311 (2004).

[12] Y. Alhassid, N. Whelan, *Phys. Rev. Lett.* **67**, 816 (1991).

[13] N. Whelan, Y. Alhassid, *Nucl. Phys.* **A556**, 42 (1993).

[14] M. Macek, P. Stránský, P. Cejnar, S. Heinze, J. Jolie, J. Dobeš, *Phys. Rev. C* **75**, 064318 (2007).

[15] M. Macek, J. Dobeš, P. Cejnar, *Phys. Rev. C* **80**, 014319 (2009).

[16] P. O. Lipas, P. Toivonen, D. D. Warner, *Phys. Lett.* **B155**, 295 (1985).

[17] D. D. Warner, R. F. Casten, *Phys. Rev. Lett.* **48**, 1385 (1982).

[18] J. N. Ginocchio, M. W. Kirson, *Phys. Rev. Lett.* **44**, 1744 (1980); *Nucl. Phys.* **A350**, 31 (1980).

[19] A. E. L. Dieperink, O. Scholten, F. Iachello, Phys. Rev. Lett. **44**, 1747 (1980); A. E. L. Dieperink, O. Scholten, *Nucl. Phys.* **A346** 125 (1980).

[20] A. Bohr, *K. Dan. Vidensk. Selsk., Mat.-Fys. Medd.* **26**, 14 (1952); A. Bohr, B. R. Mottelson, *K. Dan. Vidensk. Selsk., Mat.-Fys. Medd.* **27**, 16 (1953);

[21] A. Leviatan, *Ann. Phys.* **179**, 201 (1987).

[22] E. Canetta, G. Maino, *Phys. Lett. B* 483, 5559 (2000).

[23] P. Cejnar, J. Jolie, *Phys. Lett. B* 420, 241 (1998); *Phys. Rev. E* **58** 387 (1998).

[24] M. Macek, P. Cejnar, J. Jolie, S. Heinze, *Phys. Rev. C* **73**, 014307 (2006).

[25] P. Cejnar, M. Macek, S. Heinze, J. Jolie, J. Dobeš, *J. Phys. A: Math. Gen.* **39**, L515 (2006).

[26] A. Peres, *Phys. Rev. Lett.* **53**, 1711 (1984).

[27] M. C. Gutzwiller, *Chaos in Classical and Quantum Mechanics* (Springer, New York, 1990).

[28] L. E. Reichl, *The Transition to Chaos in Conservative Classical Systems: Quantum Manifestations* (Springer-Verlag, New York, 1992).

[29] S. Ree, L. E. Reichl, *Phys. Rev. E* **60**, 1607 (1999).

[30] N. Shrivastava, C. Kaufmann, G. Muller, *J. Appl. Phys.* **67**, 5627 (1990).

[31] P. Stránský, P. Hruška, P. Cejnar, *Phys. Rev. E* **79**, 046202 (2009); *Phys. Rev. E* **79**, 066201 (2009).

[32] P. Stránský, M. Macek, P. Cejnar, J. Dobeš, in Proc. of *13th International Symposium on Capture Gamma-Ray Spectroscopy*, Cologne, 2008, AIP Conderence Proceedings Series **1090**, 174 (Springer-Verlag, New York, 2009).

[33] M. Macek, P. Stránský, P. Cejnar, *Int. J. Mod. Phys. E*, **18**, 1058 (2009); see also arXiv: 0810.2949 [nucl-th].

[34] P. Stránský, M. Kurian, P. Cejnar, *Phys. Rev. C* **74**, 014306 (2006).

[35] Ch. Skokos, *J. Phys. A: Math. Gen.* **34** 10029 (2001).

[36] G. Alaga, K. Adler, A. Bohr, B. R. Mottelson, *Dan. Mat. Fys. Medd.* **29**, no.9 (1955).

[37] O. Scholten, in *Computational Nuclear Physics 1, Nuclear Structure*, ed. by K. Langanke, J. A. Maruhn, S. E. Koonin (Springer-Verlag, 1991).

[38] D. Bonatsos, E. A. McCutchan, R. F. Casten, *Phys. Rev. Lett.* **104**, 022502 (2010).

[39] H.-J. Stöckmann, *Quantum Chaos. An Introduction* (Cambridge Universty Press, Cambridge, UK, 1999).